Black Hole Jets, Accretion Discs and Dark Energy

William John Potter

Astrophysics Department

University of Oxford

A thesis submitted for the degree of

Doctor of Philosophy

To Mum and Dad.

Acknowledgements

I am indebted to a great number of people who have helped or encouraged me in my academic life. It would be impossible to do their actions justice or mention everyone in a few blunt words.

There are many people in the astrophysics department who have contributed towards this thesis. My supervisor Garret Cotter whose help, support and good judgement saved me a lot of time and effort and to whom I owe many an entertaining trip. My two best friends in the department Phil Bull and Rich Booth for making my three years fun and for always being happy to talk about physics. Sirichai Chongchitnan for patiently showing me how to write a paper and Steve Balbus for introducing me to the world of accretion discs and fluid dynamics. Lance Miller, Philipp Podsiadlowski, Pat Roche, Tony Lynas-Gray and Mike Jones for their academic support. My office-mates, past and present, for the debates, games, jokes and informal I.T. support. Ashling Morris and Vanessa Ferraro-Wood who prevented me from becoming incapacitated under a large pile of forms.

Away from Oxford, I would like to thank Jim Hinton and Richard White for their hospitality when visiting Leicester. Roger Blandford for repeatedly making the time to see me when I was in Stanford despite being in constant demand and Greg Madejski for being an enthusiastic and friendly face in a foreign department. I would like to thank Sebastien Fromang and especially Julien Faure for their patience and hospitality during my visit to Saclay.

Finally, I would like to acknowledge the ongoing support of my family, in particular my parents for their inexhaustible kindness, helpfulness and encouragement, and for teaching me what is important in life. My Dad for reading this thesis with painstaking attention to detail. Ros for her help, encouragement, clear advice in the face of indecision and for reading this thesis and listening to my talks. My Nan for her kindness, stories, generosity and cakes.

Abstract

Black hole jets, Accretion discs and dark energy

William John Potter

Magdalen College, University of Oxford

Submitted for the degree of Doctor of Philosophy

Trinity Term, 2013

Black hole jets and accretion discs are the most extreme objects in modern astrophysics whilst dark energy is undoubtedly the most mysterious. This thesis focuses on understanding these three topics. The majority of this thesis is dedicated to investigating the structure and properties of black hole jets by modelling their emission. I develop an inhomogeneous jet model with a magnetically dominated parabolic accelerating base, transitioning to a slowly decelerating conical jet, with a geometry set by radio observations of M87.

This model is able to reproduce the simultaneous multiwavelength spectra of all 38 Fermi blazars with redshifts in unprecendented detail across all wavelengths. I constrain the synchrotron bright region of the jet to occur outside the BLR and dusty torus for FSRQs using the optically thick to thin synchrotron break. At these large distances their inverse-Compton emission originates from scattering CMB photons. I find an approximately linear relation between the jet power and the transition region radius where the jet first comes into equipartition, transitions from parabolic to conical and stops accelerating. The decreasing magnetic field strength and increasing bulk Lorentz factor with jet power are the physical reasons behind the blazar sequence.

I calculate the conditions for instability in a thin accretion disc with an α parameter which depends on the magnetic Prandtl number, as suggested by MHD simulations. The global behaviour of the instability induces cyclic flaring in the inner regions of the disc, for parameters appropriate for X-ray binary systems, thereby offering a potential solution to a long standing problem. Finally, I calculate the effect of an interacting quintessence model of dark energy on cosmological observables. I find that a scalar-tensor type interaction in the dark sector results in an observable increase in the matter power spectrum and integrated Sachs-Wolfe effect at horizon scales.

Declaration of Authorship

The work in this thesis is based on the following 7 papers:

Chapter 2 - William J. Potter and Garret Cotter, 2012, MNRAS, 423, 756.

Chapter 3 - William J. Potter and Garret Cotter, 2013, MNRAS, 429, 1189.

Chapter 4 - William J. Potter and Garret Cotter, 2013, MNRAS, 431, 1840.

Chapter 5- William J. Potter and Garret Cotter, accepted for publication in MNRAS, 2013.

Chapter 6 - William J. Potter and Garret Cotter, in prep. 2013.

Chapter 7 - William J. Potter and Steven Balbus, in prep. 2013.

Chapter 8 - William J. Potter and Sirichai Chongchitnan, 2011, JCAP 09, 005P.

I hereby certify that the work in this thesis is wholly my own, except where explictly stated, with the following exceptions:

Chapter 2 - The text in the introduction and conclusion was written jointly by Garret Cotter and myself.

Chapter 7 - The text in Sections 7.1 and 7.2 was written by Steven Balbus and later edited by myself.

Chapter 8 - The text was written jointly by Sirichai Chongchitnan and myself.

Contents

Contents **vi**

1 Introduction **1**

1.1 Historical overview of black holes 1

1.2 Black hole jets and blazars 4

1.2.1 The Kerr metric 4

1.2.2 Blandford-Znajek process 7

1.2.3 Observations of blazars 8

1.2.4 Spectral properties and the blazar sequence 9

1.2.5 Relativistic MHD simulations and theory 11

1.2.6 Radiation processes 12

1.2.6.1 Synchrotron emission 13

1.2.6.2 Inverse-Compton emission 14

1.2.7 Acceleration of non-thermal electrons 15

1.2.7.1 Diffusive shock acceleration 16

1.3 Accretion discs 17

1.3.1 Thin accretion disc equations 17

1.3.2 Emitted spectrum of an optically thick thin disc 20

1.4 Cosmology 21

1.4.1 Cosmological distance measurements 21

1.5 Thesis structure 22

2 A Uniform Conical Jet Model **24**

2.1 Introduction 24

2.2 Jet Model . . . 27
2.2.1 Determining the Jet Parameters at the Base . . . 28
2.2.2 Magnetic Field Strength . . . 30
2.3 Electron radiative losses . . . 30
2.4 Expansion losses . . . 31
2.5 Synchrotron emission . . . 32
2.5.1 Opacity . . . 33
2.6 Inverse-Compton Scattering . . . 35
2.6.1 Obtaining the Inverse-Compton Spectrum . . . 36
2.6.2 Klein-Nishina Cross Section . . . 37
2.7 Synchrotron Seed Photons . . . 38
2.8 Doppler Boosting of Emission . . . 39
2.9 Results . . . 41
2.9.1 Modelling the SED of BL Lacertae . . . 41
2.9.2 Producing a Flat Radio Spectrum . . . 45
2.10 Conclusions . . . 47

3 An accelerating jet model with a geometry based on observations of M87 48

3.1 Introduction . . . 49
3.2 Jet Model . . . 51
3.2.1 Geometry . . . 52
3.2.2 Acceleration and deceleration . . . 53
3.2.3 Energy and particle conservation for the plasma . . . 54
3.3 Physical conditions at the base of the jet . . . 58
3.4 Synchrotron emission . . . 60
3.5 Inverse-Compton emission . . . 61
3.5.1 SSC emission . . . 61
3.5.2 Inverse-Compton scattering of external photons . . . 61
3.5.3 CMB . . . 64
3.5.4 Thin Accretion Disc . . . 65
3.5.5 Starlight . . . 65

3.5.6 Accretion disc photons scattered by the broad line region 67
3.5.7 Dusty Torus and Narrow Line Region 68
3.5.8 Observed external Compton emission 69
3.6 Particle acceleration and energy losses 70
3.7 Acceleration of electrons in the decelerating conical part of the jet 71
3.8 Equipartition considerations 72
3.9 Code 73
3.10 Results 75
3.10.1 Fit 1 - A transition region at large distances 75
3.10.2 Fit 2 - A transition region within the dusty torus 80
3.10.3 Fit 3 - A transition region within the BLR 81
3.10.4 Constraining the location of the emission region 84
3.10.5 An adiabatic or ballistic conical jet? 86
3.10.6 Discussion 88
3.11 Conclusion 91

4 Compton-dominant blazars 93

4.1 Introduction 93
4.2 Jet Model 95
4.2.1 Electron energy losses due to emission 95
4.3 Results 96
4.3.1 The different models 97
4.4 Radio emission 97
4.5 Optically thick to thin synchrotron break 98
4.5.1 Frequency core-shift 101
4.6 Fitting the multiwavelength spectra 104
4.6.1 The ballistic model 104
4.6.2 The adiabatic model 109
4.6.3 Inverse-Compton scattering of external photons 110
4.6.4 Acceleration of electrons along the jet 112
4.6.5 Compton drag 113

4.6.6 The blazar sequence . . . 113
4.7 Conclusion . . . 117

5 BL Lacs 120

5.1 Introduction . . . 121
5.2 Jet Model . . . 121
5.3 Photon-photon pair production . . . 121
5.4 External photon fields for BL Lacs . . . 124
5.5 Results . . . 125
5.5.1 Understanding the blazar sequence . . . 130
5.5.2 Scenario I - A universal jet geometry . . . 131
5.5.3 Scenario II - A dichotomy in accretion rate . . . 132
5.5.4 Using emission spectra to understand jet dynamics and properties . . . 133
5.5.5 The location of the TeV emission region . . . 134
5.5.6 High power, high synchrotron peak BL Lacs . . . 137
5.6 Conclusion . . . 138

6 Understanding the physics behind the blazar population 142

6.1 Introduction . . . 142
6.2 Results . . . 143
6.3 Summary . . . 150
6.4 Appendix A . . . 151

7 An accretion disc instability induced by a variable α - an explanation for X-ray binary state transitions 160

7.1 Introduction . . . 160
7.2 Analysis . . . 163
7.2.1 Thin disc equations . . . 163
7.2.1.1 Coordinates and dynamics . . . 163
7.2.1.2 Radiative considerations . . . 165
7.3 Instability criteria . . . 166
7.4 Numerical work . . . 169

7.5 Testing the instability criterion numerically . . . 169
7.5.1 Radiation pressure . . . 170
7.6 Time-dependent disc simulation . . . 172
7.6.1 Behaviour of the instability . . . 173
7.7 Comparison to observations . . . 175
7.8 Conclusion . . . 178

8 A gauge-invariant approach to interactions in the dark sector 179
8.1 Introduction . . . 179
8.2 Quintessence models . . . 181
8.2.1 Ratra-Peebles . . . 181
8.2.2 SUGRA . . . 182
8.2.3 Double exponential . . . 182
8.3 Evolution of background energy densities . . . 182
8.3.1 Evolution equations . . . 184
8.4 Perturbations . . . 186
8.4.1 Covariant formulation of dark sector interactions . . . 187
8.4.2 Power spectra without interactions . . . 190
8.5 Integrated Sachs-Wolfe effect . . . 191
8.6 Modelling dark sector interactions . . . 193
8.6.1 Dark matter decay . . . 193
8.6.2 Dark energy decay . . . 194
8.6.3 Scalar-tensor model . . . 195
8.7 Results . . . 196
8.7.1 Instability in the dark energy decay model . . . 196
8.7.2 Dark matter decay . . . 197
8.7.3 Scalar-tensor model . . . 200
8.8 Conclusion and discussion . . . 204

9 Conclusions 206
9.1 Future work and limitations . . . 209

Chapter 1

Introduction

The work in this thesis is broadly divided into three areas: black hole jets, accretion discs and cosmology. This introductory chapter has been arranged into background material relating to these three topics in turn. The majority of the work in this thesis deals with modelling the emission from black hole jets and so correspondingly most of the content of this Chapter is dedicated to our theoretical and observational knowledge of jets. The physics of black hole jets and accretion discs are closely interrelated and so there is significant overlap between the background material of the two areas. For fluency and brevity I have only included the background material related to accretion discs and cosmology which is also relevant to jets in this introduction. This means that Chapter 7 and section 1.3 of this introduction combined, and Chapter 8 individually can be treated as self-contained.

1.1 Historical overview of black holes

Black holes have come to epitomise all that is wonderfully predictive and profoundly unintuitive about Einstein's theory of General Relativity. The precursors to modern black holes, "Dark Stars", were first postulated by John Michell in a letter to Henry Cavendish in 1783. These were stars that were so dense that the escape velocity of a particle at their surface was greater than the speed of light. However, Dark Stars were rooted in Newtonian physics and so lacked the most interesting aspect of black holes: the event horizon. The idea of Dark Stars fell out of favour when the wave theory of light was developed and light was assumed to be massless and unaffected by gravity. It was over a hundred years until the idea of a body whose gravity is so strong that light itself cannot escape was resurrected. In 1915, only months after Einstein published his theory of General Relativity (Einstein [1915]), Karl Schwarzschild, whilst fighting on the Russian front in World War I, calculated the first exact solution to Einstein's field equations. The Schwarzschild metric components can be expressed in terms of an invariant interval $ds^2 = g_{\mu\nu}dx^\mu dx^\nu$, written in spherical polar coordinates this is

$$ds^2 = \left(1 - \frac{r_s}{r}\right) c^2dt^2 - \left(1 - \frac{r_s}{r}\right)^{-1} dr^2 - r^2d\theta^2 - r^2 \sin^2 \theta d\phi^2. \tag{1.1}$$

The Schwarzschild metric is the static solution for space-time outside a non-rotating, spherically symmetric mass distribution. Whilst at large distances this metric produces results tending to Newtonian gravity, if we are close to a sufficiently dense mass the effects of General Relativity become dominant. The most intriguing property of the metric is the existence of an event horizon at the Schwarzschild radius ($r_s = 2GM/c^2$). The event horizon is a unidirectional surface from which no particle can ever escape (classically) but particles can enter. Particles within the event horizon are inexorably drawn to the singularity at its centre. For many years a mass distribution dense enough to have an event horizon was thought to be a scientific impossibility. In 1930, at age 19, Subrahmanyan Chandrasekhar calculated the mass limit above which the fermionic pressure of electrons would be insufficient to support a star against gravitational collapse and predicted the collapse into a black hole (Chandrasekhar [1931]). This idea was initially opposed on the idealogical ground that black holes were thought to be physically impossible. In fact the Chandrasekhar mass is the maximum theoretical mass of a white dwarf before it collapses into a neutron star. Later work by Tolman, Oppenheimer and Volkoff (Tolman [1939] and Oppenheimer and Volkoff [1939]) extended Chandrasekhar's calculation to find the upper limit on the mass of a neutron star. Today neutron stars are believed to be the penultimate dense state before formation of a black hole.

For many years black holes were treated as purely theoretical curiosities. However, in the late 1950s and early 60s a class of bright, point-like, highly variable quasi-stellar objects (quasars) were observed. In contrast to stars these quasars were found to have large redshifts, which led to the realisation that they must be located at large extra-galactic distances. As observations improved it was found that quasars were very bright sources located close to the centre of a host galaxy, with a luminosity often exceeding that of all the stars contained in the galaxy. Today the only plausible method known to generate such huge amounts of energy in such a compact region is the existence of an accreting supermassive black hole.

In addition to the compact emission of an accreting disc of material, radio observations of roughly 10% of active galactic nuclei show back-to-back narrow, extended regions of radio emission stretching from the nucleus out to distances of hundreds of kiloparsecs (Antonucci [1993], Urry and Padovani [1995] and Ferrari [1998]). The associated brightness temperature of the region producing the radio emission is so large that the emission cannot be thermal due to the extreme energy requirements (Wagner and Witzel [1995]). This has led to the idea of a plasma containing a large proportion of non-thermal high-energy electrons which produce radio synchrotron emission through interaction with a tangled magnetic field in the plasma jet. These plasma jets are observed to remain collimated and relativistic until hitting a hot spot at large distances from the black hole in the case of Fanaroff-Riley type II sources (FRII), or to decelerate and break up due to instabilities at large distances in the case of FRI sources (Fanaroff and Riley [1974], Baum et al. [1995] and Laing and Bridle [2002]). It is thought that in FRII jets the jet plasma remains relativistic until kpc scales where the jet terminates in a hot spot caused by a shock as the jet collides with the ambient gas (see for example Blandford and Rees [1974] and Hardcastle [2008]). The heated, shocked gas expands to form a hot bubble or cocoon surrounding the jet called a radio lobe. The energy released in the hot spot (and contained in the radio lobes) together with observations of the speed at which the hot spot is being driven into the intergalactic medium (IGM) have allowed astronomers to estimate the energy and momentum of the plasma jet (Ferrari [1998]). The evidence for a relativistic jet also comes from observations of jets in which one jet appears far brighter than the other. Such extreme brightness ratios can only be easily explained by Doppler-boosting of the jet emission (Urry and Padovani [1995]).

Observationally, the most extreme class of these jets are called blazars. They are the most luminous and highly variable of active galactic nuclei (AGN) jets with observed superluminal motion of radio components indicating relativistic jet speeds. They are believed to be the sub-class of AGN in which one jet is travelling very close to our line of sight and so we observe the jet to be Doppler-boosted, increasing the observed brightness and decreasing the time-scale of variability of the jet emission (Wagner and Witzel [1995], Urry and Padovani [1995] and

Ulrich et al. [1997]). Having outlined the discovery and basic properties of jets, the rest of this chapter will focus on presenting the theoretical and observational background material in more detail, an understanding of which will be assumed in the rest of this thesis.

1.2 Black hole jets and blazars

1.2.1 The Kerr metric

AGN are such powerful, compact sources that it has become widely accepted that we must be witnessing black holes accreting matter. This is because black holes offer the potential to release a large fraction of the rest mass of infalling matter as heat and energy, making them the most efficient energy generators in the Universe. Uncharged black holes are usually described by the Kerr metric (Kerr [1963]): the stationary, axisymmetric solution for a point mass with angular momentum. The solution is very well studied and there are several key results which have applicability to astrophysical black holes. The 'no-hair theorems' (Israel [1967], Israel [1968], Carter [1970], Hawking [1971] and Hawking [1972]) state that the only observable properties of a black hole are its mass, charge and angular momentum (or spin). Deviations from a precise Kerr black hole have been shown to decay quickly over time due to gravitational radiation (Centrella et al. [2010]). This gives us reasonable confidence that physical black holes are well-described by the Kerr metric. For a black hole of mass M and angular momentum, $J = Mac$, the Kerr metric in spherical polar coordinates is

$$ds^2 = \left(1 - \frac{r_s r}{\rho^2}\right) c^2 dt^2 - \frac{\rho^2}{\Delta} dr^2 - \rho^2 d\theta^2 - \left(r^2 + a^2 + \frac{r_s r a^2}{\rho^2} \sin^2\theta\right) \sin^2\theta d\phi^2 ... \\ + \frac{2 r_s r a \sin^2\theta}{\rho^2} c dt d\phi, \tag{1.2}$$

where $\rho = r^2 + a^2 \cos^2\theta$, $\Delta = r^2 - r_s r + a^2$ and the black hole spin $a = J/Mc$ where J is the total angular momentum of the black hole chosen to be aligned with the z-axis. The metric fully describes the geometry of space-time, the equations of motion of a particle moving in this space-time are then derived from a variational principle. Using the Euler-Lagrange equation particle trajectories or geodesics are calculated using a Langrangian of the form $L = g_{\mu\nu}\dot{x}^\mu \dot{x}^\nu$

where a dot signifies taking a derivative with respect to an affine parameter (normally the proper time for a massive particle). This leads to the interpretation of a geodesic being the path between two points in space-time which maximises the proper time measured between the two points for a massive particle, or, alternatively, the path travelled by a particle experiencing no acceleration in its rest frame (parallel transport). The Euler-Lagrange equations are

$$\frac{\mathrm{d}}{\mathrm{d}\lambda}\left(\frac{\partial L}{\partial \dot{x}^{\mu}}\right) = \frac{\partial L}{\partial x^{\mu}}. \tag{1.3}$$

There are several useful properties derived from the metric which are used in astrophysics, which I will now briefly summarise. The first is that circular orbits for massive test particles only exist down to a radius r' known as the innermost stable circular orbit or ISCO (Hobson et al. [2006]).

$$r'^2 - 3r_s r' - 3a^2 + 4a\sqrt{2r_s r'} = 0. \tag{1.4}$$

The equivalent fraction of rest mass energy which is lost in falling from infinity down to a circular orbit at the ISCO is normally used to define the expected efficiency of energy release from accretion onto the black hole. The radius of the ISCO varies between $9r_s/2$ for a maximally retrograde spin $a = -0.5r_s$, $3r_s$ for $a = 0$ and $0.5r_s$ for a maximally prograde spin $a = 1$. The second result is the existence of two event horizons which depend on the black hole spin (a) and occur at radii $r_{\pm} = r_s \pm (\sqrt{r_s^2 - 4a^2})/2$, this can be calculated by finding the condition for a singularity in the contravariant radial metric component. In this case we confirm that these are coordinate singularities by checking that at these radii the value of the Ricci scalar remains finite. The third result is the existence of a region outside the event horizon in which only spacelike trajectories exist for massive particles, due to the g_{tt} component of the metric changing sign. This region is referred to as the ergosphere and is particularly relevant to astrophysics since it allows rotational energy to be extracted from the black hole. This mechanism was originally discovered by Roger Penrose (Penrose [1969]); it is referred to as the Penrose Process.

The extraction of rotational energy from the black hole to an infinite distance is allowed because of the existence of the ergosphere where $g_{tt} < 0$. The metric components do not depend on t or ϕ and so, from the Euler Lagrange equations (Equation 1.3), the P_t and P_ϕ components of 4-momentum are conserved along a geodesic. The energy of a particle as measured by an observer at rest located at infinity is given by $U^\mu P_\mu = cP_t$, where $U^\mu = (c, 0, 0, 0)$ is the 4-velocity of the observer. In fact, due to the conservation of P_t along a geodesic this is always valid at any point along the geodesic. Inside the ergosphere however, the 4-vector U becomes spacelike $U^\mu U^\nu g_{\mu\nu} = g_{tt} < 0$. For any spacelike 4-vector there exists a local Lorentz transformation to a frame in which the 4-vector has no temporal component (Woodhouse [1992]). So, inside the ergosphere, the energy of a particle as measured by the observer at infinity is then related only to the spatial 3-momentum of the particle, the projected component of which can be either positive and negative. Of course, a local observer inside the ergosphere will always observe the particles to have positive energy and any collisions will conserve 4-momentum (and clearly any particle with negative energy as measured by the observer at infinity must be gravitationally bound within the ergosphere). The reason it is possible for observers located at infinity and within the ergosphere to disagree on the sign of the particle's energy is because within the ergosphere any massive particle must be corotating with the black hole since $U^\mu U_\mu = c^2$ and the 4-velocity of a stationary observer U is clearly spacelike inside the ergosphere. This means that within the ergosphere the energy of a particle as measured by a local observer also includes a component depending on P_ϕ.

The Penrose process operates by allowing a particle (or two) to fall into the ergosphere and either decay into two particles or collide with another particle. For some collisions it is possible to decay so that one particle has negative $P_t = E_1/c$ and so by energy conservation, if the other particle escapes to infinity it will carry more energy than the initial energy (E_0) of the particle/particles since $E_2 = E_0 - E_1 > E_0$. The particle with a negative energy as measured by the observer at infinity will fall into the black hole, reducing the energy and momentum of the black hole and allowing global energy conservation. The Penrose process shows us that we can in principle extract large amounts of rotational energy from the black hole. In practice, however, the expectation value of energy gained from such collisions is expected to be small because of the need to fine-tune the trajectories of the two massive particles in order to produce an efficient collision and the number of such collisions occuring naturally is insufficient (Bardeen et al. [1972]). The seminal paper by Blandford and Znajek

(Blandford and Znajek [1977]) offers, as of yet, the only plausible mechanism by which the required energy to produce a poynting dominated jet can be extracted from a rotating black hole. The process is much like an electromagnetic version of the Penrose process.

In addition to the Blandford-Znajek mechanism for the extraction of energy from a rotating black hole there exists a similar Blandford-Payne (Blandford and Payne [1982]) mechanism for the extraction of energy from a rotating disc. The Blandford-Payne mechanism considers magnetic field lines anchored to the surface of a keplerian accretion disc, extending away from the disc. They calculated that for field lines with an angle $> 30^o$ from vertical, charged particles would be accelerated along the field lines away from the disc by a magneto-centrifugal force (analogous to beads on a wire). This mechanism is widely used to explain non-relativistic, or mildly relativistic outflows in accretion discs around young stars and black holes (see for example Shu et al. [1994] and Balbus and Hawley [1998]). The mechanism is not adequate to produce a highly-relativistic jet, however, because in order for a jet to be accelerated to large bulk Lorentz factors in AGN it must start magnetically dominated at the base to avoid Compton-drag (Sikora et al. [1996] and Ghisellini and Tavecchio [2010]). An outflow produced by the Blandford-Payne mechanism will contain significant mass and so will not be Poynting-dominated.

1.2.2 Blandford-Znajek process

Blandford and Znajek considered the effect of the rotation of a black hole on the magnetic field of an accreting plasma. They showed that it is possible to extract rotational energy from the black hole with a magnetic field threading the black hole's event horizon. However, unlike the Penrose process this process is expected to be efficient since the magnetic field does not have to be fine-tuned in order to extract energy as in the case of particle collisions. The Blandford-Znajek mechanism is currently believed to be the physical process responsible for the production of highly-relativistic, Poynting dominated jets from accreting black holes.

In principle the calculation of the energy extracted by an electromagnetic field threading a Kerr black hole is straightforward, however, the actual calculation quickly becomes algebraically intense and the results are difficult to understand intuitively. The calculation involves looking for force-free solutions for the electromagnetic field in the Kerr metric. The electromagnetic field tensor is $F_{\mu\nu} = \partial_\mu A_\nu - \partial_\nu A_\mu$ defined in terms of the vector potential $A_\mu = (\phi/c, \mathbf{A})$, where ϕ and $\mathbf{A}$ are the electric and magnetic vector potential respectively. Blandford and Znajek argue that sufficient charged particles are produced close to the event horizon by pair production from synchrotron radiation to allow the region to be considered force-free ($F_{\mu\nu}J^\mu = 0$) where J^μ is the current 4-vector. The conservation of current, $\nabla_\mu J^\mu = 0$ must also be satisfied and the Einstein-Maxwell equations $\nabla_\mu F^{\mu\nu} = \mu_0 J^\nu$, where ∇_μ is the covariant derivative and the homogeneous Maxwell equations are automatically satisfied by expressing $F_{\mu\nu}$ in terms of the vector potential A_μ. In this case they calculated the radial Poynting flux at the event horizon to be $\omega(\Omega_H - \omega)(B_r/(r_+^2 + a^2\cos^2\theta))^2(r_+ + a^2)\epsilon_0$, where ω is the rotational velocity of the field lines and $\Omega_H = a/(r_+^2 + a^2)$ is the angular velocity of the black hole.

To find solutions for the electromagnetic field surrounding a rotating black hole we need to specify the boundary conditions at infinity and the event horizon. This proves very difficult for all but the simplest of boundary conditions. In their paper Blandford and Znajek used a perturbative technique to calculate the properties of the field for black holes with small spins perturbed slightly from the Schwarzschild cases. For the case of a paraboloidal field this perturbative calculation gave an efficiency of 38% relative to the maximum extractable energy. The solutions are back-to-back parabolic field lines extending away from the black hole in directions perpendicular to the disc and rotating in the same direction as the black hole. It is extraordinary that this picture still forms the basis of our understanding and models of jets today, even following the development of relativistic MHD simulations (see for example McKinney [2006] and Tchekhovskoy et al. [2010]).

1.2.3 Observations of blazars

Blazars are the most luminous and highly variable of AGN. They have been observed at all wavelengths from radio to high energy γ-rays and are believed to be AGN observed at small angles to the jet axis (Urry and Padovani [1995]) resulting in Doppler-boosting of their emission. The characteristic spectral shape is a non-thermal continuum with two main peaked components: the radio through to UV/X-rays show signs of polarisation typical of synchrotron radiation whilst the second component extends from low energy X-rays through to very high energy γ-rays and is normally attributed to inverse-Compton scattering of photons from the synchrotron-emitting electrons (Abdo et al. [2010a]). The radio emission of blazars is predominantly observed to be flat or nearly flat in flux density (see for example Owen et al. [1980] and Abdo et al. [2010a]) whilst the majority of the synchrotron and inverse-Compton emission can be well described by a power law and a turnover (see Figure 6.4).

For relativistic jet speeds the emission from the jet plasma is Doppler-boosted and beamed in the direction of motion of the jets and this results in the high luminosity and rapid variability of blazars. The observation of superluminal motion was first predicted by Martin Rees (Rees [1966]) as being a relativistic illusion when observing an object travelling close to the speed of light at a small angle to the direction of observation ($\beta_{obs} = \beta \sin\theta/(1-\beta\cos\theta)$). Superluminal motion has been observed in many blazar jets (Jorstad et al. [2001]) and since superluminal motion can only occur for $\beta \geq 1/\sqrt{2}$, this immediately tells us that jets must be relativistic.

Radio observations show that AGN jets are approximately continuous axisymmetric plasma jets. Recent observations show that on large scales jets are approximately conical in geometry and measurements of the frequency dependent core-shift of M87 and other AGN favour a conical jet with conserved magnetic energy (Krichbaum et al. [2006], Kovalev et al. [2007] and Sokolovsky et al. [2011]). VLBI observations of M87 by Hada et al. [2011] show that the blunt base of the jet is within $14 - 23R_S$ of the central black hole. Observations of the geometry of the jet in M87 by Asada and Nakamura [2011] over a large range of length scales show that the jet is in fact parabolic close to the base becoming conical at $10^5 R_S$. These observations are supported qualitatively by simulations of AGN jets powered by the Blandford-Znajek mechanism (see McKinney [2006], Komissarov et al. [2007], McKinney and Blandford [2009] and Tchekhovskoy et al. [2010]) which show an accelerating parabolic base becoming conical near to the point where the plasma reaches equipartition.

1.2.4 Spectral properties and the blazar sequence

Blazars have spectra which consist of polarised synchrotron emission from radio to X-rays and inverse-Compton emission from X-rays to high energy gamma-rays produced by non-thermal electrons. The population of blazars is split into two main spectral classifications: Flat Spectrum Radio Quasars (FSRQs) and BL Lacs. FSRQs are blazars in which emission

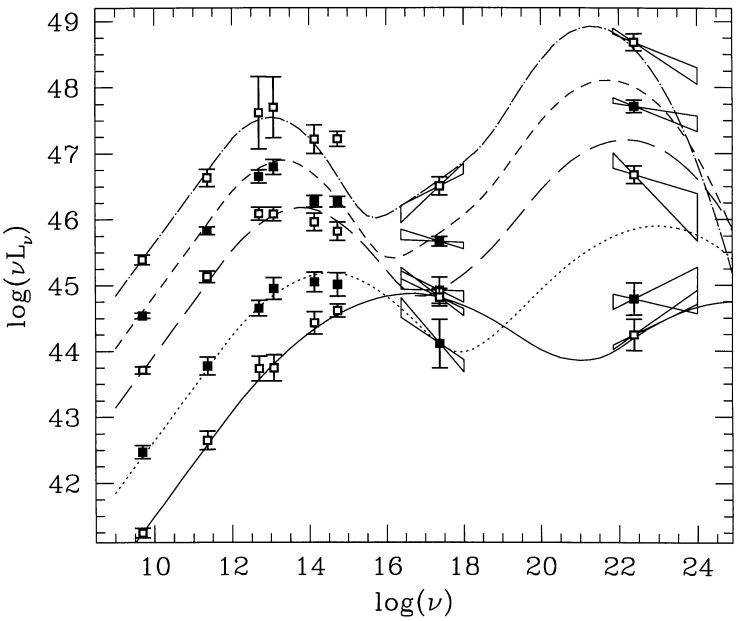

Figure 1.1: The blazar sequence, taken from Fossati et al. [1998]. This shows the anticorrelation between radio power (used as a proxy for the jet power) and peak synchrotron and inverse-Compton frequencies. We also see the increasing ratio of inverse-Compton to synchrotron power as radio power increases.

lines are visible with equivalent widths greater than 5$\mathring{A}$, BL Lacs tend to have weak or absent emission lines (Vermeulen et al. [1995]). The important work by Fossati et al. [1998] took average spectra in bins of radio power (which is a proxy for the jet power) and found a clear trend in the characteristic shape of spectra (see Figure 1.1). With increasing power they found that the peak frequency of both the synchrotron and inverse-Compton emission decreased, whilst the Compton-dominance (the ratio of power in the inverse-Compton emission relative to the synchrotron emission) increased. The lower power blazars are typically BL Lacs whilst the high power blazars are FSRQs. This trend has become known as the blazar sequence.

Unification of AGN (Antonucci [1993] and Urry and Padovani [1995]) explains blazars as a subsample of AGN with jets aligned close to the line of sight. This results in the Doppler-boosting of the jet emission, observed superluminal speeds and short timescale variability. Furthermore, it is believed that in general FSRQs correspond to high power FRII jets, while BL Lacs correspond to low power FRI type jets. This is because FRSQs have higher jet luminosities than BL Lacs (Fossati et al. [1998] and Ghisellini et al. [2009b]) and jet power is known to be a good indicator of whether a jet is an FRI or FRII (Fanaroff and Riley [1974]) with the divide occurring at approximately $0.015L_{\rm Edd}$ (where $L_{\rm Edd}$ is the Eddington luminosity (Ghisellini and Celotti [2001])). A similar divide in Eddington luminosity between FSRQs and

BL Lacs has also been found in blazars (Ghisellini et al. [2009a]), supporting the idea of AGN unification.

1.2.5 Relativistic MHD simulations and theory

The equations of MHD can be written in a Lorentz invariant form.

$$\nabla_\mu(\rho U^\mu) = 0, \qquad \nabla_\mu(T^{\mu\nu}_{EM} + T^{\mu\nu}_{M+R}) = 0, \qquad U_\nu \nabla_\mu T^{\mu\nu} = 0, \tag{1.5}$$

$$\nabla_\mu F^{\mu\nu} = \mu_0 J^\nu, \qquad \nabla_a F_{bc} + \nabla_b F_{ca} + \nabla_c F_{ab} = 0. \tag{1.6}$$

These equations represent conservation of mass, conservation of energy and momentum, the first law of thermodynamics and Maxwell's equations. The fully general relativistic MHD simulations of jet production from a black hole by the Blandford-Znajek process by McKinney [2006], Komissarov et al. [2007], McKinney and Blandford [2009], Tchekhovskoy et al. [2010] and McKinney et al. [2012] have shown that it is, in principle, possible to produce a relativistic plasma jet from accretion onto a black hole (albeit with slightly simplified physics). These simulations along with analytic work (for example Vlahakis and Königl [2003] and Beskin and Nokhrina [2006]), have allowed us to build a basic understanding of jet properties. The jet is believed to start close to the black hole as a magnetically dominated plasma with rotating field lines tied to the event horizon of the black hole. The plasma is initially accelerated by a combination of thermal and radiation pressure, and magneto-centrifugal forces (particles are accelerated by the rotation of a field line along which they travel Blandford and Payne [1982]). In order for the plasma to accelerate it must be initially collimated by external pressure forces, probably caused by the accretion disc and its wind (Komissarov et al. [2009]). Further along the jet, the magnetic energy of the plasma is slowly converted into bulk kinetic energy via acceleration by the magnetic pressure gradient produced as the jet expands radially. While the jet accelerates it has a parabolic shape but when the plasma approaches equipartition the jet stops efficiently accelerating since the inertia of the jet is now comparable to the remaining magnetic energy. The jet becomes conical, eventually losing causal contact across the jet and becoming ballistic if it is overpressured relative to the external medium (McKinney

[2006], Zakamska et al. [2008] and Komissarov et al. [2009]). These simulations and analytical calculations are qualititively compatible with observations (Asada and Nakamura [2011] and Hada et al. [2011]).

Whilst it is exciting that the general principle of jet formation from accretion onto a black hole has been verified in simulations, these simulations are not yet at the stage where detailed quantitive properties are trustworthy. Relativistic simulations are incredibly computationally expensive and so a lot of relevant physics must be neglected, most notably radiation processes and particle acceleration. Jets are known to radiate a substantial fraction of their total energy through emission from non-thermal particles and this will have an effect on the kinematics of the jet through processes such as Compton-drag (where anisotropic inverse-Compton emission results in a net change in momentum of the emitting plasma). Most importantly however, we only observe the radiation produced by jets and so in order to compare these jet models to real jets we need a realistic model for their emission. Developing a realistic model for jet emission consistent with the results of theory, simulations and observations allows us to compare the MHD properties of simulations to the spectral properties of jets. In addition we can also use observations to determine the physical parameters of the jets and better understand the physical processes which result in their production, propagation and morphological and spectral characteristics. Developing such a model to understand the physical processes and parameters of blazar jets will be the main topic addressed in this thesis in Chapters 2-6.

1.2.6 Radiation processes

The observed spectra of blazars are characterised by two humps: one extending from radio to UV or X-ray energies attributed to synchrotron emission and one extending from X-rays to high energy gamma-rays attributed to inverse-Compton emission. This non-thermal emission is fitted well by the synchrotron and inverse-Compton emission of a power-law population of electrons in a region of high magnetic field (see for example Li and Kusunose [2000], Böttcher and Chiang [2002] and Tsang and Kirk [2007]).

1.2.6.1 Synchrotron emission

In Chapters 2-6 I will make repeated use of the standard formula for the emitted synchrotron power and characteristic frequency of emission for a charged particle in a magnetic field which is derived below following the treatment by Longair [2011]. A charged particle with velocity $\mathbf{v}$ travelling at an angle θ to a magnetic field of strength $\mathbf{B}$ will experience an acceleration given by the Lorenz force law $F = e\mathbf{E} + e\mathbf{v} \times \mathbf{B}$. An accelerating charge radiates a power given by Larmor's formula $P = e^2a^2/(6\pi\epsilon_0 c^3)$, where a is the acceleration of the charge in the rest frame of the charge. The power emitted by a particle is relativistically invariant since $P = \partial E_{\text{particle}}/\partial t$ and under a Lorentz transformation both energy and time will transform as the temporal component of a 4-vector. In order to calculate the power emitted using Larmor's formula we require the acceleration of the charged particle measured in its instantaneous rest frame.

In the rest frame of the charge the acceleration will be due only to the electric field since the particle has no velocity. We calculate the electromagnetic field in the rest frame by Lorentz transforming the electromagnetic field tensor $F' = LFL$ where L is the standard Lorentz transformation tensor.

$$F'^{\mu\nu} = \begin{pmatrix} \gamma & -\gamma\beta & 0 & 0 \\ -\gamma\beta & \gamma & 0 & 0 \\ 0 & 0 & 1 & 0 \\ 0 & 0 & 0 & 1 \end{pmatrix} \begin{pmatrix} 0 & -E_x/c & -E_y/c & -E_z/c \\ E_x/c & 0 & -B_z & B_y \\ E_y/c & B_z & 0 & -B_x \\ E_z/c & -B_y & B_x & 0 \end{pmatrix} \begin{pmatrix} \gamma & -\gamma\beta & 0 & 0 \\ -\gamma\beta & \gamma & 0 & 0 \\ 0 & 0 & 1 & 0 \\ 0 & 0 & 0 & 1 \end{pmatrix} =$$

$$\begin{pmatrix} 0 & -E_x/c & -\gamma(E_y - vB_z)/c & -\gamma(E_z + vB_y)/c \\ E_x/c & 0 & -\gamma(B_z - v/c^2 E_y) & \gamma(B_y + v/c^2 E_z) \\ \gamma(E_y - vB_z)/c & \gamma(B_z - v/c^2 E_y) & 0 & -B_x \\ \gamma(E_z + vB_y)/c & -\gamma(B_y + v/c^2 E_z) & B_x & 0 \end{pmatrix} \tag{1.7}$$

The electric field in the rest frame of the particle is then given by $\mathbf{E}' = \gamma(\mathbf{v} \times \mathbf{B}) = \gamma\beta c \sin\theta \mathbf{B}$. The acceleration is given by the Lorenz force law $a = E'e/m$ and so using Larmor's formula the synchrotron power emitted by a particle is

$$P = \frac{e^4 \gamma^2 \beta^2 \sin^2 \theta B^2}{6\pi \epsilon_o m_e^2 c}. \tag{1.8}$$

It is also useful to calculate the average power emitted by an electron travelling through a small scale tangled field (or equivalently, an ensemble of electrons with an isotropic velocity distribution in a region with a constant magnetic field). Averaging the power emitted over solid angle we find the standard result

$$P = \frac{4}{3}\sigma_T \beta^2 \gamma^2 c U_B, \tag{1.9}$$

where we have simplified the expression using the Thomson cross section σ_T and the magnetic energy density $U_B = B^2/2\mu_0$. The second result, which I will repeatedly make use of in future chapters, is the characteristic frequency of synchrotron emission ν_c. A detailed derivation of the emitted spectrum of synchrotron radiation can be found in Longair [2011] which uses the Fourier transform of Larmor's equation to calculate the emitted spectrum.

$$I(\nu) = \frac{e^2}{6\pi^2 \epsilon_0 c^3} \left| \int_{-\infty}^{\infty} \dot{v}(t) e^{i\nu t} dt \right|^2 \tag{1.10}$$

The emitted synchrotron spectrum for an accelerating charge is sharply peaked around a critical value

$$\nu_c = \frac{3}{2}\omega_g = \frac{3\gamma^2 eB}{4\pi m_e} \tag{1.11}$$

where ω_g is the relativistic gyrofrequency of an electron.

1.2.6.2 Inverse-Compton emission

Inverse-Compton emission is the result of a collision between a high energy particle and lower energy photon. The result of the collision is to transfer a fraction of the particle's energy to the photon. A detailed calculation of the inverse-Compton emission is carried out in section 2.6 for an isotropic photon field and in section 3.5 for the case of a photon field which has been relativistically beamed in the rest frame of the jet plasma. In the Thomson limit ($m_e c^2 \gg \gamma E_\gamma$), in which the recoil of the electron is negligible in its rest frame, there are two useful results for the inverse-Compton emission of a particle travelling through an isotropic distribution of photons. The power emitted by inverse-Compton scattering photons is given by

$$P = \frac{4}{3}\sigma_T c\beta^2\gamma^2 U_\gamma, \tag{1.12}$$

where U_γ is the energy density of the photons. The characteristic frequency of emission in the Thomson limit is given by $\gamma^2 E_\gamma$.

1.2.7 Acceleration of non-thermal electrons

The observed double-humped spectra of blazars are well matched by the synchrotron and inverse-Compton emission from a population of non-thermal electrons. A number of physical mechanisms have been suggested in the literature which could be responsible for the acceleration of non-thermal particles in relativistic jets, however, we do not yet know which of these mechanisms is operating in blazars. These mechanisms include shock acceleration: non-relativistic (Bell [1978]), relativistic (Summerlin and Baring [2012]), oblique (Bell et al. [2011]) and shearing induced (Nishikawa et al. [2013]), and acceleration by magnetic reconnection (Zenitani and Hoshino [2001], Zenitani and Hoshino [2007] and Cerutti et al. [2012]). The detailed physics underlying magnetic reconnection and turbulence are not yet well understood due to the complexity of behaviour of MHD fluids on small scales and so, generally, it is assumed that the non-thermal electrons in jets are accelerated by shocks.

The basic principle of shock acceleration was first discovered by Enrico Fermi (Fermi [1949]). This theory was then further developed into the acceleration of high energy particles via diffusive shocks by Axford et al. [1977], Krymskii [1977], Bell [1978] and Blandford and Ostriker [1978]. This led to an understanding of the origin of Cosmic Rays (high energy particles permeating our galaxy) by acceleration in the shock fronts from supernovae explosions and predictions of a power-law slope close to that observed. Today X-ray observations of supernovae show a thin shell of synchrotron emission from high energy electrons coincident with supernovae shocks believed to be accelerated by diffusive shock acceleration (Vink [2012]).

1.2.7.1 Diffusive shock acceleration

In the following subsection I will outline the basic principle of shock acceleration following the intuitive treatment of Bell [1978] by deriving the accelerated particle spectrum for an unmagnetised, non-relativistic perpendicular shock (see references in the previous subsection for details on more complex shocks). A shock forms when a disturbance or perturbation travels through a fluid at a speed exceeding the sound speed of the fluid. Information about the disturbance propagates at the sound speed and so the shock front is the discontinuity between the shocked and unshocked fluid. Energy and momentum are conserved when a shock front passes through a fluid and these quantities allow us to calculate the conditions in the shocked and unshocked regions via the Rankine-Hugionot conditions

$$\frac{\partial \rho}{\partial t} = -\frac{\partial}{\partial x}(\rho u), \qquad \frac{\partial(\rho u)}{\partial t} = -\frac{\partial}{\partial x}(\rho u^2 + p), \qquad \frac{\partial(\rho E)}{\partial t} = -\frac{\partial}{\partial x}\left[\rho u\left(e + \frac{u^2}{2} + \frac{p}{\rho}\right)\right]. \quad (1.13)$$

where $E = e + u^2/2$ and e is the internal energy per unit mass. For a strong shock (the shock velocity is much greater than the sound speed of the unshocked gas) the properties of the shocked and unshocked fluid (subscripts 1 and 2 respectively) become, $4\rho_1 = \rho_2$ and $v_1 = 4v_2$. In the frame of the unshocked gas the shock front travels at a speed v towards the gas whilst the shocked gas travels with a speed $u = 3v/4$ towards the unshocked gas. In the frame of the shocked gas the shock front travels away at a speed $v/4$ whilst the unshocked gas travels towards the shocked gas with speed $u = 3v/4$. A high energy particle which travels across the shock front always sees a 'wall' of gas travelling towards it and so will gain energy by colliding with this wall. In diffusive shock acceleration the particle scatters off tangled magnetic field lines on either side of the shock and its velocity becomes isotropic (on average) in the rest frame of the gas. A particle which is fortunate enough to travel back through the shock front multiple times will be accelerated to a much larger energy than it initially had. In Fermi's original work particles were repeatedly reflected from randomly moving gas clouds acting as magnetic mirrors but this process was found to be inefficient as the mean energy gain per collision is proportional to the velocity of the magnetic mirrors squared $(v/c)^2 = \beta_v^2$.

In diffusive shock acceleration high energy particles are assumed to diffuse randomly in an isotropic tangled magnetic field on either side of the shock. Consider a particle with energy $P^0c = E_1$ in the shocked frame, which diffuses through the shock to the unshocked frame. In the unshocked frame it will have an increased energy $P'^0c = E_2 = L(u/c)^0_\nu P^\nu c = \gamma_u E_1(1+\beta_u \cos\theta)$. Averaging the energy gained over the distribution of solid angle of particles crossing the shock we find an average energy gain of $2\beta_u/3$ per shock crossing. Particles are being advected behind the shock at a rate $nv/4$, where n is the number density of high energy particles (which is assumed to be the same on either side of the shock as the shock speed is much less than the particle speed). The number of particles crossing the shock from the unshocked gas is given by kinetic theory to be $nc/4$ and so the fraction of particles which cross the shock and are advected downstream of the shock and lost is $(nv/4)/(nc/4) = \beta_v$. The probability of a particle which crosses downstream of the shock later recrossing the shock is $P = (1 - v/c)$ and its average energy gain is $\epsilon = 4\beta_u/3 = \beta_v$.

To find the steady state particle distribution we consider the particle distribution and energy after a shock crossings. The number of remaining particles is $N = N_0P^a$ and the average particle energy is $E = E_0(1 + \epsilon)^a$. Taking the logarithm of both distributions and eliminating a in the non-relativistic limit ($\beta_v \ll 1$, i.e. $\ln(1 + \beta) \approx \beta$) we find

$$\frac{N}{N_0} = \frac{E}{E_0}^{\ln P/\ln\epsilon}, \qquad \ln P/\ln\epsilon = -1, \tag{1.14}$$

So the differential electron distribution is $N(E)\mathrm{dE} = \mathrm{AE}^{-2}\mathrm{dE}$. This result is close to the power law index for the distribution of Cosmic rays, ~ 2.7, (Abraham et al. [2010] and Longair [2011]) and also close to the average value inferred from modelling blazar spectra. There has been much work extending this calculation to the cases of relativistic shocks (Kirk and Schneider [1987]), oblique shocks (Bell et al. [2011] and Summerlin and Baring [2012]) as well as shearing flows (Nishikawa et al. [2013]).

1.3 Accretion discs

1.3.1 Thin accretion disc equations

The majority of astrophysics boils down to the study of the emission of gas moving under the influence of gravity. The minimum energy configuration (considering only the kinetic plus gravitational potential energy of the gas and excluding thermal energy and any emitted radiation) of a body of self-gravitating gas with some net angular momentum is a disc with an axis in the direction of the net angular momentum; this way no excess kinetic energy is wasted in a way which doesn't contribute to conserved momentum. This is because the moment of inertia of a disc is the largest for any continuous density distribution. The eventual disc formation in a host of different sized astrophysical systems such as galaxy clusters, galaxies and stellar and planetary systems is inevitable (albeit on very different timescales) since forces act to maximise the entropy of a system (minimise the combined kinetic and gravitational potential energy of the gas) through dissipating any excess energy as high entropy radiation while conserving the total momentum. So the formation of self-gravitating discs is an inevitable consequence of the second law of thermodynamics combined with conservation of angular momentum.

The physical properties and emission from accretion discs were first calculated by Shakura and Sunyaev [1973]. They made the assumptions that the gas in the disc was in approximately circular orbits and the gravitational potential energy of an infalling particle was released locally as heat. They parameterised the kinematic viscosity in terms of a dimensionless number α, the thermal sound speed of the gas c_s and the disc height H as $\nu = \alpha c_s H$. At the time the cause of the viscosity was not known to be the magneto-rotational instability (Balbus and Hawley [1991] and Hawley and Balbus [1991]) i.e. $\nu \approx c_A H$, where $c_A = B/(\mu_0 \rho)$ is the Alfven velocity. In the following section I shall derive the standard thin accretion disc equations (see for example Frank et al. [2002]). Treating the gas in the disc as ideal ($P = nk_B T$, $\rho = mP/(k_B T)$), where m is the mean particle mass, the equation for hydrostatic equilibrium perpendicular to the plane of the disc using cylindrical coordinates is

$$\frac{\mathrm{dP}}{\mathrm{dz}} = -\frac{GM\rho z}{R^3}, \tag{1.15}$$

Integrating the equation (assuming the disc is thin, $z \ll R$) we find an expression for the scale height of the disc H

$$P = P_c e^{-\left(\frac{z}{H}\right)^2}, \qquad H = \sqrt{\frac{2k_B T_c R^3}{GMm}}, \tag{1.16}$$

where P_c is the central pressure, T_c is the central temperature and M is the mass of the body onto which the gas is accreting. The torque acting between annuli on circular orbits with angular velocities $\Omega = \sqrt{(GM/R^{3/2})}$ is given by

$$G = \mu A \frac{\partial v}{\partial R} \times R = \nu \rho A R \times (R \frac{\partial \Omega}{\partial R}) = 2\pi R^3 \nu \Sigma \Omega'. \tag{1.17}$$

where $\Sigma = \rho H$ is the surface density. Mass is conserved in the disc so the rate of change of mass in an annulus $\Delta M = 2\pi R \Sigma \Delta R$ is given by the net mass flux out of the annulus

$$R\frac{\partial \Sigma}{\partial t} + \frac{\partial}{\partial R}(R\Sigma v_r) = 0. \tag{1.18}$$

The rate of change of angular momentum of the annulus ($\Delta L = \Delta M R v_\phi$) is given by the net torque acting on the inner and outer boundaries ($G(R + \Delta R) - G(R)$) and the change in mass of the annulus.

$$\frac{\partial}{\partial t}(2\pi R^3 \Sigma \Omega \Delta R) = -2\pi \Delta R \frac{\partial}{\partial R}(R^3 \Sigma v_r \Omega) + \frac{\partial G}{\partial R}\Delta R, \tag{1.19}$$

$$R\frac{\partial \Sigma}{\partial t} R^2 \Omega + \frac{\partial}{\partial R}(R\Sigma v_r) R^2 \Omega + R\Sigma v_r \frac{\partial}{\partial R}(R^2 \Omega) = \frac{1}{2\pi}\frac{\partial G}{\partial R}. \tag{1.20}$$

Eliminating the first two terms by using the mass conservation equation and substituting in the torque G, we find the time-dependent diffusion equation for the surface density of the accretion disc.

$$\frac{\partial \Sigma}{\partial t} = \frac{3}{R}\frac{\partial}{\partial R}\left[R^{1/2}\frac{\partial}{\partial R}(\nu \Sigma R^{1/2})\right]. \tag{1.21}$$

If we assume a steady state thin disc with a constant accretion rate independent of radius, the first term in Equation 1.20 is zero. Integrating the second and third terms w.r.t radius we find

$$\nu \Sigma \frac{\mathrm{d}\Omega}{\mathrm{d}R} = \Sigma v_r \Omega + \frac{C}{2\pi R^3}, \tag{1.22}$$

where C is an integration constant which can be determined by the inner boundary condition of the disc. Usually, this boundary condition is taken to be that the disc is in solid body rotation close to the surface of the accreting object (e.g. star), whose surface is located at R_0. In this case, $C = \dot{M}(GMR_0)^{1/2}$ and substituting into Equation 1.22 we find the standard equation for a thin disc where $\dot{M} = -2\pi R\Sigma v_r$ is the accretion rate of the material in the disc

$$\nu\Sigma = \frac{\dot{M}}{3\pi}\left[1 - \left(\frac{R_0}{R}\right)^{1/2}\right]. \tag{1.23}$$

1.3.2 Emitted spectrum of an optically thick thin disc

Under the assumption that the rotational energy of the accreting matter is dissipated locally as heat, the emitted spectrum of a steady state, optically thick thin disc depends only on the accretion rate and is independent of the viscosity. The viscous torques remove rotational energy at a rate $G\Omega'\Delta R$ from an annulus of width ΔR. Equating the power dissipated to the power radiated by a black body with the surface area of the annulus we can calculate the associated temperature of the disc if the disc is assumed to be optically thick.

$$4\pi R\Delta R\sigma T_S^4 = G\Omega'\Delta R, \qquad T_S = \left(\frac{3G\dot{M}M}{8\pi R^3\sigma}\right)^{1/4}, \tag{1.24}$$

where T_S is the surface temperature of the disc. The final piece of information required to calculate the properties of the thin disc is an estimate of its opacity. This is usually assumed to be Kramer's opacity for a highly ionised plasma disc, so the vertical optical depth of the disc is $\tau = \Sigma\kappa_r = 6.6 \times 10^{18}\Sigma\rho T_c^{-7/2}\mathrm{m}^2\mathrm{kg}^{-1}$ (Frank et al. [1992]). The equation for radiative transfer in a plane parallel atmosphere is

$$\frac{\partial I_\nu}{\partial \tau_\nu} = -I_\nu + S_\nu, \tag{1.25}$$

We assume that locally the source function is that of a black body. The net energy flux in the z-direction is given by $F_\nu = \int (I_\nu - S_\nu)\cos\theta \mathrm{d}\Omega$ (the difference between the radiation from a hotter inner region minus the radiation from the cooler outer region). If we assume a slow temperature gradient, the intensity I_ν is only slightly larger than the black body brightness of the region, so we approximate $\partial I_\nu/\partial\tau_\nu = \partial B_\nu/\partial\tau_\nu$ and the optical depth is given by $\mathrm{d}\tau_\nu = \kappa_r\rho dz/\cos\theta$. Multiplying equation 1.25 by $\cos\theta$ and integrating over solid angle we find

$$F_\nu = -\frac{4\pi}{3\kappa_R\rho}\frac{\mathrm{d}B_\nu(T)}{\mathrm{d}z} = -\frac{16\sigma T^3}{3\kappa_r\rho}\frac{\partial T}{\partial z}. \tag{1.26}$$

Integrating the expression for the net energy flux from the centre of the disc to the surface and equating this to half the dissipated power in Equation 1.24 (because the disc has two surfaces), we find a relation between the central and surface temperatures $4T_c^4/(3\tau) = T_S^4$. This closes the system of equations and allows the properties of this idealised disc to be calculated (see section 7.2.1).

The steady-state optically thick thin disc seems to be a good approximation for many astrophysical systems such as AGN, X-ray binaries and protoplanetary discs (Frank et al. [2002]). For observed accretion rates the assumptions of the disc being optically thick and geometrically thin can be checked numerically and are found to be self-consistent. Observations of accretion discs in X-ray binaries and AGN are well fitted by the composite thermal spectrum of the Shakura-Sunyaev disc and give physically plausible parameters (Remillard and McClintock [2006] and Ghisellini et al. [2009b]).

1.4 Cosmology

In this section I will briefly outline the assumptions I have made when estimating distances and observed fluxes to blazars based on redshift information. Chapter 8 contains the details of the ΛCDM model of cosmology which is currently the most successful cosmological model consistent with observations. I will assume a ΛCDM cosmology when calculating predicted blazar spectra in Chapters 2-6.

1.4.1 Cosmological distance measurements

To calculate the observed flux from an object of known luminosity we use the formula for the luminosity distance from Hogg [1999]

$$\nu_{obs}F_{\nu_{obs}} = \frac{\nu_{emit}P_{\nu_{emit}}}{4\pi D_C^2(1+z)^2} \tag{1.27}$$

where D_C is the comoving distance of the blazar and z is the redshift. The two factors of redshift are due to the redshifting of photon frequency resulting in a decrease in power and the decrease in photon arrival time.

1.5 Thesis structure

The majority of this thesis is dedicated to the modelling and understanding of the physical processes involved in black hole jets and accretion discs with a brief foray into the realms of cosmology.

In Chapters 2 and 3 I develop the theoretical basis for a model of jet emission. Chapter 2 focuses on calculating the synchrotron and inverse-Compton emission from a simple conical jet with constant speed, conserving energy. In Chapter 3 this is generalised to a jet with an arbitrary geometry and bulk Lorentz factor and includes a detailed treatment of the relevant physics and astronomy. In Chapters 4 and 5 I use this model to fit to the spectra of different elements of the blazar population starting with the most luminous blazars (Compton-dominant FSRQs) in Chapter 4 and then less luminous blazars (BL Lacs) in Chapter 5. In these Chapters I develop a hypothesis for the physical basis underlying the different classes of blazar and in Chapter 6 I test and confirm this hypothesis by fitting the model to all of the remaining multiwavelength spectra available.

Chapter 7 moves away from jets to understanding and modelling the properties of black hole accretion discs. In this chapter I present a calculation and 1D simulation of an instability induced by a viscosity which depends on the plasma temperature in an accretion disc, as shown in simulations. I outline why the instability could plausibly occur in real accretion discs and show that its global behaviour can explain the observations of cyclic flaring behaviour in X-ray binary accretion discs.

The problem of the origin and nature of dark energy in the universe is currently one of the most important and interesting questions in cosmology. In Chapter 8 I consider the possibility of interactions (such as unstable decay) between dark energy and dark matter. Using a quintessence (scalar field) model for dark energy I use a gauge-invariant covariant formalism to calculate the effect of interactions on cosmological observables. By comparing these theoretical predictions to observations and using simple physical arguments I constrain the strength of several possible interactions between dark energy and dark matter. This

Chapter is self-contained and contains the relevant theoretical and observational/historical background for the reader.

Finally, Chapter 9 presents my conclusions and summarises the most important results from this thesis.

Chapter 2

A Uniform Conical Jet Model

In this Chapter I introduce the fundamental calculations for the synchrotron and inverse-Compton emission from a jet with a variable shape and apply these to the case of a simple conical jet model. I include a detailed treatment of the relevant radiation processes integrating the full Klein-Nishina cross section and taking into account energy losses to the electron population due to radiation. I show that this model is able to reproduce the multiwavelength spectrum of BL Lacertae across all wavelengths including radio observations. This is the first time that a jet model has been able to reproduce observations across all frequencies for a blazar. I calculate the synchrotron optical depth along the jet and show that this ballistic conical jet produces a flat radio spectrum in agreement with previous work.

2.1 Introduction

Blazars are the most luminous and highly variable of active galactic nuclei (AGN). They have been observed at all wavelengths from radio to high energy γ-rays and are believed to be AGN observed at small angles to the jet axis (Urry and Padovani [1995]) resulting in Doppler-boosting of their emission. The characteristic spectral shape is a non-thermal continuum with two main peaked components; the radio through to UV/X-rays show signs of polarisation typical of synchrotron radiation, the second component extends from low energy X-rays through to very high energy γ-rays and is normally attributed to inverse-Compton scattering of photons from the synchrotron-emitting electrons. The radio emission of blazars is predominantly observed to be flat or nearly flat in flux density (see for example Owen et al.

[1980] and Abdo et al. [2010a]) whilst the majority of the synchrotron and inverse-Compton emission can be well described by a power law and a turnover.

In general, VLBI images of AGN observed at large angles to the jet axis show a continuous axisymmetric plasma jet, which is approximately conical in geometry, (see e.g., Kovalev et al. [2007] and Krichbaum et al. [2006]) with evidence for a small degree of curvature close to the base of the jet (Asada and Nakamura [2011]) and a blunt base with a wide opening angle (Hada et al. [2011]). Recent work by Sokolovsky et al. [2011] measured the frequency dependent core-shift for 20 AGN and found the results favoured a conical jet which conserved magnetic energy.

The early and influential model of Blandford and Königl [1979] used a uniform conical structure for the jet, and was able to produce the flat radio spectrum if magnetic energy in the jet was conserved. Further investigations by Marscher [1980], Königl [1981], Reynolds [1982], Mufson et al. [1984] and Ghisellini et al. [1985] indicated that this class of model was a good fit to the observed synchrotron emission. However, at the time, γ-ray observations were rare, and replenishment of adiabatic and radiative losses in some of the models were deemed to be problematic.

More recently, models for the radio and inverse-Compton emission from relativistic jets have predominantly considered all the emission to come from a small region of relativistic plasma, and such models have the ability to match the γ-ray spectrum of flares in blazars, e.g. Kirk et al. [1998], Böttcher and Chiang [2002], Li and Kusunose [2000] and Tsang and Kirk [2007]. The spherical blob is injected with a power-law (or broken power-law) electron energy spectrum at regular time intervals and the distribution of electron energies is evolved using the continuity or Fokker-Planck equation. The resulting emission spectrum is averaged over time. The continuity/Fokker-Planck equation takes into account the change in the electron population due to both electron energy losses from emission and the injection of additional electrons, but the energy injection mechanism remains arbitrary.

Models which contain some extended jet component explicitly include those of, e.g., Marscher and Gear [1985], Kaiser et al. [2000], Markoff et al. [2000], Spada et al. [2001] and Jamil et al. [2010]. These have variously included some attempts to treat particle re-acceleration, but are often aimed at X-ray binary systems and have not been concerned with the entire spectrum of a blazar from radio to γ-ray. Recently the conical jet was investigated by Kaiser [2006] as part of an analytic study of the range of conditions in the jet plasma which could result in a flat radio spectrum, although this model also neglected the inverse-Compton component of the spectrum.

With the advent of high-quality simultaneous radio-to-γ-ray spectra, especially data from the *Fermi* satellite, we were motivated to re-visit the problem of the full blazar spectrum. In particular, we wish to stress that the ultimate goal should be a model which contains both explicit and realistic jet parameters along with a detailed treatment of the particle emission processes and energetics within the jet.

In this Chapter we set out the details of a flexible and rigorous model which will form the basis of a series of investigations into the properties of blazars. We use a simple conical jet geometry as a first-order model for the structure of the jet. Our focus is on accurately calculating both the synchrotron and the synchrotron-self-Compton components of the jet spectrum. We do this using a full Klein-Nishina calculation of the inverse-Compton scattering and integrating the synchrotron emission along the line of sight through the relativistic jet. We then compare our results with the recent observations of BL Lac from radio to γ-ray. For a conical jet this is the first time a full-spectrum fit to a blazar has been attempted, and we also recover the jet opening angle, equipartition fraction and bulk kinetic power.

In this first Chapter we investigate whether a simple ballistic conical jet can reproduce the spectrum of BL Lac without need for significant acceleration or external Compton radiation. We include radiative electron losses but we do not yet include adiabatic losses in the jet. For the relatively low-power sources such as this, we find that there is no requirement for significant re-acceleration within the jet. In the next Chapter we analyse whether this is the case for Compton-dominant high energy sources.

Most previous investigations of the conical jet have used simplifying approximations when calculating the opacity and observed synchrotron emission at small angles through the jet and approximate analytical expressions for the inverse-Compton emission. We treat the calculations of the line of sight synchrotron opacity and inverse-Compton emission thoroughly. We use numerical integration of exact expressions to calculate the inverse-Compton emission. Unlike all previous investigations we also take into account electron energy losses along the jet due to both synchrotron and inverse-Compton emission and take into account the effect of these energy losses on the line of sight synchrotron opacity.

In this Chapter we will first introduce the parameters and assumptions of our jet model including its geometry and electron population. We then calculate the inverse-Compton spectrum produced from the scattering of an arbitrary isotropic seed photon population, although we shall only consider SSC seed photons in this work. We calculate the observed synchrotron emission from the jet and the synchrotron photon population. We show that the ballistic conical jet model is consistent with recent multi-frequency observations of BL Lacertae. We show that this model reproduces the observed flat radio spectrum if the magnetic energy is conserved along the jet and that this flat radio spectrum is a property which is insensitive to the model's parameters. Finally, we explicitly show the seed photon distribution and the evolution of the electron energy distribution.

2.2 Jet Model

As described above, VLBA images of AGN indicate that jets flows are axisymmetric with a constant opening angle over much of the jet length and so can be modelled by a conical geometry. This geometry was also favoured by Sokolovsky et al. [2011] to explain the frequency dependent core-shifts they measured. We will assume that the jet has an opening angle $\theta_{\mathrm{opening}}$, initial radius R_0 and length L, all defined in the centre of momentum frame of the fluid (fluid frame), see Figure 2.1. We assume that the jet is composed of an electron-positron plasma (for simplicity we will use 'electrons' to refer to both the electrons and positrons) which is injected at the base of the jet and the electrons lose energy radiatively as they move along the jet. Further, we make the assumption that both the electrons and magnetic field are isotropically and homogeneously distributed within the fluid rest frame whilst the fluid is moving in the lab frame with an associated bulk Lorentz factor γ_{bulk}. We define the variable x as the length along the jet axis (in the fluid frame), where $x = 0$ is defined dynamically as the base of the jet and $x = L$ as the end of the jet. We can now parameterise all of our physical quantities as functions of x. We also define the radius of the jet as $R(x)$ where

$$R(x) = R_0 + x \tan\theta_{\mathrm{opening}}. \tag{2.1}$$

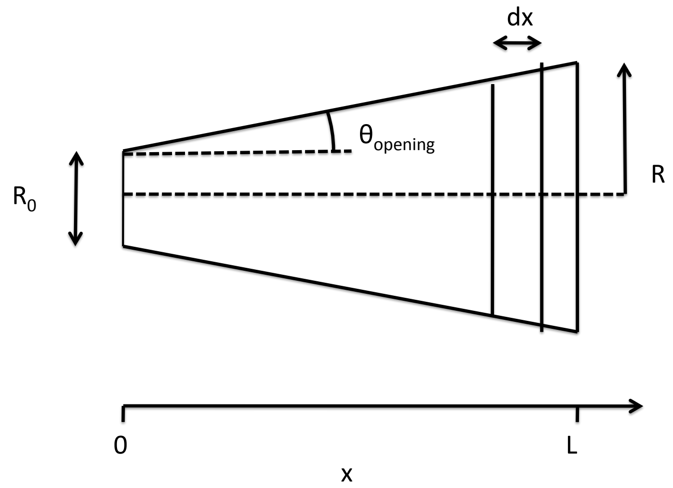

Figure 2.1: Schematic diagram of the conical jet, showing parameters defined in the fluid centre of momentum frame

2.2.1 Determining the Jet Parameters at the Base

We consider a jet with total power in the lab frame W_j. At the base of the jet the jet material has speed βc (where we assume a relativistic flow $\beta \simeq 1$), so in a length in the x-direction equal to one light-second in the lab frame the jet contains a total energy E_j equal to $1\,\mathrm{s} \times W_j$. If the jet has a bulk Lorentz factor γ_{bulk} then the energy E_j in the lab frame is related to the energy contained in one light-second in the frame of the fluid E_j^{fluid} by

$$E_j^{\mathrm{fluid}} = \frac{E_j}{\gamma_{\mathrm{bulk}}^2}, \qquad \frac{E_j}{\gamma_{\mathrm{bulk}}^2} = U_e + U_B, \tag{2.2}$$

where U_e and U_B are the electron energy and magnetic field energy contained in the first light-second of the jet in the x-direction, in the fluid frame. We define the equipartition fraction A_{equi} as

$$A_{\mathrm{equi}} = \frac{U_B}{U_e}. \tag{2.3}$$

Let us now consider the electron population in more detail. It is believed from optically thin synchrotron observations of AGN that the electron energy distribution is described by a single power law. We impose an exponential cutoff after E_{max} i.e.

$$N_e(E_e) = A E_e^{-\alpha} e^{-\frac{E_e}{E_{\mathrm{max}}}}, \tag{2.4}$$

where $N_e(E_e)$ is the initial injected electron distribution contained in the first light second of the jet, A and α are constants and α is thought to be between 1 and 3 from the theory of shock acceleration (Bell [1978], Bell et al. [2011] and Summerlin and Baring [2012]). We assume that the electron population within a section of length dx is independent of x.

For reasonable values of W_j (10^{34}W–10^{39}W) and A_{equi} (close to 1) (Maraschi and Tavecchio [2003]) the initial jet radius will be far greater than one light-second. So for reasonable opening angles consistent with observations we can assume that the radius of the jet at its base is approximately constant over the first light-second in the x-direction. We define R_0 to be the radius at the base of the jet and B_0 to be the magnetic field strength which we also assume to be approximately constant over one light-second (l_c).

$$U_e = \int_{E_{\text{min}}}^{E_{\text{max}}} E_e N_e(E_e) \mathrm{d}E_e, \qquad U_B = 4\pi R_0^2 l_c \frac{B_0^2}{2\mu_0}, \tag{2.5}$$

$$\frac{E_j}{\gamma_{\text{bulk}}^2} = U_e(1 + A_{\text{equ}}) = U_B(1 + \frac{1}{A_{\text{equi}}}), \tag{2.6}$$

$$U_e = \frac{E_J}{\gamma_{\text{bulk}}^2(1 + A_{\text{equi}})}, \qquad U_B = \frac{A_{\text{equi}} E_j}{\gamma_{\text{bulk}}^2(A_{\text{equi}} + 1)}. \tag{2.7}$$

We can use these equations to calculate the coefficient A and to find a relation between B_0 and R_0.

$$A = \frac{(2-\alpha)U_e}{(E_{\text{max}}^{2-\alpha} - E_{\text{min}}^{2-\alpha})} = \frac{(2-\alpha)E_j}{\gamma_{\text{bulk}}^2(1 + A_{\text{equi}})(E_{\text{max}}^{2-\alpha} - E_{\text{min}}^{2-\alpha})}, \tag{2.8}$$

$$R_0 = \sqrt{\frac{2U_B\mu_0}{\pi l_c B_0^2}} = \sqrt{\frac{2E_j A_{\text{equi}}\mu_0}{\gamma_{\text{bulk}}^2(\pi l_c B_0^2)(1 + A_{\text{equi}})}}. \tag{2.9}$$

We choose B_0 to be our independent parameter and determine R_0 from the above equation. For values of $B_0 \leq 10^{-4}$T, $W_j > 10^{34}$W and $\gamma_{\text{bulk}} < 100$ (Tavecchio et al. [1998] and Lobanov [2010]), $R_0 > 3 \times 10^{11}$m so for realistic jet parameters the radius far exceeds one light-second, hence, the approximation of a constant radius over the base is justified.

2.2.2 Magnetic Field Strength

For a jet with a constant bulk Lorentz factor which conserves magnetic energy in each segment, dx, is constant along the jet and for d$x = l_c$ the total magnetic energy in a segment is equal to U_B. The magnetic field will change as a function of the radius of the jet so that the total magnetic energy is conserved in a segment dx.

$$U_B = 4\pi R(x)^2 l_c \frac{B(x)^2}{2\mu_0}, \qquad B(x) = \sqrt{\frac{2\mu_0 U_B}{4\pi R(x)^2 l_c}}. \tag{2.10}$$

Substituting in the value of U_B from equation 2.10 we find.

$$B(x) = B_0 \frac{R_0}{R(x)}. \tag{2.11}$$

In this case the local magnetic energy is conserved as well as the radial and toroidal magnetic flux, however, the magnetic flux parallel to the jet axis increases with x.

2.3 Electron radiative losses

In our calculations we evolve the electron population dynamically along the jet by taking into account energy losses from synchrotron and inverse-Compton radiation. For simplicity we will consider the electrons in a slab of width one light-second as it propagates along the jet. As the slab traverses a section of the jet of width dx the electrons in the slab lose an amount of energy equivalent to that emitted by the entire section in one second, independently of the width dx of the section. This is because the section contains $n = \mathrm{d}x/l_c$ slabs of width 1 light-second and each of these slabs travels with velocity approximately c, so takes n seconds to cross the section. The evolution of the electron population along the jet due to energy losses can then be calculated using the equation below.

$$N_e(E_e, x + \mathrm{d}x) = N_e(E_e, x) - \frac{P_{tot}(x, \mathrm{d}x, E_e) \times 1s}{E_e}, \tag{2.12}$$

where P_{tot} is the total power emitted by electrons of energy E_e in a section of jet of width dx due to synchrotron and inverse-Compton processes. We can take into account the dynamic electron population by modifying the variable A to include a dependence on jet length and electron energy $A(E_e, x)$, which takes into account the changes to the electron population as a function of jet length and electron energy.

$$A(E_e, x) = A \times \frac{N_e(E_e, x)}{N_e(E_e, x = 0)}. \tag{2.13}$$

We can now calculate the synchrotron and inverse-Compton emission of a variable electron population given by

$$N_e(E_e, x) = A(E_e, x) E_e^{-\alpha} \times e^{-\frac{E_e}{E_{\max}}}. \tag{2.14}$$

2.4 Expansion losses

In this work we use a uniform conical jet model with a constant opening angle and bulk Lorentz factor. This model represents an overpressured jet which is expanding ballistically. An overpressured jet with a relativistic equation of state ($p \propto \rho^{\frac{4}{3}}$) expands freely with a constant opening angle (set by the relativistic constraint $\theta < 1/\gamma_{\mathrm{bulk}}$) and its expansion is essentially ballistic after a few scale heights (Begelman et al. [1984]). A uniform conical jet with a constant bulk Lorentz factor is necessarily ballistic. This is because its radial velocity profile is $v(r) = v_0 \frac{r}{r_{\max}}$, so the kinetic energy of plasma associated with the radial expansion is constant along the jet. In this case the boundary between the conical jet and its environment does not change over time since the conical jet occupies a fixed volume in space in the lab frame and so it does no work expanding its environment (since $p_{\mathrm{jet}} \mathrm{d}V_{\mathrm{env}} = 0$). This can be seen by considering the rest frame of the fluid element at the jet boundary, which is at rest relative to the boundary with the external medium. This means that in this ballistic model the expansion does not result in any adiabatic work done by the internal energy of the jet expanding its environment and additionally there is no conversion of the internal energy of the plasma into bulk kinetic energy (as in the case of a supernova explosion for example). Realistically, we expect fluctuations in the position of the jet boundary with time due to the fluid instabilities and inhomogeneity of the jet, however, these fluctuations will be small relative to the jet radius and will have zero mean $\langle \mathrm{d}V_{\mathrm{env}} \rangle = 0$, so will not lead to significant adiabatic expansion losses or gains to the jet.

Depending on the magnetic field configuration and particle composition the internal energy of the expanding plasma can clearly be exchanged between the particles and magnetic field, however, we emphasise that the important point is that the total internal energy is conserved (ignoring radiative losses). In this work we do not wish to embark upon a detailed treatment of the dynamics of the MHD plasma since the composition and physics of plasma jets is poorly understood. We shall instead assume that the jet plasma remains in (or close to) equipartition in the conical jet as shown by X-ray observations and brightness temperatures (Croston et al. [2005] and Homan et al. [2006]).

Of course the case of a conical, ballistic jet which suffers no adiabatic expansion losses is strictly only applicable in the case where the jet material is cold, which is unlikely to be valid for a real jet. In Chapter 3 we shall address this problem by considering the case of an accelerating jet in which the internal magnetic energy is converted into bulk kinetic energy via a magnetic pressure gradient and by investigating the effect of including adiabatic losses on the jet.

2.5 Synchrotron emission

We use the expression for the power emitted by an electron whose velocity is at an angle θ to a uniform magnetic field of strength $B(x)$ (see for example Pacholczyk [1970])

$$P(E_e, \theta, x) = \frac{e^4\gamma^2 B(x)^2\beta^2\sin^2\theta}{6\pi\epsilon_0 c m_e^2}. \tag{2.15}$$

For high energy electrons, synchrotron radiation is beamed along the velocity vector of the electron. In our model electrons are isotropically distributed in pitch angle, so integrating over θ we find

$$P_{\text{single}}(E_e, x) = \frac{2}{3\mu_0}\sigma_T c B(x)^2\beta^2\gamma^2. \tag{2.16}$$

Considering beaming effects and rotation frequency we make the simplifying assumption that electrons emit all their energy at a critical frequency ν_c (this is a reasonable assumption if we integrate over a large range of electron energies) which is given by

$$\nu_c(x) = \frac{3\gamma^2 eB(x)}{4\pi m_e}, \tag{2.17}$$

see Longair [1994]. Rearranging the above equation we can define the useful relations

$$E_e = (\epsilon(x)\nu_c(x))^{0.5}, \qquad \epsilon(x) = \frac{4\pi m_e^3 c^4}{3eB(x)}. \tag{2.18}$$

We wish to find the synchrotron emission from a slab in the jet at a distance x with width dx. The total power emitted at a critical frequency is simply the number of electrons which emit at that frequency multiplied by the power they emit.

$$P_{\rm tot}(\nu, x) = P_{\rm single}(\nu, x) N_e(\nu, x)\frac{{\rm d}x}{l_c}, \tag{2.19}$$

$$P_{\rm tot}(\nu, x) = \frac{\sigma_T B^2 \beta^2 A(E_e, x)\epsilon(x)(\epsilon(x)\nu)^{\frac{1-\alpha}{2}}{\rm d}x}{3\mu_0 m_e^2 c^3 l_c}. \tag{2.20}$$

This gives our total emitted power as a function of frequency in the centre of momentum frame of the electrons.

2.5.1 Opacity

To calculate the observed emission through the jet fluid we need to know the opacity of the plasma. We calculate the opacity using the one dimensional radiative transfer equation. Neglecting scattering in a homogeneous plasma we find (see Hughes [1991])

$$I_\nu = \frac{j_\nu}{k_\nu}(1 - e^{-k_\nu D}), \tag{2.21}$$

where I_ν is the emitted flux, j_ν is the emissivity per unit volume, k_ν is the opacity and D is the length of a section of jet plasma along our line of sight. The full synchrotron opacity is calculated by considering the absorption and emission using the Einstein A and B coefficients for an electron in a magnetic field (see e.g. Pacholczyk [1970]). The full expression for the synchrotron opacity requires numerically evaluating a Bessel function at a range of frequencies, which is computationally expensive. We shall instead use an approximate expression for the synchrotron opacity (calculated by requiring that nothing can emit more efficiently than a black body, see Longair [2011]) which is valid when the plasma is optically thick and results in a significant improvement in the running time of our code. This approximation is appropriate because when the plasma is optically thin we do not require an accurate estimate of the opacity since the fraction of scattering events depends exponentially on the optical depth and this is negligable in the optically thin regime. Using the Rayleigh-Jeans limit and associating the thermal temperature of electrons emitting at their critical frequency with the kinetic energy of those electrons via $k_B T = E_e = (\epsilon\nu)^{0.5}$ we obtain

$$I_\nu = \frac{2\epsilon^{\frac{1}{2}}\nu^{\frac{5}{2}}}{c^2} = \frac{j_\nu}{k_\nu}, \qquad k_\nu(\nu, x) = \frac{j_\nu c^2}{2\epsilon^{\frac{1}{2}}\nu^{\frac{5}{2}}}. \tag{2.22}$$

To simplify the geometry of the problem we assume that we observe at an angle smaller than the opening angle of the jet θ_{observe} in the lab frame. We consider the emission from sections of the jet of width dx, where the opacity is a function of x.

$$\begin{aligned} j_\nu(\nu, x) &= n_e(\nu, x)P(\nu, x), && (2.23)\\ j_\nu(\nu, x) &= \frac{A(E_e, x)\epsilon\sigma_T B^2\beta^2(\epsilon\nu)^{\frac{1-\alpha}{2}}}{3\pi R(x)^2 \mathrm{d}x\mu_0 m_e^2 c^3}\frac{\mathrm{d}x}{l_c}, && (2.24)\\ j_\nu(\nu, x) &= j_0(E_e, x)\nu^{\frac{1-\alpha}{2}}. && (2.25) \end{aligned}$$

So, using this in our expression for opacity, we find

$$k_\nu(\nu, x) = \frac{j_0(E_e, x)c^2\nu^{-\frac{\alpha+4}{2}}}{2\epsilon^{0.5}}. \tag{2.26}$$

Using Equation 2.21 we see that if $k_\nu D$ is small (the material is optically thin) the observed luminosity simplifies to the volume of the plasma multiplied by the emissivity as we would expect. If we observe down the jet within the opening angle we will see through to different depths at different wavelengths due to the wavelength dependence of the opacity. We see through to the layer where the total column optical depth is approximately 1 and beyond this there is an exponentially decreasing contribution from further layers. The total optical depth τ_{tot} is the sum of the optical depths from each section. If we observe at an angle θ_{observe} from the jet axis, the depth of material we see through is $\int \frac{\mathrm{d}x}{\cos\theta_{\mathrm{observe}}}$

$$\tau_{tot}(\nu, x) = \int_x^L k_\nu(\nu, x)\frac{1}{\cos\theta_{\mathrm{observe}}}\mathrm{d}x. \tag{2.27}$$

An individual segment of width $\mathrm{d}x$ will emit according to

$$P_\nu(x, \mathrm{d}x, \nu) = \pi R(x)^2 \frac{2\epsilon^{\frac{1}{2}}\nu^{\frac{5}{2}}}{c^2}(1 - e^{-k_\nu(\nu,x)\mathrm{d}x}). \tag{2.28}$$

We will observe the emission from each segment weighted by the total optical depth, which is equivalent to solving the radiative transfer equation with $j_\nu(z) = 0$.

$$P_\nu = \int_0^L P_\nu(x, dx, \nu)e^{-\tau_{tot}(\nu,x)}\mathrm{d}x. \tag{2.29}$$

To calculate the electron energy losses via Equation 2.12 we assume that in a thin section only the radiation in the radial direction is unbalanced from the adjacent sections (the optical depth in the radial direction is smaller than that along the jet axis). The expression for the total synchrotron power emitted by a segment of the jet is then given by

$$P_\nu(x, \mathrm{d}x, \nu) = \pi R(x)\mathrm{d}x \frac{2\epsilon^{\frac{1}{2}}\nu^{\frac{5}{2}}}{c^2}(1 - e^{-k_\nu(\nu,x)R(x)}). \tag{2.30}$$

2.6 Inverse-Compton Scattering

In this section we calculate the inverse-Compton emission from an arbitrary electron population and arbitrary isotropic seed photon population. Let us consider the most general case of an electron-photon collision. In the lab frame we have an electron with energy E_e. We are free to define our x-axis (not to be confused with the jet x-axis) to be aligned with the electron's momentum by a simple rotation. In these lab coordinates we have an incoming photon with energy E_γ with its momentum vector at an angle of θ to the negative x direction. We wish to calculate the scattered photon energy and angle in the lab frame after the collision.

To simplify the calculation we Lorentz transform into the electron's rest frame (where the Klein-Nishina cross section is well defined) rotate our coordinates to deal with a simple stationary head-on collision, then apply a further rotation to realign our coordinate system

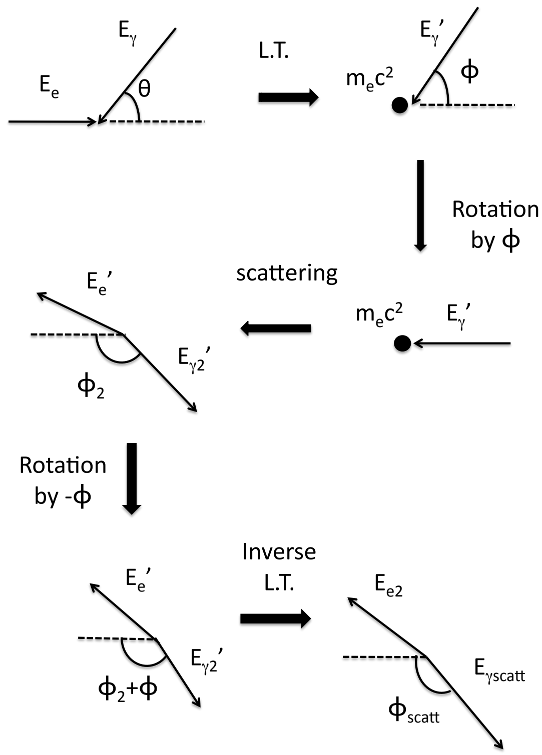

Figure 2.2: Schematic diagram of the inverse-Compton scattering process defining our choice of variables.

with our original lab x-axis and finally perform the inverse Lorentz transformation to revert to our initial lab frame. This is illustrated schematically in Figure 2.2 and is calculated using standard four-vector Lorentz transforms.

2.6.1 Obtaining the Inverse-Compton Spectrum

We have calculated the scattering angle and energy of a photon which is scattered by an electron. It remains to relate this to an emitted flux. We approach this problem by discretely summing over interval values of all the dynamic variables (E_e, E_γ, θ and ϕ_2 and x) and assigning a weight to each of the scattered photons which corresponds to the number of photons produced per second in a section of width dx. We then sum over the contributions from each section of the jet.

$$\text{Power} = \int_{E_e,E_\gamma,\theta,\phi_2,x} E_{\gamma\text{scatt}}.\text{weight}(E_e, E_\gamma, \theta, \phi_2, x) \times \mathrm{d}E_e \mathrm{d}E_\gamma \mathrm{d}\theta \mathrm{d}\phi_2 \mathrm{d}x. \tag{2.31}$$

2.6.2 Klein-Nishina Cross Section

To calculate the weight function we need the cross section for the electron-photon interaction. The Klein-Nishina cross section is the first order QED cross section for electron-photon scattering (see for example Weinberg [1995]), it is given by

$$\frac{\mathrm{d}\sigma}{\mathrm{d}\Omega_2} = \frac{1}{2}\alpha^2 r_c^2 P(E'_\gamma, \phi_2)^2 (P(E'_\gamma, \phi_2) + P(E'_\gamma, \phi_2)^{-1} - 1 + \cos^2\phi_2), \tag{2.32}$$

$$r_c = \frac{\hbar}{m_e c}, \qquad P(E'_\gamma, \phi_2) = \frac{1}{1 + \frac{E'_\gamma}{m_e c^2}(1 - \cos\phi_2)},$$

$$\mathrm{d}\Omega_2 = \pi |\sin\phi_2| \mathrm{d}\phi_2. \tag{2.33}$$

The formula relating the number of collisions between electrons of energy E_e and photons of energy E_γ is

$$\begin{aligned} \text{Collisions}(\mathrm{s}^{-1}) = \int \frac{N_e(E_e, x)}{l_c} . \frac{\mathrm{d}\sigma(E'_\gamma, \phi_2)}{\mathrm{d}\Omega_2} . n_\gamma(E_\gamma, \theta, x) \\ \times c(1 + \beta\cos\theta) . \mathrm{d}\Omega_2 \mathrm{d}E_e \mathrm{d}E_\gamma \mathrm{d}\Omega \mathrm{d}x, \end{aligned} \tag{2.34}$$

$$\mathrm{d}\Omega = \pi |\sin\theta| \mathrm{d}\theta, \tag{2.35}$$

where $c(1 + \beta\cos(\theta))$ is the relative velocity of the photon and electron (see for example Blumenthal and Gould [1970]). Since the integral of the weight function is simply the number of collisions occurring per second we find

$$\begin{aligned} \text{weight}(E_e, E_\gamma, \theta, \phi_2, x) = \frac{N_e(E_e, x)}{l_c} . \frac{\mathrm{d}\sigma(E'_\gamma, \phi_2)}{\mathrm{d}\Omega_2} \\ \times \frac{n_\gamma(E_\gamma, \theta, x)}{4\pi} . c(1 + \beta\cos\theta)\pi |\sin\phi_2| \pi |\sin\theta|. \end{aligned} \tag{2.36}$$

We replace the integral in Equation 2.31 with a discrete sum over the variables. Under the assumption that the weighting function is approximately constant for sufficiently small parameter intervals in the sum, we can convert the integral over the weighting function into a discrete sum

$$\text{Power}(W) = \sum_{E_e, E_\gamma, \theta, \phi_2, x} E_{\gamma\text{scatt}}.\text{weight}(E_e, E_\gamma, \theta, \phi_2, x) \times \mathrm{d}E_e \mathrm{d}E_\gamma \mathrm{d}\theta \mathrm{d}\phi_2 \mathrm{d}x. \tag{2.37}$$

This is our expression for the emitted power in the fluid frame. Using this method to calculate the emitted power has the advantage of calculating the inverse-Compton scattering exactly, in the limit of small step sizes in the sum, whilst also obtaining the angular dependence of the spectral energy distribution. To do this we simply carry out the sum in equation 2.37 binning scattered photons depending on both their scattered angle, which can easily be related to their observation angle, and their frequency. In this way we can calculate the emitted spectrum as a function of observation angle.

In the next section we will calculate the photon number density n_γ from the synchrotron emission.

2.7 Synchrotron Seed Photons

At high observed photon energies(> 1keV), where inverse-Compton scattering starts to dominate the blazar spectrum, the jet is optically thin to photons. To calculate the inverse-Compton emission from segments of the jet we need to calculate the photon number density $n_\gamma(x, \nu)$. When a section of the jet is optically thin ($k_\nu R(x) > 1$) an infinitesimal section of width $\mathrm{d}x$ will receive approximately the same amount of radiation from neighbouring sections as it emits parallel to the x-axis. We use the approximation that only the radiation emitted radially is unbalanced. So the volume of depth one light-second from the outer radial surface contains approximately one second of emitted power. If the section is optically thick then the emission and absorption per unit length are equal and so the photon distribution in the object is that of a blackbody. Calculating n_γ for the optically thin case we find

$$n_{\gamma\,\nu}(x, \mathrm{d}x) = \frac{L_\nu(x, \mathrm{d}x)}{2\pi h\nu R(x)\mathrm{d}x}, \tag{2.38}$$

and for the optically thick case ($k_\nu R(x) > 1$)

$$n_{\gamma\,\nu}(x, \mathrm{d}x) = \frac{8\pi\nu^2}{c^3(e^{\frac{h\nu}{k_B T}} - 1)}. \tag{2.39}$$

We define the average photon number density $n_\gamma^{av}(\nu)$

$$n_\gamma^{av}(\nu) = \sum_x \frac{n_\gamma(\nu, x)\mathrm{d}x}{L}, \tag{2.40}$$

2.8 Doppler Boosting of Emission

So far we have calculated synchrotron and inverse-Compton emission in the fluid frame. In our model the fluid is moving with a bulk Lorentz factor γ_{bulk} along the jet axis so the emission will be boosted depending on the Lorentz factor and the observation angle to the jet $\theta_{\mathrm{observe}}$. We use primed variables to denote quantities defined in the lab frame and unprimed variables for quantities defined in the fluid frame. The lab frame jet opening angle $\theta'_{\mathrm{opening}}$ is related to the fluid frame opening angle $\theta_{\mathrm{opening}}$ via

$$\gamma_{\mathrm{bulk}} \tan\theta'_{\mathrm{opening}} = \tan\theta_{\mathrm{opening}}, \tag{2.41}$$

due to length contraction of the jet axis of the cone. The observed photon frequency in the lab frame is boosted by a Doppler factor (shown below) which is obtained by Lorentz transforming a photon from the jet fluid frame into the lab frame. The total observed power is related to the emitted power in the fluid frame by multiplying by four Doppler factors: one from Doppler shift in frequency, one from increased photon arrival times and two from transforming solid angle between frames.

$$\frac{1}{\gamma(1 - \beta\cos\theta_{\mathrm{observe}})}. \tag{2.42}$$

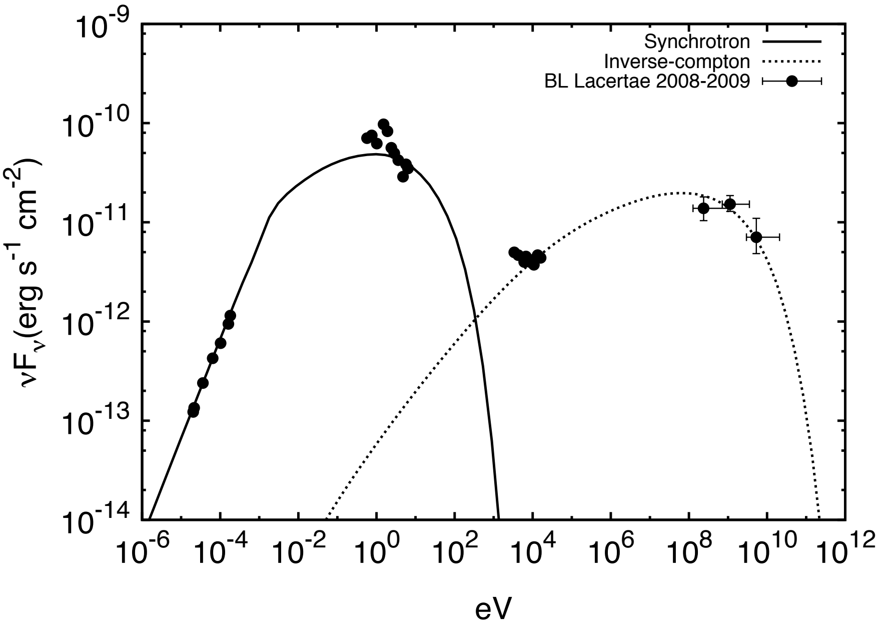

(a) A pure SSC fit to the simultaneous 2008-9 observations.

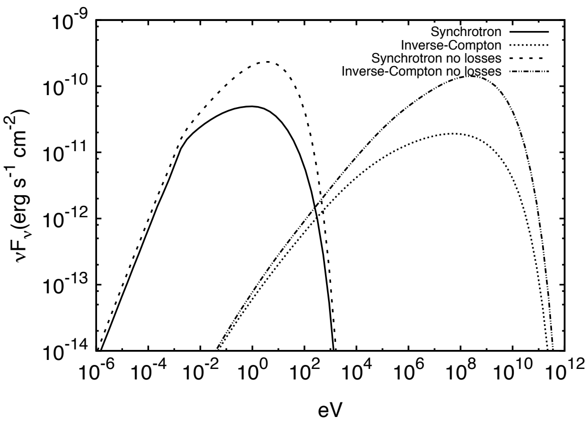

(b)

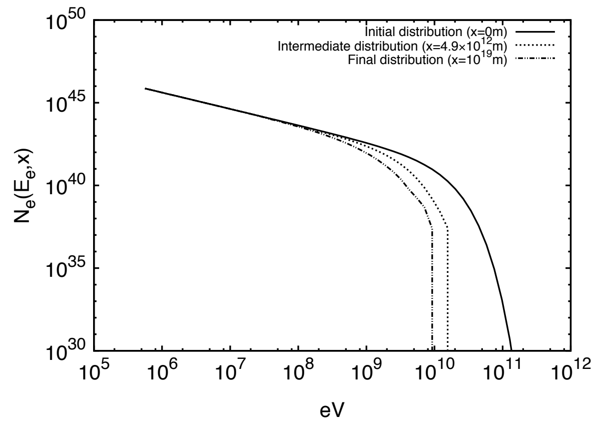

(c)

Figure 2.3: *Top:* The observed spectrum of the model fitted to the recent simultaneous multi-wavelength observations of BL Lacertae. The model reproduces the observed spectrum at all frequencies *Bottom:* The effect of electron energy losses to the jet. *R*ight: the high energy electrons have been depleted by energy losses at the end of the jet. *L*eft: energy losses have the largest effect on the high frequency synchrotron and inverse-Compton emission of the jet, but do not affect the flat radio spectrum.

The observed power in solid angle $d\Omega'$ at a Doppler boosted frequency ν', $P'(\nu')$, can then be related to the synchrotron power emitted in the fluid frame at frequency ν emitted into solid angle dΩ, $P(\nu)$, via

$$\nu' P'(\nu') = \nu' P'\left(\nu \frac{1}{\gamma(1-\beta\cos\theta_{\text{observe}})}\right) \tag{2.43}$$

$$= \nu P(\nu)\left[\frac{1}{\gamma(1-\beta\cos\theta_{\text{observe}})}\right]^4. \tag{2.44}$$

BL Lacertae has the very small cosmological redshift of $z = 0.0686$, so we take the distance to BL Lacertae to be $d = 300$Mpc and assume Euclidean space.

2.9 Results

2.9.1 Modelling the SED of BL Lacertae

In Figure 2.3a we show the results of our fluid jet model fitted to the recent simultaneous muti-wavelength observations of BL Lacertae (Abdo et al. [2011a]). We stress how well our relatively simple model fits these observations: the model fits well to the data across almost all wavelengths using only inverse-Compton scattered synchrotron seed photons from the single population of jet electrons. There is a discrepancy at the lower end of the X-ray energies, and we argue that this is likely to be from the accretion disc corona (see, e.g., Jin et al. [2011]). The optical/IR data is clearly not consistent with a smooth synchrotron component, but has been necessarily obtained with multiple instruments and may therefore suffer from absolute calibration offsets. By contrast, the optical-near IR spectrum on BL Lac obtained by Vermeulen et al. [1995] shows that the spectrum is clean and continuous in this region.

Figures 2.3b and 2.3c show the effect of including electron energy losses in the model. In Figure 2.3c we can see the evolution of the electron energy distribution along the jet. The figure shows the electron energy spectrum (contained in a slab of width one light-second) at the base of the jet immediately after injection and at the end of the jet after the slab has propagated through the entire jet and suffered maximal energy losses. We can see that losses are most significant for the highest energy electrons as we would expect, since the power of

Parameter	Value
W_j	7.63×10^{36}W
L	1×10^{19}m
B_0	3.63×10^{-5}T
R_0	7.32×10^{13}m
$A_{\rm equi}$	1
E_{min}	5.11 MeV
E_{max}	5.60 GeV
α	2
$\theta'_{\rm opening}$	9.7^o
$\theta_{\rm observe}$	2^o
$\gamma_{\rm bulk}$	12

Table 2.1: The values of the physical parameters for the model used to fit to the BL Lacertae observations

both synchrotron and inverse-Compton emission is approximately proportional to γ^2 of the electrons. The energy losses effectively lower the maximum energy cutoff of the electrons as they move along the jet.

Energy losses are most severe close to the base of the jet due to its stronger magnetic field and smaller radius. This means that losses occur predominantly in a region close to the base which is much smaller than the total jet length. This results in the jet producing a flat radio spectrum even when taking into account radiative energy losses since the electron distribution does not change significantly along the vast majority of the jet. We find that the base of the jet dominates the synchrotron and inverse-Compton emission at the highest frequencies whilst the radio synchrotron emission, which is optically thick at the base, is dominated by the outer regions of the jet with larger radii and therefore a larger surface area for emission.

In Figure 2.3b we can see the effect of the energy losses on the emitted spectrum of the jet. The figure shows that the low frequency synchrotron emission does not change significantly when losses are taken into account, however, the optically thin synchrotron emission which is dominated by the highest energy electrons at the base of the jet is reduced. The effect of losses on the highest energy electrons also results in a reduction to the highest frequency inverse-Compton emission, for which they are responsible.

From fitting to the observations of BL Lacertae we find a jet power of 7.63×10^{36}W, a maximum magnetic field $B_0 = 3.63 \times 10^{-5}$T at the base of the jet with base radius $R_0 = 7.32 \times 10^{13}$m and lab frame jet length 1.2×10^{20}m. We also find a bulk Lorentz factor $\gamma_{\rm bulk} = 12$, an electron energy index $\alpha = 2.0$ and an observation angle $\theta_{\rm observe} = 2^o$. We have fitted the observations with an equipartition jet $A_{\rm equi} = 1$ corresponding to energy being equally split between the electron population and the magnetic field. We have chosen the jet to be in equipartition because this is compatible with observations of the radio lobes of both FRII sources and Seyfert 1 galaxies (Croston et al. [2005] and Migliori et al. [2007]).

In this model we have not included any reacceleration of the electrons through internal shocks in the jet. Internal shocks are a mechanism which can convert some of the large store of kinetic energy in the bulk motion of the jet into internal energy in the electron population. This has been investigated by a number of authors (Marscher and Gear [1985], Kirk et al. [1998], Kaiser et al. [2000], Spada et al. [2001], Sokolov et al. [2004] and Jamil et al. [2010]) as a way of replenishing radiative and adiabatic energy losses of the electron population in jets. We expect that our estimates of jet opening angle and bulk Lorentz factor are larger than if we had included a form of in situ reacceleration, since a larger jet opening angle and Doppler factor reduce the effect of energy losses on the electron population. We intend to investigate the effect of different forms of reacceleration in this model in future work.

The paper presenting the observations of BL Lacertae (Abdo et al. [2011a]) uses three models to fit to the most recent observations. The first model from Finke et al. [2008] is a single zone time independent spherical SSC (synchrotron self-Compton) model. The fitted model uses a large Doppler factor of 26 and is over an order of magnitude from equipartition, it also fails to reproduce the low frequency radio emission. The second model based on work by Ciprini [2008] is a time-dependent single zone SSC it uses two different spherical blobs to fit to high and low frequency synchrotron emission and it fits well to the observations. The two blobs have Doppler factors 10 and 6.5 and the average equipartition value is $A_{equi} = 2.8$. The final model used is based on Böttcher and Chiang [2002] and is a single-zone time-dependent model with ERC (external radiation Compton) and also fits well to the data. The fit has a Doppler factor of 15, an equipartition fraction $A_{equi} = 1.48$ but also includes a energy independent particle escape time of $t_{\rm esc} = 60R/c$, which is difficult to justify physically. Whilst these models are able to fit the high energy synchrotron and inverse-Compton emission they are not able to reproduce the observed flat radio slope of the spectrum, the self-absorbed spectra they produce are steeper.

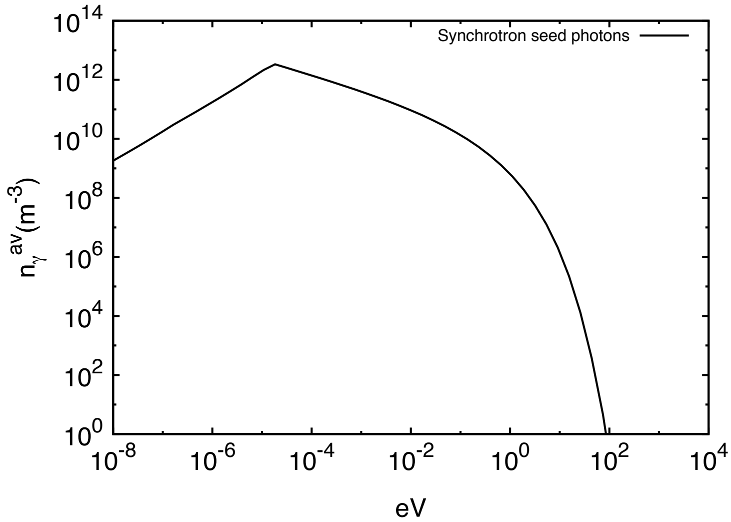

Figure 2.4: The average number density of photons plotted against energy for the model fitted to the simultaneous BL Lac observations.

One of the major achievements of the conical jet model is to reproduce the radio emission observed at low frequencies. This cannot be reproduced in fixed radius, homogeneous, one-zone SSC, two-zone SSC and ERC models (Abdo et al. [2010a] and Maraschi and Tavecchio [2003]) without introducing additional complications such as a two power law fit to the electron population or energy-independent diffusion of electrons. In fitting to the radio observations as well as to higher frequencies we gain additional constraints on our model parameters. In general we can gain the electron energy spectral index from the slope of the inverse-Compton emission (see for example Longair [1994]), the turnover of the flat spectrum at high frequencies then depends on the magnetic field strength B_0 which is strongly constrained by the synchrotron turnover at $\sim$ 1keV and the spectral index. Since blazars have such a variety of spectral behaviour with increasing variability at higher frequencies (see Ulrich et al. [1997]) it is surprising that most models neglect reproducing observations in the radio, since, for most blazars the radio is less variable and is normally observed to be close to a flat spectrum for a wide range of low frequencies. By not fitting to radio observations, models reduce the number of constraints and lack a physical mechanism to reproduce one of the most stable features of blazars.

Figure 2.4 shows the seed photon population averaged over the jet n_γ^{av} (see equation 2.40) for the models in Figure 2.3. Fundamentally, an ERC model with an unconstrained seed photon population can be used to fit almost any high frequency observation. So it is important to

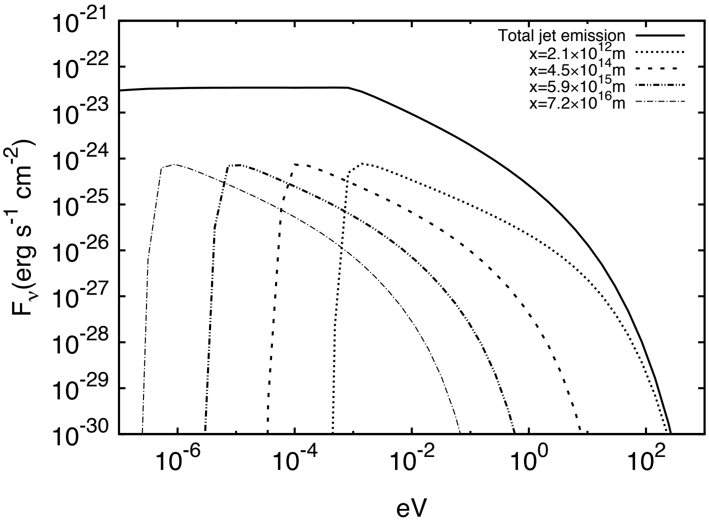

Figure 2.5: The observed luminosity of the BL Lacertae model looking at a small angle to the jet axis. The solid line is the total luminosity which is flat over a wide range in photon energy. The dashed lines show the observed contributions from thin slabs at different distances x along the jet whose sum produces the flat total distribution.

show explicitly the seed photon population used when fitting the model to the data to ensure clarity and to confirm that the photon population is realistic.

2.9.2 Producing a Flat Radio Spectrum

The observation of a near flat radio spectrum is a characteristic of most blazars (Abdo et al. [2010a]). We find that our model produces a flat spectrum which is largely insensitive to the physical parameters of the jet.

Figure 2.5 shows the overall flat spectrum produced by the model. The dashed curves show the observed emission from components at different distances along the jet. The figure illustrates the classic explanation of a flat spectrum: that different components have different turnover frequencies which add to give a flat spectrum. We believe that this is the first time this component explanation of a flat spectrum has been calculated explicitly for a conical jet orientated close to our line of sight. The figure shows that components closer to the base of the jet have turnovers at the highest frequencies and dominate the high frequency synchrotron emission (due to stronger magnetic fields and smaller radii) before their observed low frequency emission is absorbed exponentially by the outer jet material.

We have found that the production of a flat radio spectrum is largely insensitive to the parameters used in our model although the magnitude and frequency range of the flat spectrum

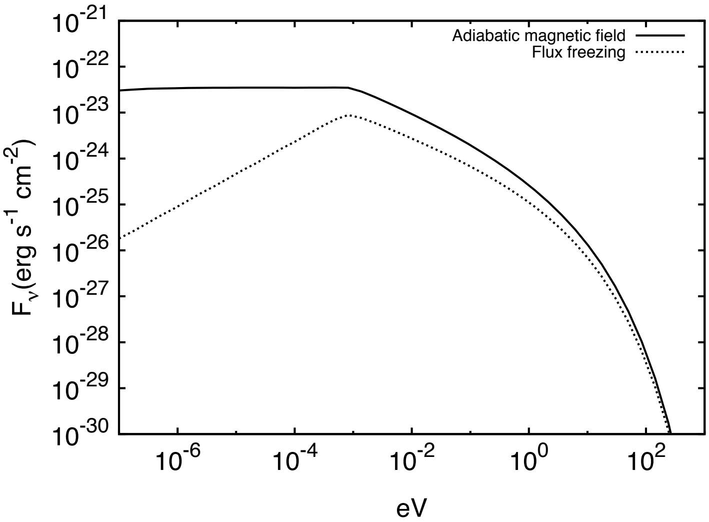

Figure 2.6: The dependence of the synchrotron emission on the functional form of $B(x)$. We can clearly see that if the magnetic energy is conserved ($B(x) \propto R^{-1}$) along the jet then the synchrotron luminosity is flat over a wide range of low frequencies. If the magnetic field evolves to conserve the flux through the surface $x = constant$ then we no longer observe a flat radio spectrum ($B(x) \propto R^{-2}$). Since a flat or nearly-flat radio is a well known characteristic of blazar-type objects, this is evidence of the conservation of magnetic energy in simple fluid jets.

do show a dependence. The most sensitive parameters are the overall jet length which affects the extent of the flat spectrum to low frequencies and the value of B_0 which affects the departure from the flat spectrum at high frequencies. This means that a flat radio spectrum is intrinsic to the uniform conical jet model which conserves magnetic energy and requires no fine-tuning.

Figure 2.6 shows the dependence of the synchrotron emission on the functional form of $B(x)$. We can see that if the magnetic energy is conserved along the jet ($B \propto R(x)^{-1}$) then the synchrotron luminosity is flat over a wide range of frequencies. If the magnetic field evolves to conserve the magnetic flux parallel to the jet axis ($B(x) \propto R(x)^{-2}$) then we no longer observe a flat radio spectrum. Since a flat or nearly-flat radio flux is a well known characteristic of blazar-type objects, this is evidence for the conservation of magnetic energy in simple fluid jets. This result was obtained by Kaiser [2006] who investigated a variety of fluid jet models and found, in agreement with us, that a model which conserved magnetic energy produced a flat spectrum whilst a model where magnetic flux is frozen parallel to the jet axis did not. However, his calculations were limited to the case of observations perpendicular to the jet axis.

2.10 Conclusions

We have re-visited the uniform conical jet model for AGN jets and, for the first time, used it to fit both the synchrotron and self-Compton components of the jet spectrum. In particular we have shown good agreement with these components in the recent multi-wavelength observations of the relatively low-jet-power source BL Lacertae from radio to γ-ray. Our model and conclusions may be summarized as:

- We demonstrate that a fluid model of an axisymmetric jet with a fixed opening angle and conserved magnetic energy fits the simultaneous observations of BL Lacertae presented by Abdo et al. [2011a].
- Our model conserves energy and particle flux along the jet. This allows us to estimate physical properties of the jet and central engine such as the total jet power and magnetic field strength from fitting the model to a blazar spectrum.
- We evolve the electron population dynamically along the jet taking into account energy losses from synchrotron and inverse-Compton emission. We calculate the inverse-Compton emission by numerically integrating the exact expression and we explicitly show the synchrotron seed photon population. Unlike previous investigations, we integrate synchrotron opacity along the line of sight through the jet plasma taking into account the emission and opacity of each section of the jet.
- We show that a conical jet model which conserves magnetic energy produces the characteristic flat radio spectrum observed in blazars in agreement with Blandford and Königl [1979] and Kaiser [2006].
- Under our conical jet assumptions, we find that for a source of this jet power ($\sim 10^{37}$W), that there is no requirement for significant re-acceleration within the jet to explain the observed spectrum.
- We find that the production of a flat radio spectrum does not require fine-tuning of the model parameters. We show that a conical jet which conserves magnetic flux parallel to the jet axis does not produce a flat radio spectrum.

Chapter 3

An accelerating jet model with a geometry based on observations of M87

The work in this Chapter extends the model presented in Chapter 2 to include a variable bulk Lorentz factor, adiabatic losses and scattering of external photon fields. The jet is chosen to have a geometry set by radio observations of the jet in M87 scaled linearly with black hole mass. Motivated by simulations and theory the jet is assumed to start with an accelerating magnetically dominated base transitioning to a slowly decelerating conical section at the point where the jet first comes into equipartition. The model includes a throrough treatment of inverse-Compton scattering of CMB, accretion disc, BLR, NLR, starlight and dusty torus with a minimal number of free parameters. The model is used to fit to observations of the most Compton-dominant FSRQ blazar. It fits very well using a jet with a high power bulk Lorentz factor observed close to the line of sight. The inverse-Compton emission is best fitted by scattering of CMB photons at large distances along the jet. We find that the jet cannot be in equipartition inside the BLR but is compatible with a transition from parabolic to conical within the dusty torus or at a larger distance.

3.1 Introduction

Radio observations show that AGN jets are approximately continuous axisymmetric plasma jets. Recent observations show that on large scales jets are approximately conical in geometry and measurements of the frequency dependent core-shift of M87 and other AGN favour a conical jet with conserved magnetic energy. VLBI observations of M87 by Hada et al. [2011] show the blunt base of the jet is within $14-23R_S$ of the central black hole. Observations of the geometry of the jet in M87 by Asada and Nakamura [2011] over a large range in length scales show that the jet is in fact parabolic close to the base and becomes conical at 10^5R_S. These observations are supported qualitatively by simulations of AGN jets powered by the Blandford-Znajek mechanism (see McKinney [2006]) which show an accelerating parabolic base which becomes conical near to the point where the plasma reaches equipartition.

The detailed mechanism behind the production of a relativistic plasma jet from a black hole is not yet fully understood. It is thought that the energy source of the jet comes from the rotation of the central black hole and that the magnetic field from the accretion disc is twisted by the rotation of the black hole creating a Poynting flux (Blandford and Znajek [1977]). We expect from simulations and theory that jets start as Poynting dominated (magnetic field dominated) and that the particles in the jet are accelerated to a large bulk Lorentz factor by the magnetic field until the jet plasma approaches equipartition where it reaches a terminal bulk Lorentz factor. The accelerating region is thought to be parabolic as indicated by observations (Asada and Nakamura [2011]), simulations (McKinney [2006]) and analytic work (Beskin and Nokhrina [2006]), whilst the outer regions of the jet are consistent with being approximately conical (Asada and Nakamura [2011], Hada et al. [2011], Sokolovsky et al. [2011] and Krichbaum et al. [2006]) with a slowly decelerating bulk Lorentz factor (Mullin and Hardcastle [2009] and De Young [2010]).

In this Chapter we develop our conical jet model from Chapter 2 (based on Potter and Cotter [2012]) to include an accelerating parabolic base which transitions to a slowly decelerating conical jet after 10^5R_S, motivated by the recent radio observations of M87 and consistent with simulations and theory. Our model conserves relativistic energy-momentum and particle number throughout the jet and includes energy losses to the particles (electrons and positrons, hereafter referred to as electrons) via radiative and adiabatic losses. We integrate the observed line of sight synchrotron opacity through the jet by transforming into the plasma rest frame. We also include the effect of inverse-Compton scattering external photons from the CMB, an accretion disc, starlight, accretion disc photons scattered by the broad line region (BLR) and accretion disc photons reprocessed by a dusty torus and narrow line region (NLR). We calculate the inverse-Compton emission from these external sources by Lorentz transforming into the rest frame of the plasma. This is the first time that an inhomogeneous jet model has included an accelerating parabolic base transitioning to a decelerating conical jet. In this Chapter we wish to develop a realistic, physically rigorous jet model motivated by and consistent with observations and simulations.

A successful jet model should be able to reproduce the simultaneous multi-wavelength observations of blazars across all wavelengths, including radio observations, which are usually neglected. To test whether our model is capable of producing realistic spectra we fit it to the simultaneous multi-wavelength spectrum of the Compton-dominant FSRQ PKS0227-369 from Abdo et al. [2010a].

Currently the most popular model of blazars are time-dependent, fixed radius, one-zone models e.g. Kirk et al. [1998], Böttcher and Chiang [2002], Li and Kusunose [2000] and Tsang and Kirk [2007]. These models consider the injection of an arbitrary electron population into a spherical blob with a constant bulk Lorentz factor and calculate the time-dependent emission from synchrotron, SSC and EC mechanisms. One-zone models best describe flaring events observed in the jets, however, they struggle to reproduce radio observations. Investigations into the effects of deceleration in one-zone models include those by Dermer and Chiang [1998] and Böttcher and Principe [2009] where plasmoids are decelerated by collisions which accelerate particles. It is important for a realistic model of blazars to be compatible with radio observations of the morphology, core-shift and flat radio spectrum, which are incompatible with one-zone models.

Investigations of extended inhomogeneous jets include those conducted by Blandford and Königl [1979], Marscher [1980], Königl [1981], Reynolds [1982], Mufson et al. [1984] and Ghisellini et al. [1985], Marscher and Gear [1985], Kaiser et al. [2000], Markoff et al. [2000], Sokolov et al. [2004], Graff et al. [2008], Pe'er and Casella [2009], Jamil et al. [2010] and Vila et al. [2011]. Early investigations of conical jets were motivated by the original work by Blandford and Königl [1979] which showed that a conical jet which conserves magnetic energy produces a flat radio spectrum.

There have been a number of investigations into accelerating or decelerating jets including those by Ghisellini and Maraschi [1989], Georganopoulos and Marscher [1998], Spada et al. [2001], Georganopoulos and Kazanas [2003] and Boutelier et al. [2008]. These investigations have included various models for acceleration and deceleration in parabolic, conical and cylindrical jets, however, no previous work has modelled both the accelerating parabolic base and decelerating conical sections of the jet or calculated the line of sight synchrotron opacity through the jet. Most investigations have variously treated some aspects of the jet physics and emission thoroughly whilst neglecting others. The early, pioneering work by Ghisellini and Maraschi [1989] is the only previous investigation to include an accelerating parabolic base transitioning to a conical jet. However, this investigation did not consider electron energy losses, inverse-Compton scattering of external photons, energy-momentum conservation along the jet or a decelerating conical section. In light of recent observations and simulations we feel it is valuable to develop a physically motivated model of jets which includes a thorough treatment of the relevant physics and which we can use to fit to blazar spectra in order to try to answer some of the fundamental questions about the blazar population.

In this Chapter we will first explain the basic properties of the jet including its geometry and variable bulk Lorentz factor. We then show how energy-momentum and particle number are conserved along the jet. We calculate the observed synchrotron emission and inverse-Compton emission from external photons from electrons in the jet. We then show the results of fitting the model to the Compton-dominant FSRQ type blazar PKS0227. Finally, we discuss the physical properties and characteristics of our model fit.

3.2 Jet Model

We develop the conical jet model presented in Chapter 2. In this Chapter we wish to extend the model to include a variable geometry, a variable bulk Lorentz factor, inverse-Compton scattering of external photons and adiabatic energy losses.

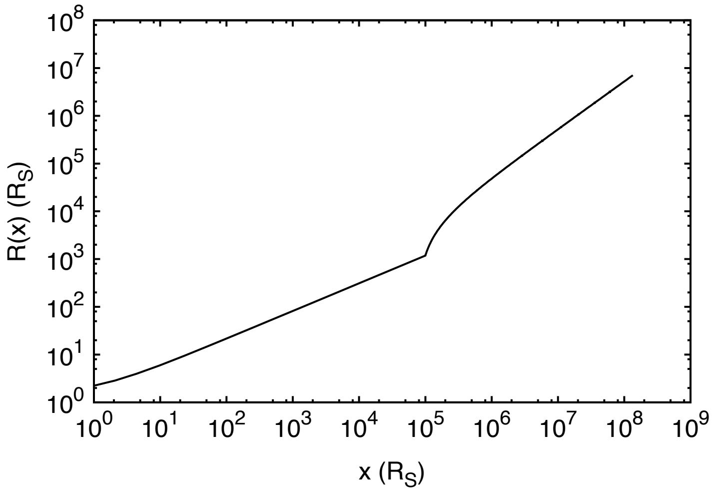

Figure 3.1: The geometry of our jet as used in the model fit to PKS0227 where the dimensions are given in terms of the Schwarzschild radius of the black hole. The jet starts with a parabolic geometry fixed to match observations of M87 and transitions to a conical geometry at $x_{\text{con}} = 10^5 R_S$, with lab frame half-opening angle θ_{opening}.

3.2.1 Geometry

We choose our model to have a parabolic base which transitions to a conical jet at a lab frame distance x_{con} from the black hole. The radius of the jet $R(x)$ is given by

$$R(x) = R_0 + A_{\text{par}} x^{B_{\text{par}}} \qquad \text{for} \quad x \leq x_{\text{con}}, \tag{3.1}$$

$$R(x) = R_0 + A_{\text{par}} x_{\text{con}}^{B_{\text{par}}} + (x - x_{\text{con}}) \tan(\theta_{\text{opening}}) \;\; \text{for} \quad x > x_{\text{con}} \tag{3.2}$$

where x is the lab frame jet length and θ_{opening} is the lab frame half opening angle of the jet. We fit the geometry of our model to the observed geometry of M87 (Asada and Nakamura [2011]), though we leave the opening angle of the conical section of the jet as a free parameter since this is likely to vary with the bulk Lorentz factor of the jet as $\sim \frac{1}{\gamma_{\text{bulk}}}$. We assume the geometry of our jet scales linearly with black hole mass. This means that the entire geometry of our jet is described by only two free parameters (the others are set by the observations of M87) the black hole mass M and the lab frame conical half-opening angle θ_{opening}.

We do not expect the geometry of the inner region of all AGN jets to be the same as that of M87, however, it is very interesting to see whether a jet with this geometry is compatible with the observations of a blazar. Our model is flexible and so can incorporate any length-radius relation if new information on the geometry of other AGN jets becomes available in the future.

3.2.2 Acceleration and deceleration

We set the bulk Lorentz factor of the jet plasma to be a function of x. We use the relationship between the bulk Lorentz factor and the jet radius predicted by theory (Beskin and Nokhrina [2006]) and consistent with simulations (McKinney [2006])

$$\gamma_{\rm bulk}(x) \propto x^{1/2}. \tag{3.3}$$

Setting the bulk Lorentz factor at the base of the jet to be γ_0 and the maximum Lorentz factor at the end of the accelerating parabolic region to be $\gamma_{\rm max}$, for $x \leq x_{\rm con}$ the bulk Lorentz factor is given by

$$\gamma_{\rm bulk}(x) = \gamma_0 + \left(\frac{\gamma_{\rm max} - \gamma_0}{x_{\rm con}^{1/2}}\right) x^{1/2} \quad \text{for} \quad x \leq x_{\rm con}. \tag{3.4}$$

Once the jet has reached equipartition it can no longer significantly accelerate the plasma by converting magnetic energy into bulk kinetic energy and so the jet stops accelerating and becomes conical. The jet now slowly decelerates (Laing and Bridle [2002], Hardcastle et al. [2005], Mullin and Hardcastle [2009] and De Young [2010]) due to interaction with its environment and Compton-drag. In this model we will assume the bulk Lorentz factor decreases with $\log(x)$. The conical section of the jet starts with a bulk Lorentz factor $\gamma_{\rm max}$ and decelerates by the end of the jet at $x = L$ to a Lorentz factor of $\gamma_{\rm min}$. Under these assumptions the bulk Lorentz factor is given by

$$\gamma_{\rm bulk}(x) = \gamma_{\rm max} - \left(\frac{\gamma_{\rm max} - \gamma_{\rm min}}{\log\left(\frac{L}{x_{\rm con}}\right)}\right) \log\left(\frac{x}{x_{\rm con}}\right), \quad x \geq x_{\rm con}. \tag{3.5}$$

The dependence of the deceleration of a jet with jet length is not well known so we have assumed this logarithmic decrease. We find that if the jet decelerates strongly at a particular length scale it leads to excess radio emission at the corresponding radio frequency which is not compatible with the observed flat spectrum. We therefore require a smoothly decreasing function, such as a power law or logarithmic decrease, in order to fit the flat radio spectrum. We have chosen a logarithmic decrease, however, we find that there are no significant differences in the spectrum produced by power-law or logarithmic deceleration. Our model is flexible so we can easily change the dependence of the bulk Lorentz factor to accommodate the results of any new observations.

3.2.3 Energy and particle conservation for the plasma

In our model the jet plasma starts magnetically dominated at the base, this magnetic energy is converted to bulk kinetic energy of the plasma as the jet is accelerated in the parabolic region by a Poynting flux (McKinney [2006] and Komissarov et al. [2009]). We do not attempt to model the physical mechanism behind the plasma acceleration since in this investigation we are interested primarily in the observed emission of the jet which depends only on the physical properties of the plasma.

We treat the plasma as being an isotropic perfect fluid in its instantaneous rest frame along the whole jet. This corresponds to the magnetic field being randomly oriented on small scales and isotropic and the particles being relativistic with an isotropic velocity distribution in the rest frame of the plasma. This is an idealised situation since it requires the magnetic field and electrons to isotropise after a section of plasma has been accelerated or decelerated, whilst this is the highest entropy state for the plasma we assume the timescale over which the plasma isotropises is short compared to the acceleration timescale and this may not be valid. However, this assumption of a plasma in which both the magnetic field and particle distribution are isotropic and homogeneous in its rest frame is used in almost all models of jet emission.

The magnetic field close to the base of the jet, where the plasma is Poynting dominated, is expected to be approximately parabolic (McKinney [2006]) and so the electromagnetic stress-energy tensor is not that of a perfect fluid. However, in models of jet emission, we are only interested in the regions closer to equipartition where high energy particles exist or are accelerated. In these regions close to or downstream of shocks we expect the magnetic field to be much more turbulent and so the approximation of an isotropic tangled field is appropriate for these jet regions which contribute significantly to the overall emission.

We treat the field as tangled on small scales and particles as relativistic so that $P = \frac{\rho}{3}$.

The energy-momentum tensor in the rest frame $T'^{\mu\nu}$ is given by

$$T'^{\mu\nu} = \begin{pmatrix} \rho & 0 & 0 & 0 \\ 0 & \frac{\rho}{3} & 0 & 0 \\ 0 & 0 & \frac{\rho}{3} & 0 \\ 0 & 0 & 0 & \frac{\rho}{3} \end{pmatrix}, \tag{3.6}$$

where ρ is the total energy density in the plasma rest frame and $\rho = \rho_e + \rho_B$ where ρ_e is the particle energy density and ρ_B is the energy density of the magnetic field. For a section of plasma which is travelling with a bulk Lorentz factor $\gamma_{\text{bulk}}(x)$ in the lab frame its energy-momentum tensor in the lab frame $T^{\mu\nu}$ is given by

$$T^{\mu\nu}(x) = \Lambda^{\mu}_{\ \text{a}} T'^{\text{ab}} \Lambda^{\nu}_{\ \text{b}} = \begin{pmatrix} \frac{4}{3}\gamma_{\text{bulk}}(x)^2\rho & \frac{4}{3}\gamma_{\text{bulk}}(x)^2\rho & 0 & 0 \\ \frac{4}{3}\gamma_{\text{bulk}}(x)^2\rho & \frac{4}{3}\gamma_{\text{bulk}}(x)^2\rho & 0 & 0 \\ 0 & 0 & \frac{\rho}{3} & 0 \\ 0 & 0 & 0 & \frac{\rho}{3} \end{pmatrix}, \tag{3.7}$$

where $\Lambda^{\mu}_{\ \nu}$ is the Lorentz transformation tensor and we have assumed that the jet is always relativistic so that $\beta \approx 1$. In order to satisfy the conservation of energy and momentum along the jet our energy-momentum tensor must satisfy $\nabla_\mu T^{\mu\nu} = 0$. In the lab frame our jet does not depend on time and quantities only have an x dependence so all other derivatives reduce to zero. To conserve the total energy-momentum in a slice of width one metre as it propagates along the jet we also need to take into account the change in cross-sectional area of the jet (which is invariant under a Lorentz boost in the x-direction) as it expands.

$$\frac{\partial}{\partial x}(\pi R^2(x) T^{1\nu}(x)) = \frac{\partial}{\partial x}\left(\frac{4}{3}\gamma_{\text{bulk}}(x)^2 \pi R^2(x)\rho(x)\right) = 0. \tag{3.8}$$

We also need to conserve the number of existing energetic electrons in the jet as the bulk Lorentz factor of the jet changes, so our electron energy density must satisfy the continuity equation.

$$\nabla_\mu J^\mu = \frac{\partial}{\partial x}(\pi R^2(x)\rho_{\text{e}}(x) U(x)^1) = 0, \tag{3.9}$$

where ρ_{e} is the electron energy density in the rest frame and $U(x)^\mu$ is the lab frame four velocity of the plasma. These two conservation equations can be used to calculate the rest frame magnetic energy density and electron energy density as the jet accelerates and magnetic energy is converted into bulk kinetic energy. We use the finite difference formulations of Equations 3.8 and 3.9 to evolve our magnetic field and electron population along the jet. We do this by calculating the synchrotron and inverse-Compton emission of the initial electron population, $N(x, E_e)$, in a section of lab frame width $\mathrm{d}x$. Our code calculates an appropriate width $\mathrm{d}x$ adaptively, such that the shortest radiative lifetime of the population is resolved and the radius of the jet does not change by more than 5% over the width of the section. We then calculate the resulting electron spectrum as a result of radiative and adiabatic losses over the section using Equations 3.58 and 3.59. In our code we also allow for the injection of electrons (with the same initial electron spectrum given by Equation 3.25) produced from shock acceleration in the section, so our modified electron spectrum including energy losses and particle injection becomes $N'(x, E'_e)$

$$\begin{aligned} N'(x, E'_e) = N(x, E_e) \quad - \quad & \frac{P_{\text{tot}}(x, \mathrm{d}x', E_e) \times 1\text{m}}{cE_e} \\ & + A_{\text{inj}}(x, \mathrm{d}x) E_e^{-\alpha} e^{-E_e/E_{\max}}, \end{aligned} \tag{3.10}$$

where E'_e is defined in Equation 3.57 as the energy E_e after adiabatic losses have been taken into account and $P_{\text{tot}}(x, \mathrm{d}x', E_e)$ is the total emitted power from the section of rest frame width $\mathrm{d}x'$ from Equation 3.59. The rest frame magnetic energy injected into electrons in a slab of rest frame width 1m is $\pi R(x)^2 \Delta\rho_{\text{inj}}(x)$, so $A_{\text{inj}}(x, \mathrm{d}x)$ is determined via

$$\pi R^2(x) \Delta\rho_{\text{inj}}(x) = \int_{E_{\min}}^{\infty} A_{\text{inj}}(x, \mathrm{d}x) E_e^{1-\alpha} e^{-E_e/E_{\max}} \mathrm{d}E_e. \tag{3.11}$$

In this investigation we will not inject electrons arbitrarily along the jet, so we take $A_{\text{inj}}(x, \mathrm{d}x) = 0$. We wish to include the possibility of an arbitrary injection of electrons in these calculations, however, since this will allow us to investigate the effect of flaring sections of the jet in future work. We use the continuity Equation 3.9 to calculate the overall normalisation of the modified electron spectrum in the rest frame of the next section starting at $x + \mathrm{d}x$

$$\mathrm{Norm} = \frac{\gamma_{\mathrm{bulk}}(x)}{\gamma_{\mathrm{bulk}}(x + \mathrm{d}x)}, \tag{3.12}$$

This takes into account the effect of differential length contraction on the number density of electrons as the population moves along the jet. The modified electron spectrum contained in one metre of the jet is given by

$$N''(x + \mathrm{d}x, E'_e) = \mathrm{Norm} \times N'(x, E'_e). \tag{3.13}$$

We now need to ensure conservation of the total energy-momentum along the jet. In the accelerating part of the jet we determine the magnetic field in the section located at $x + \mathrm{d}x$ using the finite difference formulation of Equation 3.8

$$\begin{aligned} &\gamma_{\mathrm{bulk}}(x)^2(\rho_{\mathrm{B}}(x) + \rho'_{\mathrm{e}}(x))\pi R^2(x) = \\ &\gamma_{\mathrm{bulk}}(x + \mathrm{d}x)^2(\rho_{\mathrm{B}}(x + \mathrm{d}x) + \rho''_{\mathrm{e}}(x + \mathrm{d}x))\pi R^2(x + \mathrm{d}x), \end{aligned} \tag{3.14}$$

where the energy densities are defined as

$$\begin{aligned} \rho'_e(x) \quad &= \quad \frac{\int_{E_{\mathrm{min}}}^{\infty} E'_e N'(x, E'_e)\mathrm{d}E'_e}{\pi R^2(x)}, \qquad \rho_B(x) = \frac{B^2(x)}{2\mu_0}, \\ \rho''_e(x + \mathrm{d}x) &= \frac{\int_{E_{\mathrm{min}}}^{\infty} E'_e N''(x + \mathrm{d}x, E'_e)\mathrm{d}E'_e}{\pi R^2(x + \mathrm{d}x)}, \end{aligned} \tag{3.15}$$

In the accelerating part of the jet the initial electron distribution at the beginning of the section starting at $x + \mathrm{d}x$ is given by

$$N(x + \mathrm{d}x, E_e) = N''(x + \mathrm{d}x, E_e). \tag{3.16}$$

We assume that the plasma in the conical part of the jet is always in equipartition and the jet is ballistic so no longer suffers adiabatic losses as in Chapter 2. In this case the bulk kinetic energy of the jet is converted into the acceleration of electrons and amplification of the magnetic field (though a process such as shock acceleration or magnetic reconnection as discussed in more detail in Section 3.3) as the jet decelerates and so we use Equation 3.8 to determine the amount of energy injected into electrons in a slab of rest frame width 1m $\Delta\rho_{\rm dec}(x+{\rm d}x)\pi R(x+{\rm d}x)^2$.

$$\gamma_{\rm bulk}(x)^2(\rho_{\rm B}(x)+\rho'_{\rm e}(x))\pi R^2(x) = \gamma_{\rm bulk}(x+{\rm d}x)^2 ...$$
$$\times(\rho_{\rm B}(x+{\rm d}x)+\rho''_{\rm e}(x+{\rm d}x)+\Delta\rho_{\rm dec}(x+{\rm d}x))\pi R^2(x+{\rm d}x), \tag{3.17}$$

where we ensure the jet remains in equipartition in the conical section via the constraint

$$\rho_{\rm B}(x+{\rm d}x) = \rho''_{\rm e}(x+{\rm d}x)+\Delta\rho_{\rm dec}(x+{\rm d}x). \tag{3.18}$$

The electron spectrum at $x+{\rm d}x$ in the decelerating part of the jet is given by

$$N(x+{\rm d}x, E_e) = N''(x+{\rm d}x, E_e) + C(x+{\rm d}x)E_e^{-\alpha}e^{-E_e/E_{\rm max}}, \tag{3.19}$$

$$\Delta\rho_{\rm dec}(x+{\rm d}x)\pi R(x+{\rm d}x)^2 = C(x+{\rm d}x)\int_{E_{min}}^{\infty} E_e^{1-\alpha}e^{-E_e/E_{\rm max}}{\rm d}E_e. \tag{3.20}$$

3.3 Physical conditions at the base of the jet

We wish to calculate the magnetic field strength and electron population in the rest frame in terms of the physical parameters of the jet. For a relativistic jet with total kinetic luminosity of W_j, $\frac{W_j}{c}$ is equal to the total energy in a section of plasma of width one metre in the x direction in the lab frame E_j.

$$E_j = T^{00}(x=0){\rm d}V = \frac{4}{3}\gamma_0^2\rho(x=0)\pi R_0^2, \tag{3.21}$$

$$\rho(x=0) = \frac{3E_j}{4\pi R_o^2 \gamma_0^2}, \tag{3.22}$$

$$\rho(x=0) = \rho_B(x=0) + \rho_e(x=0), \qquad A_{\text{equi}}(x) = \frac{\rho_B(x)}{\rho_e(x)}, \tag{3.23}$$

$$\rho_B(x=0) = \frac{B_0^2}{2\mu_0}, \tag{3.24}$$

We assume that the high energy electrons have been accelerated through shocks (Bell [1978]) or magnetic reconnection (Zenitani and Hoshino [2001] and Zenitani and Hoshino [2007]). Our code is flexible and allows us to inject an arbitrary electron population at different distances along the jet so we are not tied to a specific mechanism for particle acceleration. In this Chapter we characterise the spectrum as being a power law with index α with an exponential cutoff at energy E_{max} and with a minimum energy E_{min}. A power law electron distribution with an exponential cutoff is an approximation to the steady state solution to the diffusion loss equation for a shock including radiative energy losses (see for example Bregman [1985]). The number of electrons contained in a slab of width one metre in the rest frame of the plasma is given by

$$N_e(x=0, E_e) = A(x=0) E_e^{-\alpha} e^{-\frac{E_e}{E_{\text{max}}}}. \tag{3.25}$$

In general, our electron distribution will evolve due to energy losses and additional injection of electrons to take a more general form where $A(x, E_e)$ becomes a function of electron energy and length along the jet. Our initial value of electron energy density is therefore

$$\rho_e(x=0) = \int_{E_{\text{min}}}^{\infty} E_e \frac{N_e(x=0, E_e)}{\pi R_0^2} \mathrm{d}E_e. \tag{3.26}$$

These equations specify the evolution of the plasma along the jet conserving energy-momentum and electron number density. We now turn our attention to calculating the observed synchrotron emission from the jet.

3.4 Synchrotron emission

In this section we will generalise the calculation of synchrotron emission from Chapter 2 to the case of a jet with a variable bulk Lorentz factor. In the lab frame we wish to calculate the observed luminosity at a given observation angle of the jet. To do this we will calculate the emission and absorption of synchrotron radiation corresponding to an observed lab frame frequency and observation angle as it propagates along the jet by Lorentz transforming into the rest frame at every section of the jet. Observed synchrotron radiation at a frequency ν and angle θ_{obs} corresponds to an emitted frequency ν' and angle θ'_{obs} in the rest frame of a section of plasma with bulk Lorentz factor γ_{bulk} given by a Lorentz transformation

$$\nu' = \frac{\nu}{\delta_{\mathrm{Doppler}}(x)}, \quad \delta_{\mathrm{Doppler}}(x) = \frac{1}{\gamma_{\mathrm{bulk}}(x)(1-\beta(x)\cos(\theta_{\mathrm{obs}}))}, \tag{3.27}$$

$$\theta'_{\mathrm{obs}} = \cos^{-1}\left(\frac{\cos(\theta_{\mathrm{obs}})-\beta(x)}{1-\beta(x)\cos(\theta_{\mathrm{obs}})}\right), \quad \gamma_{\mathrm{bulk}}(x) = \frac{1}{\sqrt{1-\beta(x)^2}}. \tag{3.28}$$

We track photons emitted from interior sections of the jet as they move through outer sections by transforming into the rest frame of each section. For a given observed lab frame frequency ν all the contributing synchrotron photons from different sections with different bulk Lorentz factors will have the same frequency ν' and emission angle θ'_{obs} in the rest frame of the section at x. This means that in order to calculate the emission at an observed frequency ν we need to calculate the synchrotron emission at different frequencies ν' in sections of plasma with different bulk Lorentz factors. To calculate the line of sight opacity to a section we need to integrate the opacity at rest frame frequency ν' across the rest frame path lengths of all the outer sections.

We use the result from Chapter 2 for the distance travelled through the plasma by a synchrotron photon in the rest frame

$$\mathrm{d}r' = \gamma_{\mathrm{bulk}}\mathrm{d}x\left(\frac{1}{\cos(\theta_{\mathrm{obs}})} - \beta(x)\right), \tag{3.29}$$

where $\mathrm{d}r'$ is the total rest frame distance travelled by the photon. We use the equations for the synchrotron emission and opacity $k_\nu(\nu, x)$ from Chapter 2. Using the formulae for the synchrotron opacity from Chapter 2 we find the observed optical depth to a section to be given by

$$\tau_{tot}(\nu, x) = \int_x^L k_\nu(\nu'(x), x)\mathrm{d}r'. \tag{3.30}$$

The observed synchrotron emission from the jet is given by

$$\nu P_{\nu\,\mathrm{obs}} = \sum_x \delta_{\mathrm{Doppler}}(x)^4 \nu' P_\nu(x, \mathrm{d}x, \nu') e^{-\tau_{tot}(\nu,x)}, \tag{3.31}$$

where the length of an emitting section in the rest frame of the plasma $\mathrm{d}x'$ is related by a Lorentz contraction to the lab frame section length $\mathrm{d}x$.

3.5 Inverse-Compton emission

3.5.1 SSC emission

To calculate the SSC emission we use the result of the emission produced in the plasma rest frame from Chapter 2. Since the high energy emission is optically thin the only modification to the earlier result is that we need to Doppler-boost the emission from each section individually. We use Equation 3.36 to calculate the inverse-Compton power emitted by a section in its rest frame per log bin of rest frame frequency (corresponding to $\nu' P'_\nu$).

$$\nu P_\nu = \sum_x \nu'(x) P'_\nu(\nu'(x), x, \mathrm{d}x)\delta_{\mathrm{Doppler}}(x)^4. \tag{3.32}$$

3.5.2 Inverse-Compton scattering of external photons

In this work we consider the six most likely sources of external photons to the jet: the CMB, radiation directly from the accretion disc, starlight and radiation from the accretion disc scattered by free electrons in the BLR and reprocessed by a dusty torus and NLR. Inverse-Compton scattering of external photons has been investigated by a number of authors including Dermer et al. [1992], Dermer and Schlickeiser [1993], Sikora et al. [1994], Böttcher and Bloom [2000] and Hardcastle and Croston [2011].

The full calculation for the inverse-Compton emission of an axisymmetric external photon field by an isotropic electron distribution takes the form of a seven dimensional integral. In order to make the problem computationally tractable we make a number of simplifying approximations. Firstly we assume that, in a collision with an electron, the scattered photon travels with a velocity parallel to the electron's initial velocity. This approximation is commonly used when considering inverse-Compton scattering of photons (Dermer et al. [2009]) and is justified because the scattered photon's energy is a steep function of its scattering angle with significant scattering energies occurring for photons travelling close to the electron's initial velocity, due to conservation of momentum.

For a jet with a significant bulk Lorentz factor, radiation which is isotropic relative to the black hole is Doppler-boosted in the rest frame of the jet plasma, such as the CMB, starlight, BLR, NLR and dusty torus photons. The radiation is Doppler-boosted in the plasma rest frame so that it is beamed along the jet axis in the opposite direction to the jet material with a characteristic opening angle $\sim \frac{1}{\gamma_{\rm bulk}}$. This means that for large values of $\gamma_{\rm bulk}$ almost all external photons travel close to the jet axis. We shall make the approximation that all the external photons travel in the negative x-direction to reduce the dimensionality of the integral to 3. This approximation is strictly valid only in the limit of large $\gamma_{\rm bulk}$, however, the scattered energy of the photons depends on the incident photon direction through $\propto (1+\beta\cos(\theta))$ so for a small change in opening angle $\frac{1}{\gamma_{\rm bulk}}$ the scattered photon energy will not change significantly. The total number density of external photons is therefore increased by a single Doppler factor and their energy is also increased by a Doppler factor in the rest frame of the plasma (since we have effectively integrated over solid angle).

In the case of external photons travelling directly from the accretion disc we make similar approximations. We approximate the scattered photon velocity to be parallel to the initial electron velocity. We also approximate the external accretion disc photons to travel in the positive x-direction, this is justified because the brightest part of the accretion disc is closest to the black hole (at a few Schwarzschild radii) and so the base of the jet is not illuminated isotropically by the accretion disc. The most energetic photons illuminate the disc from behind in the frame of the black hole.

In contrast to the case of photons from the CMB, starlight, BLR, NLR and dusty torus, photons directly from the accretion disc are de-boosted, so Lorentz transforming into the plasma rest frame results in the photon angles diverging away from x-axis. This means that our approximation is only justified in the case that the radius of the jet is smaller than the distance from the accretion disc. If this is not the case then the approximation results in an underestimate of the inverse-Compton emission from accretion disc photons, however, neither the Doppler factor nor scattering cross section depend very steeply on the angle of the photons from the x-axis for the case of photons illuminating the jet from behind so the results should not differ significantly from a more detailed treatment (see for example Dermer et al. [2009]). Since most previous investigations have assumed de-boosted accretion disc photons are not relevant to inverse-Compton emission it is interesting to see whether this emission is significant.

With these approximations we can use a modified version of the inverse-Compton scattering formula from Chapter 2 to calculate the inverse-Compton emission from external photon sources. By using these approximations we have eliminated the integration over θ. Instead, we only consider scattering from electrons travelling at an angle θ where this angle corresponds to photons scattered in the lab frame at the observation angle of the jet $\theta_{\rm obs}$. This angle θ is easily related to the observation angle of the jet via a Lorentz transformation which in the case of CMB, starlight, BLR, NLR or dusty torus photons we calculate to be.

$$\theta = \cos^{-1}\left(\frac{\cos(\theta_{\rm obs}) - \beta(x)}{1 - \beta(x)\cos(\theta_{\rm obs})}\right), \tag{3.33}$$

and for the case of external photons directly from the accretion disc

$$\theta = \pi - \cos^{-1}\left(\frac{\cos(\theta_{\rm obs}) - \beta(x)}{1 - \beta(x)\cos(\theta_{\rm obs})}\right). \tag{3.34}$$

Fixing the value of θ using one of Equations 3.33 or 3.34 we find the inverse-Compton emission of external photons to be

$$\begin{aligned} \mathrm{weight}(E_e, E_\gamma, \theta, \phi_2, x) &= N_e(E_e, x).\frac{\mathrm{d}\sigma(E'_\gamma, \phi_2)}{\mathrm{d}\Omega_2} \\ &\times n_\gamma(E_\gamma, \theta, x).c(1 + \beta_e\cos\theta)\pi|\sin\phi_2|. \end{aligned} \tag{3.35}$$

$$\text{Power}(W) = \sum_{E_e,E_\gamma,\theta,\phi_2,x} E_{\gamma\text{scatt}}.\text{weight}(E_e,E_\gamma,\theta,\phi_2,x) \\ \times \mathrm{d}E_e \mathrm{d}E_\gamma \mathrm{d}\phi_2 \mathrm{d}x'. \quad (3.36)$$

where β_e is the electron velocity divided by c. We now proceed to calculate the number density of external photons in the plasma rest frame for the six sources. In the following subsections quantities defined in the lab frame of the jet are primed and quantities in the rest frame of the jet plasma are not primed.

3.5.3 CMB

We use the blackbody distribution to find n_γ for the CMB at redshift z with $T = 2.73(1+z)$K.

$$n'_\gamma(\nu') = \frac{4\pi}{c}\frac{2\nu'^2}{c^2(e^{\frac{h\nu'}{k_bT}}-1)} = \frac{8\pi\nu'^2}{c^3(e^{\frac{h\nu'}{k_bT}}-1)}. \quad (3.37)$$

We average the Doppler factor over solid angle to find the mean Doppler factor for photons emitted isotropically in the black hole rest frame which is γ_{bulk}. The frequency of the photons and their arrival rate are both boosted by a Doppler factor. The number density per unit frequency of photons is therefore unaltered since the increase in arrival rate is compensated by the stretching of the frequency bin occupied by the photons.

$$\delta_{\text{Dopp}}(x)n'_\gamma(\nu')d\nu' = n_\gamma(\nu)d\nu, \qquad \delta_{\text{Dopp}}(x) = \gamma_{\text{bulk}}, \quad (3.38)$$

$$n_\gamma(\nu) = \delta_{\text{Dopp}}(x)n'_\gamma\left(\frac{\nu}{\delta_{\text{Dopp}}(x)}\right)\frac{d\nu'}{\delta_{\text{Dopp}}(x)d\nu'},\ n_\gamma(\nu) = n'_\gamma(\nu'). \quad (3.39)$$

From these equations we find that the total energy density of CMB photons in the plasma rest frame $U_{\text{phot}} = \int h\nu n_\gamma(\nu)\mathrm{d}\nu$ is proportional to the bulk Lorentz factor squared as we expect from Equation 3.7.

3.5.4 Thin Accretion Disc

We consider a thin accretion disc (Shakura and Sunyaev [1973]) around a black hole of mass M accreting at a rate $\dot{M}$. Since we do not know the likely black hole spin parameters of these AGN we will conservatively assume a slowly rotating black hole. We treat the thin disc as a radiating blackbody.

$$\mathrm{d}L = \frac{3G\dot{M}M}{2r^2}\mathrm{d}r = 2\sigma T^4 2\pi r \mathrm{d}r, \tag{3.40}$$

$$T = \left(\frac{3G\dot{M}M}{8\sigma\pi r^3}\right)^{\frac{1}{4}}, \tag{3.41}$$

$$L_\nu = \int_{r_{in}}^{r_{out}} \frac{4\pi h r \nu'^3}{c^2\left(e^{\frac{h\nu'}{k_b T}-1}\right)}\mathrm{d}r, \qquad r_{in} = \frac{6GM}{c^2}. \tag{3.42}$$

We make the approximation that the accretion disc luminosity is emitted isotropically and consider the photon density at a radius R from the disc in the lab frame.

$$n'_\gamma = \frac{L_{\nu'}}{4\pi R^2 h\nu' c}. \tag{3.43}$$

The photon number density and frequency both decrease by a Doppler factor when they are Lorentz transformed into the plasma rest frame. Again we use the value of the Doppler factor averaged over solid angle

$$n_\gamma(\nu) = n'_\gamma(\nu\delta_{\mathrm{Dopp}}(x)), \quad \delta_{\mathrm{Dopp}}(x) = \gamma_{\mathrm{bulk}}. \tag{3.44}$$

3.5.5 Starlight

Inverse-Compton scattering of starlight by jets has been investigated previously by Hardcastle and Croston [2011]. In this work we are fitting to a powerful Compton-dominant blazar so we expect its host galaxy to be a giant elliptical. Work by Lauer et al. [1995] and Faber et al. [1997] found that the luminosity density at the centre of giant ellipticals is considerably lower than that of smaller elliptical or disk galaxies with the luminosity density at 30pc in the most massive ellipticals found to be typically between $2 - 10L_\odot\mathrm{pc}^{-3}$. These large ellipticals have relatively flat cores over which the luminosity density goes as $\rho_L \propto r^a$ with $-1.3 < a < -1.0$ (Lauer et al. [1995]). At larger distances the luminosity density decreases as $\rho_L \propto r^{-4}$ (Tremaine et al. [1994]). In M87 the flat core with a luminosity density power law index $a = -1.3$ extends out to 40kpc (Cohen and Ryzhov [1997]). Using the typical values above to model the seed photon population due to starlight along the jet we choose a luminosity density given by

$$\rho_L(r) = \frac{5L_\odot(30\,\mathrm{pc})^{1.2}}{r^{1.2}}(\,\mathrm{W\,pc^{-3}}) \;\text{ for }\; 1\,\mathrm{pc} \geq r \leq 40\,\mathrm{kpc}, \tag{3.45}$$

$$\rho_L(r) = \frac{\rho_L(r = 40\,\mathrm{kpc})(40\,\mathrm{kpc})^4}{r^4}(\,\mathrm{W\,pc^{-3}}) \;\text{ for }\; r > 40\,\mathrm{kpc}, \tag{3.46}$$

where the luminosity density is assumed to be constant within the central 1pc of the galaxy. We calculate the total enclosed stellar mass in the core of the galaxy corresponding to this luminosity density to be $4.0 \times 10^{12} M_\odot$ using a mass to light ratio of 10, this is consistent with the expected stellar mass in the core of a large elliptical galaxy. We calculate the energy density of starlight observed by the jet plasma at a distance x along the jet ($\rho_{\mathrm{star}}(x)$) by the integral

$$\rho_{\mathrm{star}}(x) = \int_x^{100\mathrm{kpc}} \frac{4\pi r^2 \rho_L(r)}{4\pi r^2 c}\mathrm{d}r = \int_x^{100\mathrm{kpc}} \frac{\rho_L(r)}{c}\mathrm{d}r, \tag{3.47}$$

where we have started the integral at the position of the jet section, x, since the starlight from regions $r < x$ will illuminate the jet from behind and so will be strongly Doppler-deboosted. We have also made use of the spherical symmetry of the problem to simplify the integral, since all observers inside a spherically symmetric emitting surface see the same isotropic luminosity and surface brightness (due to Newton's shell theorem). This means that we can calculate the observed energy density for an observer at the origin in order to simplify the integral, since this is the same as the luminosity observed by the plasma at $r = x$. Using this integral we find the energy density of starlight at a distance of 1pc from the centre of the galaxy to be $\approx 2 \times 10^{-12}\mathrm{Jm^{-3}}$. This is in agreement with the value quoted in Hardcastle and Croston [2011] for the energy density in starlight at the centre of an elliptical galaxy.

We assume that the starlight is predominantly due to K-type stars which typically dominate the spectra of elliptical galaxies. We choose the photon distribution to be that of a 5000K blackbody since this corresponds to the surface temperature of a typical K-type star. In practice it is difficult to accurately model the interstellar radiation field at the centre of a powerful FSRQ since the detailed properties of the stellar population will vary substantially between galaxies. We include starlight in our model for completeness and to investigate whether there is evidence of inverse-Compton scattering of starlight from fitting to the spectrum of PKS0227.

3.5.6 Accretion disc photons scattered by the broad line region

To calculate the number density of accretion disc photons scattered by the broad line region in the lab frame we use the result from Dermer et al. [2009].

$$n'_\gamma(E'_\gamma) \approx \frac{n_e^{\mathrm{BLR}}(R)\sigma_{\mathrm{T}} L_{\mathrm{acc}}(E'_\gamma)}{4\pi R c E'_\gamma}, \tag{3.48}$$

where $n_{\mathrm{e}}^{\mathrm{BLR}}(R)$ is the free electron number density. The authors calculated this result assuming that accretion disc photons are Thomson scattered by free electrons in the BLR. The result assumes that the scattered radiation field is isotropic in the lab frame so the photon number density and energy in the plasma rest frame are related to that in the lab frame by a Lorentz transformation.

$$n_\gamma(E_\gamma) = n'_\gamma\left(\frac{E'_\gamma}{\delta_{\mathrm{Dopp}}(x)}\right), \quad \delta_{\mathrm{Dopp}}(x) = \gamma_{\mathrm{bulk}}. \tag{3.49}$$

where we have used the value of the Doppler factor averaged over solid angle. We assume the BLR extends out to $R_{\mathrm{BLR}} = 0.019\left(\frac{\lambda L_\lambda(5100\mathring{A})}{10^{44}\mathrm{erg\,s^{-1}}}\right)^{0.69}$ pc (Kaspi et al. [2005]), which we take to be 0.5pc for the most powerful FSRQ type blazars such as PKS0227. To calculate the value of n_e^{BLR} we assume a constant number density of electrons out to R_{BLR} and a covering fraction for the BLR, $\eta_{\mathrm{BLR}} = 0.1$ (as assumed in Ghisellini and Tavecchio [2008] and Sikora et al. [2009]). The covering fraction is given approximately by

$$\eta_{\mathrm{BLR}} = \int \frac{n_e^{\mathrm{BLR}}\sigma_{\mathrm{T}}}{4\pi R^2} 4\pi R^2 \mathrm{d}R \approx n_e^{\mathrm{BLR}}\sigma_{\mathrm{T}} R_{\mathrm{BLR}}. \tag{3.50}$$

For our chosen covering fraction and BLR radius this gives $n_e^{\mathrm{BLR}} = 1.0 \times 10^{11}\mathrm{m}^{-3}$.

3.5.7 Dusty Torus and Narrow Line Region

We now calculate the number density of photons scattered by clumps of dust in the torus and narrow line region (NLR) surrounding the black hole. At a distance x from the black hole the surface temperature of the dust facing towards the accretion disc, T_{dust}, is given by (Nenkova et al. [2008a])

$$T_{\text{dust}} = 1500 \left(\frac{x}{x_d}\right)^{0.39} K \qquad x \leq 9x_d,$$

$$T_{\text{dust}} = 640 \left(\frac{9x}{x_d}\right)^{0.45} K \qquad x > 9x_d. \tag{3.51}$$

where $x_d = 0.4(L_{\text{acc}}/10^{37}W)^{1/2}$pc is the dust sublimation distance and L_{acc} is the total accretion disc luminosity. We assume a clumpy dust cloud distribution where the number density of clouds is given by $n_{\text{cloud}} \propto x^{-q}$ with $1 \leq q \leq 2$ following Nenkova et al. [2008a]. We also assume that the distribution of cloud sizes is independent of x. The hot torus absorbs and reprocesses a fraction (the covering fraction) η_T of the incident accretion disc radiation. We use a covering fraction of $\eta_T = 0.1$ taken from the ratio of accretion disc to dusty torus emission in Nenkova et al. [2008b]. We further assume that this hot torus extends from the dust sublimation distance x_d out to $\sim 10x_d$ as indicated by observations (Elitzur [2006] and Nenkova et al. [2008b]). We assume that the NLR has a covering fraction $\eta_{\text{NLR}} = 0.07$ (Mor et al. [2009]) and extends from the outer radius of the torus ($x = 10x_d$) out to a distance x_{outer}, typically around 1kpc (Bennert et al. [2006]).

We now calculate the number density of photons from this dust distribution. Taking the average cross-sectional area of a cloud σ_{cloud} independent of x, the cloud number density and the covering fraction, we can calculate the emissivity of the dust as a function of distance from the black hole. The average emissivity of the dust $j(x)$ at a distance x will be proportional to the number density of clouds at x, so $j(x) = j_0 x^{-q}$

$$\eta_T L_{\text{acc}} = \text{const.} \int_{x_d}^{10x_d} n_{\text{cloud}}(x)\sigma_{\text{cloud}} 4\pi x^2 \text{d}x = j_0 \int_{x_d}^{10x_d} 4\pi x^2 x^{-q} \text{d}x. \tag{3.52}$$

From this equation we can calculate j_0 for both the torus and NLR (with the appropriate torus and NLR quantities interchanged). Since the bulk Lorentz factor of the jet is large we only consider emission from spherical shells at a radius greater than the distance of the jet section from the black hole, since radiation emitted from behind the jet is Doppler-deboosted in the rest frame of the jet. We use Newton's shell theorem to calculate the energy density of radiation inside an emitting shell of dust. We assume clouds re-emit the absorbed accretion disc radiation as a black body with a temperature given by Equation 3.51 (this is the correct dust temperature since we are only interested in the emission from the surface of clouds facing back towards the jet and black hole). In this case the number density of photons from dust outside a distance x in the lab frame is given by

$$n'_{\nu}(x,\nu') = \int_{x}^{x_{\mathrm{outer}}} \frac{j(\nu',x)}{4\pi x^2 ch\nu'} 4\pi x^2 \mathrm{d}x, \tag{3.53}$$

where $j(x,\nu')$ is the appropriate blackbody distribution normalised to the correct emissivity.

$$j(x,\nu') = \frac{\pi j_0 x^{-q}}{\sigma T_{\mathrm{dust}}(x)^4} . \frac{2h\nu'^3}{c^2} . \frac{1}{e^{h\nu'/k_B T_{\mathrm{dust}}(x)} - 1}. \tag{3.54}$$

The number density of photons in the plasma rest frame is then given by

$$n_{\nu}(x,\nu) = n'\left(x, \frac{\nu}{\delta_{\mathrm{Dopp}}}\right), \qquad \delta_{\mathrm{Dopp}} = \gamma_{\mathrm{bulk}}(x). \tag{3.55}$$

In this work we take the value of $q = 1$ for the cloud distribution as suggested by Mor et al. [2009] from fitting to observations.

3.5.8 Observed external Compton emission

The observed inverse-Compton emission from the external photons is related to the emission in the rest frame by

$$\nu F_{\nu} = \sum_{x} \nu'(x) F'_{\nu}(\nu'(x), x, \mathrm{d}x) \delta_{\mathrm{Doppler}}(x)^4. \tag{3.56}$$

3.6 Particle acceleration and energy losses

We take into account radiative and adiabatic losses to the electron population as it traverses along the jet. We use Equation 3.59 to take into account the effects of radiative losses to the population due to both synchrotron and inverse-Compton emission. In addition to radiative losses in this investigation we will also consider adiabatic losses in the accelerating parabolic section of the jet. We assume the conical section of the jet is ballistic and so does not suffer adiabatic losses as in Chapter 2. We use the formula from Kaiser [2006] to include adiabatic losses to a relativistic electron population.

$$E' = E\left(\frac{V'}{V}\right)^{-\frac{1}{3}} = E\left(\frac{R}{R'}\right)^{\frac{2}{3}}, \tag{3.57}$$

$$N'(E') = N(E), \tag{3.58}$$

where E is the initial energy of an electron, V is the initial volume of the section and R the initial radius, primed quantities are those after expansion. Considering the electron distribution contained in a slab of width one metre in the rest frame, we use the following equation to take into account radiative energy losses to the electron population as it travels along the jet.

$$N_e(E_e, x + \gamma_{\mathrm{bulk}}\mathrm{d}x') = N_e(E_e, x) - \frac{P_{\mathrm{tot}}(x, \mathrm{d}x', E_e) \times 1m}{cE_e}, \tag{3.59}$$

where P_{tot} is the total power emitted by electrons of energy E_e in a section of rest frame jet width $\mathrm{d}x'$ due to synchrotron and inverse-Compton emission. The energy losses for the synchrotron and SSC emission are the same as those calculated in Chapter 2. We have simplified the calculation of the inverse-Compton scattering of external photons by considering only the scattering events which lead to photons travelling at the observation angle. To calculate the electron energy losses from this anisotropic photon field we must take into account the average energy lost from isotropic electrons encountering a narrow beam of external radiation. In this case we can use the formula in Chapter 2 (Equation 2.37) for the total power emitted by an isotropic electron distribution scattering an isotropic photon field using the value of n_γ calculated above for the external photon fields. After radiative losses have been taken into account we then apply Equation 3.58 to the population to take into account adiabatic losses in the accelerating parabolic section.

3.7 Acceleration of electrons in the decelerating conical part of the jet

Observations of AGN jets show evidence for in situ acceleration occurring along the jet. High energy optical synchrotron electrons are observed at distances beyond that expected from their synchrotron lifetime (see Meisenheimer et al. [1997] and Jester et al. [2001]). Observations also indicate that jet material decelerates away from the base though the jet remains relativistic until the hot spot (Laing and Bridle [2002], Hardcastle et al. [2005] and De Young [2010]). In our model, bulk kinetic energy is converted into electron energy in the rest frame of the plasma as the jet decelerates once it has become conical. This is a natural result of conservation of energy-momentum in our model since a decelerating jet loses kinetic energy and so must gain internal energy (or do work on its environment) to conserve energy. We have assumed that the excess bulk energy is converted into both particle acceleration and amplification of the magnetic field to maintain equipartition throughout the conical section of the jet.

In this work we simulate the effect of acceleration of electrons by the injection of a fixed power law distribution of electrons continuously along the jet which conserves energy-momentum in the decelerating part of the jet. Observations of AGN jets show a continuous variation in optical spectral index along the jet with evidence for continuous acceleration taking place along the jet (Jester et al. [2001]) and so converting bulk kinetic energy to internal electron energy through deceleration is a natural way in which to explain these observations. This is the first time, however, that conversion of bulk kinetic energy into accelerating electrons through deceleration has been considered self-consistently in a continuous conical jet with a variable Lorentz factor.

The acceleration of these electrons is currently thought to be caused by either shock acceleration or magnetic reconnection, however, the precise acceleration mechanism is unknown. We have not assumed a particular acceleration mechanism in this work but simply assumed that this process produces a non-thermal power-law of electrons since this is compatible with observations and is predicted by shock acceleration and magnetic reconnection (Bell et al. [2011], Summerlin and Baring [2012] and Zenitani and Hoshino [2007]). Shocks can originate from a variety of mechanisms including the collision of shells of plasma travelling at different speeds as the jet decelerates (Spada et al. [2001]), shear acceleration (Rieger and Mannheim [2002]) or external pressure driven recollimation shocks (Komissarov and Falle [1998]). Variations of models in which in situ acceleration of electrons occurs are popular and have been investigated by many authors including Kaiser et al. [2000], Spada et al. [2001] and Jamil et al. [2010]. Recently it has been suggested that electrons could be accelerated by magnetic reconnection in jets since it can result in anisotropic acceleration of electrons which can potentially explain the extreme magnitude and short duration of γ-ray flares (Cerutti et al. [2012]).

We assume that the injected electrons have the same spectrum as the initial electron population (Equation 3.25). In this investigation we will assume that the injected electron distribution is the same along the jet. In practice the power law exponent and maximum energy cutoff will depend on the detailed properties of the acceleration mechanism and plasma (see e.g Bell [1978] and Bell et al. [2011]) but this is beyond the scope of our current investigation.

We calculate the evolution of the electron distribution along the jet by taking into account radiative energy losses on the electron population (and adiabatic losses on the remaining electrons in the parabolic section). We determine the energy density of electrons injected into the plasma due to deceleration by Equation 3.17.

3.8 Equipartition considerations

Observations indicate that on large scales the jet plasma is close to equipartition (Croston et al. [2005]). Observations of brightness temperatures of the cores of jets also indicate that the jet plasma is close to equipartition when sources are in a quiescent state, however, in some cases shocks are believed to produce regions where the plasma becomes particle dominated associated with flaring (Homan et al. [2006]). It is thought that jets are produced via the interaction of electromagnetic fields with a rotating black hole (Blandford and Znajek [1977]). Current models of jet production start with a magnetically dominated region which accelerates particles to form the jets we observe. Simulations indicate that the jet becomes conical when the plasma nears equipartition (McKinney [2006] and Komissarov et al. [2009]). This makes physical sense since the magnetic field has done work accelerating the electron plasma and in equipartition the remaining magnetic energy is not large enough to accelerate the jet substantially. In this model we force the jet plasma to be in equipartition after the point at which the jet becomes conical by the injection of accelerated, non-thermal electrons.

For a given total jet power we expect the synchrotron and SSC emission to be brightest when the jet is close to equipartition from a reversal of the minimum energy argument for synchrotron emitting lobes (Burbidge [1959]). If the accelerating region is magnetically dominated we therefore expect the synchrotron emission to be brightest at the point where the jet becomes conical since the bulk Lorentz factor, jet power and magnetic field will be largest at this point and will then decrease along the conical section.

3.9 Code

We use the equations given in the preceding sections and Chapter 2 to calculate the emission from the electrons along the jet. In order to make the problem computationally tractable we must discretise the electron population, sections of the jet and the particle acceleration resulting from the deceleration. Our code uses logarithmic bins of electron energy where the bin of energy E_e has a width $\mathrm{d}E_e = 0.3E_e$, so the total electron population for PKS0227 spans approximately 40 energy bins and for high frequency peaked BL Lacs this increases to approximately 60 bins. The jet sections are determined adaptively so that either the shortest radiative lifetime is resolved or the jet radius does not increase by more than 5%, this results in jets typically being composed of 200-600 cylindrical sections. At each decelerating section the equipartition fraction of the jet is calculated and additional electrons ($\Delta\rho_{\mathrm{dec}}$ in Equation 3.17) are only injected if this equipartition fraction differs from 1 by more than 10% so that we are not continually limited to resolving the shortest electron radiative lifetime.

We have chosen the above values for discretisation so that increasing the resolution/number of bins does not noticeably affect the spectrum produced from the jet, whilst this allows our code to produce a spectrum for a jet in 15-30 seconds running on a single processor core.

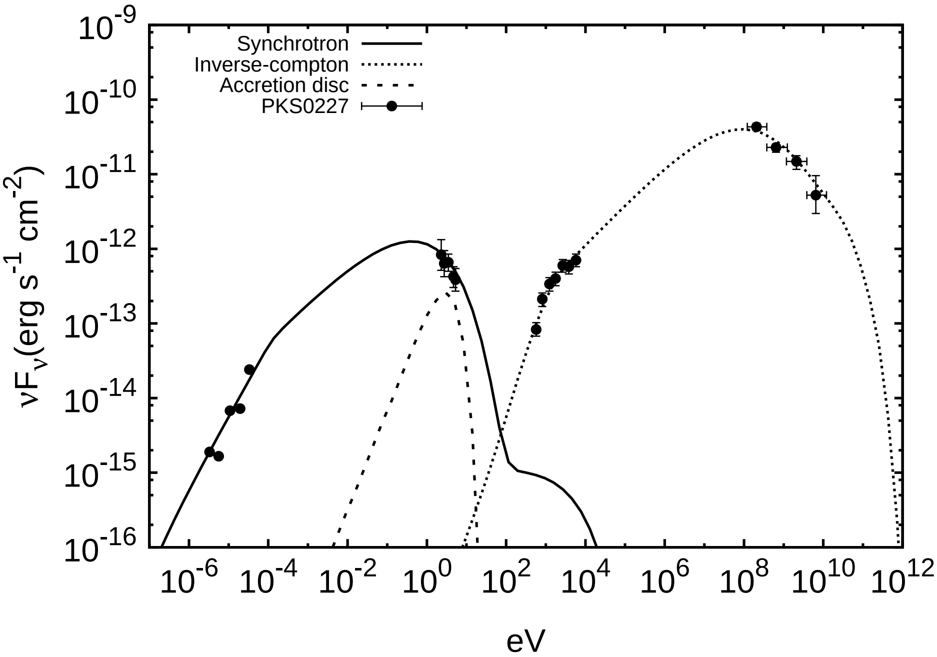

Figure 3.2: The results of fitting the model to the SED of PKS0227. The model fits the observations very well across all wavelengths including radio observations. We find the model fit requires a high jet power, high Lorentz factor jet observed at a small angle to the jet axis. We find that the inverse-Compton peak is due to scattering of Doppler-boosted high-redshift CMB with a small contribution from scattering NLR photons at the highest gamma-ray energies.

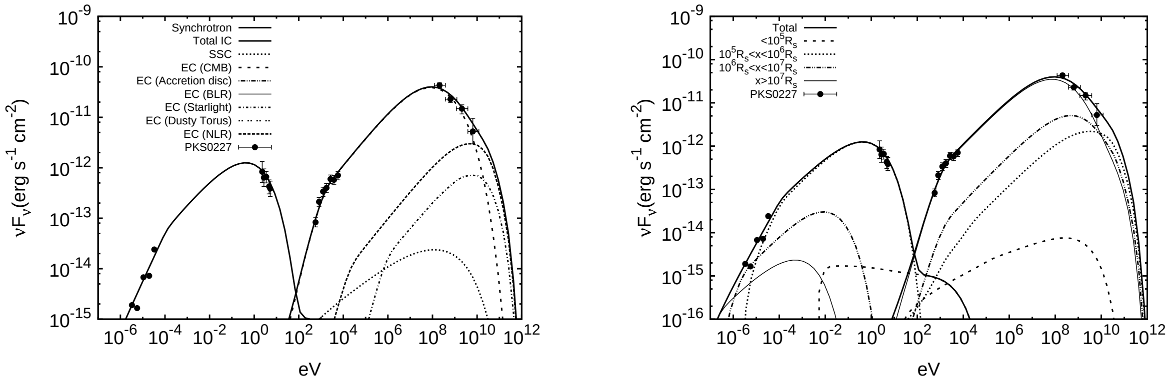

(a) (b)

Figure 3.3: The different inverse-Compton components in Figure a and the jet emission from different distances in Figure b, using a transition region at large distances. Figure a shows that the inverse-Compton emission is produced by scattering CMB photons with a small contribution from NLR at the highest gamma-ray energies. Figure b shows that the optically thin synchrotron emission is dominated by the transition region, with the radio emission coming from larger distances as we expect. The inverse-Compton emission originates at large distances from the central black hole from scattering CMB photons.

3.10 Results

In this Chapter we have set out to develop a physically realistic jet model which is consistent with observations and simulations and includes all the relevant physics to accurately predict its emission. In order to test whether the model can potentially describe real blazars we shall try to fit to the spectrum of the most Compton-dominant FSRQ from (Abdo et al. [2010a]) PKS0227-369. We choose a Compton-dominant blazar since in Chapter 2 we showed that a simpler version of this model was able to reproduce the spectrum of BL Lacertae, a relatively weak powered object. Compton-dominant blazars are thought to represent high-powered blazars (Fossati et al. [1998]) so it is interesting to see if our model is capable of reproducing the spectra of the two extremes of the blazar population. We assume a standard ΛCDM cosmology (Komatsu et al. [2011]) to calculate the distance to PKS0227 which has a redshift of $z = 2.115$ (Abdo et al. [2010a]).

We will first show the results of fitting our model to the data using a transition region at different distances along the jet: at large distances $>$ 10pc, within the dusty torus $\sim$pc and within the BLR $<$ 0.5pc. One of the most important current questions about jets is where the gamma-ray emission originates from. Using our realistic continuous jet model we attempt to fit the quiescent jet emission of PKS0227 and try to constrain the location of the quiescent jet emission.

3.10.1 Fit 1 - A transition region at large distances

We first attempt to fit the spectrum using a transition region at large distances outside the dusty torus and BLR as implied by the geometry of M87 where the jet transitions from parabolic to conical at $10^5 R_s$, corresponding to a distance of 66pc.

In Figure 3.2 we show the results of fitting the model by eye to the simultaneous multi-wavelength spectrum of PKS0227. We see that the model fits very well to the observations across all wavelengths including radio data points with a transition region at a lab frame distance of 34pc and a jet radius of 0.64pc. In Table 3.1 we show the model parameters for this fit to PKS0227. We find that the fit to the observations requires a high power ($W_j = 1.2 \times 10^{39}$W), high bulk Lorentz factor jet ($\gamma_{\rm max} = 45$), observed at a small angle to the line of sight ($\theta_{\rm obs} = 0.8^o$). This is consistent with our expectations of Compton-dominant FSRQs

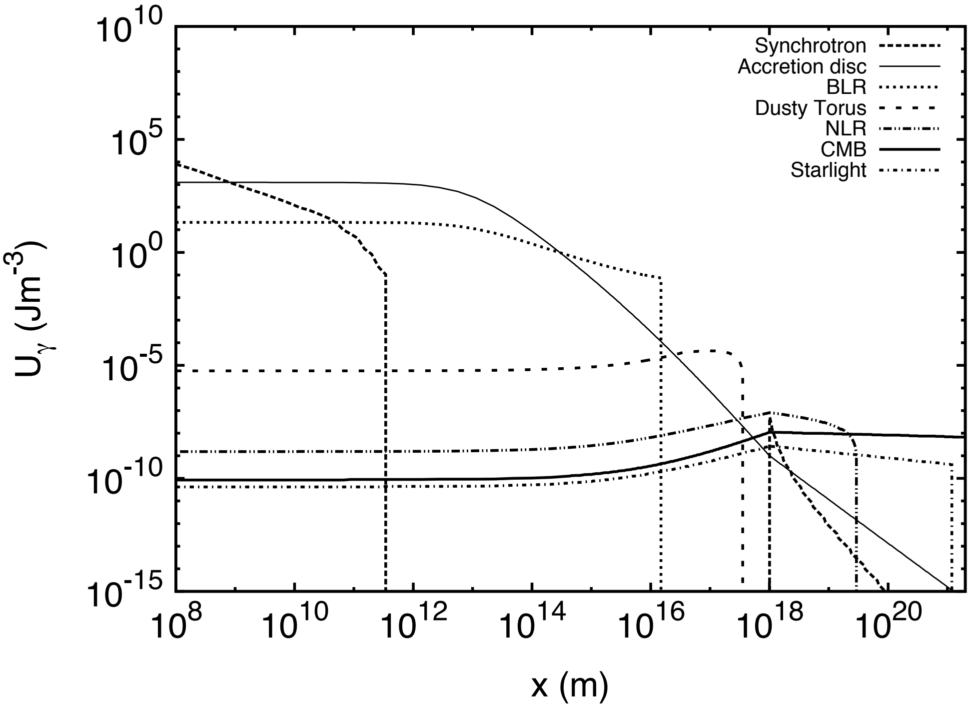

Figure 3.4: The energy density of the different radiation sources in the rest frame of the jet at different distances along the jet for Fit 1 to PKS0227. We see that the acceleration of the jet results in a steady increase in the Doppler-boosting of the BLR, dusty torus, NLR, CMB and starlight up to the transition region. At different distances along the jet different external photon sources become dominant as we expect. At the transition region ($x = 1.02 \times 10^{18}$m) the NLR is the dominant energy density resulting in the highest energy gamma-ray emission, however, the CMB becomes the dominant energy density at the largest distances along the jet where the majority of inverse-Compton emission is produced.

Parameter	Fit 1	Fit 2	Fit 3
W_j	1.2×10^{39}W	1.5×10^{39}W	1.2×10^{39}W
L_{acc}	8.3×10^{38}W	8.3×10^{38}W	8.3×10^{38}W
M_{acc}	$3.4 \times 10^{9} M_\odot$	$1.5 \times 10^{8} M_\odot$	$2.0 \times 10^{9} M_\odot$
L	2×10^{21}m	10^{21}m	2×10^{21}m
θ_{obs}	0.8^o	0.8^o	1.5^o
θ_{opening}	3^o	3^o	3^o
$A_{\text{equi}}(x=0)$	0.01	0.01	0.01
M	$3.4 \times 10^{9} M_\odot$	$1.5 \times 10^{8} M_\odot$	$4.5 \times 10^{7} M_\odot$
α	1.9	1.7	1.5
E_{min}	10.2 MeV	15.3 MeV	102 MeV
E_{max}	7.22 GeV	643 MeV	435 MeV
γ_0	4	4	4
γ_{max}	45	48	15
γ_{min}	35	38	10
x_{outer}	1kpc	1kpc	1kpc

Table 3.1: The values of the physical parameters used in the model fits to the multi-wavelength observations of PKS0227 as shown in Figures 3.2 and 3.6 and 3.8.

being FRII type AGN observed close to the jet axis (Urry and Padovani [1995]). We find that the jet has a maximum bulk Lorentz factor of 45 and the conical section of the jet decelerates to a bulk Lorentz factor of 35 by $x = 2 \times 10^{21}$m. For these parameters the magnetic field strength in the plasma rest frame at the transition region is relatively low, 2.03×10^{-6}T, required by the low synchrotron peak frequency and Compton-dominance of the blazar. We find a value of the electron spectral index $\alpha = 1.9$ close to the value expected from standard diffusive shock acceleration.

At these large distances the Compton-dominance is due to inverse-Compton scattering of CMB seed photons with a small contribution by NLR photons at the highest gamma-ray energies (see Figure 3.3a). In Figure 3.4 we show the energy density of the different radiation fields measured in the plasma rest frame at different distances along the jet for this fit. We see that the NLR dominates at the transition region but the CMB is the dominant photon source at large distances along the jet.

We include starlight seed photons in our model, however, we find that inverse-Compton emission from the CMB dominates the emission from starlight, as shown in Figure 3.3a, except at the highest energies. This is because the energy density in the CMB increases as $\propto (1+z)^4$, so whilst the energy density in starlight is significantly larger at $z = 0$, we find that the CMB photons are more significant for high-redshift Compton-dominant blazars such as PKS0227 (see Figure 3.4). The inverse-Compton scattering of starlight is also reduced relative to that of the CMB due to the decreased Klein-Nishina cross section for the higher energy starlight photons.

We find that accretion disc photons directly from the disc are the dominant photon energy density close to the base of the jet (within a few R_S of the black hole) but quickly become dominated by other photon sources due to the Doppler-deboosting and the $\frac{1}{x^2}$ dependence of the photon number density (see Figure 3.4). We find that for our fit to PKS0227 the Compton-dominance is due to inverse-Compton scattering of CMB and NLR photons in the conical jet region, as shown in Figure 3.3a. Previous investigations have ignored the contribution of CMB photons to the inverse-Compton emission. This is because in a BL Lac type object with a low bulk Lorentz factor jet at low redshift the CMB is dominated by SSC photons. We find that due to the high bulk Lorentz factor and high redshift of our model fit the CMB becomes the dominant photon source at large distances along the jet, $> x_{\mathrm{outer}}$, when taking into account the Doppler-boosting of the CMB into the rest frame of the plasma and including the redshift dependence of the CMB number density.

This is an interesting result since it has implications for the Cosmic evolution of Compton-dominant blazars. If their Compton-dominance is due to inverse-Compton scattering of CMB photons then we might expect to see a redshift dependence of the Compton-dominance of blazars, with increasing Compton-dominance at higher redshift (since the energy in the CMB scales as $(1+z)^4$). This could explain why most Compton-dominant blazars are observed at high redshifts. We might also expect to see rarer high powered, high Lorentz factor blazars at large redshift due to the increase in comoving volume and due to the larger number of major mergers in elliptical galaxies which host FRII sources. In practice it may be difficult to disentangle all these evolutionary effects, however, we might expect that high Lorentz factor blazars at low redshift are less Compton-dominant than the same sources at high redshift where the CMB has a higher blackbody temperature.

Figure 3.3b shows the total emission from different sections of the jet. The synchrotron emission is dominated by the transition region of the jet due to its high bulk Lorentz factor and higher magnetic field strength than outer parts of the jet. The low frequency radio emission originates from farther along the jet where the jet radius is larger. The inverse-Compton emission is dominated by the transition region and outer parts of the jet where electrons are accelerated through shocks in the decelerating part of the jet and radiate this energy slowly, primarily through scattering NLR photons at distances $x < x_{\mathrm{outer}}$ and CMB photons at larger distances.

In Figure 3.5 we show the evolution of the electron population in a slab as it travels along the jet in fit 1. A small amount of energy is injected into electrons at the base of the jet which quickly cool both radiatively and adiabatically from high to low energies due to the large magnetic field strength. The population is replenished by the shock at the base of the conical section located at $10^5 R_s = 1.08 \times 10^{18}$m where the plasma is in equipartition. The population then suffers radiative losses as it travels away from the shock, though less severely than at the base of the jet.

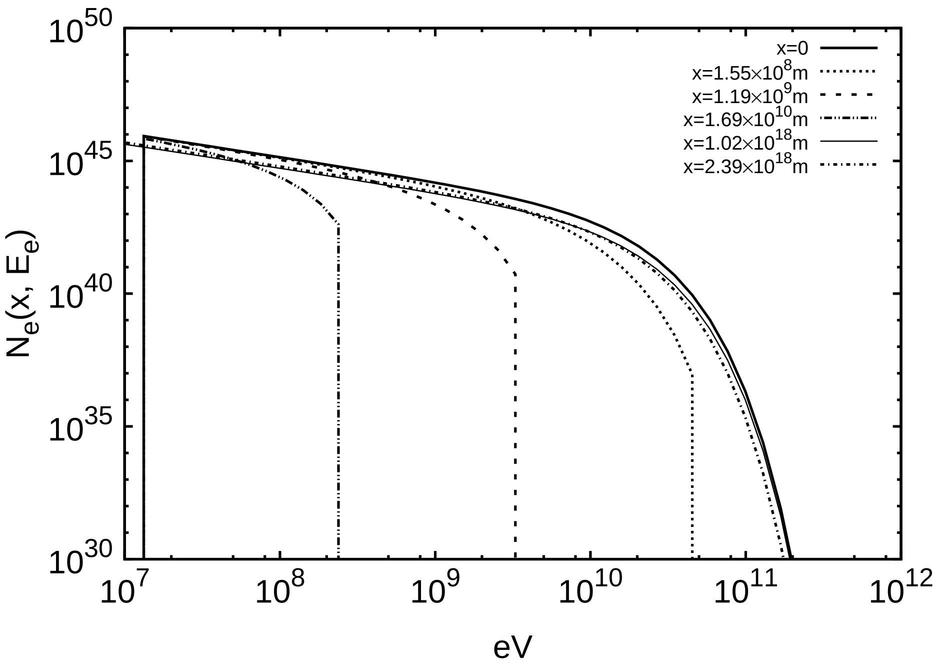

Figure 3.5: The evolution of the electron population contained in a slab of width 1m in the plasma rest frame as it travels along the jet in Fit 1. At the base of the jet, at $x = 0$, the electron population given by Equation 3.25. The electrons suffer large radiative and adiabatic losses in the compact accelerating region due to the high magnetic field strength and so the population quickly cools with the highest energy electrons cooling fastest. The population cools until it reaches the shock at the base of the conical section at $10^5 R_s = 1.02 \times 10^{18}$m where additional electrons are accelerated and the plasma is in equipartition. The population then proceeds to cool radiatively as it moves away from the shock but with a substantially greater radiative lifetime than at the base of the jet. This behaviour is repeated as the electrons are accelerated in the decelerating part of the jet.

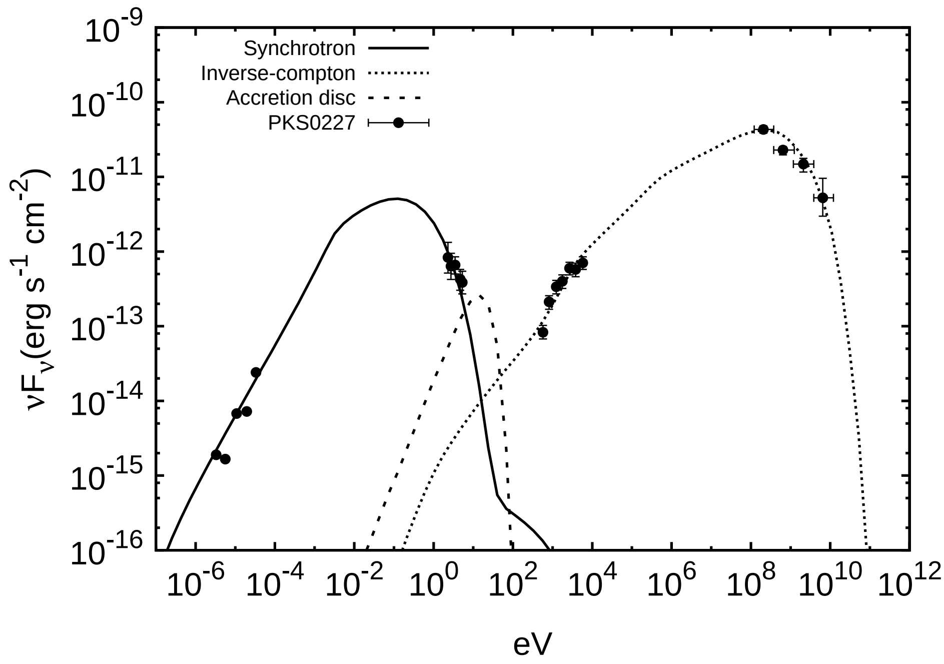

Figure 3.6: This figure shows the results of fitting the model to the SED of PKS0227 using a transition region within the dusty torus. The model fits the observations well across all wavelengths including radio observations. We find the model fit requires a high jet power, high Lorentz factor jet observed at a small angle to the jet axis. We find that the inverse-Compton peak is due to scattering of Doppler-boosted dusty torus photons at high energies and CMB photons at low energies.

3.10.2 Fit 2 - A transition region within the dusty torus

We now try to fit the spectrum using a transition region within the dusty torus but outside the BLR. An emission region within the dusty torus has been investigated previously using one and two-zone models by Błażejowski et al. [2000], Arbeiter et al. [2002], Sikora et al. [2009] and Tavecchio et al. [2011].

In Figure 3.6 we show the results of our model fitted by eye to the simultaneous multi-wavelength spectrum of PKS0227. The model fits well to the spectrum across all wavelengths with a transition region located at a distance 1.5pc from the central black hole with a jet radius of 9.0×10^{14}m. A transition region at this distance corresponds to a black hole mass of $1.5 \times 10^{8} M_{\odot}$ if the jet has the same geometry as M87 scaled linearly with black hole mass. In Table 3.1 we show the parameters used in the fit. Most of the jet parameters are very close to the values found for the fit at large distance in the previous section. Again the fit requires a high power ($W_j = 1.5 \times 10^{39}$W), high bulk Lorentz factor jet ($\gamma_{\rm max} = 48$) observed close to the jet axis $\theta_{\rm obs} = 0.8^o$. The maximum bulk Lorentz factor is 48, which decelerates to 38 by

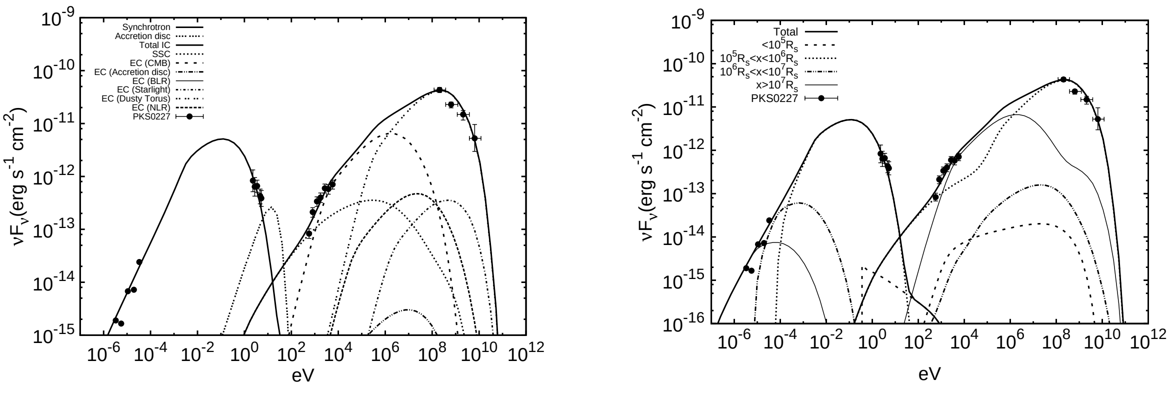

(a) (b)

Figure 3.7: The different inverse-Compton components in Figure a and the jet emission from different distances in Figure b, using a transition region within the dusty torus (Fit 2). Figure a shows that the inverse-Compton emission is produced by scattering dusty torus photons at high energies whilst the X-ray emission is due to scattering CMB photons. Figure b shows that the optically thin synchrotron emission is dominated by the transition region, with the radio emission coming from larger distances as we expect. The high energy inverse-Compton emission originates close to the transition region within the torus whilst the X-ray emission due to scattering CMB photons comes from further along the jet.

$x = 10^{21}$m.

In Figure 3.7a we show the different components of the inverse-Compton emission for the fit. We see that the dusty torus photons produce the highest energy gamma-rays with the CMB responsible for the low energy X-rays as in fit 1. Due to the relatively high magnetic field strength in the transition region, 4.81×10^5T, the jet produces SSC emission which contributes to the lowest energy X-ray observations. In Figure 3.7b we show the emission from different distances along the jet. The synchrotron emission is dominated by the transition region as we expect from the discussion in section 8, with the radio emission coming from larger distances along the jet. The high energy inverse-Compton emission is dominated by the transition region within the dusty torus, whilst the X-ray emission originates from scattering CMB photons at large distances.

3.10.3 Fit 3 - A transition region within the BLR

Finally we investigate modelling the spectrum using a transition region within the BLR. An emission region within the BLR has been investigated by many authors including Sikora et al. [1994], Böttcher and Bloom [2000], Ghisellini and Tavecchio [2008] and Dermer et al. [2009], and is the most popular location for the gamma-ray emission in blazars due to the ability to

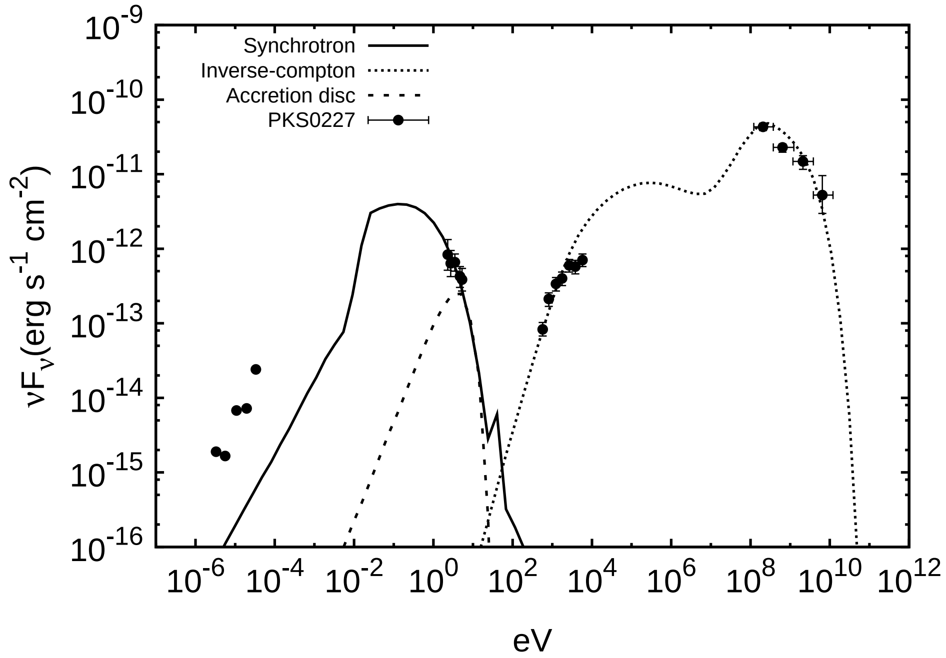

Figure 3.8: The results of fitting the model to the SED of PKS0227 using a transition region within the BLR. The model fits the high energy synchrotron and gamma-ray observations reasonably well but is unable to reproduce the radio observations due to the short radiative lifetime of electrons within the BLR. The fit requires a low maximum electron Lorentz factor to match the gamma-ray peak frequency and a high minimum electron Lorentz factor in order to not overproduce the observed X-ray emission with SSC. We find that the inverse-Compton peak is due to scattering of Doppler-boosted BLR photons at high energies and SSC photons at low energies.

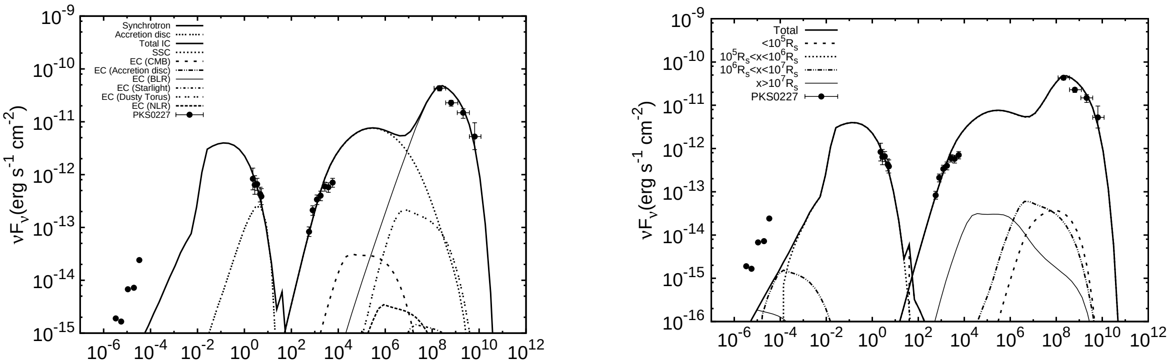

(a) (b)

Figure 3.9: The different inverse-Compton components in Figure a and the jet emission from different distances in Figure b, using a transition region within the BLR (Fit 3). Figure a shows that the inverse-Compton emission is produced by scattering BLR photons at high energies whilst the X-ray emission is due to SSC. Figure b shows that the optically thin synchrotron emission is dominated by the transition region, with an absence of radio emission from larger distances. Both the high and low energy inverse-Compton emission originate from close to the transition region within the BLR due to the high magnetic field strength.

reproduce short flaring timescales.

In Figure 3.8 we show a fit to the spectrum of PKS0227 using a transition region within the BLR and dusty torus. We show the parameters fitted by eye to the observations in Table 3.1. The transition region is located at a distance 0.45pc from the black hole with a jet radius of 2.7×10^{14}m. This corresponds to a black hole mass of $3.0 \times 10^{7} M_{\odot}$ if the jet has the same geometry as M87 scaled linearly with black hole mass. We see that whilst the model is able to reproduce the high energy gamma-rays and optical synchrotron, it is unable to fit the radio or X-ray observations. We find that due to the short radiative lifetime of electrons in the BLR, most of the jet power is quickly radiated away leaving insufficient energy in the jet at larger distances outside the BLR to reproduce the radio emission (see Figure 3.9b). This is because the energy in particles is being depleted quickly and in order to maintain equipartition the remaining magnetic energy is constantly converted into replenishing the electrons, resulting in most of the jet power being radiated away.

The high energy inverse-Compton emission is produced by scattering BLR photons with a low maximum electron Lorentz factor of 851 (see Figure 3.9a). The high magnetic field strength at the transition region due to the small jet radius, 4.59×10^{-4}T, is required to reproduce the high energy synchrotron peak for this low maximum electron energy. However, this high magnetic field also results in a large amount of SSC emission at X-ray energies which in turn requires a very high minimum electron Lorentz factor of 200 to fit to the X-ray data and not overproduce the observed X-ray emission. This very narrow range of electron energies is also difficult to understand in the context of shock acceleration where electrons are accelerated from low to high energies in a power law.

The short radiative lifetime within the BLR due to the high magnetic field strength and large external photon energy density means that any energy contained in high-energy electrons in the jet is quickly radiated away. This means that either the jet is still magnetically dominated at these distances or that only occasional transient bursts of intense particle acceleration occur within the BLR (possibly causing the observed short-timescale gamma-ray flares) so that the majority of the jet's energy is carried to larger distances as required to reproduce radio observations and by the energy requirements of radio lobes.

We find that the inferred black hole mass of a transition region within the BLR is relatively low and the high peak frequency of the corresponding accretion disc radiation makes fitting the spectrum difficult. In this fit we use a separate black hole mass for the accretion disc $M_{\rm acc}$ and jet geometry M. For the value of $M_{\rm acc}$ we use $2 \times 10^9 M_\odot$ found by Ghisellini et al. [2009b] from fitting an accretion disc to the spectrum.

3.10.4 Constraining the location of the emission region

We find that both a transition region at large distances and a transition region within the dusty torus are able to reproduce the spectrum of PKS0227 well. However, we find that a transition region (where the jet comes into equipartition in our model and starts emitting) within the BLR is unable to reproduce the observations due to the short radiative lifetimes of electrons within the BLR. We find that the jet must still be magnetically dominated within the BLR since the plasma is unable to maintain a state close to equipartition due to high radiative energy losses which quickly drain the jet of energy. This means it is unable to produce sufficient radio emission at large distances and is also incompatible with the proportion of jet energy deposited in radio lobes. It is possible that occasional bursts of particle acceleration occur within the BLR (which could be responsible for short timescale gamma-ray flares).

We find that both fits to the spectrum of PKS0227 using a transition region at large distances and within the dusty torus require large jet power, high bulk Lorentz factor jets observed close to the line of sight. This is consistent with Compton-dominant sources being FRII type jets. For both these fits we find that the X-ray emission is due to inverse-Compton scattering of the CMB at large distances. This is the first time that the CMB has been investigated in a model for blazar emission so this is an interesting result.

The black hole mass corresponding to a transition region located at $10^5 R_s$ as in M87 is $3.4 \times 10^9 M_\odot$ and $1.5 \times 10^8 M_\odot$ for fits 1 and 2 respectively. A previous investigation by Ghisellini et al. [2009b] found a black hole mass of $2 \times 10^9 M_\odot$ by modelling an accretion disc spectrum to PKS0227. This black hole mass is close to the value of fit 1 which uses a transition region at large distances but is substantially larger than fit 2 with a transition region inside the dusty torus.

Whilst our mass estimate of the black hole inferred from fit 1 is close to that found by Ghisellini et al. [2009b] the values of our jet parameters differ considerably from theirs. This is due to fundamentally different approaches to modelling the jet. In their model they consider a single compact blob which produces the observed inverse-Compton emission from scattering BLR photons whilst the optical observations are matched using thermal accretion disc, torus and corona components. Since they only consider a single emitting region they do not attempt to reproduce the radio data. In this model they find a bulk Lorentz factor of 14, substantially smaller than in our jet, a viewing angle of 3^o, slightly larger than in our fit and a total jet power which is higher by over an order of magnitude 2.38×10^{40}W, however, their model includes one proton per electron. These very different parameters are due to fundamentally different model assumptions. It is worth pointing out that no attempt is made to fit the model to the observed radio data and the synchrotron radiation does not fit the optical data since this is fitted by the thermal components, so the non-thermal synchrotron emission is not well constrained.

The geometry of M87 suggests that the transition region where the jet plasma approaches equipartition is at relatively large distances from the black hole, $>$ 10pc for black holes of mass $> 10^9 M_\odot$. This puts the transition region outside the BLR and outside or near to the outer edge of the dusty torus so we do not expect photons from these regions to dominate the external radiation field at these distances (see Figure 3.4). We find that this is consistent with our model of the observed spectrum of PKS0227 which is well fitted by a transition region at a distance 34pc from the black hole where the inverse-Compton emission is due primarily to scattering of CMB photons. The transition region may not occur at $10^5 R_s$ for every jet as it could depend on the jet power, mass loading etc. If this were the case we might expect a jet with a high bulk Lorentz factor to have a transition region at a larger distance than the comparatively low power jet in M87, in order to accelerate to a higher bulk Lorentz factor. This is not the case for fit 2 where the transition region would have to be located at $7500 R_s$ to be compatible with the black hole mass estimate of Ghisellini et al. [2009b]. For these reasons we favour a scenario in which the transition region occurs at large distances outside the BLR and dusty torus.

From the Figures 3.2 and 3.6 we see that one of the distinguishing features between a transition region at large distances or within the dusty torus is the location of the optically thick to thin synchrotron break. Since the optically thin synchrotron emission is dominated by

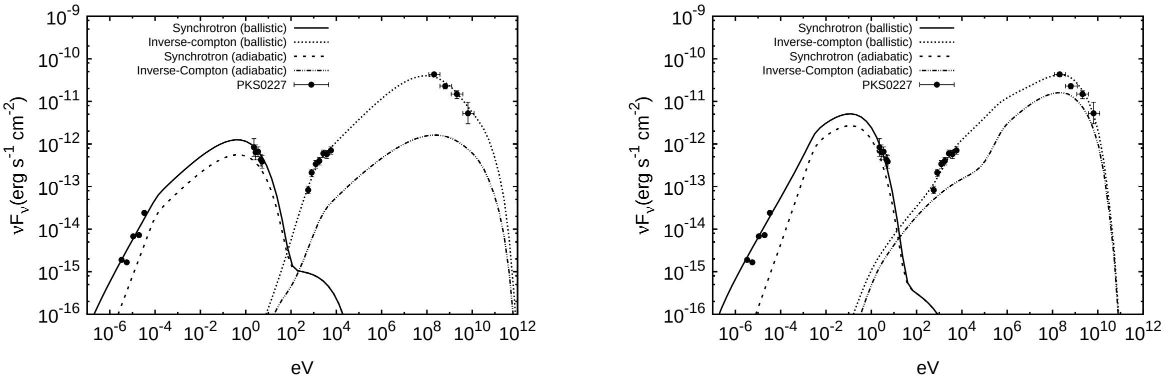

(a) (b)

Figure 3.10: Fits 1 and 2 to the spectrum of PKS0227 with and without adiabatic losses in the conical section of the jet. The Figure shows that the result of adiabatic losses on the electron population is to severely reduce the amount of inverse-Compton radiation, especially from scattering CMB photons at large distances. The radio emission is reduced as the jet loses additional energy to adiabatic losses at large distances where the radio emission originates. We find it difficult to reproduce the spectrum using a transition region at large distances with adiabatic losses without using a large bulk Lorentz factor. We also find it difficult to reproduce the spectrum using a transition region within the dusty torus due to the reduction in X-ray and radio emission.

the transition region (see Figures 3.3b and 3.7b) the location of the transition region largely determines the frequency at which the optically thick to thin break occurs. We see that the frequency at which the flat self-absorbed radio spectrum becomes optically thin and changes gradient increases for a transition region at a smaller distance along the jet as we expect due to the increased magnetic field and smaller jet radius. This feature could potentially be used to distinguish between a transition region at large distances or within the dusty torus. We wish to investigate whether this can be used to constrain the emission region in the near future.

3.10.5 An adiabatic or ballistic conical jet?

In this Chapter we have assumed that the parabolic accelerating region of the jet expands adiabatically whilst the conical region is ballistic. In Chapter 2 we proposed that a continuous conical jet with a constant opening angle and bulk Lorentz factor would not suffer adiabatic losses because it does no work expanding its environment (since the volume occupied by the jet is constant with time in the lab frame). In an idealised homogeneous jet the velocity profile in the direction perpendicular to the jet axis scales linearly with expansion and so small sections of the jet maintain a constant perpendicular velocity and are effectively ballistic.

Whilst these arguments are based on an idealised situation, a conical jet with an opening angle $\theta_{\mathrm{opening}}\gamma_{\mathrm{bulk}} > 1$ is not causally connected laterally and analytic work by Zakamska et al. [2008] found that far away from the black hole a conical jet will always become causally disconnected. This seems to be the case for jet parameters inferred from observations of GRBs (Kohler and Begelman [2012]). Work reproducing the large scale observed emission and polarisation of FRI jets using MHD models by Laing and Bridle [2004] found that jets were better described by non-adiabatic jets as opposed to adiabatic jets. It is therefore worth testing the effect of including adiabatic losses in the conical section of our model.

In Figure 3.10 we show the results of including adiabatic losses on fits 1 and 2. We find that in fit 1 adiabatic losses cool the high energy electrons more quickly than scattering the CMB and so the inverse-Compton emission is vastly reduced. In the case of adiabatic losses we find it difficult to fit the spectrum of PKS0227 with a transition region at large distances without using very large bulk Lorentz factors. In the case of fit 2 we also find that adiabatic losses substantially decrease the inverse-Compton emission from the jet, especially the X-ray emission which was due to scattering CMB photons. We also find that adiabatic losses result in a decrease in the radio emission at large distances due to the adiabatic energy losses along the jet. We find it difficult to fit the spectrum of PKS0227 at radio and X-ray energies using a transition region within the dusty torus including adiabatic losses.

For these reasons we favour a ballistic conical section of the jet. This could be a result of the assumptions we have made when fitting the spectrum with our jet model. We have assumed that the jet comes into equipartition at the transition from parabolic to conical and the jet maintains equipartition outwards from this region. This is motivated by simulations which indicate the jet transitions to conical when the plasma approaches equipartition and from observations which seem to indicate that the jet plasma is observed to be close to equipartition with fairly continuous optical emission requiring continuous particle acceleration along the jet. In this Chapter we have assumed a simple scenario in which the jet suddenly transitions to equipartition, however, it is likely that some particle acceleration and emission comes from the magnetically dominated region of the jet and this could affect our conclusions. We intend to investigate different mechanisms for particle acceleration along the jet in the near future.

We have found that the X-ray emission is well fitted by inverse-Compton scattering of

CMB photons at large distances along the jet. This X-ray emission is severely reduced if the conical section is adiabatic and becomes difficult to reproduce by non-thermal emission from the jet. The X-ray emission may also be due to the accretion disc corona so an inability to reproduce the X-ray emission with the jet does not necessarily exclude an adiabatic conical jet.

3.10.6 Discussion

In this work we have attempted to model the quiescent state of the blazar PKS0227 since this constrains the average jet parameters. Short term variability is observed on time-scales as short as hours or minutes for the most highly variable blazars (Aharonian et al. [2007]). The quiescent emission from our jet model comes from large distances with long electron cooling times (∼years for fit 1 and ∼days for fit 2), so is not easily compatible with this short timescale variability. In this work we wish to initially investigate the average quiescent emission from different elements of the blazar population in order to check that our model is able to reproduce their spectra and to find any trends in the quiescent jet parameters. Once we are confident that our model is able to reproduce the quiescent spectra of both BL Lacs and FSRQs with reasonable jet parameters, we will investigate whether we can reproduce flaring spectra by allowing flares to occur within the parabolic region of the jet. The parabolic region of the jet is more compact with shorter cooling timescales due to the higher magnetic field strength and energy density of external photons, so this region is more likely to be responsible for short timescale flaring.

It is important to emphasise that whilst our model is more complicated than a single zone model it does not possess many more free parameters. We have attempted to minimise the number of free parameters in our model by making reasonable simplifying physical assumptions and using the results of previous work observing and modelling the external radiation fields. The CMB is well constrained by observations and possesses no free parameters, however, the emission and distribution of the NLR is less well known. We have fixed most of the free parameters using values from previous observations and modelling of the BLR, dusty torus and NLR and we have left only the outer radius x_{outer} of the NLR as a free parameter since this seems to vary the most significantly. In these fits we have not injected an arbitrary electron population into arbitrary sections along the jet, we have injected a small amount of the initial jet power (1%) into electrons at the very base of the jet (to illustrate the resulting spectrum from electrons at the base of the jet whilst not affecting the fit to observed data, see Figure 3.3b). The acceleration of electrons in the decelerating section of the jet is determined entirely by Equation 3.17 in terms the other jet parameters in Table 3.1 and assuming equipartition in the conical section. Along with the fixed geometry this leaves our model with twelve free parameters which we vary when fitting the spectrum (W_j, L, L_{acc}, $\theta_{\rm obs}$, $\theta_{\rm opening}$, M, α, $E_{\rm min}$, $E_{\rm max}$, $\gamma_{\rm max}$, $\gamma_{\rm min}$ and $x_{\rm outer}$). This number of free parameters is comparable to single-zone models with broken power-law electron distributions.

We have tested the effect of changing the functional form of the deceleration of the bulk Lorentz factor along the jet (Equation 3.5). In our model the bulk kinetic energy of the jet is spread evenly on a logscale along the jet from deceleration. We find that strongly decelerating the jet over a particular distance scale effectively boosts the relative amount of emission from that section of the jet. This means that if the jet decelerates strongly over a scale $\sim 10^5 R_s$ then the amount of optical synchrotron and SSC emission is boosted relative to the radio emission and inverse-Compton scattering of CMB photons. Similarly, if the jet is chosen to decelerate strongly at larger scales, the amount of low frequency radio and inverse-Compton emission increases relative to the optical synchrotron and SSC emission. We find that strong deceleration on an intermediate length scale leads to a bump in the characteristic radio frequencies of that section. This deviation from a flat radio spectrum is not something seen in radio observations of blazars and so we disfavour strong deceleration of the jet on an intermediate length scale $10^{17} - 10^{19}$m. We find that deceleration which decreases as the logarithm of the jet distance, as we have assumed (Equation 3.5), distributes power more evenly along the jet resulting in a radio spectrum which is smooth and close to flat, consistent with observations.

We find that electrons injected into the parabolic section of the jet quickly radiate all their energy away due to the large magnetic fields and high energy density in the seed photon field (see Figure 3.9b). We also find that the emission of these electrons tends to be dominated by the emission from the conical section of the jet, since the inner regions of the accelerating parabolic section have a lower bulk Lorentz factor and so are not so strongly Doppler-boosted.

Since all the energy injected into electrons in the inner parts of the parabolic region is quickly radiated away and does not contribute as significantly to the observed spectrum it is difficult to constrain the amount of energy injected into accelerating electrons in this region. Since we expect the jet to be magnetically dominated in the parabolic region we have assumed that a small percentage of the magnetic energy goes into the acceleration of the electrons at the base of the parabolic section. This means that our estimated jet power is a lower bound because the total jet power would increase if a larger proportion of magnetic energy were converted into particle energy in the inner parabolic region, without a significant increase in observed emission.

We find that the low frequency radio emission of the jet is dominated by the conical sections with the lowest bulk Lorentz factors and largest radii (see Figure 3.3b). This is partly because the regions with high bulk Lorentz factors are strongly Doppler-boosted so the synchrotron opacity in these sections is effectively the synchrotron opacity for a much lower energy radio photon than that observed. The synchrotron opacity increases steeply at low frequencies so the radio emission from regions with high bulk Lorentz factors is suppressed and the strongly decelerated regions with larger radii dominate the radio. We see that the model is able to fit to the nearly flat radio spectrum of PKS0227 very well. Including the effects of deceleration and the conversion of bulk kinetic energy into particle acceleration means that the electron energy losses are replaced as they travel along the decelerating conical part of the jet as expected from observations of optical synchrotron emission far from the base of a jet (Meisenheimer et al. [1997] and Jester et al. [2001]). This mechanism to rejuvenate the high energy electron population has been investigated a number of times previously, however, this is the first investigation that has included the effects of deceleration in a continuous conical jet which conserves energy-momentum and particle number.

Most previous investigations have neglected radio observations and concentrated on one or two-zone models which are disconnected from the large scale radio emission of the jet. We have demonstrated that our rigorous, physically motivated, inhomogeneous jet model fits well to the simultaneous multiwavelength spectrum of PKS0227 across all wavelengths, including radio observations. This allows us to better constrain the regions where emission may occur in the jet by reproducing the radio and large scale emission of the jet whilst conserving energy along the jet. We find the results of this initial application of our model to a blazar very promising and we intend to use this model to conduct a more detailed study of a sample of Compton-dominant blazars in the near future to see if our results hold for other blazars and to try to distinguish between a transition region at large distances or within the dusty torus.

3.11 Conclusion

In this Chapter we have developed a realistic jet model which includes an accelerating, magnetically dominated, parabolic base which transitions to a slowly decelerating conical jet with a jet geometry set by recent radio observations of M87 and consistent with simulations and theory. This is the first time that an accelerating parabolic region transitioning to a decelerating conical region has been treated in a jet model for the spectra of a blazar. We calculate the observed line of sight synchrotron opacity to each section along the jet by Lorentz transforming into the rest frame of the plasma. We calculate the inverse-Compton emission from accretion disc photons directly from the disc, BLR, dusty torus, NLR, starlight and CMB photons by Lorentz transforming the radiation into the plasma rest frame. Our model conserves relativistic energy-momentum and particle number along the jet and we take into account radiative and adiabatic losses to the electron population.

We assume that the jet is initially magnetically dominated until it transitions from parabolic to conical at $10^5 R_s$, where the jet stops accelerating and the plasma approaches equipartition. Electrons are accelerated at this transition region and electron energy losses are replenished along the jet by the conversion of bulk kinetic energy into particle energy as the jet decelerates so that the plasma is kept in equipartition throughout the conical section of the jet. We use the model with a geometry and acceleration set by VLBI observations of M87 and simulations to fit to the simultaneous multi-wavelength spectrum of the Compton-dominant FSRQ PKS0227.

We investigate a transition region located outside the dusty torus, within the dusty torus and within the BLR. We find that our model fits very well to the spectrum across all wavelengths including radio observations with a transition region at either large distances from the central black hole, or within the dusty torus. We find that due to the short radiative lifetime we are unable to reproduce the radio observations using a transition region within the BLR.

We find that within the BLR the jet must still be magnetically dominated in order for the jet to transport sufficient energy to larger distances, however, this does not exclude occasional transient bursts of intense particle acceleration.

We find that our fits using transition regions outside the BLR both require high power ($\sim 10^{39}$W), high bulk Lorentz factor jets (> 40) viewed at a small angle to the jet ($\sim 1^o$). We find an inferred black hole mass of $3.4 \times 10^9 M_\odot$ for the transition region outside the dusty torus and $1.5 \times 10^8 M_\odot$ for a transition region within the dusty torus using observations of the geometry of M87 scaled linearly with black hole mass. The inferred black hole mass of the transition region at large distances, which completely determines the inner geometry of the jet, is close to the black hole mass found by Ghisellini et al. [2009b] ($2 \times 10^9 M_\odot$). We find that the optically-thick to thin synchrotron break depends on the location of the transition region and can potentially be used to distinguish between the two emission locations.

We find that by including the redshift dependence of the CMB and boosting into the plasma rest frame the Compton-dominance of the transition region at large distances, 34pc, is well fitted by inverse-Compton scattering of CMB photons. This could explain why Compton-dominant blazars are powerful, high bulk Lorentz factor blazars which are preferentially at high redshift due to the temperature dependence of the CMB $\propto (1 + z)$. We find that the X-ray emission for both transition region fits outside the BLR can be fitted well by scattering of CMB photons on large scales if the conical section of the jet is ballistic.

Chapter 4

Compton-dominant blazars

In this Chapter I use the model presented in Chapter 3 to fit to the simultaneous multiwavelength spectra of the six most Compton-dominant blazars. I constrain the radius of the jet where the plasma first comes into equipartition using the optically thick to thin synchrotron break. The jet radius is found to be large (as confirmed by an analytic calculation), incompatible with the transition region occurring within the BLR or dusty torus. The slope of the radio spectrum is found to favour a ballistic jet which starts in equipartition at the transition region and becomes particle dominated further along the jet. I find that all these blazars require high power jets with large bulk Lorentz factors observed close to the line of sight as we expect from the blazar sequence and in agreement with the results of Chapter 3.

4.1 Introduction

In this Chapter we set out to investigate whether our jet model is capable of fitting to the spectra of a sample of Compton-dominant blazars and to investigate what physical properties these blazars have in common. We wish to find out whether the physical parameters we found for PKS0227 in Chapter 3 hold for other Compton-dominant blazars, in particular, if we are able to distinguish between models in which the transition region occurs within the dusty torus or further along the jet using the optically thick to thin synchrotron break. This is the first time a realistic extended jet model has been used to fit to the spectra of a sample of blazars, so it is interesting to see whether our model, which is based on the observed geometry of the jet in M87, is capable of fitting to a sample of real blazars. For this sample we choose the six most Compton-dominant blazars (after PKS0227) from Abdo et al. [2010a] in order to test our model and predictions from Chapter 3.

Compton-dominant blazars are thought to represent the most intrinsically powerful jets in the blazar sequence (Fossati et al. [1998]). In this scenario we use the radio luminosity of blazars as a proxy for their kinetic luminosity and take an average of the multi-wavelength spectra in bins of radio power. A general progression towards higher Compton-dominance and decreasing peak frequency of synchrotron and inverse-Compton emission for more powerful objects was found by Fossati et al. [1998]. It is currently believed that the Compton-dominance of powerful blazars originates from inverse-Compton scattering of external photons (Meyer et al. [2012]). It is thought that powerful objects with more luminous accretion discs and broad line regions (BLRs) create a larger seed photon distribution for inverse-Compton scattering than in BL Lac type objects where the dominant photon source is synchrotron seed photons. It is believed that radiative cooling of accelerating electrons via inverse-Compton scattering of BLR photons leads to the lower inverse-Compton peak frequencies in Compton-dominant objects (Maraschi et al. [2008]).

In Chapter 3 we considered scattering of synchrotron, accretion disc, BLR, dusty torus, NLR, starlight and CMB photons and found that PKS0227 was best fitted by inverse-Compton scattering of CMB or dusty torus seed photons. We found that the low inverse-Compton peak frequency resulted from the lower peak energy of CMB and dusty torus photons relative to synchrotron seed photons. We found that the Compton-dominance was due to the increase in external photon density due to Doppler-boosting in the high bulk Lorentz factor jet. The low synchrotron peak frequency was caused by the base of the conical section of the jet having a lower magnetic field due to the high black hole mass and the assumed linear scaling of the M87 jet geometry with black hole mass. This was the first time that such a scenario has been suggested for the Compton-dominance of blazars, however, this was also the first time that a realistic model of an extended jet had been used to model the spectrum of a Compton-dominant blazar.

In this Chapter we will first briefly introduce our jet model. We compare several adiabatic and ballistic jet models to the radio emission of the six most Compton-dominant blazars in Abdo et al. [2010a] (after PKS0227). We use the slope of the radio emission and the frequency of the optically thick to thin synchrotron break to distinguish between a transition region within the dusty torus or at futher distances along the jet. We then show the results of fitting the surviving models to the multi-wavelength spectra of the six blazars. We compare the physical parameters inferred from the model fits to the results of Chapter 3 in order to determine whether our model is capable of reproducing the quiescent spectra of a sample of blazars. We comment on our results in light of current ideas on the blazar population and unification.

4.2 Jet Model

To fit to the spectra of the Compton-dominant blazars we use a model with an accelerating parabolic base transitioning to a slowly decelerating conical jet with a geometry set by the recent radio observations of the jet of M87 (Asada and Nakamura [2011]). For full details of the model see Chapter 2 and 3 based on Potter and Cotter [2012] and Potter and Cotter [2013a]).

4.2.1 Electron energy losses due to emission

In this Chapter we have modified our treatment of electron energy losses from Chapter 3 to include the decrease of individual electron energies with radiation losses. In Chapter 3 we included radiative energy losses to the electron population due to both synchrotron and inverse-Compton emission, however, we neglected the decrease of electron energy due to radiative losses and used the approximation that electrons radiate the majority of their emission close to their initial electron energy. This approximation resulted in an increase in speed of our jet code and did not produce a significant change in the emitted spectrum of the jet, however, the value of $E_{\max}$ is underestimated for a fit to a spectrum. To include the transfer of electrons down through energy bins as they radiate we modify Equation 3.59 to become

$$
\begin{aligned}
N_e(E_e, x+\gamma_{\mathrm{bulk}}\mathrm{d}x') = N_e(E_e, x) &- \frac{P_{\mathrm{tot}}(x, \mathrm{d}x', E_e)\times 1\mathrm{m}}{cE_e(1-1/\mathrm{d}E_e)} \\
&+ \frac{P_{\mathrm{tot}}(x, \mathrm{d}x', E_e\mathrm{d}E_e)\times 1\mathrm{m}}{cE_e\mathrm{d}E_e(1-1/\mathrm{d}E_e)}.
\end{aligned}
\tag{4.1}
$$

where $N_e(E_e, x + \gamma_{\rm bulk}{\rm d}x')$ is the number of electrons of energy E_e contained in a slab of width 1m (in the x-direction) in the plasma rest frame, $P_{\rm tot}(x, {\rm d}x', E_e)$ is the total power radiated by electrons of energy E_e through synchrotron and inverse-Compton emission in the jet section located at a lab frame distance x with a width dx' in the plasma rest frame and dE_e is the fractional difference in energies between adjacent electron energy bins in our code. The first term in Equation 4.1 corresponds to the number of electrons lost from the energy bin through radiative energy losses when crossing the section of width ${\rm d}x'$ in the plasma rest frame. The second term corresponds to the increase in the number of electrons in the energy bin due to higher energy electrons cascading down in energy following radiative losses. When taking into account the decrease in electron energy as the electron radiates, Equation 3.10 should also be modified to include the electron gain and loss terms above.

4.3 Results

In this section we shall try to constrain the properties of the jet by fitting our model by eye to the simultaneous multi-wavelength observations of the six most Compton-dominant blazars (after PKS0227) J0349.8−2102, J0457.1−2325, J0531.0+1331, J0730.4−1142, J1504.4+1030 and J1522.2+3143 from Abdo et al. [2010a]. First we compare the radio observations with the calculated radio emission from several different jet models. We then use the optically thick to thin synchrotron break to attempt to constrain the location of the transition region of the jet. We calculate an analytic formula for the observed synchrotron break frequency of a general jet plasma described by a relativistic perfect fluid. We use this to confirm the results of our model and to infer the properties of parabolic and conical jets by comparing our calculations with observations of the frequency dependent core-shift in jets. Finally, we fit the multiwavelength spectra using the jet models compatible with the radio observations and optically thick to thin synchrotron break. Throughout this Chapter we assume a standard ΛCDM cosmology with $H_0 = 71{\rm kms^{-1}Mpc^{-1}}$ and $\Omega_\Lambda = 0.73$.

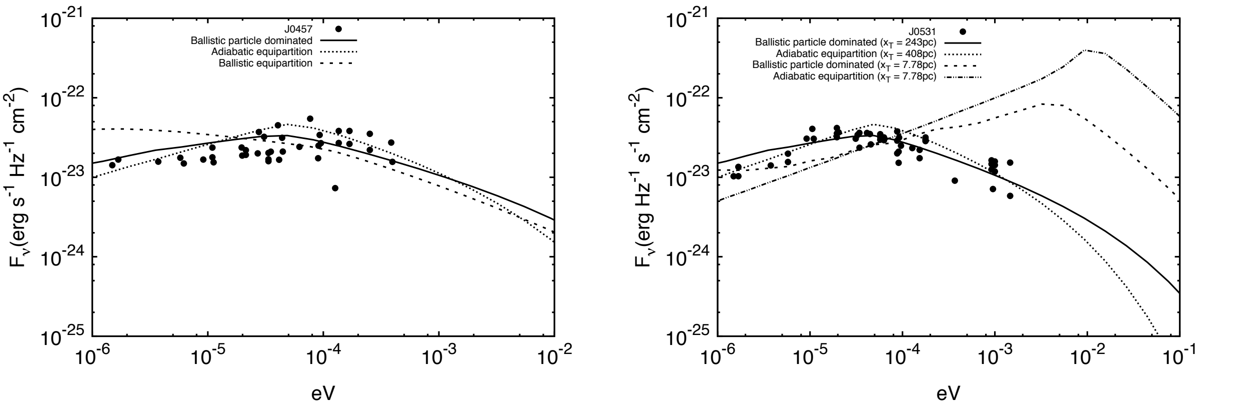

(a) Radio emission of J0457.

(b) Optically thick to thin synchrotron break in J0531.

Figure 4.1: *a*: The results of fitting different jet models to the radio emission of J0457. We see that the ballistic equipartition jet does not match the radio observations well at low frequencies. The adiabatic equipartition model fits the optically thick radio slope well as does a ballistic model which becomes particle dominated beyond the transition region ($U_e/U_B \propto x^{-1}$ from $x_T \leq x \geq 100x_T$). *b* Fits to the radio emission of J0531 using adiabatic and ballistic jet models with a transition region located at x_T within the dusty torus and at larger distances along the jet (as implied by a transition region at $10^5 R_S$ in M87). The change in gradient of the flux from optically thick to optically thin at 3×10^{-5}eV is well matched by transition regions at large distances along the jet $\sim$ 100pc and excludes a transition region within the dusty torus at a few pc since the jet remains optically thick up to much higher frequencies than the observed break.

4.3.1 The different models

In this Chapter we wish to constrain the physical properties of the jet by fitting different models to the observations of the six blazars. In Chapter 3 we found that a ballistic equipartition jet best fitted the observations of PKS0227, whilst an adiabatic equipartition jet struggled to reproduce its Compton-dominance with plausible bulk Lorentz factors. Here we will investigate models in which the conical section of the jet is adiabatic or ballistic with a transition region located outside the BLR. In these models we will also consider cases where the plasma deviates from equipartition along the conical section, however, we still assume that the transition region is in equipartition.

4.4 Radio emission

In Chapter 3 we found that the spectrum of PKS0227 was best fitted by models in which the conical section of the jet was ballistic. In Figure 4.1a we show the radio emission from three models compared to the radio data of J0457. We find that the radio observations of these six Compton-dominant blazars have radio slopes which are in general steeper than the radio emission produced by the ballistic equipartition jet model from Chapter 3, as shown in Figure 4.1a. We find that the ballistic equipartition jet tends to overproduce low frequency radio emission compared to the data. This suggests that if the jet is ballistic and conical it becomes particle dominated outwards from the transition region since this reduces the radio synchrotron emission at larger distances, whilst maintaining the Compton-dominance from scattering external photons. The radio emission from both the adiabatic jet in equipartition and the ballistic jet which becomes particle dominated fit the radio data well, whilst the ballistic equipartition model does not. Previous investigations modelling blazar spectra have usually neglected radio observations but our results show that it is important to consider the radio emission when constraining the physical properties of jets. In Chapter 3 we struggled to reproduce the observed Compton-dominance of PKS0227 using an adiabatic conical jet in equipartition without using very high bulk Lorentz factors. This suggests that the conical section of the jet may be ballistic starting in equipartition at the transition region and becoming more particle dominated further down the jet as magnetic energy continues to dissipate and accelerate electrons.

We find that in order to reproduce the observed radio slope of these blazars, the equipartition fraction of the ballistic jet should decrease roughly as $A_{\mathrm{equi}} = U_B/U_e = 2x_T/(x_T + x)$ for $x_T \geq x \geq 100x_T$ (where x_T is the distance of the transition region) as shown in Figure 4.1a. The radio data does not constrain the emission from the jet at distances beyond ∼10kpc and so we find that the ballistic jet becomes particle dominated by a factor of 50 at a distance of $100x_T$ but is not well constrained after this. Beyond this, the ballistic jet could stay particle dominated, tend back towards equipartition or become even more particle dominated.

4.5 Optically thick to thin synchrotron break

In Chapter 3 we found that models in which the transition region occured either within the dusty torus or at further distances along the jet were able to fit well to the spectrum of PKS0227. The main difference between the two models was the location of the optically thick to thin synchrotron break due to the different radii and magnetic field strengths of the transition regions in the two fits. Figure 4.1b shows the fits to the spectrum of J0531 in which the jet has a transition region located within the dusty torus and further along the jet corresponding to a distance $10^5 R_s$ as in the jet of M87. We see that in order to reproduce the relatively low frequency of the optically thick to thin synchrotron break at $\approx 3\times10^{-5}$eV, a transition region outside the dusty torus at a distance of several 100pc is required. If the jet comes into equipartition within the dusty torus then the jet exceeds the radio emission due to the optically thick to thin synchrotron break occuring at a higher frequency than indicated by the observations. This result holds for both the ballistic jet which becomes particle dominated and the adiabatic equipartition jet. This is interesting since for these large distances the inferred black hole mass of the jet agrees with the black hole mass found independently from fitting the accretion disc spectrum to J0531 only if the transition region occurs at $10^5 R_s$, as we have assumed based on observations of M87. It is worth noting that we find it difficult to reproduce both the radio and gamma-ray data using a jet model with a transition region within the dusty torus.

The frequency at which the synchrotron emission becomes optically thin can be calculated analytically in the case of a jet with a total jet power W_j, bulk Lorentz factor γ_{bulk}, radius R, and equipartition fraction $A_{\text{equi}} = U_B/U_e$. In this case the synchrotron opacity can be calculated using Equation 2.26, assuming the plasma can be approximately described as a relativistic perfect fluid in the plasma rest frame (Equation 3.7) and the synchrotron emission is approximated to occur at the synchrotron critical frequency (Equation 2.17).

$$k_\nu = \frac{j_\nu c^2}{2\epsilon^{1/2}\nu^{5/2}}, \qquad E_e^2 = \epsilon\nu, \tag{4.2}$$

$$j_\nu = \frac{\sigma_T A B^2 \epsilon^{\frac{3-\alpha}{2}} \nu^{\frac{1-\alpha}{2}}}{3\pi R^2 \mu_0 m_e^2 c^3}, \qquad \epsilon = \frac{4\pi m_e^3 c^4}{3eB}. \tag{4.3}$$

We can parameterise A, which is the normalisation constant for the electron distribution in a slab of width 1m ($N_e = AE^{-\alpha}$), in terms of the power law index of the electron distribution α and the maximum and minimum electron energies E_{min} and E_{max}. Similarly we can express the magnetic field strength in terms of other known quantities.

$$B = \sqrt{\frac{3W_j\mu_0 A_{\rm equi}}{2\gamma_{\rm bulk}^2 c\pi R^2(1+A_{\rm equi})}}, \tag{4.4}$$

$$A = \frac{3W_j}{4\gamma_{\rm bulk}^2 c(1+A_{\rm equi})}.\left[\frac{(2-\alpha)}{E_{\rm max}^{2-\alpha}-E_{\rm min}^{2-\alpha}})\right]. \tag{4.5}$$

In the case of $\alpha = 2$ the factor $(2-\alpha)/(E_{\rm max}^{2-\alpha}-E_{\rm min}^{2-\alpha})$ should be replaced by $1/\ln(E_{\rm max}/E_{\rm min})$ in the above and following equations. We can now substitute these values into Equations 4.2 and 4.3 to find an expression for the synchrotron opacity.

$$\begin{aligned} k_\nu = &\frac{\sigma_T}{8\pi\mu_0 m_e^2 c^2(1+A_{\rm equi})}.\frac{2-\alpha}{E_{\rm max}^{2-\alpha}-E_{\rm min}^{2-\alpha}}.\left(\frac{4\pi m_e^3 c^4}{3e}\right)^{\frac{2-\alpha}{2}} \\ &\times\left(\frac{3\mu_0 A_{\rm equi}}{2c\pi(1+A_{\rm equi})}\right)^{\frac{2+\alpha}{4}}.\frac{W_j^{\frac{6+\alpha}{4}}\nu^{\frac{-(4+\alpha)}{2}}}{R^{\frac{6+\alpha}{2}}\gamma_{\rm bulk}^{\frac{6+\alpha}{2}}}. \end{aligned} \tag{4.6}$$

This expression is quite general and is valid for any homogeneous plasma which is described as a relativistic perfect fluid in the plasma rest frame. In our present discussion we are interested in calculating the jet radius at which a given synchrotron frequency becomes optically thick, for a plasma in equipartition. We assume that the plasma becomes optically thick to a frequency when $k_\nu {\rm d}x = 1$, where both ν and ${\rm d}x$ are measured in the plasma rest frame. The lifetimes of electrons emitting synchrotron radiation at radio frequencies are long, so the length scale ${\rm d}x$ will be determined such that the jet radius and magnetic field strength change significantly, reducing the synchrotron opacity. We take this length scale to be the distance over which the jet radius doubles. For a conical jet this requirement corresponds roughly to ${\rm d}x = R$ because in the lab frame the conical half opening angle is expected to be approximately $\theta = 1/\gamma_{\rm bulk}$ and the lab frame length is related to that in the plasma rest frame by a length contraction ${\rm d}x' = \gamma_{\rm bulk}{\rm d}x$. Calculating $k_\nu R = 1$ and rearranging we find

$$R = \left[\frac{\sigma_T}{8\pi\mu_0 m_e^2 c^2 (1+A_{\mathrm{equi}})} \cdot \frac{2-\alpha}{E_{\mathrm{max}}^{2-\alpha} - E_{\mathrm{min}}^{2-\alpha}} \cdot \right]^{\frac{2}{4+\alpha}} \cdot$$
$$\left[\left(\frac{4\pi m_e^3 c^4}{3e} \right)^{\frac{2-\alpha}{2}} \left(\frac{3\mu_0 A_{\mathrm{equi}}}{2c\pi(1+A_{\mathrm{equi}})} \right)^{\frac{2+\alpha}{4}} \right]^{\frac{2}{4+\alpha}} \cdot \frac{W_j^{\frac{6+\alpha}{2(4+\alpha)}}}{\gamma_{\mathrm{bulk}}^{\frac{6+\alpha}{4+\alpha}} \nu}. \tag{4.7}$$

We see that for a conical jet in which the electron distribution, equipartition fraction, bulk Lorentz factor and jet power remain constant, the radius of the jet at which the synchrotron emission at frequency ν becomes optically thick is simply inversely proportional to the frequency ν, $R \propto \nu^{-1}$.

We will now use this formula to estimate the radius of the transition region from the spectrum of J0531. We shall use the physical parameters from Table 4.1, derived from the ballistic particle dominated jet fit to J0531 shown in Figures 4.1b and 4.2. The observed frequency at which the synchrotron break occurs is approximately 3×10^{-5}eV = 7.25GHz and this corresponds to a plasma rest frame frequency $\nu_{\mathrm{obs}} \approx 2\gamma_{\mathrm{bulk}}\nu/(1+z)$. In this case we find $R \approx 7.7$pc. In our model using a scaled M87 jet geometry the radius of the transition region is $2000R_s$ at a distance $10^5 R_s$ from the central black hole. This places the transition region at a distance 380pc from the black hole corresponding to a black hole mass of $\approx 3.8 \times 10^{10} M_\odot$. This estimate roughly agrees with the inferred black hole mass of our fit, $2.5 \times 10^{10} M_\odot$, and reinforces the conclusion that in the case of powerful, Compton-dominant blazars the majority of the synchrotron emission comes from relatively large distances from the central black hole.

4.5.1 Frequency core-shift

We can use the general result in Equation 4.6 to compare to observations of the frequency dependent core-shift in AGN jets. Previous calculations of the core-shift have assumed a constant bulk Lorentz factor (Königl [1981] and Lobanov [1998]). Observations seem to show that generally $x_{\mathrm{core}} \propto \nu_{\mathrm{obs}}^{-k}$, with a mean value $k \approx 1$ and a tail towards lower values of k (Sokolovsky et al. [2011]). We shall use our formulae to calculate the expected frequency core-shift in the case of the three conical jet models in Figure 4.1a: the adiabatic equipartition jet, the ballistic equipartition jet and the ballistic particle dominated jet, and we shall also consider the case of a parabolic accelerating jet. Core-shift measurements generally probe frequencies from 1-40GHz which correspond to large distances (≈ 2000pc for the fit to J0531) down to several tens of Schwarzschild radii close to the base of the jet (43GHz corresponds to $14-23R_s$ in M87, Hada et al. [2011]). With this large range of distances it is interesting to calculate the expected core-shift relation for both the outer conical and inner parabolic sections of the jet. Assuming that the electron distribution remains fairly constant along the region of interest we use the formula.

$$k_\nu \mathrm{d}x \propto \frac{A_{\mathrm{equi}}^{\frac{2+\alpha}{4}}}{(1+A_{\mathrm{equi}})^{\frac{6+\alpha}{4}}} \cdot \frac{W_j^{\frac{6+\alpha}{4}} \mathrm{d}x}{R^{\frac{6+\alpha}{2}} \gamma_{\mathrm{bulk}} \nu_{\mathrm{obs}}^{\frac{4+\alpha}{2}}}. \tag{4.8}$$

Let us assume that in the lab frame $R \propto x^n$ and the bulk Lorentz factor $\gamma_{\mathrm{bulk}} \propto x^m$. In this case the rest frame distance $\mathrm{d}x$ over which the jet radius changes by a fixed fraction is proportional to $\mathrm{d}x \propto x/\gamma_{\mathrm{bulk}} \propto R^{1/n}/\gamma_{\mathrm{bulk}}$. To be compatible with the core-shift measurements ($x \propto \nu_{\mathrm{obs}}^{-1}$), in general, requires that the equipartition fraction of the jet also depends on distance $A_{\mathrm{equi}} \propto x^w$. Let us also allow the remaining jet power in a section to change along the jet, $W_j \propto x^u$, due to adiabatic losses for example. We can use Equation 4.8 to calculate the expected core-shift properties of a blazar in the simplifying cases of $A_{\mathrm{equi}} \gg 1$, constant A_{equi} and $A_{\mathrm{equi}} \ll 1$.

$$k = \frac{2(4+\alpha)}{(6+\alpha)(2n-u)+4(w+2m-1)}, \qquad A_{\mathrm{equi}} \gg 1, \tag{4.9}$$

$$k = \frac{2(4+\alpha)}{(6+\alpha)(2n-u)+4(2m-1)}, \qquad A_{\mathrm{equi}} = \text{constant}, \tag{4.10}$$

$$k = \frac{2(4+\alpha)}{(6+\alpha)(2n-u)-(2+\alpha)w+8m-4}, \qquad A_{\mathrm{equi}} \ll 1. \tag{4.11}$$

To calculate the core-shift relation in the case of an accelerating parabolic jet ($n = 0.5$, $m = 0.5$) we assume that the jet is magnetically dominated close to the base of the jet so $A_{\mathrm{equi}} \gg 1$, most of the jet power is not radiated away until larger distances, $u = 0$, and $\alpha \approx 2$. In order for the parabolic jet to produce the core-shift relation $k = 1$ (compatible with the innermost part of the jet in M87, Hada et al. [2011]), we require that $w = 1$ which means the equipartition fraction increases along the parabolic section $A_{\mathrm{equi}} \propto x$. The jet plasma actually becomes more magnetically dominated further along the parabolic section and so contains a smaller proportion of its energy in non-thermal electrons. Simulations find that jets start with a parabolic shape $R \propto x^{1/2}$ and an accelerating bulk Lorentz factor $\gamma_{\rm bulk} \propto x^{1/2}$ (for example McKinney [2006]), so this result is useful as this is the first time that the frequency core-shift has been calculated for a parabolic accelerating jet. In our formula we have assumed that the jet is oriented close to our line of sight so the Doppler factor, $\delta_{\rm Doppler} \propto \gamma_{\rm bulk}$, however, this is only valid for blazars and needs to be modified for jets which are oriented at larger angles to our line of sight, such as M87.

Let us now consider a conical ballistic jet ($n = 1$, $m = 0$) which is originally particle dominated and becomes more particle dominated ($w = -1$) further along the jet. Again we assume that the majority of the jet power is not radiated away until further along the jet $u = 0$. In this case we assume that $A_{\rm equi} \ll 1$. So in the case of the ballistic particle dominated model with $\alpha \approx 2$, we calculate a core-shift relation $x \propto \nu_{\rm obs}^{-0.75}$. In the study by Sokolovsky et al. [2011] they found that the mean core-shift relation was $k = 1$, however, this distribution is relatively wide with a median value of $k = 1.2$ and a range $0.67 \geq k \geq 2$ (with one outlying point at $k = 0.29$), so it does not exclude this model. Let us now consider the conical ballistic jet in equipartition ($n = 1$, $w = 0$) which suffers no electron energy losses ($u = 0$) and has a constant bulk Lorentz factor ($m = 0$). The early calculation by Königl [1981] found a relation $x \propto \nu^{-1}$ independent of α for this type of jet model, which is consistent with observations. From Equation 4.7 we see that using our assumptions and $R \propto x$ we recover the well known $x \propto \nu_{\rm obs}^{-1}$ relation.

Finally, we consider the conical adiabatic equipartition jet with constant bulk Lorentz factor ($n = 1$, $m = 0$, $w = 0$). In this case the jet power decreases due to adiabatic losses on the electrons (since the jet is constantly in equipartition) so approximately $W_j \propto R^{-2/3}$ and $u = -2/3$. For the case $\alpha \approx 2$ we find $k = 0.69$, which is just within the range of values of k found by Sokolovsky et al. [2011]. The model which best fits the core-shift measurements is the simple ballistic conical jet in equipartition. However, this model does not fit the radio slopes of these Compton-dominant blazars well, as shown in Figure 4.1a. Both the adiabatic equipartition jet and ballistic particle dominated jets fit the radio slope well but differ from the mean observed core-shift relation $x \propto \nu_{\rm obs}^{-1}$. The core-shift relations we have calculated for these models are both lower than the mean $k = 1$ value with both models just within the observed distribution of k from a sample of 20 objects from Sokolovsky et al. [2011]. These results show that the frequency core-shift measurement is valuable in distinguishing between different jet models and geometries.

4.6 Fitting the multiwavelength spectra

In the previous two subsections we have shown that the low-frequency observations indicate that the jet first comes into equipartition at large distances along the jet outside the BLR and dusty torus. The radio observations indicate that if the conical section of the jet is ballistic then it becomes particle dominated further along the jet and if the jet is adiabatic then the jet remains close to equipartition. We shall now attempt to fit the six multiwavelength spectra using models in which the jet transitions from parabolic to conical at $10^5 R_s$ with either a ballistic conical section which starts in equipartition at the transition region and becomes particle dominated further along the jet or an adiabatic conical jet in equipartition.

4.6.1 The ballistic model

Figure 4.2 shows the results of fitting the ballistic model to the six Compton-dominant FSRQs. The model starts in equipartition and becomes particle dominated at larger distances along the jet. The equipartition fraction changes as $U_B/U_e = 2x_T/(x_T + x)$ for $x_T \geq x \geq 100x_T$ and $U_B/U_e = 1/50$ for $x > 100x_T$, where x_T is the distance of the transition region along the jet in the lab frame. The model fits very well to the observed spectra across all wavelengths. We show the physical parameters of the fits to the spectra in Table 4.1. We find that for all six blazars their inverse-Compton emission and Compton-dominance is well fitted by scattering of Doppler-boosted CMB photons. The different components contributing to the inverse-Compton emission are shown in Figure 4.3a. This is a significant result since it is widely believed that Compton-dominance is due to inverse-Compton scattering of BLR scattered photons (Maraschi et al. [2008]). This is the first time that a realistic extended jet model has been used to fit to the spectrum of a sample of blazars and these new results show that it is important to consider the jet as a whole, including radio observations, to determine the

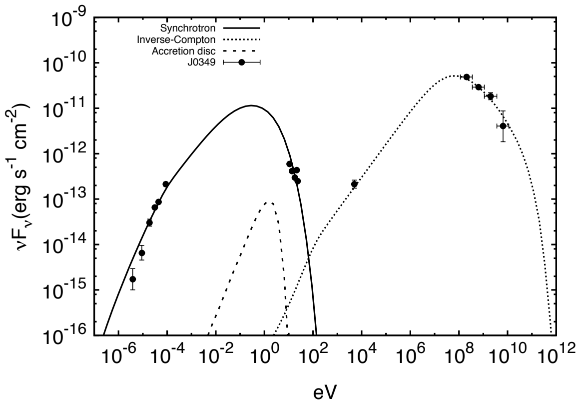

(a) J0349

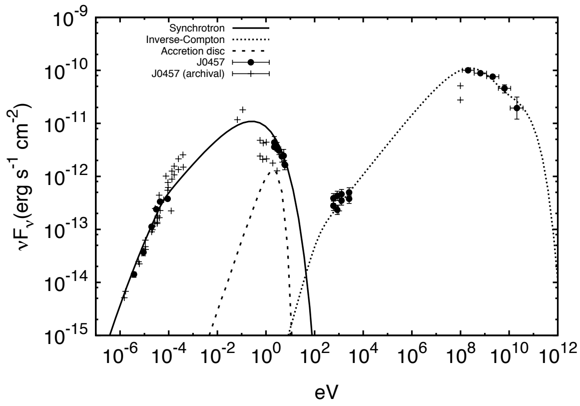

(b) J0457

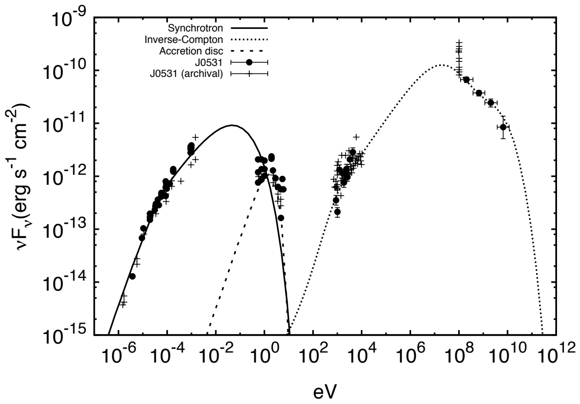

(c) J0531

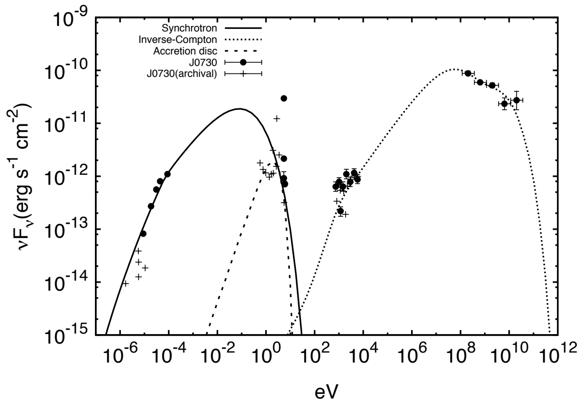

(d) J0730

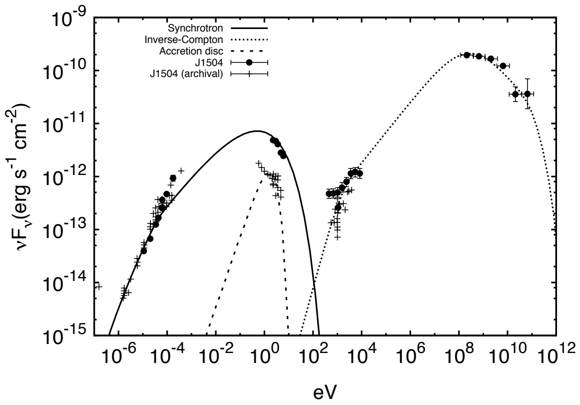

(e) J1504

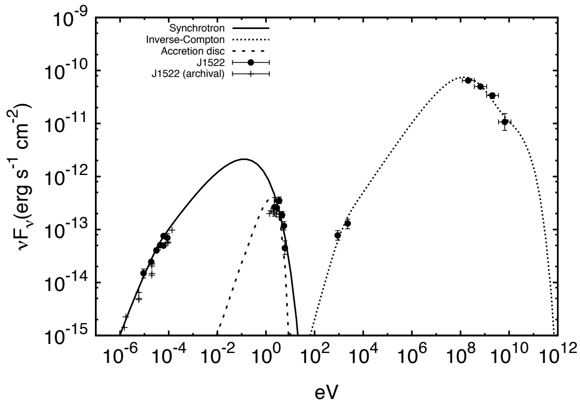

(f) J1522

Figure 4.2: The results of fitting the ballistic jet model to the SEDs of J0349, J0457, J0531, J0730, J1504 and J1522. The model fits the observations very well for all six blazars across all wavelengths. We find that the inverse-Compton emission of all the blazars is well described using CMB seed photons with a small contribution to the highest energy emission by scattering of NLR photons.

Parameter	J0349.8 −2102	J0457.1−2325	J0531.0+1331	J0730.4−1142	J1504.4+1030	J1522.2+3143
W_j	5.0×10^{39}W	1.7×10^{39}W	5.0×10^{39}W	4.5×10^{39}W	5.5×10^{39}W	1.5×10^{39}W
L	5×10^{20}m	1×10^{21}m	2×10^{21}m	1×10^{21}m	1×10^{21}m	1×10^{21}m
E_{min}	5.11 MeV	5.11 MeV	15.3 MeV	15.3 MeV	15.3 MeV	15.3 MeV
E_{max}	8.10 GeV	8.48 GeV	4.06 GeV	4.55 GeV	17.3GeV	5.48 GeV
α	1.5	1.85	1.65	1.7	1.85	1.65
$\theta'_{\mathrm{opening}}$	3^o	3^o	3^o	3^o	3^o	3^o
$\theta_{\mathrm{observe}}$	1.0^o	1.0^o	1.0^o	1.0^o	1.0^o	1.0^o
γ_0	4	4	4	4	4	4
γ_{max}	30	35	25	28	45	40
γ_{min}	15	20	15	15	20	20
M	$8.0 \times 10^9 M_\odot$	$1.4 \times 10^{10} M_\odot$	$2.5 \times 10^{10} M_\odot$	$2.0 \times 10^{10} M_\odot$	$2.5 \times 10^{10} M_\odot$	$1.3 \times 10^{10} M_\odot$
L_{acc}	8.3×10^{38}W	4.2×10^{38}W	3.3×10^{39}W	2.5×10^{39}W	2.5×10^{39}W	4.2×10^{38}W
x_{outer}	2kpc	2kpc	3kpc	1kpc	1kpc	1kpc
B_T	2.65×10^{-6}T	7.57×10^{-7}T	1.02×10^{-6}T	1.08×10^{-6}T	5.93×10^{-7}T	6.70×10^{-7}T

Table 4.1: The values of the physical parameters used in the ballistic model fits shown in Figure 4.2. We also include the value of the magnetic field strength in the plasma rest frame at the transition region for the fits (B_T).

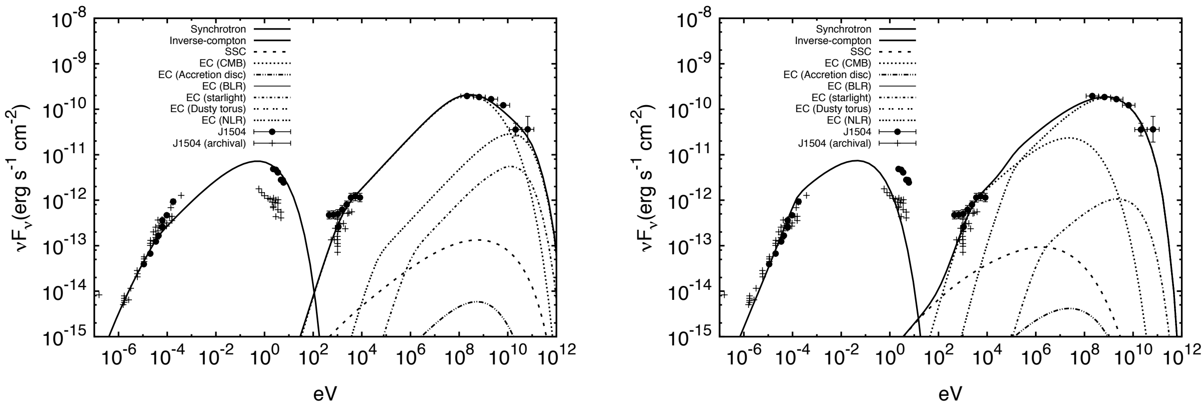

(a) J1504 ballistic (b) J1504 adiabatic

Figure 4.3: The different components of the inverse-Compton emission for the fit to J1504 for the two models. Figure a shows that the inverse-Compton emission in the ballistic model is primarily due to scattering of CMB seed photons with a small contribution from NLR photons required to fit to the highest energy data point. Figure b shows that in the adiabatic model the inverse-Compton emission is primarily due to scattering NLR photons with a contribution from scattering CMB photons at X-ray energies. For these Compton-dominant blazars we find that the SSC emission is sub-dominant due to the comparatively low magnetic field strength at the transition region of the jet.

physics governing these objects.

We find consistently for all these blazars that fits to their spectra require high power, high bulk Lorentz factor jets observed close to the line of sight. This is consistent with our expectations from the blazar sequence (in radio power) and from AGN unification since we expect Compton-dominant blazars to be high power, high bulk Lorentz factor FRII-type jets observed close to the line of sight. We also find that for these objects the black hole masses (which completely determines the geometry of the parabolic region and the transition region) that are inferred from the fits to the spectra are all large $> 10^9 M_\odot$. This is consistent with Compton-dominant blazars being large elliptical galaxies with powerful FRII type jets.

We find that the black hole mass inferred from the distance of the transition region agrees with that inferred independently from fitting the accretion disc spectrum to J0531 only if the transition region occurs at $10^5 R_s$ as in the jet of M87. This supports the idea that the transition region occurs at $10^5 R_s$ in jets and scales linearly with black hole mass.

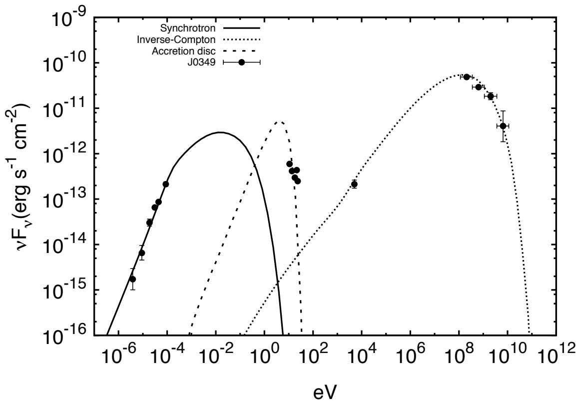

(a) J0349

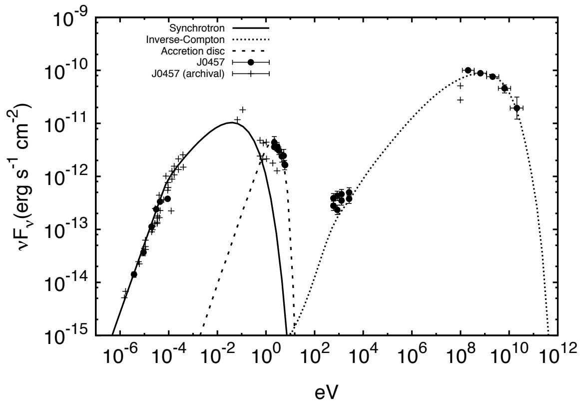

(b) J0457

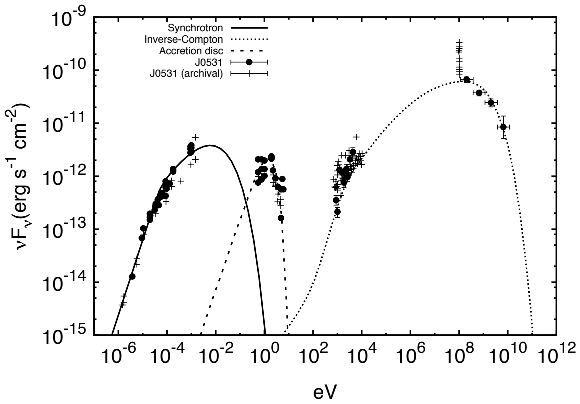

(c) J0531

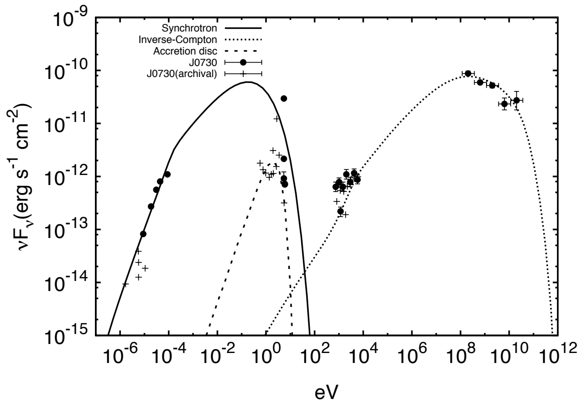

(d) J0730

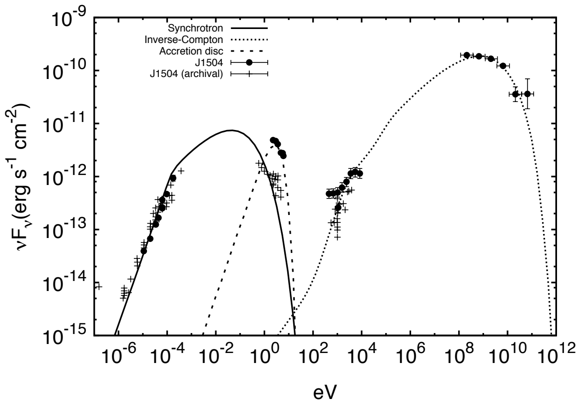

(e) J1504

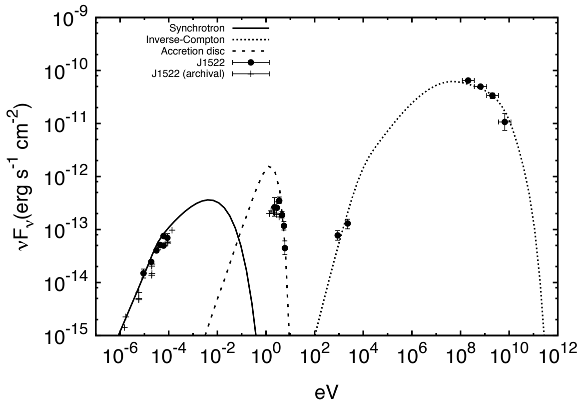

(f) J1522

Figure 4.4: The results of fitting the adiabatic jet model to the SEDs of J0349, J0457, J0531, J0730, J1504 and J1522. The model fits the observations well across all wavelengths, although for some of the blazars, the model requires very high bulk Lorentz factors ($\gamma_{\rm bulk} = 100$ for J1522). We find that the inverse-Compton emission of all the blazars is well described using NLR seed photons with a contribution to the X-ray emission from scattering of CMB photons.

4.6.2 The adiabatic model

Figure 4.4 shows the results of fitting the adiabatic jet model in equipartition to the observations of the six Compton-dominant blazars. The model fits the data well across all wavelengths, however, to fit the Compton-dominant spectra requires very high bulk Lorentz factors as shown in Table 4.2. The high bulk Lorentz factors are required in order that the rate of inverse-Compton emission from scattering CMB and NLR photons is not much smaller than the rate of adiabatic losses. In the case of J1522 we find that the adiabatic equipartition model struggles to reproduce the Compton-dominance of the spectrum and requires an extreme value for the bulk Lorentz factor at the transition region $\gamma_{\mathrm{bulk}} = 100$, this is much higher than the expected value of the bulk Lorentz factor in blazars inferred from superluminal motion (Jorstad et al. [2001]). For this reason and the low value of k calculated in Section 4.5.1 for the frequency core-shift we disfavour the adiabatic equipartition jet.

We find that the fits all require high power, high bulk Lorentz factor jets observed close to the line of sight as we expect for Compton-dominant blazars and in agreement with the ballistic fits. We find that all the fits have transition regions at large distances outside the BLR and dusty torus with large inferred black hole masses $> 10^9 M_\odot$. The inverse-Compton emission is due primarily to the scattering of NLR and CMB photons at large distances along the jet. We show the different components of the inverse-Compton emission for the fit to J1504 in Figure 4.3b. As for the ballistic model, the black hole mass inferred from the distance of the transition region agrees with that inferred independently from the accretion disc spectrum of J0531 if the transition region occurs at $10^5 R_s$ as in the jet of M87.

We have also considered an adiabatic model in which the jet is in equipartition after the transition region but with some electron acceleration occuring at smaller distances along the jet, in order to produce the gamma-rays and help reduce the bulk Lorentz factor. In this case we find that accelerating electrons within the dusty torus tends to produce too much synchrotron emission due to the relatively high energy density in the magnetic field compared to the external photon field (both measured in the plasma rest frame) resulting in the overproduction of synchrotron emission. Accelerating electrons in the BLR also suffers from a similar problem unless the location of the acceleration is fine-tuned to be close to the outer radius of the BLR. This is because the energy density in the BLR is relatively constant with distance x, whilst $U_B \propto x^{-2}$. So the Compton-dominance, which is approximately proportional to U_γ/U_B, increases towards the outer radius of the BLR. In an accelerating jet model the plasma has a lower bulk Lorentz factor at small distances within the parabolic region and BLR, so the emission is not so strongly Doppler-boosted as that from further along the jet, close to or beyond the transition region. We do not find that accelerating electrons within the BLR in the quiescent state is able to reproduce the observed data well and requires fine-tuning of the acceleration region within the BLR. For these reasons we do not favour this scenario in order to explain the quiescent spectra.

4.6.3 Inverse-Compton scattering of external photons

Our model uses a jet geometry based on radio observations of the jet in M87 scaled linearly with black hole mass. For large black hole masses ($> 10^9 M_\odot$) the distance of the transition region of the jet, where the jet is expected to be close to equipartition, is > 10 pc. This is consistent with our finding that BLR photons do not contribute significantly to the inverse-Compton emission of these Compton-dominant blazars since the BLR region is expected to be < 1 pc (Kaspi et al. [2005]). This means that the synchrotron bright transition region of our jet is outside the BLR and so the BLR photons will illuminate the jet from behind and be Doppler-deboosted. We expect the transition region of the jet to dominate the high energy emission because the plasma is in equipartition and has the highest bulk Lorentz factor at this point, giving the largest Doppler-boosting of the emission. From a reversal of the minimum energy argument (Burbidge [1959]) we know that for a given total energy, a plasma emits the most synchrotron power when the plasma is close to equipartition. This is found to be near to the transition region in jet simulations where the jet transitions from parabolic to conical (McKinney [2006] and Komissarov et al. [2009]).

We show the different components of the inverse-Compton emission for the ballistic jet fit to blazar J1504 in Figure 4.3. The figure shows that the inverse-Compton emission is dominated by scattering of CMB photons with a small contribution from scattering NLR photons at high energies. For a jet with a transition region outside the BLR and dusty torus we expect CMB and NLR photons to dominate the external photon field (see Figure 3.4 in Chapter 3). At low redshifts we expect the energy density in starlight at the centre of an elliptical galaxy to

Parameter	J0349.8 −2102	J0457.1−2325	J0531.0+1331	J0730.4−1142	J1504.4+1030	J1522.2+3143
W_j	8.0×10^{39}W	8.0×10^{39}W	1.4×10^{40}W	3.0×10^{40}W	2.0×10^{40}W	8.0×10^{39}W
L	1×10^{21}m	2×10^{21}m	2×10^{21}m	1×10^{21}m	2×10^{21}m	2×10^{21}m
$E_{\rm min}$	5.11 MeV	5.11 MeV	10.2 MeV	15.3 MeV	10.2 MeV	15.3 MeV
$E_{\rm max}$	1.28 GeV	2.03 GeV	1.14 GeV	4.55 GeV	2.87 GeV	1.09 GeV
α	1.3	1.6	1.55	1.7	1.9	1.5
$\theta'_{\rm opening}$	3^o	3^o	3^o	3^o	3^o	3^o
$\theta_{\rm observe}$	1.25^o	1.0^o	0.8^o	1.0^o	0.8^o	0.6^o
γ_0	4	4	4	4	4	4
$\gamma_{\rm max}$	25	50	40	50	60	100
$\gamma_{\rm min}$	10	30	30	30	30	30
M	$8.0 \times 10^{9} M_\odot$	$2.0 \times 10^{10} M_\odot$	$4.2 \times 10^{10} M_\odot$	$2.0 \times 10^{10} M_\odot$	$1.5 \times 10^{10} M_\odot$	$3.0 \times 10^{10} M_\odot$
$L_{\rm acc}$	5.0×10^{40}W	1.7×10^{39}W	6.8×10^{39}W	2.5×10^{39}W	8.3×10^{39}W	1.7×10^{39}W
$x_{\rm outer}$	1kpc	1kpc	1kpc	1kpc	1kpc	1kpc
B_T	4.02×10^{-6}T	8.05×10^{-7}T	6.34×10^{-7}T	1.56×10^{-6}T	1.41×10^{-6}T	2.68×10^{-7}T

Table 4.2: The values of the physical parameters used in the adiabatic equipartition model fits shown in Figure 4.3. We also include the value of the magnetic field strength in the plasma rest frame at the transition region for the fits (B_T).

dominate CMB photons (Hardcastle and Croston [2011]). However, these Compton-dominant objects are observed at relatively high redshifts so the CMB energy density is larger since $\rho_{\rm CMB} \propto (1+z)^4$. So we expect the CMB to be the dominant scattered photon field several kiloparsecs from the central black hole. This is interesting since Compton-dominant blazars are observed predominantly at high redshift, which is exactly what we would expect if their inverse-Compton emission were due to scattering CMB photons. Our model predicts that as we go to low redshifts where the energy density of the CMB decreases, high power, high bulk Lorentz factor blazars should become less Compton-dominant than an equivalent blazar at high redshift. We wish to investigate whether this prediction for the Compton-dominance of low redshift blazars holds in future work.

In order for an electron distribution to produce a Compton-dominant spectrum from SSC emission we require that the synchrotron energy density is so high that a "Compton-catastrophe" occurs. This happens when electrons emit so much synchrotron radiation that the synchrotron radiation field becomes dense enough to produce frequent scattering of photons so that electrons lose more energy through inverse-Compton scattering than synchrotron emission. In a jet with a fixed total energy and equipartition fraction we require a small jet radius at the transition region in order for the synchrotron radiation field to be dense enough for a "Compton-catastrophe" to occur. We find that in such small radius/large magnetic fields the synchrotron radiation emitted by the highest energy electrons far exceeds the observed energy of the synchrotron peak frequency and so we are unable to fit to the observed spectra using SSC emission.

4.6.4 Acceleration of electrons along the jet

We find that the electron distribution power law indices are lower than expected from parallel shock acceleration ($\alpha = 2$) for these Compton-dominant blazars. This suggests acceleration by oblique shocks (Bell et al. [2011] and Summerlin and Baring [2012]), possibly a stationary recollimation shock at the transition region or acceleration by magnetic reconnection (Zenitani and Hoshino [2001] and Zenitani and Hoshino [2007]). We see clear evidence for this in the spectrum of the blazar J0531 where the synchrotron emission starts self-absorbed and close to flat and retains a steep gradient when the spectrum becomes optically thin (see Figure 4.4c).

This optically thin spectrum requires a steep electron spectral index to fit to the observed emission. In all these objects we also see that the inverse-Compton emission rises steeply from low energies to its peak. This steep peak is also consistent with a low electron spectral index. This is an interesting result since we found in Chapter 2 that the spectrum of BL Lacertae was consistent with an electron spectral index $\alpha = 2$, compatible with a parallel shock. We wish to investigate whether other BL Lac type objects require spectral indices that are higher than those of Compton-dominant objects. This could imply a difference in the electron acceleration mechanism in different blazars possibly due to the different powers and bulk Lorentz factors of their jets.

4.6.5 Compton drag

In this investigation we have not explicitly calculated the effect of Compton drag on the jet plasma since we do not know the additional amount of deceleration caused by the entrainment of matter surrounding the jet. We have used the simple prescription for the deceleration of the jet set out in Equation 5 of Chapter 3 and fitted the deceleration parameters for a spectrum. We find for both the ballistic and adiabatic fits that the majority of the jet's initial energy is not radiated away through anisotropic scattering of external photons and so the effect of Compton drag on the jet plasma is comparable to or smaller than half of the total amount of deceleration in the fits ($\Delta\gamma_{\mathrm{bulk}} < 0.2\gamma_{\mathrm{max}}$). In the case of BL Lacs whose emission is dominated by synchrotron and SSC emission we do not expect Compton drag to be a significant contribution to the jet deceleration. This is because synchrotron and SSC emission from an isotropic electron distribution in a small scale tangled field are emitted isotropically in the plasma rest frame and so do not result in deceleration of the jet. This means that we are justified in not explicitly calculating the deceleration due to Compton drag in these Compton-dominant FSRQs or BL Lacs since the contribution of Compton drag to the total deceleration of the jet is, comparable to or smaller than, that of entrainment.

4.6.6 The blazar sequence

We find that the slowly decelerating conical region, which is responsible for the radio emission, produces a nearly flat radio spectrum which is consistent with observations. The frequency at which the observed synchrotron spectrum transitions from optically thick to optically thin emission is governed chiefly by the black hole mass which sets the radius of the bright transition region (the base of the conical region) and largely determines the magnetic field strength at this point. The transition from optically thick to optically thin synchrotron emission at these comparatively low energies (as shown in the spectra of J0457 and J0531) implies large black hole masses for these blazars. This is because a transition to optically thin synchrotron emission at low frequencies implies a low magnetic field strength at the base of the conical region and therefore a large radius as shown in Equation 4.7.

The base of the conical region in our model is in equipartition and so is responsible for producing the highest energy optically thin synchrotron emission. The peak frequency of the synchrotron emission is then governed by the Doppler factor, the magnetic field strength at the base of the conical region and the maximum electron energy. We find that the low synchrotron peak frequency of these Compton-dominant blazars is due to their large black hole masses which result in the transition region occuring far from the black hole with large radii. These large radii result in relatively low magnetic field strengths at the bright transition region which produce the low peak frequency synchrotron emission. We therefore expect that low powered BL Lac objects with high synchrotron peak frequencies should have lower black hole masses than low synchrotron peak frequency objects such as Compton-dominant objects.

This can be illustrated through the following simple calculation. We assume that the base of the conical region at a distance $10^5 r_s$ from the central black hole with a radius $2000 r_s$ is in equipartition and has the maximum bulk Lorentz factor $\gamma_{\rm max}$, so we expect it to dominate the optically thin synchrotron emission. For an electron distribution with a maximum Lorentz factor γ_e and an initial kinetic luminosity W_j using the formula for the synchrotron critical frequency (Equations 4.2 and 4.3) we find

$$U_B = \frac{B_T^2 \pi R_T^2}{2\mu_0} \times \frac{4\gamma_{max}^2}{3} \approx \frac{W_j}{2c}, \qquad R_T = 2000\frac{GM}{c^2}, \tag{4.12}$$

$$\nu_{\rm peak} = \frac{3\delta_{\rm Dopp} e E_{\rm max}^2}{4\pi(1+z)m_e^3 c^4} \cdot \sqrt{\frac{3W_j\mu_0}{4\gamma_{\rm max}^2 \pi c (2000GM/c^2)^2}}, \tag{4.13}$$

$$\nu_{\rm peak} \propto W_j^{1/2}/M_{BH}, \tag{4.14}$$

where a subscript T denotes the value of a quantity at the transition region, M_{BH} is the central black hole mass, β is the velocity of the jet divided by c, $\theta_{\rm obs}$ is the observation angle to the jet axis, z is the redshift and $\delta_{\rm Dopp}$ is the Doppler factor for the jet. We have assumed that half the initial jet power is contained in the magnetic field at the transition region where the plasma is in equipartition. We have also assumed that the plasma is described by a relativistic perfect fluid in its rest frame. From this we see that for objects which differ only by black hole mass $\nu_{\rm peak} \propto 1/M_{BH}$. If we further assume that in general the jet power is a fixed fraction of the Eddington luminosity then $W_j \propto M_{BH}$ and so $\nu_{\rm peak} \propto M_{BH}^{-1/2}$. If blazar jets are reasonably well described by a scaled M87 geometry this could even be used as a rough estimate of the black hole mass of a blazar based on its synchrotron peak frequency.

It would be an exciting result if the black hole mass of a blazar largely determines the peak frequency of its synchrotron emission. It is perhaps not surprising if in general FSRQs have higher black hole masses than BL Lacs. If jet power is fundamentally related to accretion, as currently believed, then we would expect powerful FSRQs to be accreting at a higher rate, and therefore to have larger black hole masses than lower power BL Lacs. In this scenario we would expect to find a trend like the blazar sequence where powerful objects are Compton-dominant and have lower peak frequencies of emission than less powerful BL Lac type objects with smaller jet radii (due to smaller black hole masses) and correspondingly higher magnetic field strengths. We interpret this as due to the bulk Lorentz factor of the jet, redshift and the black hole mass (which determines the size of the jet). If we assume a jet geometry similar to that observed in M87 we expect the jet to transition from parabolic to conical at $10^5 R_s$. The jet radius at this point is a function only of black hole mass (if we assume the M87 geometry scaled linearly with black hole mass) and so the magnetic field strength and synchrotron peak frequency decrease with increasing black hole mass. For BL Lac type objects with low black hole masses the radius of the jet at the point where it transitions to conical and is in equipartition is smaller than in a more powerful source with a higher black hole mass and this results in the increased magnetic field strength. An empirical correlation between jet power and black hole mass has been found by several authors by comparing observed radio luminosity against black hole mass for AGN (Lacy et al. [2001], McLure and Jarvis [2004] and Liu et al. [2006]), however, this correlation has been disputed (Oshlack et al. [2002], Woo and Urry [2002] and Ho [2002]).

If we assume that all AGN jets have approximately the same geometry as the M87 jet we can derive a simple relationship for the peak synchrotron frequency in blazars. In fitting to the optically thick to thin synchrotron break of these blazars we are essentially fitting the size of the jet radius where the synchrotron emission is brightest. In our model we then associate this emitting region with the region where the jet transitions from parabolic to conical. The determination of this radius from fitting to a spectrum is a rigorous result which holds independently of the particular M87 jet geometry we have chosen. In this work our assumption that the geometry of the jet scales linearly with black hole mass is based on the expectation that the radius of the jet close to the black hole scales with the size of the black hole event horizon which depends linearly on the black hole mass. Of course it is likely that the geometry of individual jets depends on other quantities such as jet power, bulk Lorentz factor and the environment. We do not yet know from observations or simulations exactly how these factors affect the jet geometry so we assume a simple scaling with black hole mass. It is important to note that if the inner parabolic geometry of jets is not well described by this simple model this will mainly affect the inferred black hole mass of our fits and not the other physical parameters of the model. This is the first investigation which has attempted to constrain the physical parameters of a sample of blazars using a realistic, extended model.

The trend of decreasing peak frequency of inverse-Compton emission with jet power can also be explained using this model. Low powered BL Lac type objects with low black hole masses have relatively high magnetic field strengths at the base of the conical section. This means that the synchrotron emission will overwhelm CMB photons (especially since BL Lacs are observed at lower redshifts than FSRQs and have lower bulk Lorentz factors) and the inverse-Compton emission will be due primarily to scattering of relatively high frequency synchrotron photons. This results in an inverse-Compton peak occurring at a higher frequency in BL Lacs than in Compton-dominant objects. This is because the inverse-Compton peak frequency is proportional to the peak frequency of the seed photons $\nu_{\rm peak} \propto \gamma^2 \nu_{\rm seed}$ (for $E_{\rm max} \gg h\nu_{\rm peak}$) and synchrotron photons have a higher peak frequency than CMB photons.

For increasing black hole mass, the magnetic field strength decreases at the base of the conical section. The synchrotron peak frequency decreases and consequently the SSC peak frequency will also decrease. For higher powered, high bulk Lorentz factor jets with lower magnetic field strengths Doppler-boosted CMB photons will now dominate the photon distribution within the jet at large distances and electrons will lose most of their energy through scattering CMB photons instead of emitting synchrotron photons. This produces the Compton-dominance of these objects and the low inverse-Compton peak frequency is due to the comparatively low CMB frequency.

In this Chapter we have not attempted to explain the short timescale variability in Compton-dominant blazars but, instead, the quiescent emission. The models we have investigated, which fit well to the quiescent emission, have electron acceleration occuring at large distances along the jet where the light-crossing time of the jet and electron cooling times are both much larger than the short flaring timescales observed (hours/minutes, Aharonian et al. [2007]). These flares could, however, be produced by acceleration of electrons in the parabolic region of the jet where the radius of the jet is smaller, the magnetic field strength is higher and the jet is still within the BLR/dusty torus. This means that short timescale variability is compatible with our jet model.

In this Chapter we have shown that a ballistic jet model which becomes particle dominated beyond a transition region located $>$ 10pc fits the multiwavelength data of the six most Compton-dominant blazars (after PKS0227) from Abdo et al. [2010a]. We have demonstrated that using a realistic extended jet model allows us to gain constraints on the jet by reproducing radio observations. In the next Chapter we will investigate whether our model is able to reproduce the spectra of BL Lac type blazars and if our idea of a blazar sequence based on bulk Lorentz factor and black hole mass holds for a sample of BL Lacs.

4.7 Conclusion

In this Chapter we have used the realistic extended jet model from Chapter 3 to fit to the simultaneous multi-wavelength spectra of six Compton-dominant blazars. Our model includes a magnetically dominated accelerating parabolic base transitioning to a slowly decelerating conical jet with a jet geometry set by radio observations of M87 and consistent with simulations and theory. Comparing different models of the conical section to the radio data, we find that the radio slope is well matched by both an adiabatic equipartition jet and a ballistic jet which starts in equipartition at the transition from parabolic to conical, and becomes particle dominated further along the jet. We use the optically thick to thin synchrotron break to constrain the radius of the jet where the jet first comes into equipartition. We find that this requires a transition region located outside the dusty torus at large distances along the jet $>$ 10pc, consistent with a transition region occuring at $10^5 R_s$ as in the jet of M87. We calculate an analytic expression for the radius at which a plasma becomes optically thick to an observed frequency and use this to confirm our numerical results. We then use this formula to calculate the expected frequency core-shift relations for the jet models under consideration. We find that for the adiabatic equipartition conical jet the core-shift relation, $x \propto \nu^{-k}$, has a value $k = 0.69$, lower than suggested by observations.

We find that the ballistic particle dominated jet fits very well to the observations across all wavelengths including radio observations whilst the adiabatic equipartition jet requires very high bulk Lorentz factors to reproduce the Compton-dominance of some of the blazars $\gamma_{\rm bulk} > 50$. This is the first time a realistic, extended jet model has been used to fit to a sample of blazars. We find that the fits to all these blazars require high power ($> 10^{39}$W), high bulk Lorentz factor (> 20) jets observed close to the line of sight ($< 2^o$) consistent with the blazar sequence and unification and in agreement with the results from Chapter 3. We find that the inverse-Compton emission of these objects is well fitted by scattering of CMB seed photons due to the redshift dependence of the CMB and strong Doppler-boosting. We find that all these blazars have large inferred black hole masses ($> 10^9 M_\odot$) using a jet geometry set by radio observations of M87 scaled linearly with black hole mass. For the blazar J0531 we find that the black hole mass inferred from fitting the jet model to the optically thick to thin synchrotron break agrees with the black hole mass estimated independently from the prominent accretion disc spectrum only if the transition region occurs at $10^5 R_s$ as in M87. For these large black hole masses, consistent with massive elliptical galaxies, we find that the brightest part of the jet is located at $10^5 R_s$, outside the broad line region and dusty torus.

We find a relatively low value for the electron distribution power law index from fitting to the steep optically thin synchrotron emission and inverse-Compton peak ($\alpha < 1.9$), implying acceleration by oblique shocks or magnetic reconnection. We postulate a new interpretation of the blazar sequence in terms of increasing black hole mass, jet power and bulk Lorentz factor. Higher power blazars have larger black hole masses and larger radius jets with lower magnetic fields than low power BL Lacs. This results in high power blazars having lower synchrotron peak frequencies and less SSC emission than low power blazars with higher magnetic fields. High power blazars also have large bulk Lorentz factors and so scatter high-redshift CMB photons at large distances resulting in the low inverse-Compton peak frequency of Compton-dominant blazars.

These results illustrate the importance of using a realistic, physically motivated model for blazar jets to calculate their spectra and estimate their physical properties. In the next Chapter we will test these concepts further by fitting to the spectra of a sample of BL Lac type objects.

Chapter 5

BL Lacs

In this Chapter I use the model presented in Chapters 2, 3 and 4 to fit to a sample of six BL Lac type blazars. I calculate the attenuation of gamma-rays via pair production from all the ambient photon fields in the plasma rest frame and integrate the line of sight pair production opacity along the jet. I find that the model fits very well to the spectra of all six blazars. Most of the BL Lacs require fits with lower jet power, smaller bulk Lorentz factors and smaller radius transition regions compared to the Compton-dominant blazars modelled in Chapter 3. This supports my hypothesis that the blazar sequence is a result of a decreasing transition region radius and increasing bulk Lorentz factor with jet power. I find that, due to absorption by pair production, the gamma-ray spectrum of Markarian 421 cannot be reproduced with SSC emission even with very large bulk Lorentz factors and instead favours scattering of CMB photons. I use my model to fit to non-simultaneous SEDs of the four high power, high synchrotron peak (HSP) BL Lacs recently found by Padovani et al. [2012]. I find that the model fits well to the spectra with parameters typical of high power BL Lacs except for high maximum electron energies which are the cause of their high peak frequency emission.

I set forward two hypotheses to understand the physical properties of FSRQ and BL Lac jets depending on the distribution of black hole masses in blazars. The first hypothesis is that of a universal jet geometry which scales linearly with black hole mass, so BL Lacs have smaller black hole masses than FSRQs. The second hypothesis, based on indirect mass measurents, is that FSRQs and BL Lacs have similar black hole masses. This leads to the idea of an accretion mode dichotomy analagous to that in X-ray binary systems.

5.1 Introduction

In this Chapter we will first briefly introduce our jet model from Chapter 3. We calculate the integrated optical depth along the jet for absorption of gamma rays due to pair production and show the results of fitting our model to six BL Lac type blazars. We then comment on the inferred physical parameters of the BL Lacs we find from fitting to their spectra and whether these results are consistent with our predictions for the blazar population from Chapter 4. We discuss the results and those from Chapter 4 in the context of the blazar sequence and unification. We comment on the location of the high energy emission region in our jet model fit to the spectrum of Markarian 421 and investigate the constraints placed on the size of the region by the attenuation of gamma rays from pair production. Finally, we investigate the physical properties of four high power, high synchrotron peak frequency (HSP) BL Lacs by fitting our model to their SEDs and commenting on their relation to the blazar sequence.

5.2 Jet Model

We use as the basis of this investigation the jet model presented in Chapter 3. The jet model consists of an accelerating parabolic base transitioning to a slowly decelerating conical jet with a geometry set by the recent radio observations of the jet of M87 (Asada and Nakamura [2011]). For full details of the model see Chapters 2, 3 and 4 (based on Potter and Cotter [2012], Potter and Cotter [2013a] and Potter and Cotter [2013b] respectively).

5.3 Photon-photon pair production

In this Chapter we model the spectra of BL Lac type blazars. Unlike the powerful Compton-dominant blazars that we modelled in Chapter 4, BL Lac blazars have observed spectra which can extend up to TeV energies. For these very high energy photons we need to take into account the production of electron-positron pairs from collisions between these high energy photons and ambient photons. When such a collision occurs the two photons are converted into an electron pair where each electron has approximately half the energy of the high energy photon and travels in approximately the same direction as the high energy photon. For two photons with energies E_1 (high energy photon) and E_2 (ambient photon) and velocities forming an angle θ to each other, the threshold energy of the ambient photon $E_{\rm thresh}$ above which pair production can occur is given by

$$E_{\rm thresh} = \frac{2m_e^2c^4}{E_1(1-\cos\theta)}. \tag{5.1}$$

The total cross section for pair production is given by (Gould and Schréder [1967])

$$\sigma_{\gamma\gamma} = \frac{1}{2}\pi r_0^2(1-\beta_e^2)\left[(3-\beta_e^4)\ln\left(\frac{1+\beta_e}{1-\beta_e}\right) - 2\beta(2-\beta_e^2)\right]. \tag{5.2}$$

$$\beta_e = \left(1 - \frac{2m_e^2c^4}{E_1E_2(1-\cos\theta)}\right)^{1/2}, \qquad r_0 = \frac{e^2}{4\pi\epsilon_0 m_e c^2}, \tag{5.3}$$

where β_e is the electron velocity in the centre of momentum frame divided by c and r_0 is the classical electron radius. We wish to calculate the fraction of high energy photons absorbed through pair production as they travel along the jet. We calculate the pair production optical depth of each section of the jet in the rest frame of the section. The total optical depth for a photon of energy E_1 emitted at an angle $\theta_{\rm observe}$ to the jet axis in the lab frame from a section at lab frame distance x' along the jet due to synchrotron photons is

$$\begin{aligned}\tau_{\gamma\gamma1}(E_1,x') &= \sum_{x=x'}^{x=L}\sum_{E_2=E_{\rm thresh}}^{E_2=\infty}\sum_{\theta=0}^{\theta=\pi}{\rm d}r(x)(1-\cos\theta)...\\ &\times n_{\rm synch}(E_2,x)\frac{\sin\theta}{2}\sigma_{\gamma\gamma}(E_1'(x),E_2,\theta){\rm d}E_2{\rm d}\theta,\end{aligned}$$

$${\rm d}r(x) = \gamma_{\rm bulk}(x)^2\left(\frac{1}{\cos\theta_{\rm observe}} - \beta(x)\right){\rm d}x', \tag{5.4}$$

$$E_1'(x) = \frac{\delta_{\rm Dopp}(x')}{\delta_{\rm Dopp}(x)}E_1, \quad \delta_{\rm Dopp}(x) = \frac{1}{\gamma_{\rm bulk}(x)(1-\beta(x)\cos\theta_{\rm obs})} \tag{5.5}$$

where $n_{\rm synch}(E_2,x)$ is the number density of synchrotron photons in the plasma rest frame and ${\rm d}r(x)$ is the distance travelled by the photon through a section of rest frame width ${\rm d}x'$ in the rest frame of the plasma (see Chapter 2). We have taken into account the relative

Doppler-boosting of the initial photon of energy E_1 into sections with different bulk Lorentz factors by defining the rest frame photon energy $E_1'(x)$ to be the photon energy in the relevant section of the jet. We have assumed that the synchrotron photons are isotropically distributed in the rest frame of the plasma and we have integrated the total optical depth through the jet to the section at a lab frame distance x.

The total optical depth for pair production due to CMB, BLR, dusty torus, NLR and starlight photons is

$$\tau_{\gamma\gamma 2}(E_1, x') = \sum_{x=x'}^{x=L} \sum_{E_2=E_{\mathrm{thresh}}}^{E_2=\infty} \mathrm{d}r(x)(1-\cos\theta) n_{\mathrm{EC}}(E_2, x) ... \\ \times \sigma_{\gamma\gamma}(E_1', E_2, \theta)\mathrm{d}E_2, \tag{5.6}$$

$$\theta = \pi - \cos^{-1}\left(\frac{\cos\theta_{\mathrm{obs}} - \beta(x)}{1-\beta(x)\cos\theta_{\mathrm{obs}}}\right), \tag{5.7}$$

$$n_{\mathrm{EC}}(E_2, x) = n_{\mathrm{CMB}}(E_2, x) + n_{\mathrm{BLR}}(E_2, x) + n_{\mathrm{star}}(E_2, x) ... \\ + n_{\mathrm{dusty\,torus}}(E_2, x) + n_{\mathrm{NLR}}(E_2, x), \tag{5.8}$$

where we have Lorentz transformed the CMB, BLR, dusty torus, NLR and starlight photons into the plasma rest frame and assumed that the photons are strongly Doppler-boosted so that the majority of photons travel approximately parallel to the jet axis (see Chapter 3). Finally, the total optical depth due to accretion disc photons is given approximately by

$$\tau_{\gamma\gamma 2}(E_1, x') = \sum_{x=x'}^{x=L} \sum_{E_2=E_{\mathrm{thresh}}}^{E_2=\infty} \mathrm{d}r(x)(1-\cos\theta) n_{\mathrm{acc}}(E_2, x) \\ \times \sigma_{\gamma\gamma}(E_1', E_2, \theta)\mathrm{d}E_2, \tag{5.9}$$

$$\theta = \cos^{-1}\left(\frac{\cos\theta_{\mathrm{obs}} - \beta_x}{1-\beta(x)\cos\theta_{\mathrm{obs}}}\right), \tag{5.10}$$

where we have Lorentz transformed the number density of accretion disc photons into the plasma rest frame as calculated in Chapter 3. The total optical depth due to pair production from all these photon fields is given by

$$\tau_{\gamma\gamma\mathrm{tot}}(E_1, x') = \tau_{\gamma\gamma 1}(E_1, x') + \tau_{\gamma\gamma 2}(E_1, x') + \tau_{\gamma\gamma 3}(E_1, x'). \tag{5.11}$$

So the fraction of high energy photons with energy E_1 emitted from a section of the jet at lab frame distance x observed is

$$\mathrm{fraction}(E_1, x) = \mathrm{e}^{-\tau_{\gamma\gamma\mathrm{tot}}(E_1, x')}, \tag{5.12}$$

In the current work we neglect the subsequent emission of pair produced electrons. This is justified since in synchrotron-dominated high peak frequency BL Lacs (HBLs) only a small fraction of the total particle energy is emitted via high energy photons. The conversion of high energy photons into electron-positron pairs will reduce the amount of high energy emission observed from HBLs. It is important to consider pair production when modelling HBLs since the observation of TeV photons can be used to constrain the size of the high energy emitting region. This is because compact emission regions located close to the base of the jet will have a larger number density of both synchrotron and ambient photons than larger regions at larger distances emitting the same power and so compact regions may be opaque to TeV photons. Constraints on the location, size and bulk Lorentz factors of high energy emission regions in one-zone models have been investigated by many authors including Begelman et al. [2008], Böttcher et al. [2009] and Dermer et al. [2012]. This is the first investigation which calculates the effect of pair production in an extended jet model by Lorentz transforming ambient photon fields into the plasma rest frame and integrating the pair production optical depth along the jet.

5.4 External photon fields for BL Lacs

It is generally observed that BL Lac spectra are dominated by a featureless synchrotron continuum at optical wavelengths. It is thought that this is due to a weak or absent BLR and dusty torus, and synchrotron emission which dominates the accretion disc spectrum (Vermeulen et al. [1995]). In contrast FSRQ spectra have emission line features with broad emission lines (Ghisellini et al. [2011]). The inverse-Compton emission of BL Lacs is normally attributed to SSC emission whilst the inverse-Compton emission of FSRQs is thought to be primarily due to scattering external photons from the BLR and dusty torus (Meyer et al. [2012]). In Chapter 4 we found that the inverse-Compton emission of a sample of Compton-dominant blazars was incompatible with SSC emission but was well fitted by scattering of external photons (CMB and NLR photons). In this Chapter we shall initially assume that the inverse-Compton emission of our BL Lacs is due to SSC emission and neglect BLR, accretion disc, dusty torus and NLR photons before attempting to fit the spectra using external photons. It is interesting to see whether these BL Lac spectra can be fitted with SSC emission or whether they require external photon fields to fit the spectra.

The jets of BL Lacs are thought to correspond to FRI jets and so we shall attempt to fit the BL Lac spectra with shorter jets than in Chapter 4 where we were fitting to powerful Compton-dominant sources.

5.5 Results

In this section we show the results of fitting our model to the multi-wavelength observations of six BL Lac type blazars ($J0222.6+4302$, $J0855.4+2009$, $J1015.2+4927$, $J1104.5+3811$, $J1751.5+0935$ and $J2158.8-3014$) selected by the availability of redshifts and good quality simultaneous multiwavelength spectra across radio, optical, X-ray and γ-rays from Abdo et al. [2010a]. The spectrum for Mkn421 from Abdo et al. [2010a] contains multiple sets of data and so we have instead used the simultaneous multiwavelength data from the *Fermi* campaign on Mkn421 (Abdo et al. [2011b]).

In our model we have initially assumed that the size of the jet scales linearly with black hole mass with a transition region that occurs at a distance $10^5 R_s$ with a radius $2000R_s$ set from radio observations of M87. In fitting our model to a spectrum we find a radius for the transition region, R_T, which gives us an inferred black hole mass, M, for each fit. We discuss the assumption of a jet geometry which scales linearly with black hole mass and the implications of alternative scenarios in sections 5.2-5.4.

We show the results of fitting our model to the blazars in Figure 5.1. The model fits very

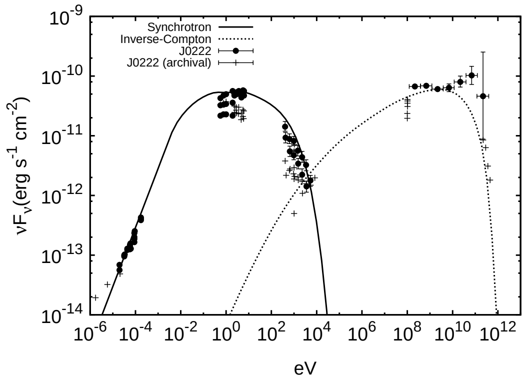

(a) J0222

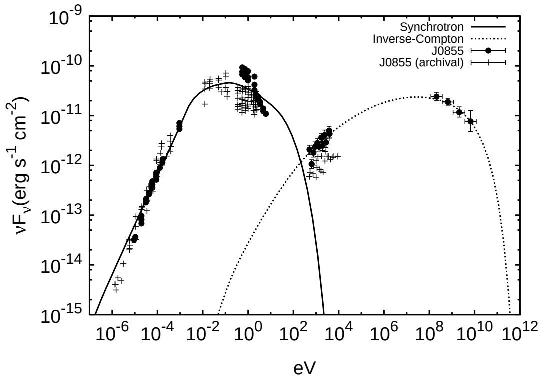

(b) J0855

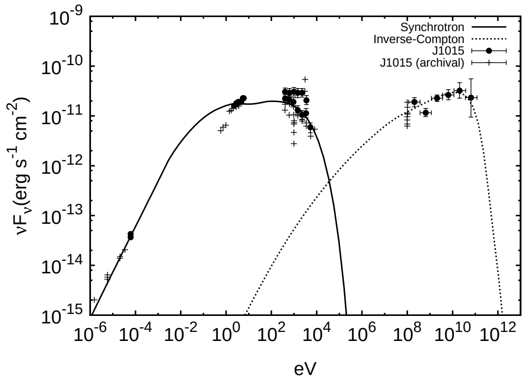

(c) J1015

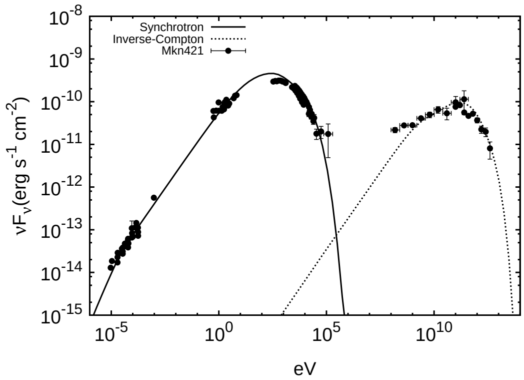

(d) Mkn421

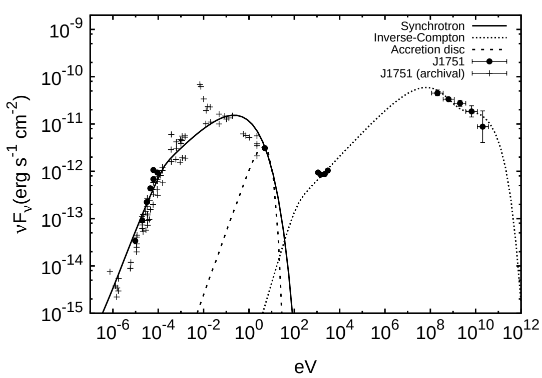

(e) J1751

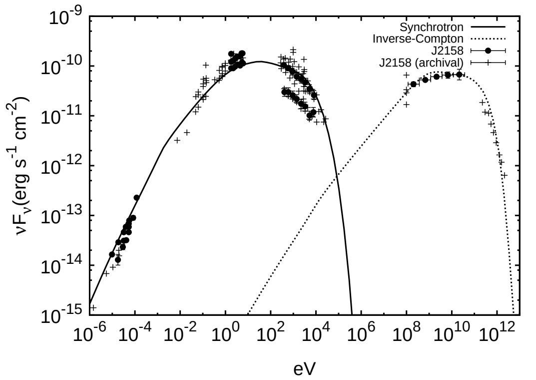

(f) J2158

Figure 5.1: The results of fitting our model to the SEDs of J0222, J0855, J1015, Mkn421, J1751 and J2158. The model fits the observations well for all objects across all wavelengths. We find that the inverse-Compton emission of all the blazars, except J1751 and Mkn421, are well fitted by SSC emission. We find that the low peak frequencies of J1751 imply that the blazar is a more powerful Compton-dominant blazar at low redshift.

Parameter	J0222	J0855	J1015	Mkn421	J1751	J2158
W_j	1.0×10^{38}W	1.6×10^{38}W	2.4×10^{37}W	6.0×10^{36}W	2.1×10^{38}W	1.6×10^{37}W
L	5×10^{20}m	5×10^{20}m	1×10^{21}m	3×10^{20}m	2×10^{21}m	1×10^{21}m
E_{min}	5.11 MeV	5.11 MeV	5.11 MeV	5.11 MeV	5.11 MeV	5.11 MeV
E_{max}	16.2 GeV	5.11 GeV	32.2 GeV	338 GeV	4.06 GeV	51.1 GeV
α	1.6	1.63	1.5	1.55	1.98	1.7
$\theta'_{\mathrm{opening}}$	3^o	5^o	5^o	5^o	3^o	5^o
$\theta_{\mathrm{observe}}$	1.0^o	1.0^o	3.5^o	3.0^o	1.0^o	2.0^o
γ_0	4	4	4	4	4	4
γ_{max}	12	8	10	12	34	15
γ_{min}	8	6	3	9	18	7
R_T	2.5×10^{14}m	6.8×10^{14}m	9.8×10^{13}m	3.7×10^{15}m	1.1×10^{16}m	1.7×10^{14}m
M	$4.2 \times 10^{7} M_\odot$	$1.2 \times 10^{8} M_\odot$	$1.7 \times 10^{7} M_\odot$	$6.3 \times 10^{8} M_\odot$	$1.8 \times 10^{9} M_\odot$	$2.9 \times 10^{7} M_\odot$
L_{acc}	–	–	–	–	3.3×10^{37}W	–
x_{outer}	–	–	–	–	1kpc	–

Table 5.1: The values of the physical parameters used in the model fits shown in Figure 5.1.

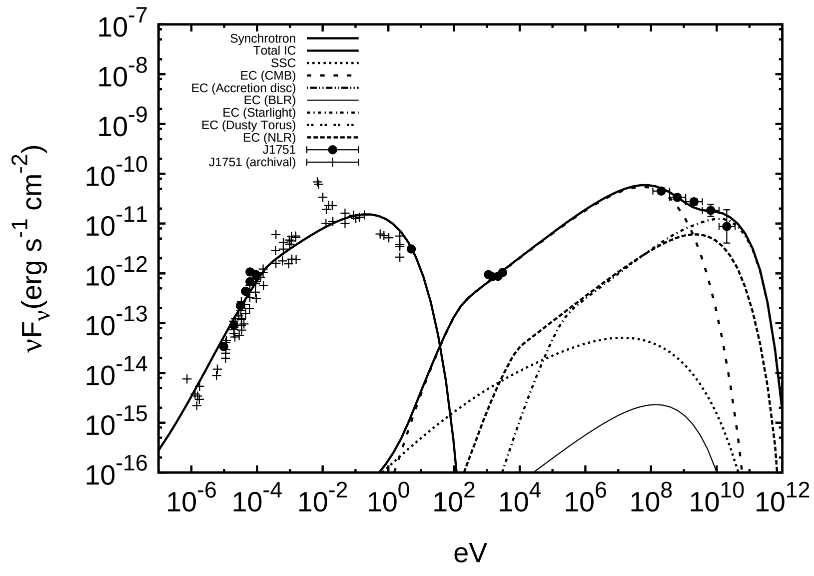

(a) J1751

Figure 5.2: The different components of the inverse-Compton emission for the fit to J1751. The inverse-Compton emission is primarily due to scattering of CMB seed photons with a small contribution of starlight required to fit to the highest energy data-point. For these Compton-dominant blazars we find that the SSC emission is sub-dominant due to the comparatively low magnetic field strength at the transition region of the jet.

well to all the spectra across all wavelengths. We find that the inverse-Compton emission of the majority of blazars (except for J1751 and Mkn421) is due to SSC emission as is commonly found for BL Lac type objects (Boettcher [2010]). We find that these blazars (excluding J1751) are relatively low power, low bulk Lorentz factor objects with smaller radius transition regions (where the jets first reach equipartition) compared to the Compton-dominant blazars we fitted in Chapter 4.

This is an important result since it shows that our model is able to successfully fit to a variety of blazar spectra from different sections of the blazar population, including radio observations. It is encouraging to find that the physical parameters of our fits are consistent with our predictions from Chapter 4 and also with the blazar sequence (Fossati et al. [1998]). We find, in agreement with the blazar sequence and previous investigations, that BL Lac type objects are relatively low power blazars in which the inverse-Compton emission is predominantly due to SSC emission. In Chapter 4 we found that Compton-dominant blazars were high power blazars in which the inverse-Compton emission was predominantly due to scattering of the CMB.

We find that the blazar J1751 has a larger power, bulk Lorentz factor and transition region radius than the other BL Lac blazars. The physical parameters of the fit seem closer to those of the Compton-dominant blazars found in Chapter 4. We find that in order to reproduce the low frequency synchrotron peak, the fit requires a large transition region (and a large inferred black hole mass if the transition region occurs at $10^5 R_s$ as in M87). We are unable to fit the inverse-Compton emission with SSC emission due to the low magnetic field strength required to produce the low peak synchrotron frequency. We find that BLR and dusty torus photons are unable to reproduce the observed high energy emission and archival synchrotron data simultaneously. This is because the archival observations show that the synchrotron emission becomes optically thin at the relatively low energy $\sim 10^{-4}$eV, requiring a low magnetic field strength and large transition region (see Chapter 4 Equation 4.7). This large transition region is located at a distance 18pc from the black hole in our fit, placing it outside the BLR and dusty torus. Somewhat surprisingly, we find that the inverse-Compton emission of J1751 is well fitted by scattering of CMB photons even at the comparatively low redshift $z = 0.322$, if the jet has a large bulk Lorentz factor. These characteristics indicate that the blazar has similar physical properties to the Compton-dominant blazars from Chapter 4 but is located at low redshift where the CMB has a lower energy density.

This is intriguing since in Chapter 4 we found that the inverse-Compton emission of Compton-dominant blazars was best fitted by scattering of Doppler-boosted high redshift CMB photons. We predicted that if the inverse-Compton emission of high power Compton-dominant blazars was due to scattering of CMB photons, then at low redshift we should see blazars with the same physical parameters but with less Compton-dominance due to the red-shifting of the energy density of the CMB ($\rho_{\mathrm{CMB}} \propto (1+z)^4$). J1751 appears to be a blazar matching the description of a high power, high bulk Lorentz factor jet with a large transition region but a lower Compton-dominance due to its low redshift. We find this evidence for the inverse-Compton scattering of CMB photons significant and we intend to investigate whether other high power, high bulk Lorentz factor jets at low redshift are compatible with their inverse-Compton emission being mainly produced by scattering of CMB seed photons.

Whilst we might expect the jet power, bulk Lorentz factor and radius of the transition region to be related, it is not clear how we expect these parameters to impact the mechanism of particle acceleration in jets. For the high power Compton-dominant sources investigated in Chapter 4 we found that the electron distribution power-law index was considerably lower than the value $\alpha = 2$ predicted by diffusive parallel shock acceleration (Bell [1978]). We find that all of these blazars require power-law indices less than or equal to 2. Spectral indices less than 2 are predicted in the case of oblique shock acceleration (Bell et al. [2011] and Summerlin and Baring [2012]) and magnetic reconnection (Zenitani and Hoshino [2007]). We find that the maximum electron energy tends to be lower in higher power objects and increases in lower power objects, however, we do not find an obvious physical reason for this. This trend is usually explained by stronger radiative cooling of accelerating electrons in higher power FSRQs with luminous BLRs (Ghisellini et al. [2009b]). In our model, however, we find that the region responsible for the high energy emission (the transition region) is relatively large for high power blazars and is located outside the BLR, so electrons are not strongly radiatively cooled. We find that for all the blazars (except Mkn421) the maximum electron energy ($E_{\max}$) is between $4-55$GeV while Mkn421 requires a much larger maximum electron energy 338GeV, considerably higher than the other blazars.

We find that the radio spectra of the blazars (excluding J1751) are close to flat in flux and so are better fitted with a ballisitic equipartition jet rather than either an adiabatic equipartition jet or a ballistic jet starting in equipartition at the transition region and becoming more particle dominated further along the jet ($A_{\rm equi} = 2x_T/(x + x_T)$ for $x_T \geq x \geq 100x_T$). In Chapter 4 we found that the multiwavelength spectra were best fitted by a ballistic conical jet starting in equipartition at the transition region and becoming more particle dominated further along the jet. We wish to investigate whether, for a larger sample, BL Lacs are best fitted by jets with ballistic equipartition conical sections whilst FSRQs favour ballistic jets which become particle dominated along the conical section. This would imply an important, fundamental difference between BL Lac and FSRQ jets.

5.5.1 Understanding the blazar sequence

In Chapter 4 we hypothesised that the blazar sequence could be explained if the radius of the transition region and bulk Lorentz factor of the jet were to increase with the jet power. In this Chapter and Chapter 4 we have shown that FSRQs are well fitted by high power jets with large radius transition regions and large bulk Lorentz factors whilst BL Lacs are well fitted by lower power jets with smaller radius transition regions and lower bulk Lorentz factors.

We have shown that our model is able to fit well to a sample of BL Lacs using a jet model which stops accelerating and comes into equipartition at smaller distances with a smaller jet radius than the sample of FSRQs fitted in Chapter 4. This is a very interesting result which confirms the prediction of Chapter 4. The link between jet power and the jet radius at the transition region not only allows us to explain the physics behind the blazar sequence but also to learn how the jet dynamics are affected by the properties of the jet. Depending on the relationship between black hole mass and jet power we find two interpretations of our results: either a universal jet geometry which scales linearly with black hole mass or a dichotomy in accretion rate between BL Lacs and FSRQs.

5.5.2 Scenario I - A universal jet geometry

Our jet model is based on observations of the jet in M87 scaled linearly with black hole mass. We have shown that this model is able to fit well to both BL Lacs and FSRQs, if FSRQs have large black hole masses $10^9 - 10^{10} M_\odot$ with large bulk Lorentz factors and BL Lacs have smaller black hole masses $10^7 - 10^9 M_\odot$ with smaller bulk Lorentz factors. This range of black hole masses coincides with the expected range of black hole masses for AGN (Vestergaard et al. [2008]). In the case of a few FSRQs with accretion disc spectra visible above the jet emission, it is possible to find an independent estimate of the black hole mass. In these cases we find that this black hole mass agrees with the black hole mass inferred from the jet model in which the transition region occurs at $10^5 r_s$. Unfortunately, in BL Lacs the jet emission tends to overwhelm the accretion disc spectra and so it is difficult to estimate the black hole mass via this method. This scenario of a universal jet geometry would seem logical if blazars all accrete at approximately the same Eddington fraction, so that the accretion power depends linearly on the black hole mass. This scenario would predict a linear relation between the jet power and the jet radius at the transition region.

Black hole mass estimates for blazars are mostly indirect and suffer from large uncertainties in their calibration (Woo and Urry [2002], Fine et al. [2010], Shen et al. [2011] and Shaw et al. [2012]). However, systematic studies of FSRQ and BL Lac spectra using black hole mass estimates based on emission line widths and virial estimates have found that the black hole masses of FSRQs and BL Lacs do not seem to differ substantially, with BL Lacs, in fact, having larger black hole masses on average (Shaw et al. [2013]). If we believe these measurements this leads us to a second interpretation of our results.

5.5.3 Scenario II - A dichotomy in accretion rate

If there is no systematic difference between the black hole masses in FSRQs and BL Lacs then our results indicate that the transition region occurs at a distance and radius which depends mainly on the jet power (or accretion rate) and is not strongly dependent on the black hole mass. We have found that our sample of BL Lacs have lower jet powers and smaller radius transition regions than FSRQs. If the black hole masses of FSRQs and BL Lacs are similar this means that the jet power in BL Lacs is a smaller fraction of the Eddington luminosity than in FSRQs, as has been suggested by Ghisellini and Tavecchio [2008]. This would support the idea of a dichotomy in the accretion modes of FSRQs and BL Lacs. It has been previously suggested that FSRQs have large Eddington accretion rates with radiatively efficient thin discs while BL Lacs have much lower Eddington accretion rates and radiatively inefficient discs (see for example Ghisellini et al. [2009a] and Meyer et al. [2011]). We can make a rough estimate of the Eddington luminosity by using a fiducial black hole mass for BL Lacs of $5 \times 10^8 M_\odot$ taken from Shaw et al. [2013]. Using this mass we estimate a range of luminosities $0.001L_{\mathrm{Edd}} - 0.03L_{\mathrm{Edd}}$ for the BL Lacs fitted in this Chapter. Taking the same fiducial mass for the FSRQs fitted in Chapter 4 we estimate a range of luminosities $0.2L_{\mathrm{Edd}} - 0.9L_{\mathrm{Edd}}$.

Our results would link this dichotomy in accretion mode to the properties of the jet produced in the two modes. FSRQs accreting at high rates produce jets which accelerate over larger distances reaching larger bulk Lorentz factors and radii before coming into equipartition at the transition region than the jets of BL Lacs. This would also be consistent with AGN unification in which BL Lacs correspond to FRI type jets whilst FSRQs correspond to FRII type jets (Urry and Padovani [1995]).

5.5.4 Using emission spectra to understand jet dynamics and properties

Without trustworthy black hole mass estimates for blazars it is difficult to distinguish between the two scenarios above. However, we have shown that the dynamics and geometry of a jet depends on the jet power. This is exciting because these results can be used to inform MHD simulations and allow us to better understand the physical processes responsible for jet production. For example, we can interpret the larger bulk Lorentz factor of FSRQ jets as being caused by different initial mass loading in FSRQ and BL Lac jets. In general, we would expect the final bulk Lorentz factor of a jet to depend on the initial equipartition ratio of the jet. A section of the jet plasma starts with an energy, $E = E_M + E_p$, split between magnetic and particle energies. In the simplest scenario the jet accelerates until the magnetic and particle energies are approximately equal, converting magnetic energy into bulk particle energy. This gives a final bulk Lorentz factor $\gamma = E/(2E_p) = \sigma/2$ where σ is a measure of the initial mass loading of the jet. From this simple reasoning we might expect that jets with larger bulk Lorentz factors have a smaller initial mass loading. Our results would then suggest that higher power FSRQ jets have less mass loading than BL Lac jets.

In scenario II we expect a quantitive difference in the disc properties of FSRQs and BL Lacs. It has been suggested that at low Eddington accretion rates discs favour radiatively inefficient ADAF type solutions in which a hotter thick disc surrounds the black hole (Narayan and Yi [1995]). In this case we expect the mass loading resulting from the pair production of hard X-ray disc photons and the entrainment of disc material to be more efficient for a hotter, thick ADAF. This would support the result that the bulk Lorentz factors of FSRQ jets are higher then BL Lacs because the mass loading in BL Lac jets is larger than in FSRQs.

These results demonstrate the value of using a realistic, extended jet model of emission to relate the different spectra of blazars to the dynamic properties of jets. In the next Chapter we will use our model to fit to a much larger sample of FSRQs and BL Lacs in order to test whether our hypothesis of a relation between jet power and radius of the transition region holds for the blazar population as whole.

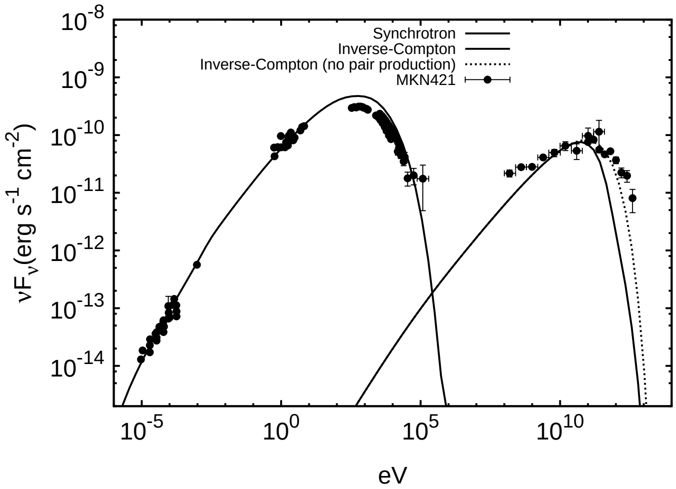

Figure 5.3: A fit to Mkn 421 using a highly relativistic, compact, adiabatic, conical emission region, decelerating rapidly within one hundred parsecs (see Table 5.2 for the parameters of the fit). We have attempted to fit the inverse-Compton emission of Mkn 421 using SSC radiation, however, we find that the large magnetic field strength required to create sufficient high energy SSC emission produces a synchrotron radiation peak at a higher energy than observed. We find that in order to produce sufficient SSC emission requires too many synchrotron photons so that the region is optically thick to TeV photons due to pair-production.

5.5.5 The location of the TeV emission region

One of the most intensely-debated current questions about blazar jets is where the region responsible for the observed TeV emission is located. Most previous investigations have assumed that the emission region is compact and located at 100-1000 Schwarzschild radii from the black hole with high Doppler factors in order to explain the timescale of the TeV emission (Finke et al. [2008]). In our model based on radio observations of the jet of M87 we assume the high energy emission region is located at $10^5 R_s$ from the black hole where the jet has a radius $2000R_s$. An emission region at exactly this distance is suggested by observations of a 20 day flare in 3C279 (Abdo et al. [2010b]).

This places the TeV emitting region at a distance 6.3pc with radius 3.8×10^{15}m for Mkn421 in our model fit, approximately compatible with the upper bound on the FWHM of the radio core $< 3 \times 10^{15}$m of Mkn 421 found with VLBI (Charlot et al. [2006]) and at a similar distance to the flaring region $>$ 14pc found by Agudo et al. [2011] using VLBI measurements of OJ287. We find that matching the inverse-Compton via SSC emission is not feasible since it requires such a high number density of synchrotron photons to produce the required Compton-dominance ratio as to make the region optically thick to TeV photons. We find with this large

Parameter	Mkn 421
W_j	3.0×10^{37}W
L	3×10^{18}m
E_{min}	5.11 MeV
E_{max}	57.3 GeV
α	1.6
θ'_{opening}	3.0^o
θ_{observe}	2.0^o
γ_0	4
γ_{max}	50
γ_{min}	3
R_T	5.9×10^{13}m
M	$1.0 \times 10^7 M_\odot$

Table 5.2: The values of the physical parameters used in the model fit shown in Figure 5.3.

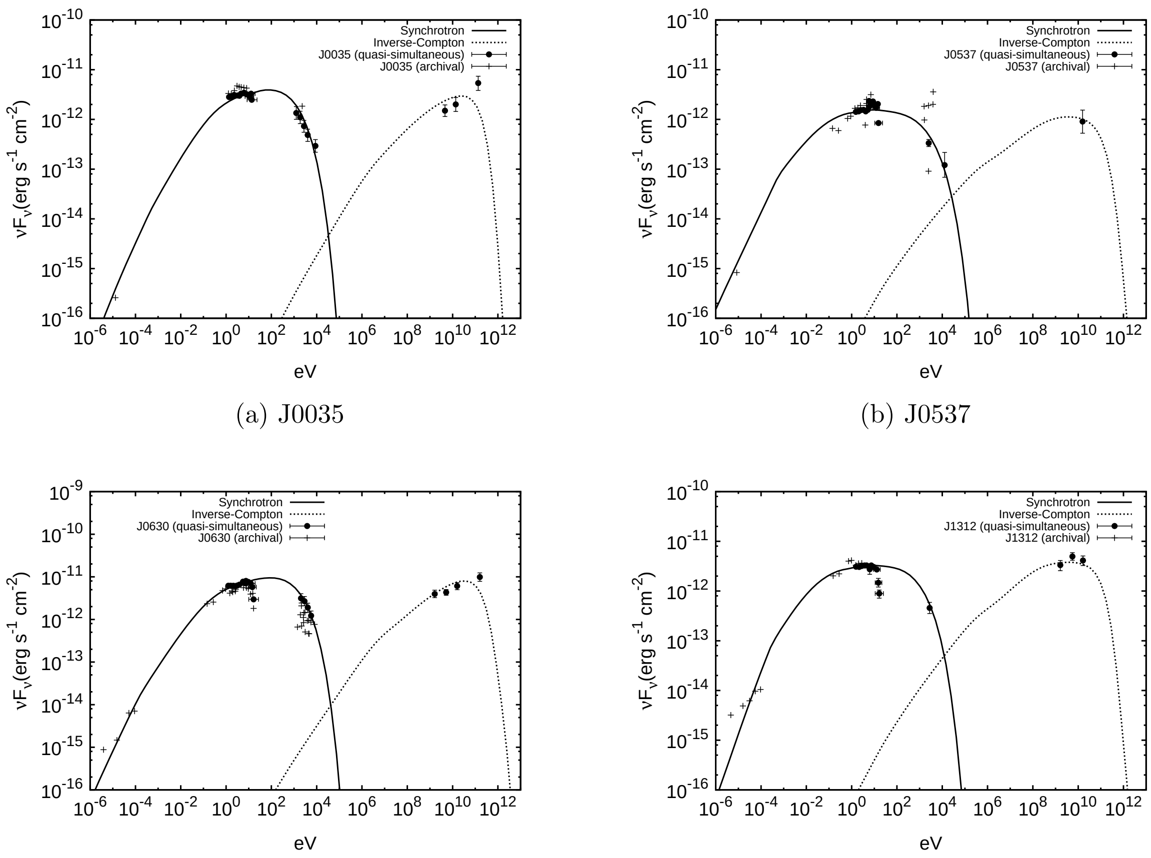

(a) J0035

(b) J0537

(c) J0630

(d) J1312

Figure 5.4: The results of fitting our model to the SEDs of the four high power, high synchrotron peak frequency BL Lacs J0035, J0537, J0630 and J1312 taken from Padovani et al. (2012). The data is not simultaneous and so we use these fits simply to try to understand the reason for the high peak frequencies of emission in these BL Lacs. The data shows absorption by neutral hydrogen at $\approx$ 10eV which was used to estimate the photometric redshift of the blazars by Rau et al. (2012). The model fits the observations well for all blazars across all wavelengths, the parameters of the fits are shown in Table 5.3. We find that the high synchrotron peak frequencies are caused by high maximum electron energies whilst the remaining jet parameters are consistent with other relatively high power BL Lacs.

Parameter	J0035.2+1515	J0537.7−5716	J0630.9−2406	J1312.4−2157
W_j	5.0×10^{37}W	8.0×10^{37}W	2.1×10^{38}W	2.3×10^{38}W
L	1×10^{20}m	1×10^{21}m	1×10^{20}m	1×10^{21}m
$E_{\rm min}$	5.11 MeV	5.11 MeV	5.11 MeV	5.11 MeV
$E_{\rm max}$	40.6 GeV	102 GeV	81.0 GeV	81.0 GeV
α	1.3	1.75	1.3	1.6
$\theta'_{\rm opening}$	4^o	4^o	4^o	4^o
$\theta_{\rm observe}$	1.0^o	1.5^o	1.0^o	1.2^o
γ_0	4	4	4	4
$\gamma_{\rm max}$	14	12	14	10
$\gamma_{\rm min}$	10	6	10	6
R_T	4.6×10^{14}m	9.14×10^{14}m	2.28×10^{15}m	2.74×10^{15}m
M	$7.7 \times 10^7 M_\odot$	$1.54 \times 10^8 M_\odot$	$3.84 \times 10^8 M_\odot$	$4.62 \times 10^8 M_\odot$

Table 5.3: The values of the physical parameters used in the model fits shown in Figure 5.4.

emission region and small magnetic field the inverse-Compton emission is primarily due to the scattering of external CMB and starlight photons.

Our model involves an emission region with a larger radius at a larger distance from the black hole than that generally assumed in the literature. The reason for assuming a much smaller radius is to explain the TeV flaring timescales of several minutes due to the light crossing time for the emitting region. In this Chapter we are only concerned with modelling the quiescent emission from blazars and we have found that this emission originates at large distances along the jet, however, our jet model is still compatible with flares occuring at shorter distances, consonant with short flaring timescales.

We find that the radio synchrotron spectrum is compatible with an optically thin single power law, implying a relatively large synchrotron bright, transition region and large inferred black hole mass $6.3 \times 10^8 M_\odot$ in our model. This does not preclude flares occuring at smaller distances along the jet, however, we have found that in Mkn 421 compact regions travelling at typical bulk Lorentz factors ~ 10 are opaque to TeV photons. The common solution to this problem is to increase the Lorentz factor and the radius of the compact region so that the observed Doppler-boosted light crossing time of the region is still compatible with minute timescales (e.g. bulk Lorentz factors > 50, Begelman et al. [2008]). It seems unlikely that a low power blazar like Mkn 421 with relatively slow observed superluminal motions of 2-3c (Marscher [1999]) should have a jet with a bulk Lorentz factor of 50. We find that in our model fit the maximum bulk Lorentz factor is 12.

In Figure 5.3 we show a fit for the quiescent spectrum of Mkn 421 using a compact, adiabatic, conical jet with a high bulk Lorentz factor of 50 decelerating to a Lorentz factor of 3 at a distance of one hundred parsecs. This small region with a high bulk Lorentz factor has been suggested by previous investigations and we have decelerated the jet on pc scales as suggested by Charlot et al. [2006] to explain the lack of superluminal VLBI measurements (although a lack of observed superluminal motion on pc scales does not mean a jet is not relativistic, Charlot et al. [2006]). We find that even with this high bulk Lorentz factor the emission region is still optically thick to TeV photons. This is because in order for a region to emit the observed ratio of synchrotron to inverse-Compton emission through SSC it requires a large number density of synchrotron photons to scatter, however, a large number density of synchrotron photons means that the emission region is then optically thick to TeV photons. For these reasons we argue that the inverse-Compton emission observed in the quiescent spectrum of Mkn 421 is unlikely to be due to SSC radiation.

Most previous investigations have either neglected the pair production opacity due to external photons or not Lorentz transformed the photon fields into the plasma rest frame where they are Doppler-boosted. The location of the TeV emission region is difficult to resolve with current instruments, however, future instruments such as CTA, which provide better angular and temporal resolution and sensitivity, would be very useful in investigating the location of the TeV emission. We intend to investigate whether it is possible to put further constraints on the size and location of the TeV emitting region by modelling the flares of blazars in the near future.

5.5.6 High power, high synchrotron peak BL Lacs

Recently a number of high power BL Lacs with high synchrotron peak frequencies (HSPs) have been discovered by Padovani et al. [2012]. These blazars are at odds with the general anticorrelation between the peak frequencies of emission and radio power, known as the blazar sequence. We have fitted our jet model to the four non-simultaneous spectral energy distributions (SEDs), presented in Padovani et al. [2012], to understand how the properties of these blazars differ from those forming the standard blazar sequence. We show the fits to the non-simultaneous data in Figure 5.4, the parameters of the fits are shown in Table 5.3.

The observations show absorption from neutral hydrogen at ≈ 10eV. This absorption feature was used by Rau et al. [2012] to obtain redshift estimates for the blazars. We find that the power of these BL Lacs is relatively high ($\sim 10^{38}$W) but consistent with the range of powers we find for the six BL Lacs with simultaneous multiwavelength observations. The radius of the transition region is also similar to the higher power BL Lacs in this small sample. We find that the high peak synchrotron frequencies are caused by the high maximum energies of the non-thermal electrons ($40-100$GeV) but the other properties of the fits such as the jet power, bulk Lorentz factor and transition region radius are similar to the high power BL Lacs J0855 and J0222. The jet properties are substantially different from the FSRQs fitted in Chapter 4 and even from the BL Lac J1751, which appears to have many FSRQ characteristics. We find that the inverse-Compton emission of these four BL Lacs can only be fitted by SSC, due to the high peak frequency of emission. This leads us to conclude that these blazars are, in fact, fairly typical BL Lacs, except for the relatively high maximum electron energies compared to BL Lacs of similar power. These BL Lacs have been selected from a large sample on the basis of their high peak frequency of emission and so it is not surprising that they have relatively large maximum electron energies since this quantity varies considerably within the BL Lac population and strongly effects the peak synchrotron frequency ($\nu \propto \gamma_{\max}^2 B$).

In Chapter 4 we postulated that the anticorrelation between peak frequency of emission and jet power of blazars is caused by a correlation between the radius of the transition region and the jet power. This results in higher peak frequencies of both synchrotron and inverse-Compton emission for low power blazars due to larger magnetic field strengths. We find that the transition region radii for these four high power HSP BL Lacs are larger than lower power BL Lacs and considerably smaller than the sample of high power FSRQs from Chapter 4. We also find that their inverse-Compton emission is produced by SSC while their bulk Lorentz factors are smaller than in the FSRQs fitted in Chapter 4. The properties of these BL Lacs are, therefore, consistent with our hypothesis.

5.6 Conclusion

In this Chapter we use the realistic extended jet model based on observations of the jet in M87 from Chapter 3 to investigate six BL Lac type blazars. We calculate the absorption of high energy photons due to photon pair production by Lorentz transforming the ambient synchrotron, accretion disc, BLR, dusty torus, NLR, CMB and starlight photon distributions into the plasma rest frame and integrating the optical depth along the jet. Our model fits very well to the simultaneous multiwavelength spectra of all these blazars across all wavelengths including radio observations. We find that five out of the six BL Lac spectra are fitted by relatively low power jets with low bulk Lorentz factors and smaller radius transition regions (where the jet first comes into equipartition, stops accelerating and is brightest in synchrotron and SSC emission) compared to the powerful Compton dominant blazars fitted in Chapter 4. These results are consistent with our predictions from Chapter 4 and the blazar sequence.

We find that one of the BL Lacs, J1751, requires a large jet power, bulk Lorentz factor and radius transition region. Furthermore, we find that in order to fit both the synchrotron and high energy emission of J1751 its inverse-Compton emission must be due to scattering of low redshift CMB photons in agreement with our prediction of Compton-dominant blazars at low redshift from Chapter 4. We find that four out of six of the BL Lacs have gamma-ray emission best fitted by SSC.

We have tested our predictions from Chapter 4: blazars with large jet powers have large bulk Lorentz factors and larger radius transition regions. We find empirical evidence for this scenario using the 13 fits to blazar spectra from this work and Chapters 3 and 4. We find a clear link between the jet power of a blazar and the radius of the transition region of the jet where the plasma first comes into equipartition and becomes synchrotron bright. This leads us to an understanding of the physical basis of the blazar sequence. BL Lacs with low jet powers have larger magnetic field strengths in the synchrotron bright transition region than high power FSRQs and so have higher peak frequency synchrotron and SSC emission. FSRQs have large bulk Lorentz factors and so scatter external CMB photons at large distances leading to their Compton-dominance and lower inverse-Compton peak frequency.

We can interpret this result in one of two obvious scenarios. In the first scenario we assume jets have a universal geometry which scales linearly with black hole mass and BL Lacs have lower black hole masses than FSRQs. This scenario is sensible if most blazars accrete at a similar Eddington fraction and this leads to a prediction of a linear relation between jet power and the transition region radius. The range of black hole masses we infer from fitting this model to the sample of blazars in this and the previous Chapter using the observed jet geometry of M87 coincides with the range of black hole masses found from large galaxy surveys ($10^7 - 2 \times 10^{10} M_\odot$). In the case of FSRQs with accretion disc spectra visible above the jet emission, the black hole mass found from fitting the accretion disc spectrum agrees with that inferred from our model fit if the transition region occurs at $10^5 R_s$ as in M87.

If we instead assume that BL Lacs and FSRQs have similar masses (as suggested by indirect measurements of black hole mass) we arrive at a second scenario: a dichotomy of accretion modes between FSRQs and BL Lacs. In this case we find that FSRQs are accreting at a higher Eddington rate than BL Lacs as has been suggested previously. In this scenario we can intepret the different bulk Lorentz factors and length of accelerating regions as being due to different mass loading from two accretion modes. If BL Lacs contain hot, thick, radiatively inefficient discs they can more efficiently pair produce from hard X-ray photons and entrain disc material close to the jet base. This could increase the mass loading of the jet and decrease its final bulk Lorentz factor and the length required to accelerate relative to FSRQs with radiatively efficient, thin discs and lighter mass loading.

We find that in order for the quiescent high energy emission region in Mkn421 to be transparent to the observed TeV photons, we require that the inverse-Compton emission is due to scattering external photons and is not due to SSC. The radius of the transition region in our fit, 3.8×10^{15}m, implies a central black hole mass $6.3 \times 10^8 M_\odot$, using a model with a jet geometry based on radio observations of the jet in M87 scaled linearly with black hole mass (Asada and Nakamura [2011]). In this case we find that the inverse-Compton emission is due to scattering of CMB photons. We also attempt to fit the spectrum of Mkn421 using a compact conical jet with a high bulk Lorentz factor of 50, decelerating rapidly over one hundred parsecs to a Lorentz factor of 3. We find that even with this high Lorentz factor SSC emission is absorbed by pair production and is not able to reproduce the observed spectrum. We find that in order to reproduce the correct Compton-dominance using SSC emission requires a large number density of synchrotron photons to scatter, which results in the absorption of TeV photons via pair-production.

Finally, we fit the non-simultaneous multiwavelength SEDs of the four recently discovered high power, high synchrotron peak (HSP) BL Lacs from Padovani et al. [2012]. We find that their high peak frequencies of emission are caused by their relatively high maximum electron energies ($40 - 100$GeV). The other jet properties of these blazars are typical of the higher power BL Lacs we fit to in this Chapter ($W_j \sim 10^{38}$W) and we find that their inverse-Compton emission is due to SSC. The transition region radii for these four blazars are consistent with our hypothesis of a correlation between radius and jet power. We find their bulk Lorentz factors and jet powers are significantly lower than the Compton-dominant FSRQs fitted in Chapter 4. We conclude that these blazars have properties typical of other high power BL Lacs and are therefore unlikely to be HSP FSRQs as has been suggested.

This is the first time a realistic, extended jet model has been used to fit to the spectra of a sample of BL Lac type blazars. We find these results very interesting and our model provides empirical evidence for a simple monoparametric unification of blazars depending on jet power, as suggested by the blazar sequence. In the next Chapter we will investigate whether our results hold for the blazar population as a whole.

Chapter 6

Understanding the physics behind the blazar population

This is the concluding Chapter of my work modelling blazars. In this Chapter I use the model developed in Chapters 2-5 to fit to the remaining 32 blazars with simultaneous multiwavelength spectra and redshifts available from the *Fermi* sample (Abdo et al. [2010a]). The model fits with unprecedented detail to all these blazars. I find strong empirical evidence for the predicted physical relation in Chapters 4 and 5; namely that the radius of the transition region and maximum bulk Lorentz factor increase with jet power. This is important since it provides an explanation for the basis of the blazar sequence.

I conclude that if black hole mass measurements can be believed, my results offer strong evidence for a scenario in which two accretion modes exist in blazars resulting in BL Lac and FSRQ type jets, analogous to the relationship between accretion mode and jet properties in X-ray binary systems. These sub-Eddington and Eddington accretion modes result in BL Lacs and FSRQs which have the expected properties of FRI and FRII jets observed close to the line of sight, as suggested by unification. These results are very exciting as they offer explanations and evidence for many long standing questions and hypotheses about blazars and AGN jets.

6.1 Introduction

It has recently been observed that the jet in M87 has a parabolic base out to 10^5 Schwarzschild radii becoming conical beyond this distance (Asada and Nakamura [2011]). This is consistent with state of the art numerical simulations which show the jet base starts magnetically dominated and accelerates in the parabolic region reaching a terminal bulk Lorentz factor at equipartition after which the jet becomes ballistic and conical (McKinney [2006], Komissarov et al. [2009], Tchekhovskoy et al. [2010] and McKinney et al. [2012]). In this Chapter we use a model for the emission of a realistic jet motivated by and consistent with these recent observations and simulations in order to test this emerging picture of jets and to try to determine their properties.

We use the realistic extended jet model for emission from Chapters 2-5 (based on Potter and Cotter [2012], Potter and Cotter [2013a], Potter and Cotter [2013b] and Potter and Cotter [2013c]) to fit to the remaining 32 blazars with simultaneous multiwavelength observations and redshifts from the *Fermi* sample (Abdo et al. [2010a]). This model is the first to be able to simultaneously match the observations of blazars across all frequencies, including radio data, by considering the extended large scale structure of the jet. In being able to match the radio observations of jets we are able to tightly constrain the radius of the jet at the transition region by fitting the break frequency above which the synchrotron emission becomes optically thin (which sensitively depends on the radius at which the jet first approaches equipartition). This is the first time a realistic extended jet model has been used to constrain the dynamical and structural properties of a large sample of blazars by fitting to their spectra. We include the fits to the remaining 32 SEDs not fitted in Chapter 5 and the fitted parameter values for all 38 blazars (plus the 4 quasi-simultaneous HSP BL Lacs from Padovani et al. [2012] fitted in Chapter 5) in Appendix A.

6.2 Results

We show the key results of fitting this model to spectra of the 38 blazars with simultaneous multiwavelength observations and the 4 HSP BL Lacs from Padovani et al. [2012] (fitted in Chapter 5) in Figure 6.1. We find an approximately linear relation between the total jet power and the radius where the jet transitions from parabolic to conical, stops accelerating and first comes into equipartition. The results also confirm that the blazar population can be divided into FSRQs with the highest power jets and BL Lacs with low power jets (Ghisellini and Tavecchio [2008] and Ghisellini et al. [2009a]).

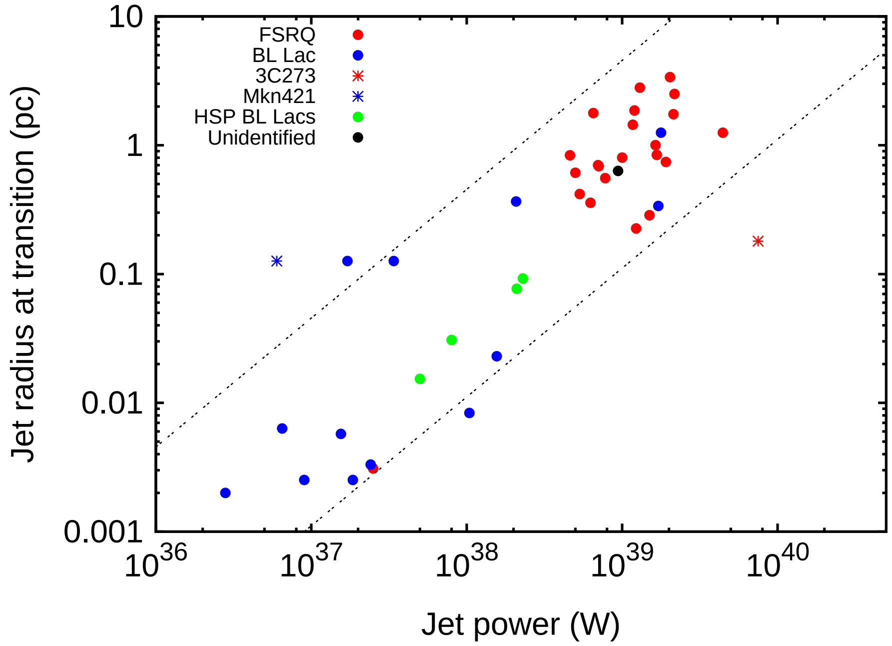

(a)

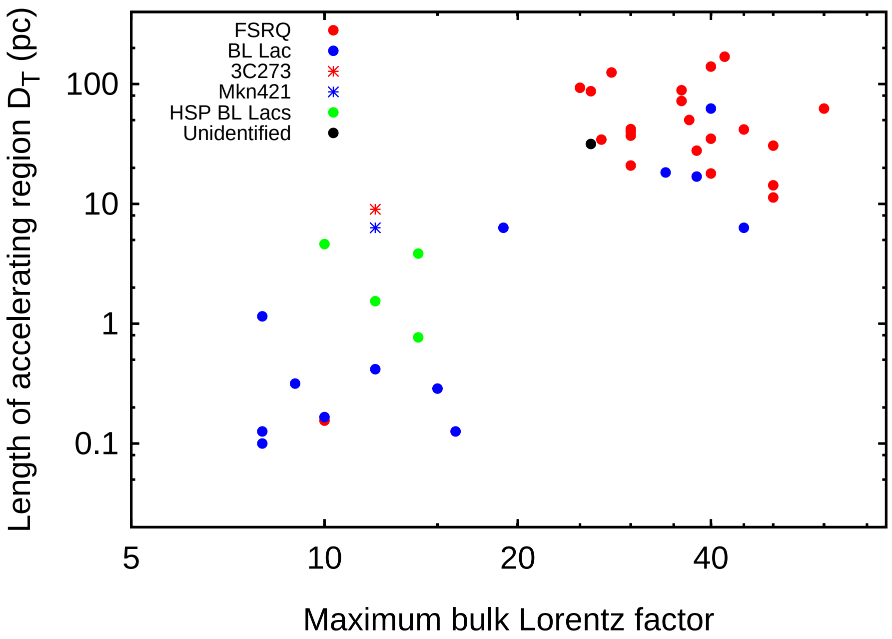

(b)

Figure 6.1: The results of fitting our model to all 38 blazars with simultaneous multiwavelength spectra and redshifts and the 4 quasi-simultaneous HSP BL Lac SEDs from Chapter 5. Figure a shows the distance of the jet transition region plotted against the jet power for all fits. We see a clear correlation between the jet power and radius of the transition region as suggested in our previous work. BL Lacs have systematically smaller radius transition regions than FSRQs, with an approximately linear correlation between the two as illustrated by the dashed lines. We have highlighted the two outliers to the relation, Markarian 421 and 3C273. We argue that these two blazars are atypical since Mkn421 is one of the closest known blazars and 3C273 is the one of the most powerful (and seems to be misaligned). Figure b shows the maximum bulk Lorentz factor plotted against the radius of the transition region. We see that the bulk Lorentz factor is systematically larger for FSRQs than BL Lacs and increases with the distance over which the jet accelerates as we expect.

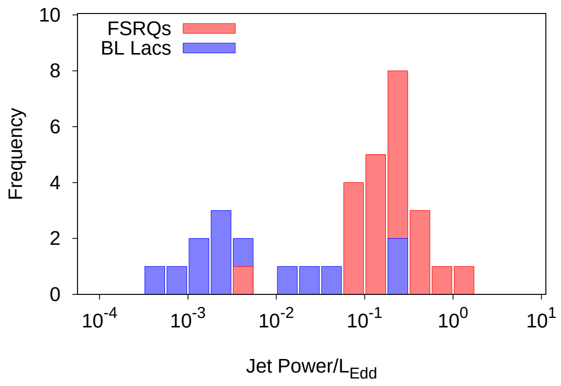

(a)

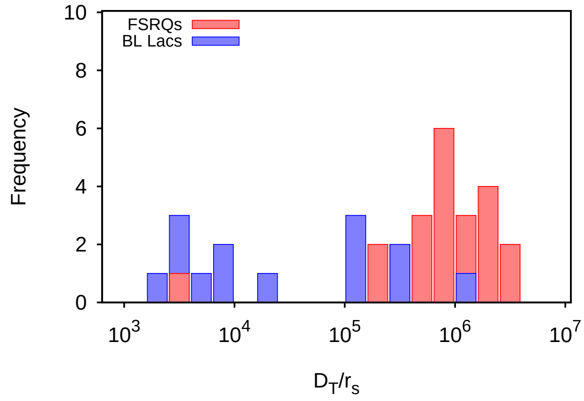

(b)

Figure 6.2: The distribution of fractional Eddington luminosity and the distance to the jet transition region under the assumption of a constant black hole mass of $5 \times 10^8 M_\odot$ for all 38 blazars with simultaneous observations. Figure a shows a clear dichotomy in the fractional Eddington luminosity between BL Lacs and FSRQs suggestive of two accretion modes. Figure b shows that the accelerating transition region extends out to larger distances in FSRQs than BL Lacs, this could be responsible for the different maximum bulk Lorentz factors shown in Figure 6.1b.

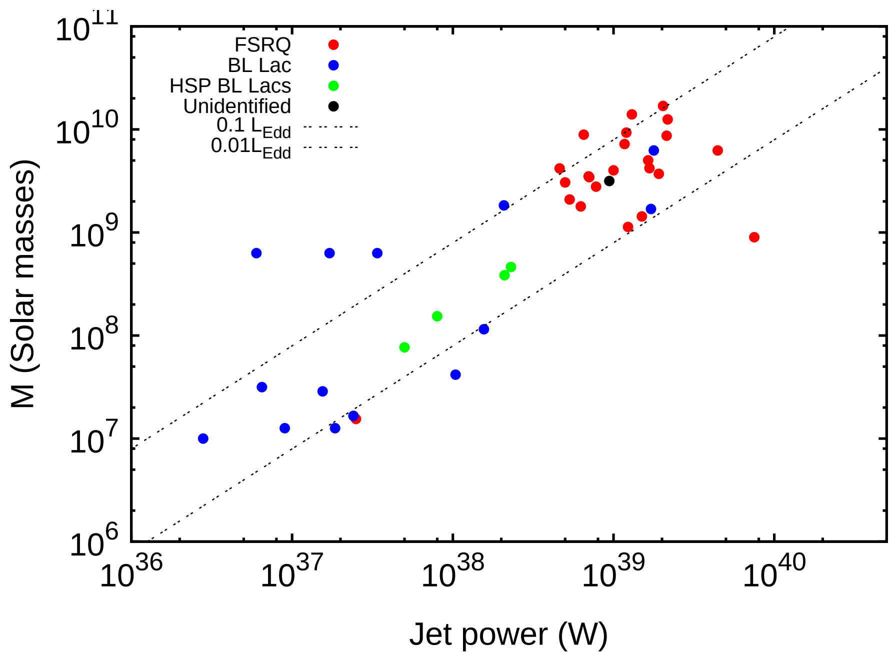

Figure 6.3: The inferred black hole mass of the fits plotted against jet power assuming the transition region occurs at a distance of $10^5 r_s$ as in M87. The range of black hole masses is compatible with that found from large galaxy surveys (10^7–$10^{10} M_\odot$). We naturally find a linear relation between jet power and the radius of the transition region if we assume all blazars are accreting at a similar Eddington fraction $0.01 - 0.1 L_{Edd}$.

We also find a clear correlation between the radius of the jet at the transition region and the maximum bulk Lorentz factor of the jet shown in Figure 6.1b. This is very significant for two reasons: firstly, it has long been thought from unification that FSRQ and BL Lac type blazars correspond to FRII and FRI type jets observed at small angles to the line of sight (Urry and Padovani [1995]) and secondly, from theoretical and numerical work, we expect jets with larger bulk Lorentz factors to accelerate over larger distances, with the precise form of the dependence giving us information about the geometry of the magnetic field lines in the accelerating region of the jet (Vlahakis and Königl [2003], Beskin and Nokhrina [2006] and Komissarov et al. [2009]). For the first time we see strong evidence confirming both these ideas from systematically studying the SEDs of a large sample of blazars.

We have fitted these blazar spectra by eye, however, we are confident of the results in Figure 6.1a, since they are supported by simple, physical arguments. We find an absence of low power blazars with large emitting regions and high power blazars with small emitting regions. This is to be expected because low power blazars with large emitting regions would have very low magnetic field strengths at the transition region. Their peak synchrotron and SSC frequencies would be very low and their SSC emission would be very weak, making them undetectable with current γ-ray observations. Low power blazars are observed to have high peak frequencies of emission, with no synchrotron break visible at low frequencies. This is not compatible with low power blazars with large transition regions. High power blazars with small radius transition regions would produce spectra with synchrotron break frequencies occurring at too high frequencies (see Figure 4.1b). In addition SSC emission would dominate their γ-ray emission and this would not allow them to become Compton-dominant due to the self-limiting nature of SSC emission. For these reasons we are confident in the results shown in Figure 6.1.

We find that we are only able to fit the quiescent gamma ray emission from FSRQs if the jets scatter CMB photons at large distances along the jets and the jets remain relativistic until kpc scales (as in FRII jets, Blandford and Rees [1974]). The inverse-Compton emission of most BL Lacs requires a dominant SSC component to match their spectra and we find that they do not have such large bulk Lorentz factors as FSRQs. In addition, we notice that the radio spectra of FSRQs in the sample are systematically steeper than the flat radio spectra of

BL Lacs. We find that this requires that FSRQ jets become more particle dominated at large distances past the transition region while BL Lac jets remain close to equipartition along the jet. This distinction could be responsible for the morphological differences between FRII and FRI jets (where a magnetised jet can be susceptible to additional MHD instabilities such as the kink instability Mizuno et al. [2012]).

We expect most FSRQs to be associated with FRII jets and most BL Lacs to be associated with FRI type jets because it is known that the jet power is a strong indicator of the jet morphology (Fanaroff and Riley [1974]). It is thought that FRII jets need to be sufficiently powerful not to be decelerated by their environment and become subsonic on pc scales. This has been used to predict the FRI/FRII divide in power (Bicknell [1995]). We do not suggest that the blazar classification, based on line widths, is the direct cause of the jet morphology (since line widths are clearly an indirect measurement of the accretion process) but that it provides a good indicator of the jet power and thereby the FR classification of the jet. Figure 6.2a shows that overall the blazar classification corresponds to high and low power jets, however, there is clearly an overlapping region where the blazar classification loses its descriminating power. This is analogous to evidence that high and low excitation radio galaxies (HERGs and LERGs) are related to the accretion mode, with HERGs having high Eddington accretion rates and radiatively efficient thin discs and LERGs corresponding to a sub-Eddington radiatively inefficient mode (Hardcastle et al. [2009]). There is also evidence for the broad association of HERGs with FRII type jets and LERGs with FRI jets, however, there also exist a small proportion of FRII LERGs and FRI LERGs (Hardcastle et al. [2007]). It seems likely that choosing a particular observational classification for AGN/blazars which broadly divides the population by accretion power leads to an association of the classification with FR type. It is important to remember, however, that the observational classification is not the primary, causal variable but could still be a good indirect indicator of the jet power and environment. This leads to regions in which the relation between observational and FR classification breaks down. We find that our results provide strong evidence for the association of most FSRQs with FRII jets and most BL Lacs with FRI jets. We have also found evidence for the distinct physical properties of FRI and FRII jets which could lead to their morphological definitions.

Besides constraining the dependence of the jet structure and dynamics on blazar parameters in unprecedented detail, we can also use our model to understand the physics behind the blazar sequence (Fossati et al. [1998]) for the first time. We find a linear relation between the jet power and the radius of the transition region which dominates the optically thin synchrotron emission in our jet. The transition region dominates the optically thin synchrotron emission because this is the point at which the plasma first comes into equipartition (a plasma with a fixed total energy radiates synchrotron power most efficiently close to equipartition) and has its maximum Lorentz factor. Low power blazars have smaller radius transition regions than high power blazars and since $B^2 \propto W_j/(R^2\gamma_{\rm bulk}^2)$ the magnetic field strength is larger in BL Lacs compared to FSRQs. This results naturally in the anticorrelation between peak synchrotron frequency and jet power seen in the blazar sequence because the peak synchrotron frequency depends linearly on the magnetic field strength, which is larger in BL Lacs than FSRQs.

Furthermore, we find that in low power blazars with compact transition regions and high magnetic field strengths the number density of synchrotron photons is large and so the inverse-Compton emission is due to scattering high frequency SSC photons. The Compton-catastrophe prevents SSC blazars from becoming significantly Compton-dominant as required by many FSRQs. Meanwhile high power blazars with higher bulk Lorentz factors and larger transition regions with lower magnetic field strengths emit less power through synchrotron emission and so the number density of synchrotron photons is too low to reproduce their gamma-ray emission via SSC. The large bulk Lorentz factor allows them to scatter low energy CMB photons at large distances along the jet resulting in their low inverse-Compton peak frequencies and Compton dominance. This coherent picture of a changing transition region radius and bulk Lorentz factor allows us to understand the structural and dynamic changes in jets which produce the blazar sequence as suggested in Chapters 4 and 5.

We can go one step further and motivate this emerging jet paradigm by using the results of black hole mass estimates. Shaw et al. [2013] found that BL Lacs have black hole masses with a range $10^{8.5} - 10^9 M_\odot$ while FSRQs had a similar range $10^8 - 10^9 M_\odot$ with slightly lower masses on average (Shaw et al. [2012]). While individual mass estimates are quite uncertain these indirect mass estimates indicate that BL Lac and FSRQ masses are similar with BL Lacs being slightly larger (though less well constrained due to a lack of strong emission lines).

Taking into account the similar black hole masses of FSRQs and BL Lacs and, for simplicity, assuming a constant fiducial mass of $5 \times 10^8 M_{\odot}$ we can plot the distribution of fractional Eddington luminosity as a function of the jet power of a blazar and also the distance at which the transition region occurs in their jets. It is very interesting to find that the BL Lacs and FSRQs naturally split into the bimodal distribution in these quantities shown in Figure 6.2. BL Lacs have low Eddington accretion rates $\sim 10^{-3} L_{Edd}$ while FSRQs have larger Eddington accretion rates $0.1 - 1 L_{Edd}$. This is exactly the behaviour suggested by X-ray binary jets in which accreting black holes produce low power, mildly relativistic jets in a radiatively inefficient sub Eddington state, while the transition from this low state to a thin radiatively efficient disc with a high accretion rate temporarily produces a highly relativistic jet (Fender et al. [2004]).

We propose that our results offer the first solid evidence for this scenario in blazars by fitting a realistic physically rigorous model for jet emission to accurately estimate the jet power by fitting to radio observations. We find that FSRQs have high accretion rates around the Eddington luminosity, producing fast jets which accelerate over large distances and become particle dominated at large distances whilst maintaining their bulk Lorentz factors (characteristic of FRII jets). BL Lacs represent the X-ray binary low/hard state with a radiatively inefficient disc accreting at a low Eddington fraction and producing slower jets which accelerate over smaller distances. They remain magnetised and close to equipartition at large distances, breaking up due to instabilities characteristic of FRI type jets. The different bulk Lorentz factors are likely to be related to the different accretion modes in the two cases, with a hot, thick, radiatively inefficient accretion disc in BL Lacs entraining more disc material at the base of the jet and resulting in a larger mass loading and lower final bulk Lorentz factor than in FSRQs whose thin discs are radiatively efficient.

Alternatively, if we ignore the results of indirect black hole mass estimates in blazars due to their unreliability, we must consider a different scenario. If all blazar jets scale only with black hole mass (as assumed in MHD simulations and theoretical work) we can infer the black hole mass by constraining the transition region to occur at $10^5 r_s$ in all jets (as in M87), shown in Figure 6.3. In this case we find black hole masses in the range $10^7 - 10^{10} M_{\odot}$ consistent with galaxy surveys. We also find that BL Lacs have smaller black hole masses than FSRQs and the linear relation between jet power and transition region radius means that all these blazars have approximately the same Eddington accretion fraction between $0.01 - 0.1L_{Edd}$. The scenario of a universal jet structure which scales linearly with black hole mass is appealing for its simplicity and is assumed in current state of the art GRMHD jet simulations (for example Komissarov et al. [2009], Tchekhovskoy et al. [2010] and McKinney et al. [2012]). There are two problems with this scenario however: the first is that this trend is not consistent with indirect measurements of black hole masses and the second is that this scenario doesn't explain the difference we find in bulk Lorentz factors between BL Lacs and FSRQs. Also, this does not tie in with the connection between accretion mode state and jet production from X-ray binaries or the expected correspondence of FRI and FRII jets to BL Lacs and FSRQs as we expect from unification. For these reasons we currently favour a bimodal accretion mode between BL Lacs and FSRQs linked to the FRI/FRII dichotomy. Obviously, the most direct way in which to settle this would be through a comparison to reliable black hole mass measurements for blazars.

6.3 Summary

In this Chapter we have shown that our jet model with a magnetically dominated accelerating parabolic base transitioning to a slowly decelerating conical jet is able to fit to observations of blazar jets with unprecedented detail across all frequencies. This offers support for the emerging picture of jets motivated by observations and simulations. We find that in fitting to a large sample of blazar spectra we are able to constrain dynamic and structural properties of blazar jets. Our two main results are: the discovery of a linear correlation between the radius of the transition region of the jet and the jet power; a relation between the maximum bulk Lorentz factor and the distance over which the jet accelerates before reaching equipartition. These results allow us to understand the physical origin of the blazar sequence for the first time but also offer evidence for an accretion mode dichotomy in AGN analogous to that observed in X-ray binary systems and consistent with a correspondence between BL Lac and FSRQs, FRI and FRII jet properties and the mode of accretion.

6.4 Appendix A

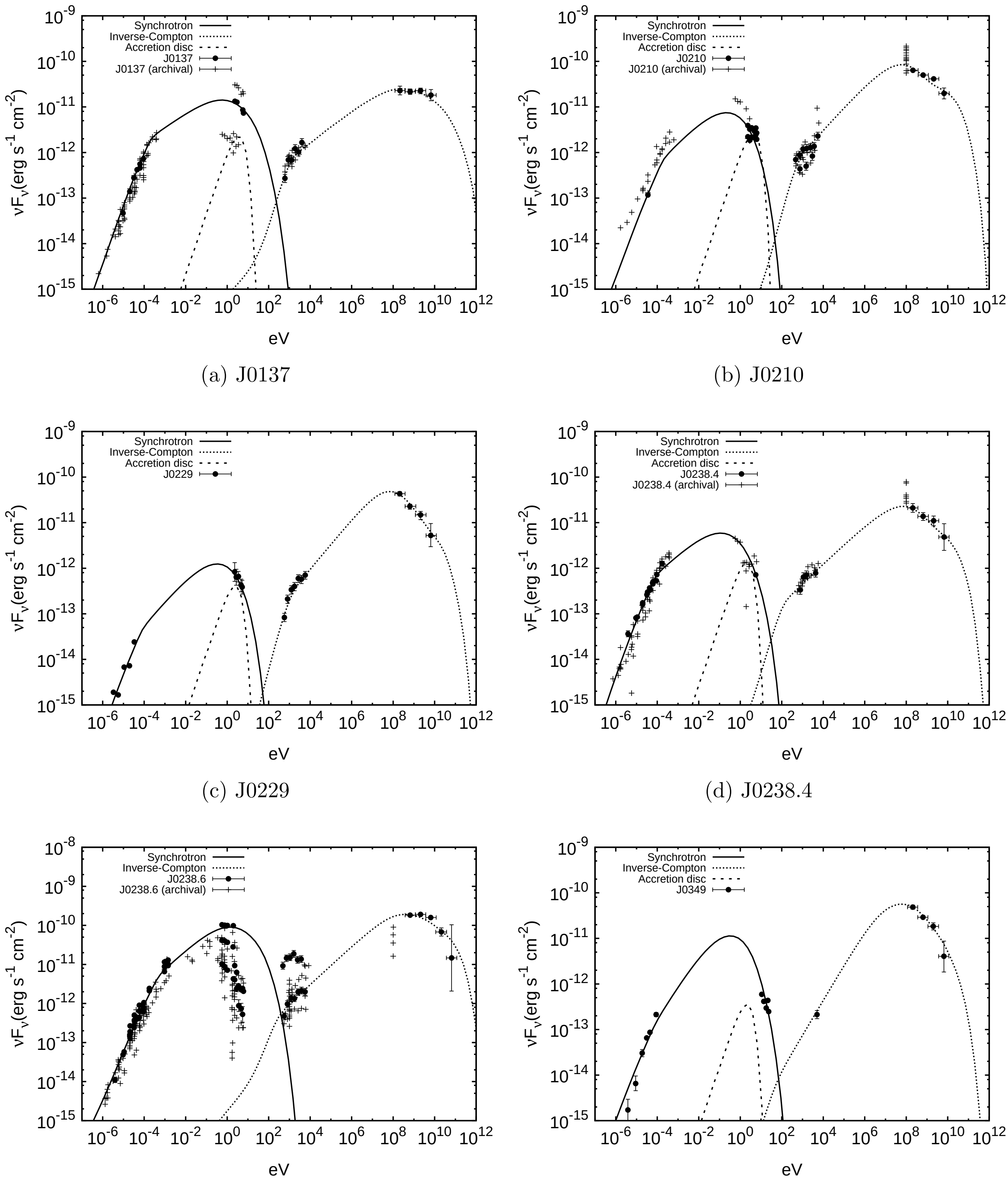

(a) J0137

(b) J0210

(c) J0229

(d) J0238.4

(e) J0238.6

(f) J0349

Figure 6.4: The fits to the SEDs of the remaining 32 blazars with simultaneous multiwavelength observations and redshifts from Abdo et al. [2010a], not fitted in Chapter 5. The model is able to fit very well to all of the spectra including radio observations.

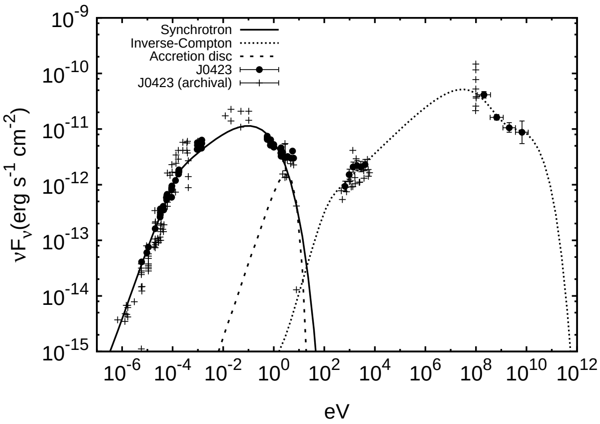

(a) J0423

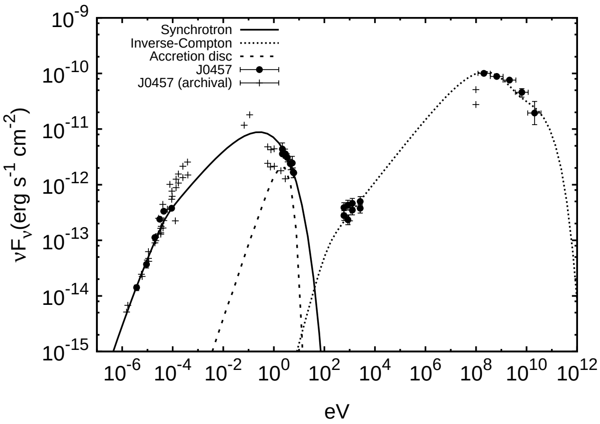

(b) J0457

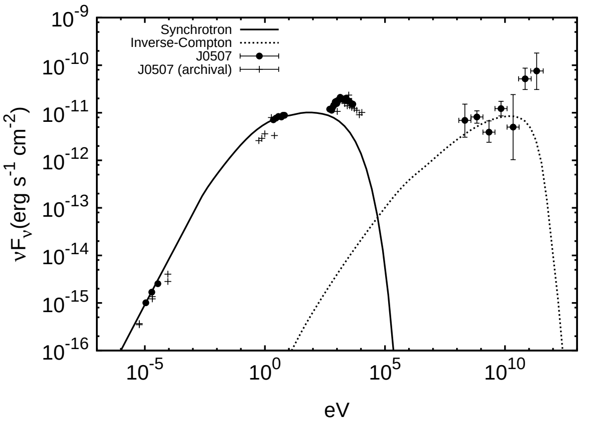

(c) J0507

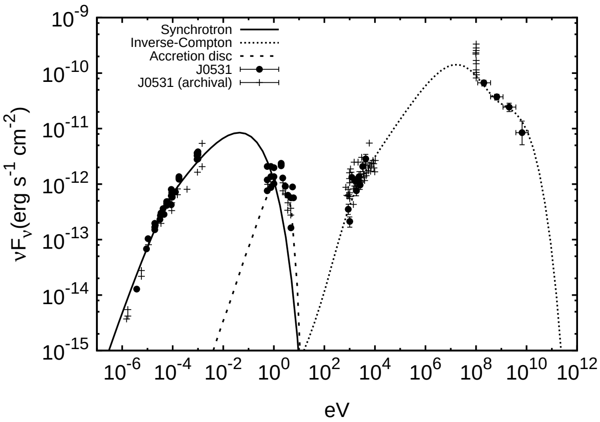

(d) J0531

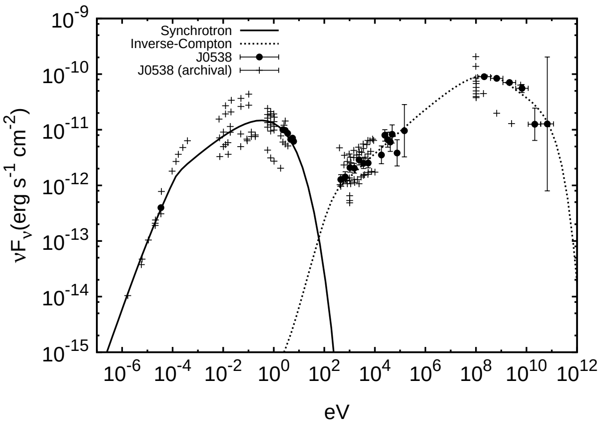

(e) J0538

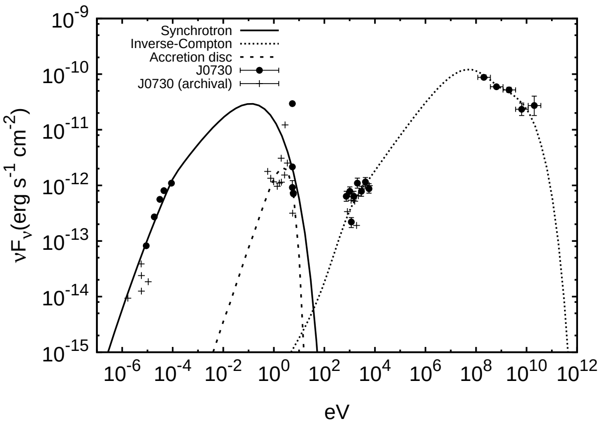

(f) J0730

Figure 6.5

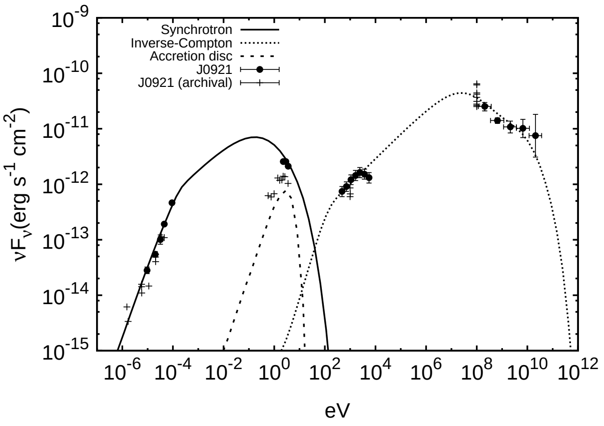

(a) J0921

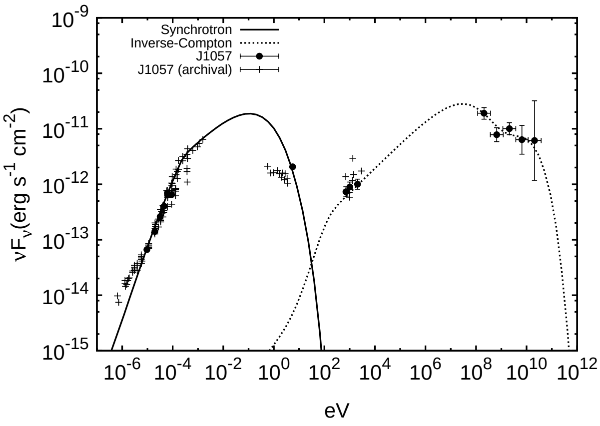

(b) J1057

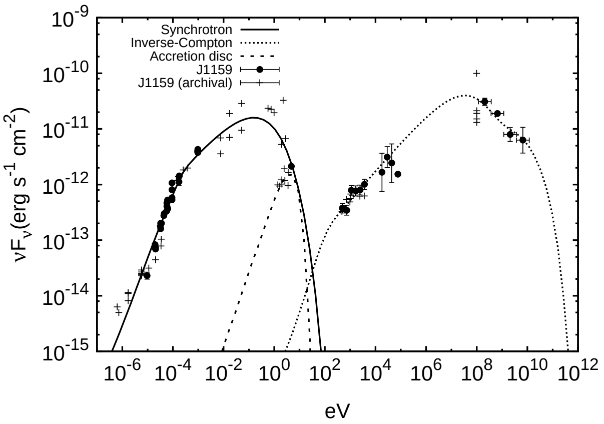

(c) J1159

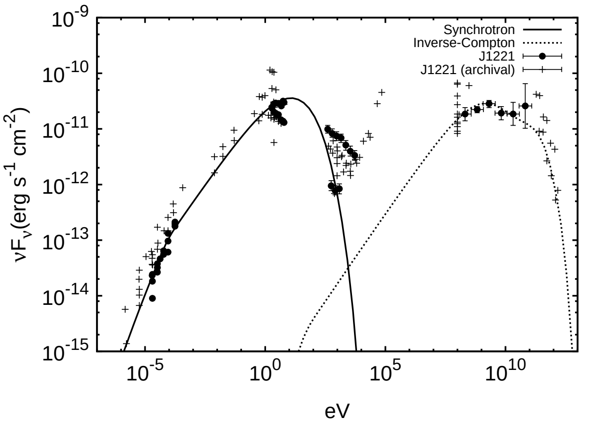

(d) J1221

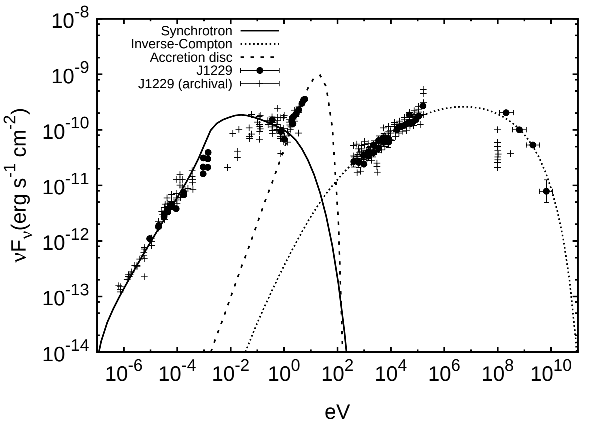

(e) J1229

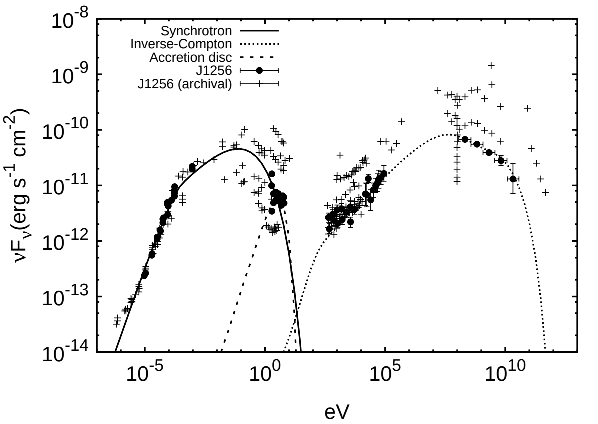

(f) J1256

Figure 6.6

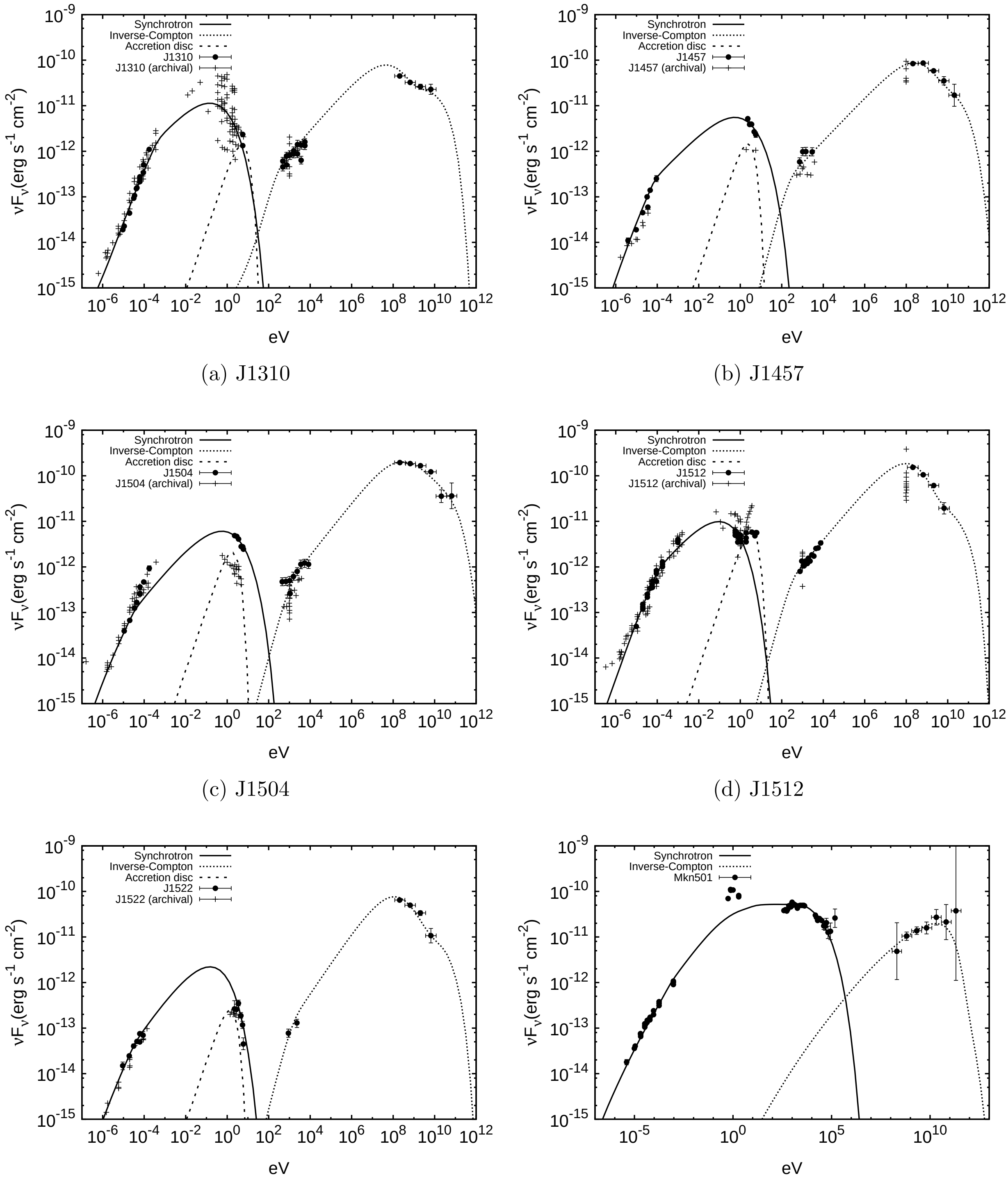

(a) J1310

(b) J1457

(c) J1504

(d) J1512

(e) J1522

(f) Mkn501

Figure 6.7

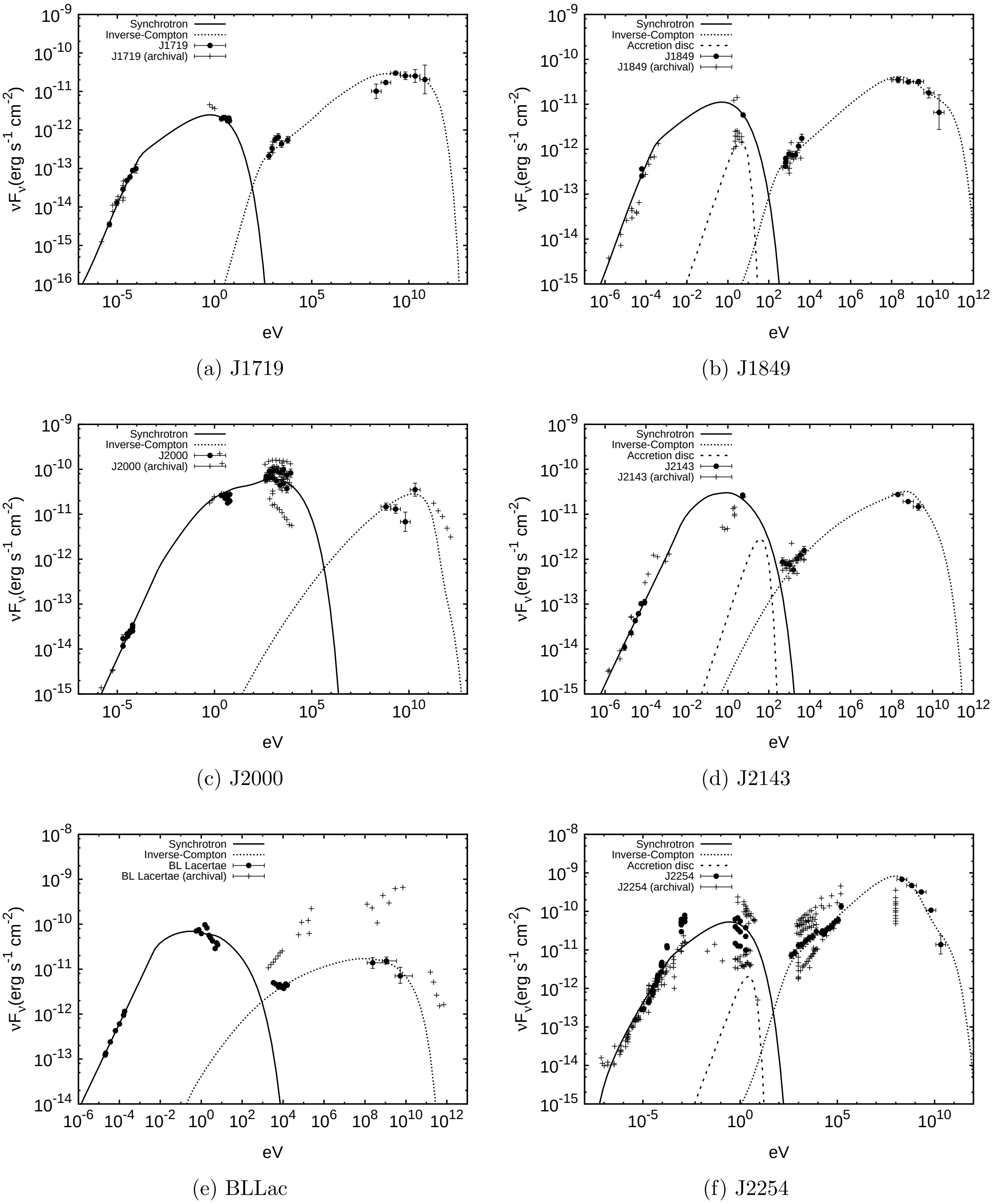

(a) J1719

(b) J1849

(c) J2000

(d) J2143

(e) BLLac

(f) J2254

Figure 6.8

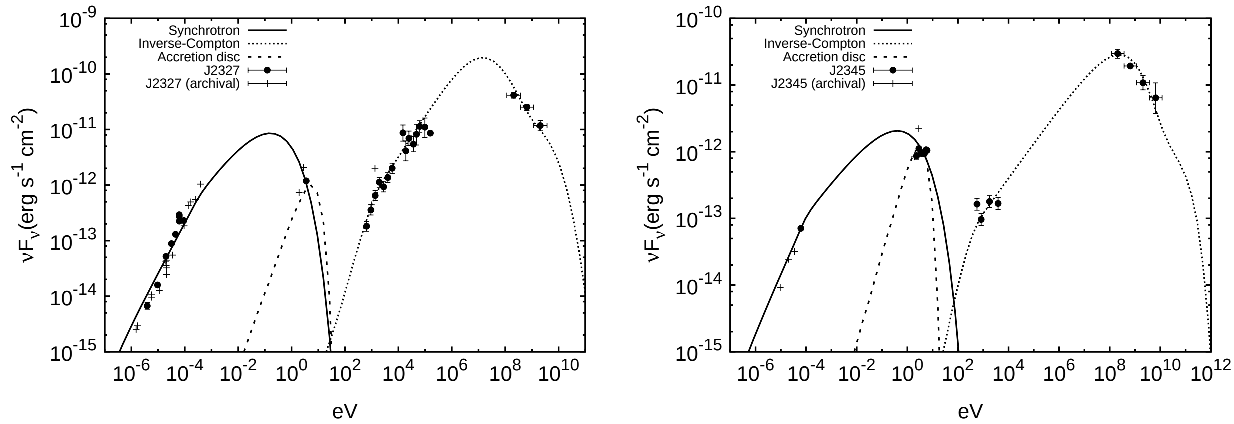

(a) J2327

(b) J2345

Figure 6.9

Blazar	W_j(W)	L(m)	$E_{\max}$(MeV)	α	θ_{observe}	$\gamma_{\max}$	$\gamma_{\min}$	L_{acc}(W)	R_T(m)	B_T(T)	$M(M_\odot)$
J0035	5.0×10^{37}	10^{20}	40.6	1.3	1^0	14	10	1.67×10^{38}	4.57×10^{14}	5.91×10^{-5}	7.69×10^{7}
J0137	7.06×10^{38}	1×10^{21}	22.8	2.35	1^0	27	16	2.5×10^{38}	2.04×10^{16}	2.58×10^{6}	3.44×10^{9}
J0210	7.78×10^{38}	2×10^{21}	5.11	2.01	1^0	38	20	4.27×10^{38}	1.65×10^{16}	2.38×10^{-6}	2.78×10^{9}
J0222	1.04×10^{38}	5×10^{20}	16.2	1.6	1^0	12	8	1.67×10^{38}	2.48×10^{14}	0.000184	4.17×10^{7}
J0229	7×10^{38}	1×10^{21}	8.1	1.9	1^0	40	30	4.17×10^{38}	2.08×10^{16}	1.7×10^{-6}	3.5×10^{9}
J0238.4	1.2×10^{39}	1×10^{21}	8.1	2.15	1.2^0	25	15	3.42×10^{38}	5.52×10^{16}	1.34×10^{-6}	9.29×10^{9}
J0238.6	1.71×10^{39}	1×10^{21}	14.4	2.01	1^0	38	25	5.7×10^{38}	1.01×10^{16}	5.78×10^{-6}	1.69×10^{9}
J0349	1.67×10^{39}	1×10^{21}	6.74	1.45	1^0	30	8	8.33×10^{38}	2.5×10^{16}	2.91×10^{-6}	4.21×10^{9}
J0423	1×10^{39}	2×10^{21}	4.06	2.11	1^0	30	18	1.99×10^{38}	2.38×10^{16}	2.37×10^{-6}	4.01×10^{9}
J0457	8.5×10^{38}	1×10^{21}	8.1	1.85	1^0	33	20	3.33×10^{38}	5.94×10^{16}	7.95×10^{-7}	1×10^{10}
J0507	1.85×10^{37}	2×10^{21}	32.2	1.5	2^0	16	10	8.55×10^{37}	7.46×10^{13}	0.000193	1.26×10^{7}
J0531	2.17×10^{39}	2×10^{21}	2.87	1.6	1^0	28	13	1.39×10^{39}	7.43×10^{16}	1.2×10^{-6}	1.25×10^{10}
J0537	8.0×10^{37}	1×10^{21}	102	1.75	1.5^0	12	6	1.25×10^{35}	9.14×10^{14}	4.36×10^{-5}	1.54×10^{8}
J0538	1.78×10^{39}	1×10^{21}	10.2	2.2	1^0	40	22	6.84×10^{38}	3.71×10^{16}	1.52×10^{-6}	6.25×10^{9}
J0630	2.1×10^{38}	1×10^{20}	81	1.3	1	14	10	1.25×10^{35}	2.28×10^{15}	2.42×10^{-5}	3.85×10^{8}
J0730	2.14×10^{39}	1×10^{21}	4.55	1.7	1^0	26	15	1.08×10^{39}	5.17×10^{16}	1.84×10^{-6}	8.7×10^{9}
J0855	1.56×10^{38}	5×10^{20}	5.11	1.63	1^0	8	6	8.33×10^{36}	6.85×10^{14}	0.000122	1.15×10^{8}
J0921	1.91×10^{39}	1×10^{21}	8.1	2.1	1^0	30	18	8.55×10^{38}	2.2×10^{16}	3.53×10^{-6}	3.71×10^{9}
J1015	2.41×10^{37}	1×10^{21}	32.2	1.5	3.5^0	10	3	2.5×10^{37}	9.88×10^{13}	0.000266	1.66×10^{7}
J1057	9.41×10^{38}	1×10^{21}	4.06	2.1	1^0	26	20	5.7×10^{37}	1.88×10^{16}	3.36×10^{-6}	3.16×10^{9}
J1159	5.33×10^{38}	2×10^{21}	3.45	1.95	1^0	30	15	1.14×10^{38}	1.24×10^{16}	3.31×10^{-6}	2.09×10^{9}
J1221	1.71×10^{37}	1×10^{21}	32.2	1.75	2^0	19	10	1.14×10^{37}	3.75×10^{15}	3.11×10^{-6}	6.31×10^{8}
J1229	7.5×10^{39}	1×10^{21}	3.22	1.2	8.5^0	12	8	1.97×10^{39}	5.35×10^{15}	7.22×10^{-5}	9×10^{8}
J1256	1.64×10^{39}	1×10^{21}	3.22	2.1	1^0	37	18	1.99×10^{38}	2.98×10^{16}	1.97×10^{-6}	5.01×10^{9}

Table 6.1: The values of the physical parameters used in the fits from this Chapter (shown in Figures 6.4–6.9) and Chapter 5.

Blazar	W_j(W)	L(m)	$E_{\max}$(MeV)	α	θ_{observe}	$\gamma_{\max}$	$\gamma_{\min}$	L_{acc}(W)	R_T(m)	B_T(T)	$M(M_\odot)$
J1310	1.5×10^{39}	1×10^{21}	2.56	1.95	1^0	50	30	2.28×10^{38}	8.47×10^{15}	4.89×10^{-6}	1.43×10^{9}
J1312	2.3×10^{38}	1×10^{21}	81	1.6	1.2^0	10	6	2.5×10^{34}	2.74×10^{15}	2.96×10^{-5}	4.62×10^{8}
J1457	1.17×10^{39}	1×10^{21}	14.4	2.05	1^0	36	25	5.7×10^{38}	4.29×10^{16}	1.18×10^{-6}	7.22×10^{9}
J1504	2.04×10^{39}	1×10^{21}	17.3	1.85	1^0	42	16	1.5×10^{39}	1×10^{17}	5.72×10^{-7}	1.69×10^{10}
J1512	4.62×10^{38}	2×10^{21}	3.22	1.9	1^0	45	35	7.69×10^{37}	2.48×10^{16}	1.03×10^{-6}	4.18×10^{9}
J1522	6.52×10^{38}	1×10^{21}	5.73	1.65	1^0	36	18	1.08×10^{38}	5.28×10^{16}	7.18×10^{-7}	8.89×10^{9}
J1719	3.39×10^{37}	1×10^{21}	8.1	2.2	1^0	45	25	1.42×10^{36}	3.75×10^{15}	1.85×10^{-6}	6.31×10^{8}
J1751	2.08×10^{38}	2×10^{21}	4.06	1.98	1^0	34	18	3.33×10^{37}	1.09×10^{16}	2.08×10^{-6}	1.83×10^{9}
J1849	6.25×10^{38}	1×10^{21}	8.1	2.2	1^0	40	25	8.55×10^{37}	1.07×10^{16}	3.13×10^{-6}	1.79×10^{9}
J2000	2.8×10^{36}	1×10^{21}	128	1.6	4^0	8	4	1.14×10^{37}	5.94×10^{13}	0.000188	1×10^{7}
J2143	2.5×10^{37}	5×10^{20}	3.08	1.45	3^0	10	6	1.14×10^{37}	9.19×10^{13}	0.000291	1.55×10^{7}
J2158	1.55×10^{37}	1×10^{20}	51.1	1.7	2^0	15	7	2.5×10^{37}	1.71×10^{14}	8.2×10^{-5}	2.87×10^{7}
J2254	4.44×10^{39}	3×10^{21}	6.43	2.05	0.8^0	60	35	2.28×10^{38}	3.71×10^{16}	1.6×10^{-6}	6.25×10^{9}
J2327	1.23×10^{39}	3×10^{21}	1.81	1.5	0.8^0	50	32	7.12×10^{38}	6.73×10^{15}	5.58×10^{-6}	1.13×10^{9}
J2345	5×10^{38}	2×10^{21}	8.1	1.95	1.3^0	50	35	5.7×10^{37}	1.82×10^{16}	1.3×10^{-6}	3.06×10^{9}
Mkn421	6×10^{36}	3×10^{20}	338	1.55	3^0	12	9	2.5×10^{36}	3.75×10^{15}	2.91×10^{-6}	6.31×10^{8}
Mkn501	6.5×10^{36}	1×10^{20}	228	1.68	6.5^0	9	2	8.55×10^{36}	1.88×10^{14}	8.06×10^{-5}	3.16×10^{7}
BL Lac	9×10^{36}	5×10^{20}	8.1	1.95	3^0	8	5	8.33×10^{36}	7.48×10^{13}	0.000268	1.26×10^{7}

Chapter 7

An accretion disc instability induced by a variable α - an explanation for X-ray binary state transitions

In this Chapter I investigate the effect of a variable α parameter in thin accretion discs as suggested by MHD simulations. Using the standard thin disc formalism I calculate the conditions for stability of the accretion disc. I find that if α has a sufficiently sensitive dependence on the magnetic Prandtl number, this results in an instability in the accretion disc analogous to that in dwarf novae. I calculate the instability criteria and investigate the global behaviour of the instability using a time-dependent thin disc simulation. I find that the instability induces a limit cycle in α in the inner regions of the disc. The instability results in an unsustainable increase in the accretion rate and temperature of the inner section of the disc. The inner region undergoes cyclic flares as the unstable region propagates outwards and drains mass from the inner disc, entering a quiescent stage before flaring again. I calculate the spectrum of the disc in the different states and find it is able to explain observations of flaring in X-ray binary systems, thereby offering a first physical explanation for a long standing problem.

7.1 Introduction

Accretion discs are noteworthy for their remarkable variability. Cataclysmic variables, in particular dwarf novae (DN), are one of the most intensively studied variable disc systems (e.g.

Frank et al. [2002]). These are generally analysed using the so-called α-formalism, in which the turbulent stress is assumed to be linearly proportional to the pressure (on dimensional grounds), the proportionality constant being denoted as α. Within the α-formalism (and somewhat more generally, e.g. Balbus and Papaloizou [1999]), the combination of mass and angular momentum conservation leads to a diffusion equation, the characteristic timescale of which is often referred to as the 'viscous time'. The viscous time is a measure of the time for a fluid element to drift radially inward across a characteristic disc radius, and is generally the longest time scale associated with the accretion process. It is then convenient to assume that the more rapid heating and cooling processes always maintain an effective thermal equilibrium while the disc itself slowly evolves.

In α disc theory, an infinitesimal surface density perturbation satisfies its own diffusion equation. Under conditions in which the diffusion coefficent for this perturbation is negative, this leads to dynamical instability. Applied to classical DN theory, negative diffusion occurs only at temperatures at which hydrogen is thermally ionized (and the form of the radiative opacity correspondingly complex). The ensuing *nonlinear* behaviour corresponds to a limit cycle about the unstable equilibrium, which is identified with the repeated outbursts characteristic of DN.

CV systems are not the only binary accretors to show variability. An equally well-known class of objects is X-ray transients (Remillard and McClintock [2006]). The evolution of these sources is quite complex, and associated with higher temperatures *not* characteristic of hydrogen ionisation. Indeed, in the regime of interest, the opacity should be well-described by a simple Kramers' law in the outer part of the disc and by electron scattering in the inner regions (Frank et al. [2002]). Another mechanism must be at work.

The observed changes in the radiative states of X-ray transients strongly suggest that the inner region of a Shakura and Sunyaev [1973] α disc is severely disrupted when a transition from the thin disc state occurs. The difficulty is that there seems to be no obvious reason why a viable, stable, classical α disc should suddenly and spontaneously break down. Two suggestions that have been studied are i.) that evaporation by a (disk-fed) tenuous corona may preferentially remove the inner disc (Meyer et al. [2000]), ii.) that the existence of another type of accretion solution, hot and diffuse, within a characteristic transition radius somehow induces the disk to make the transition (Narayan and Yi [1995]).

In this Chapter we revisit the problem of X-ray transients within the framework of α disk theory, with an eye toward understanding X-ray transients, incorporating a particularly important finding of MHD turbulence theory. Within the classical formalism, the α parameter is regarded as a simple mathematical constant. But its true behaviour is obviously more complex than this, as can be seen by considering the magnetic response of a cool, resistive gas versus a hot, fully-ionized plasma. The idea that the ratio of the (microscopic) viscosity to resistivity, known as the magnetic Prandtl number $\mathrm{P_m}$, may influence the saturated value of the stress tensor for MHD turbulence (Balbus and Hawley [1998]) appears to be true, at least in the regimes accessible to numerical simulation (Lesur and Longaretti [2007], Fromang et al. [2007], Simon and Hawley [2009], Longaretti and Lesur [2010] and Simon et al. [2011]). When $\mathrm{P_m}$ is near unity, the radial-azimuthal component of the stress increases monotonically with this number. Turbulent dynamos, in particular, behave very differently depending upon whether $\mathrm{P_m}$ is greater or less than one (Schekochihin et al. [2004]). Large Pm dynamos are easily excited in driven turbulent simulations. Small Pm dynamos are much more difficult to excite, show lower rms levels of fluctuations, and much less spatial coherence. It would be very surprising indeed if MHD turbulent discs were completely indifferent to all this, but this aspect of disc theory is widely ignored.

In liquid metals and stellar interiors, Pm $\ll 1$. In X-ray discs, however, it is likely that $\mathrm{P_m} \ll 1$ and $\mathrm{P_m} \gg 1$ regions both are present (Balbus and Henri [2008]). The $\mathrm{P_m} = 1$ transition radius typically occurs at 50–100 Schwarzschild radii. CV systems, associated with white dwarfs, have no such transition radius, and do not exhibit the dramatic changes in radiative states seen in X-ray transients. We are led, therefore, to consider the behaviour of accretion discs for which the scaled stress (i.e. α) is not a mere constant, but is a dynamic variable in its own right whose value depends upon Pm.

The instability criteria for a thin disc with a variable α depending on the magnetic Prandtl number has been investigated previously by Takahashi and Masada [2011]. They calculated the mathematical conditions for a density perturbation to become unstable in a gas or radiation pressure dominated disc with either a Kramers' opacity or electron scattering opacity. In this Chapter we will focus on understanding the physical mechanism behind this instability and investigate its time-dependent global behaviour, specifically, in relation to the observed flaring behaviour of X-ray binary systems.

7.2 Analysis

7.2.1 Thin disc equations

We use the standard thin disc alpha formalism (Frank et al. [2002]). These equations are based on the assumption that the disc is cool (sound speed much less than rotation speed; in this sense thin), and in thermal and dynamical equilibrium. The gas is thus on nearly circular orbits, and the rotational energy is locally dissipated as heat before being efficiently radiated. Another important assumption of this model is that the dissipation is localized close to the midplane so that the vertical flux of radiation is nearly constant with height above the dissipation layer; the dynamics could be very different if the dissipation is well above the midplane. For ease of reference and to establish notation we review the fundamental equations.

7.2.1.1 Coordinates and dynamics

We use a standard R, ϕ, z cylindrical coordinate system for the disc, where R is the distance from the rotation axis, ϕ the azimuthal angle, and z the vertical coordinate. The gas moves in circular orbits about a central mass M. The Keplerian angular velocity Ω is a function of R only and given by

$$\Omega^2(R) = \frac{GM}{R^3}, \tag{7.1}$$

where G is the usual gravitational constant. The velocity vector is $\boldsymbol{v}$ with components v_R, v_ϕ, v_z. Fluctuations from Keplerian flow will be denoted by δv_R, etc.

The gas pressure and mass density are denoted as P and ρ respectively. They are related by the usual ideal gas equation of state

$$P = \rho c_S^2 \equiv \frac{\rho k T}{m}, \tag{7.2}$$

where c_S is the isothermal sound speed and m is the mean mass per particle. The magnetic field, which we use here only in formal, place-holding sense, is denoted as $\boldsymbol{B}$. The magnetic energy density is much less than the thermal energy density and an order of magnitude yet smaller than the rotational energy density. The Alfvén velocity is

$$\boldsymbol{v_A} \equiv \frac{\boldsymbol{B}}{\sqrt{\mu_0 \rho}}, \tag{7.3}$$

where μ_0 is the vacuum permittivity.

The disc is presumed to be turbulent due to the magnetorotational instability (hereafter MRI, Balbus and Hawley [1998]), and the dominant $R\phi$ component of the turbulent stress tensor is $T_{R\phi}$. It is formally given by

$$T_{R\phi} = \langle \rho (\delta v_R \delta v_\phi - v_{AR} v_{A\phi}) \rangle, \tag{7.4}$$

where the angle brackets denote a suitable average (e.g., Balbus and Papaloizou [1999]). We shall henceforth refer to $T_{R\phi}$ as "the stress".

The stress has dimensions of pressure, and it is natural to scale this dependence out, leaving a dimensionless quantity α:

$$T_{R\phi} \equiv \alpha P, \tag{7.5}$$

the pressure P is evaluated at the midplane. It is also useful to introduce a form of the stress with dimensions of a velocity, i.e., with the midplane density scaled out. This is denoted $W_{R\phi}$,

$$W_{R\phi} \equiv \alpha c_S^2. \tag{7.6}$$

The α parameter is, of course, *not* a constant in our analysis, but will depend upon the magnetic Prandtl number Pm (Balbus and Henri [2008]).

$$\mathrm{Pm} = \frac{\nu}{\eta} \simeq 5.9 \times 10^{-29} \frac{T_c^4}{\rho}. \tag{7.7}$$

A strictly isothermal disc in hydrostatic equilibrium has a vertical gaussian profile with an e-folding scale height of $H = \sqrt{2} c_S / \Omega$. We will follow the long-established practice of multiplying by $2H$ to go from volume-specific to area-specific quantities in a thin disk.

The combination of mass and angular momentum conservation leads to an evolutionary equation for the midplane-to-surface disk column density Σ (Pringle [1981]; Balbus and Papaloizou [1999]):

$$\frac{\partial \Sigma}{\partial t} = \frac{2}{\sqrt{GM}R}\frac{\partial}{\partial R}\left[R^{1/2}\frac{\partial}{\partial R}(\Sigma R^2 W_{R\phi})\right], \tag{7.8}$$

describing the time evolution of the system. It is easy to see that if

$$\frac{\partial(\Sigma W_{R\phi})}{\partial \Sigma} < 0, \tag{7.9}$$

the perturbations $\delta\Sigma$ of the column density obey a diffusion equation with a negative diffusivity and are thus unstable. The partial Σ-derivative is taken assuming radiative equilibrium, discussed below.

7.2.1.2 Radiative considerations

The volume-specific rate at which energy is extracted from the differential rotation, and under the assumption of local dissipation turned into heat, is $-T_{R\phi}d\Omega/d\ln R$ (Balbus and Hawley [1998]). If the effective radiating surface temperature is T_s then the equation of thermal balance is

$$-HT_{R\phi}\frac{\mathrm{d}\Omega}{\mathrm{d}\ln R} = \sigma T_s^4, \tag{7.10}$$

where σ is the Stefan-Boltzmann constant. (A factor 2 has been cancelled on both sides.) The surface temperature T_s is related to the central midplane temperature T_c by the equation

$$T_c^4 = \frac{3\tau}{4}T_s^4, \tag{7.11}$$

where τ is the midplane-to-surface optical depth. We shall assume an opacity which is a combination of Kramers' opacity and the electron scattering opacity

$$\kappa = \kappa_K + \kappa_e = (6.6\times 10^{22}\rho T_c^{-3.5} + 0.4)\mathrm{cm}^2\mathrm{g}^{-1}, \tag{7.12}$$

in cgs units (Frank et al. [1992] and Takahashi and Masada [2011]). We have chosen to use the free-free Kramers' opacity in the above expression and numerical work (following Takahashi and Masada [2011]). We find that using the bound-free opacity instead ($5\times 10^{24}\mathrm{cm}^2\mathrm{g}^{-1}$, Frank et al. [2002]) results in Kramers' opacity dominating the electron scattering opacity throughout the disc in the region $\mathrm{Pm}\approx 1$. This means that using the bound-free opacity the disc instability criterion is given by (7.28), whereas using the free-free opacity the instability criterion is instead given by (7.24). In the next section we show that an accretion disc with a dominant electron scattering opacity becomes more easily unstable than a disc with a dominant Kramers' opacity. We find that aside from changing the instability criterion, the time-dependent global behaviour of the instability (see section 6) remains qualitatively unchanged by our choice for Kramers' opacity.

The optical depth of the disc is given by

$$\tau = \Sigma\kappa. \tag{7.13}$$

With both radiative and dynamical equilibrium holding for the unperturbed disc solution, the instability criterion (7.9) is equivalent to (Frank et al. [2002])

$$\frac{\partial T_s}{\partial \Sigma} < 0, \tag{7.14}$$

which is generally more convenient to use.

7.3 Instability criteria

We now turn to calculating the precise conditions for the instability criterion (7.14) to occur within the standard α formalism. Substituting (7.5) into (7.10) we find an expression for the surface temperature at constant radius

$$T_s^4 \propto \alpha T_c \Sigma. \tag{7.15}$$

Taking the partial derivative of both sides w.r.t. Σ at constant radius

$$4T_s^3 \frac{\partial T_s}{\partial \Sigma} \propto \frac{\partial(\alpha T_c \Sigma)}{\partial \Sigma}. \tag{7.16}$$

Eliminating T_s from (7.15) using (7.11) we find

$$T_c \propto (\alpha\tau\Sigma)^{1/3}. \tag{7.17}$$

Substituting this into (7.16)

$$4T_s^3 \frac{\partial T_s}{\partial \Sigma} \propto \frac{\partial(\alpha^{4/3}\Sigma^{4/3}\tau^{1/3})}{\partial \Sigma}, \tag{7.18}$$

$$\begin{aligned} 4T_s^3 \frac{\partial T_s}{\partial \Sigma} &\propto \ldots \\ &\ldots \frac{1}{3}\alpha^{1/3}\Sigma^{1/3}\tau^{-2/3}\left(4\Sigma\tau\frac{\partial \alpha}{\partial \Sigma} + 4\alpha\tau + \Sigma\alpha\frac{\partial \tau}{\partial \Sigma}\right). \end{aligned} \tag{7.19}$$

The quantities T_s, Σ, α and τ are always positive so only the bracketed quantity containing derivatives on the RHS can be negative and satisfy (7.14). Our general instability criterion becomes

$$\left(4\frac{\partial \ln \alpha}{\partial \ln \Sigma} + 4 + \frac{\partial \ln \tau}{\partial \ln \Sigma}\right) < 0. \tag{7.20}$$

This equation shows that if α is a steeply changing function of the disc properties this can cause an accretion instability in the disc. This is analogous to the instability in DN accretion discs where the opacity is a steep function of T_c around the ionisation temperature of hydrogen and this can lead to a transition between disc states (Faulkner et al. [1983] and Latter and Papaloizou [2012]). The instability induced by a variable α may be particularly relevant in light of the observed transitions between spectral states of X-ray binaries. If the opacity can be expressed in the standard power law form $\tau \propto \Sigma\rho T_c^m$ we can calculate T_c as a function of Σ using (7.17).

$$\tau \propto \Sigma^{\frac{11+2m}{7-2m}}\alpha^{\frac{2m-1}{7-2m}} \tag{7.21}$$

The instability criterion in (7.20) becomes

$$\left(\frac{9-2m}{7-2m}\right)\frac{\partial \ln \alpha}{\partial \ln \Sigma} + \left(\frac{13-2m}{7-2m}\right) < 0. \tag{7.22}$$

We see that in the case of constant α we recover the instability criterion for the opacity in dwarf nova ($7/2 < m < 13/2$). However, if we choose the electron scattering opacity ($\tau \propto \Sigma$), which is relevant for the inner region of the accretion disc (Frank et al. [2002]) and allow for a variable α, we can immediately calculate the instability condition from (7.20)

$$\frac{\partial \ln \alpha}{\partial \ln \Sigma} < -\frac{5}{4}. \tag{7.23}$$

From this equation we see that if α decreases sufficiently steeply with increasing surface density this induces an instability in the accretion rate of the disc. Conveniently, the same instability criterion is also valid in the case of Kramers' opacity $m = -7/2$. Simulations show that α increases sharply when the magnetic Prandtl number approaches unity and previous work by Balbus and Henri [2008] has calculated that the magnetic Prandtl number is expected to approach unity at a distance of approximately 50 Schwarzschild radii in a thin disc with physical parameters appropriate for an X-ray binary. Assuming a power law dependence for α, $\alpha \propto \mathrm{Pm}^n \propto T_c^{4n}/\rho^n$ and using (7.17) and (7.23) we find that the inner disc, dominated by the electron scattering opacity is unstable if

$$\alpha \propto \mathrm{Pm}^n, \;\; \text{unstable for} \;\; n > 2/3. \tag{7.24}$$

If α increases faster than $\mathrm{Pm}^{2/3}$ this results in an instability in the accretion disc in agreement with the more general instability analysis of Takahashi and Masada [2011]. Simulations suggest that α does indeed increase sharply with magnetic Prandtl number in the region $\mathrm{Pm} \approx 1$, with the power law index lying around the unstable value, $0.25 \lesssim n \lesssim 0.9$, depending on the properties of the simulations (Longaretti and Lesur [2010] and Simon et al. [2011]). We therefore expect this instability to occur in accretion discs around black holes. This result is particularly interesting since it can provide an explanation for the observed transition between spectral states in the accretion discs of X-ray binaries. We shall investigate the global behaviour of the instability using a simple time-dependent numerical simulation of a thin disc with a variable α in the next section.

We shall first, however, calculate the instability criterion in the more general case of a power-law form for the opacity $\tau \propto \Sigma\rho T^m$. Substituting α and τ into (7.17) we find

$$T_c \propto \Sigma^{(6-2n)/(7-2m-9n)}, \tag{7.25}$$

$$T_{\rm s} \propto \Sigma^{(13+9n-2m+2mn)/(4(7-2m-9n))}. \tag{7.26}$$

So our disc instability criterion becomes

$$\frac{13+9n-2m+2mn}{4(7-2m-9n)} < 0. \tag{7.27}$$

Taking the opacity of the outer disc to be given by Kramers' Law ($m = -7/2$) we find the instability criterion for $\alpha \propto \mathrm{Pm}^n$

$$\alpha \propto \mathrm{Pm}^n, \;\; \text{unstable for} \;\; n > 14/9. \tag{7.28}$$

We shall now turn our attention to the behaviour of the instability in a simulated disc to understand how the instability manifests itself.

7.4 Numerical work

In our numerical work in the following sections we use the following functional dependence of α with Pm

$$\alpha(\mathrm{Pm}) = \alpha_{\rm min} + (\alpha_{\rm max} - \alpha_{\rm min}) \left(\frac{\mathrm{Pm}^u}{\mathrm{Pm}^u + 1} \right), \tag{7.29}$$

where $\alpha_{\rm min}$ and $\alpha_{\rm max}$ are the minimum and maximum values of α. We choose this function because it tends smoothly to the required asymptotic values for α, and in the limit of small Pm, behaves as $\alpha \propto \mathrm{Pm}^u$, so the critical values of u and n should be comparible (see Equation 7.24). The opacity of the disc is given by 7.12.

7.5 Testing the instability criterion numerically

We have plotted the solutions of α as a function of Σ for several values of u in Figures 7.1a, b and c. In these Figures we have neglected radiation pressure, which we consider in section 7.5.1. For values $u \gtrsim 0.9$, there are multiple solutions for α and T_c for a given value of Σ. This value of u is similar to the criterion derived for the pure power law form for α in (7.24) as we expect, since in the small Pm limit the expression in (7.29) becomes $\alpha \propto \mathrm{Pm}^u$. The Figure shows the expected limit cycle behaviour for a disc instability analogous to the limit cycle induced by the changing opacity in the accretion discs of DN. For the case $u \gtrsim 0.9$ we find there is a region in which three possible solutions exist with a lower branch of solutions extending to small values of Σ and the upper branch extending to large Σ. The upper and lower branches of solutions are truncated at the lowest and highest Σ values bounding the region with multiple solutions respectively. This means that the value of α jumps discontinuously from the lower to upper branch of solutions when increasing Σ from small values. If u is larger than unity, $u > 1$, the solutions overlap over a significant range of values of Σ so the value of α (and the associated accretion rate) remains on the upper branch even if Σ then decreases below its original value. This provides the required hysteresis in the system.

7.5.1 Radiation pressure

For completeness, we plot the solutions for T_c as a function of Σ including both gas and radiation pressure in the disc in Figure 7.1d. This shows a more complex structure than the purely gas pressure dominated solutions resulting from the rapid change in the sound speed when the pressure transitions from gas to radiation pressure dominated regimes. The upper branch of radiation pressure dominated solutions is not physical, however, since for these solutions the sound speed becomes comparable to the rotational velocity of the material. The disc cannot be considered 'thin' in these regimes and so an analysis based on a thin disc formalism is not self-consistent.

In our time-dependent simulations in the next section we shall neglect radiation pressure in the disc. This is because a thin disc becomes both thermally and viscously unstable when radiation pressure dominates gas pressure (Lightman and Eardley [1974] and Shakura and Sunyaev [1976]) and their is ongoing research into the role of radiation pressure in determining the viscosity (Hirose et al. [2009b], Hirose et al. [2009a] and Janiuk and Czerny [2011]). We find that in our simulations neglecting the radiation pressure is a good approximation in the initial and quiescent disc states where gas pressure dominates radiation pressure, however, in the flaring disc sections with larger values of α and $\mathrm{Pm} > 1$, this approximation breaks down. This is because the regime in which we are interested $\mathrm{Pm} \approx 1$ is also the region in which

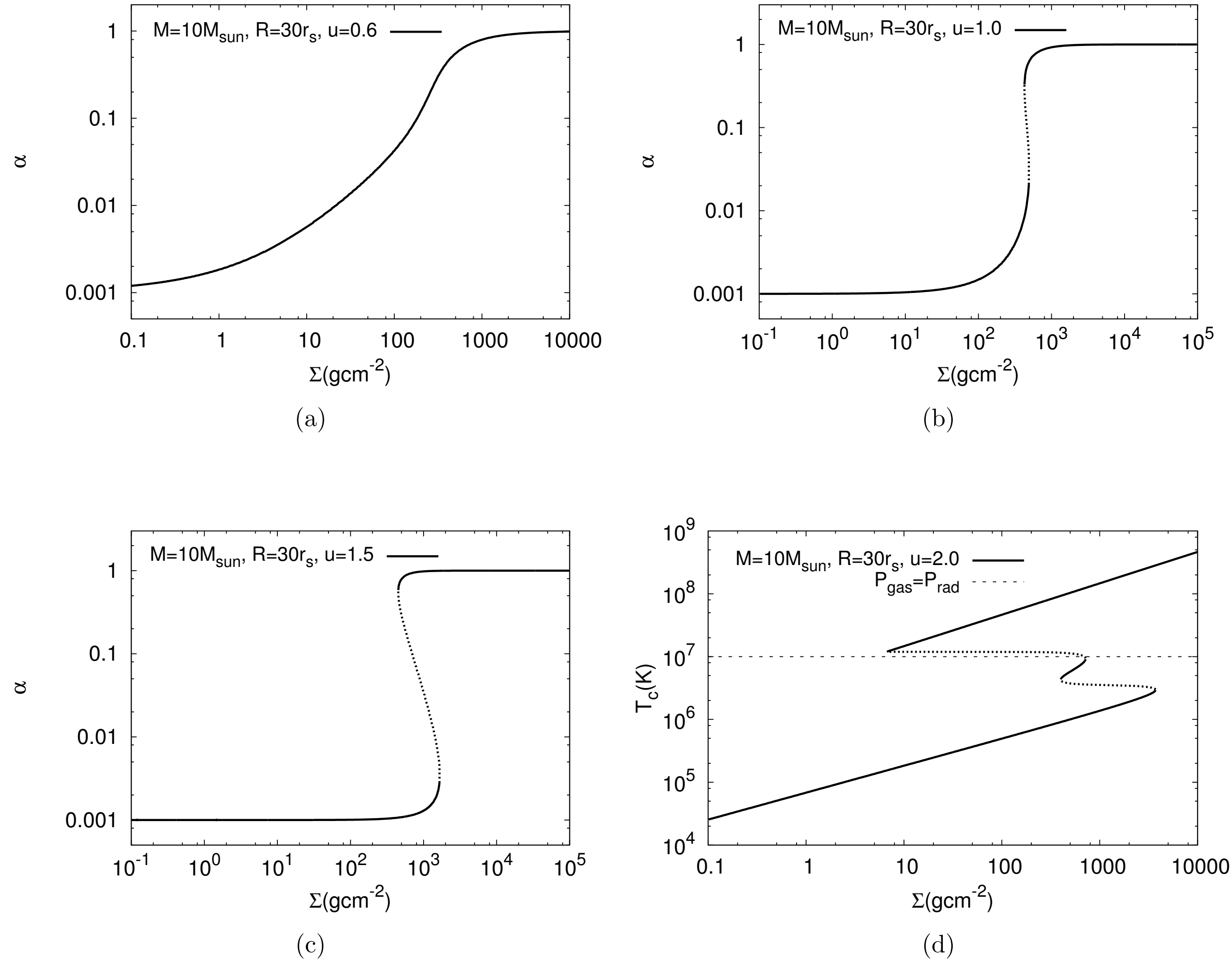

Figure 7.1: *a–c*: The solutions for α as a function of Σ for different values of u plotted in the case of a black hole of mass $10M_{\odot}$ at a radius $30r_s$ from the black hole neglecting radiation pressure. We find that if $u \gtrsim 0.9$ the solution behaves as an unstable limit cycle with two overlapping branches of stable solutions and a physically inaccessible region (dotted line). *d*: The solutions for central temperature T_c as a function of Σ when including both the radiation and gas pressures. Additional radiation pressure dominated solutions are permitted, however, these high temperature solutions are not self-consistent since the disc can no longer be considered thin (H≪R).

M	$10M_\odot$
$\dot{M}$	$0.001M_{Edd}$
α_{min}	0.001
α_{max}	1

Table 7.1: The values of physical parameters used in our 1D numerical simulations shown in Figures 7.2 and 7.3.

the radiation pressure becomes comparable to, or exceeds, the gas sound speed. This is most easily illustrated by noting that the magnetic Prandtl number is directly proportional to the square of the radiation sound speed ($c_S^{\rm rad} \approx 6.5 \times 10^4 \sqrt{\rm Pm}$ ms^{-1}), which becomes relevant for Pm $\gtrsim 1$. Since for radiation pressure $P_{\rm rad} \propto T_c^4$, it increases much more rapidly with increased temperature than the gas sound speed and so we expect that the flaring regions of the disc to be radiation pressure dominated and potentially thick. The purpose of this paper is to demonstrate that a variable α can result in an accretion disc instability and to understand the physics controlling the global behaviour of this instability. Due to the limitations of thin disc theory we do not expect the results of a time-dependent thin disc simulation to encapsulate the precise details of the unstable disc but we aim to demonstrate that such an instability is likely to occur in X-ray binaries and to give an indication of its expected behaviour and the governing physics.

7.6 Time-dependent disc simulation

We have conducted a simple 1D time-dependent simulation of a thin accretion disc with an α-parameter which depends on the magnetic Prandtl number. We divide the disc into logarithmically separated radial bins and solve (7.8) using a finite difference scheme with adaptive timesteps. We choose our boundary condition at the outermost part of the disc to be the analytic solution to the thin disc equations and our innermost boundary condition to be $T = \rho = 0$ for $R < 3r_s$. The innermost boundary condition is chosen because we expect a significantly lower density to be present inside the innermost stable circular orbit for the black hole. We show the physical parameters we have used in our disc simulation to produce Figures 7.2 and 7.3 in Table 7.1.

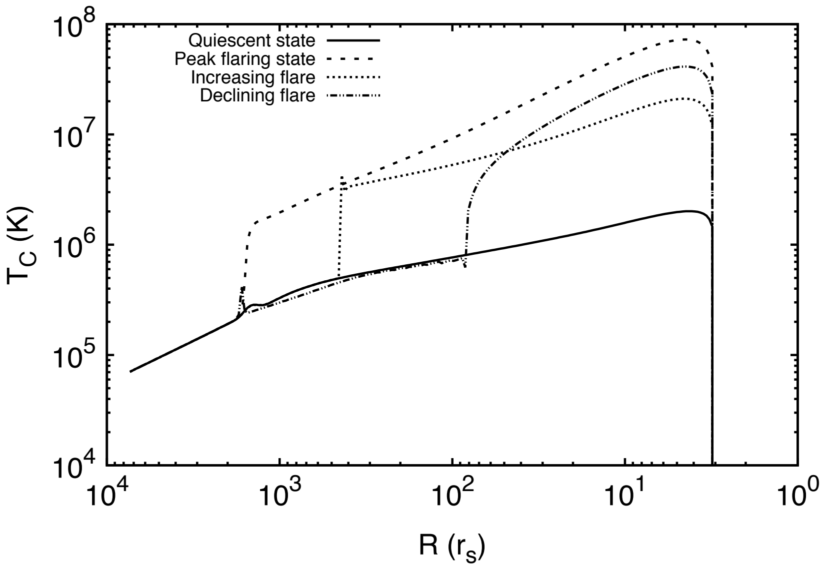

Figure 7.2: Snapshots of the disc in the quiescent, flaring and intermediate states with $u = 1.5$ from our 1D simulation.

7.6.1 Behaviour of the instability

We find that the instability displays very interesting global behaviour in our disc simulation. When the Pm in a region of the disc approaches unity (for $u > 0.9$) the value of α jumps discontinuously from small to large values and this causes the local accretion rate and temperature of the region to increase since $\dot{M} \propto \Sigma \alpha c_s H$. The instability is not localised to this region, however, since increasing the accretion rate in one region also results in an increased accretion rate in neighbouring regions (because they are coupled via the diffusion equation, 7.8). These neighbouring regions may then become unstable themselves if the increased accretion rate and temperature are sufficient to increase the Prandtl number so that Pm ≈ 1, causing α to jump to the upper branch of solutions (see Figure 7.1). The increased accretion rate (and value of α) will continue to propagate outwards in radius from the initially unstable region until it reaches a radius at which the induced increase in accretion rate and surface density, Σ, are insufficient for Pm to approach unity and cause α to increase discontinuously to the upper branch of solutions. At this point the increased accretion rate in the inner region of the disc becomes unsustainable since the accretion rate in the outer region of the disc is now lower than that in the unstable interior region due to the lower value of α. The different accretion rates result in the mass contained in the unstable inner region being drained from the outside inwards because the viscous timescale required to replenish mass decreases with radius. The cycle repeats once the mass in the depleted inner regions (now with α on the lower branch of solutions) has been replenished by accretion from the outer stable parts of the disc and the Prandtl number becomes large enough to cause α to increase discontinuously in a region of the inner disc.

Numerically, the process behaves as a limit cycle with a quiescent period in which the depleted inner regions accrete mass, followed by a flaring state where the value of α in a region jumps to the upper branch of solutions, causing an increase in accretion rate and temperature. The instability then propagates from the hottest innermost region of the disc outwards to $R \sim 1000r_s$ where it stalls. A region of depleted mass then propagates back inwards emptying the inner part of the disc of mass. The stages of this process are shown in Figure 7.2. We find that the detailed behaviour of the instability depends on the parameters in our chosen function. The instability propagates outwards and inwards with a speed related to the viscous timescale of the relevant region of the disc. So the time in the quiescent state is approximately $t_q \propto t_{vis}(R \approx 1000r_s) \sim 0.01 \times (1000r_s)^2/(\alpha_{min}c_sH)$ and the flaring timescale is given by $t_f(R \approx 1000r_s) \propto t_{vis} \sim 0.01 \times (1000r_s)^2/(\alpha_{max}c_sH)$. The relative fraction of time spent in the flaring and quiescent states is given approximately by $\alpha_{min}/\alpha_{max}$.

The parameter u in (7.29) determines whether the disc is unstable as discussed in section 3. It also determines the "noisiness" of the flaring with larger values of u resulting in a clean cyclic behaviour where the disc instability propagates outwards in one wave and this is followed by a wave of depleted mass propagating back inwards in one motion. For unstable values of u closer to the critical value $u = 0.9$ we find that the edge of the flaring region propagates both outwards and inwards many times before the inner region becomes depleted and enters the quiescent state. This is caused by the increase in the width of the region containing multiple solutions for larger values of u, so the upper branch of solutions exists down to lower values of Σ.

For our chosen function of α in (7.29) we find numerically that for values of u such that multiple solutions exist for α, the gradient $\partial(\ln\alpha)/\partial(\ln\Sigma)$ of the middle branch of solutions always satisfies our criterion for instability (7.20) as we expect. In our simulations the disc instability manifests itself as a limit cycle in α, with the value of α jumping discontinuously from a lower branch of solutions to an upper branch. This is not quite the same physical behaviour as suggested by the initial instability criterion in (7.23), which was a criterion for an unstable (but continuous) increase in the surface density of a region. We find that in practice, regions which satisfy the criterion for unstable growth always have multiple solutions of α (and correspondingly T_c) forming a limit cycle. This is because physically we expect T_s to always increase with Σ in the disc and so a region with $\partial T_s/\partial\Sigma < 0$ must necessarily be multiple valued to ensure that T_s always increases with Σ for the physically accessible paths in the solution space. The solutions formally satisfying the instability criterion are physically inaccessible for a disc in thermal equilibrium and so the instability in our simulations is due solely to the unstable limit cycle behaviour as explained in detail at the start of this section. The presence of a limit cycle should not come as a surprise since the analogous disc instability in dwarf novae also manifests itself as a limit cycle in which the region of unstable solutions (by the criterion in (7.22)) is not physically accessible.

It is worth mentioning that the existence of the unstable behaviour requires that the equilibrium surface density of at least one part of the disc exceeds the maximum value of the lower branch of solutions. Clearly a disc with a very low surface density at all radii will not be unstable since the equilibrium surface density will exist on the lower branch of stable solutions. This could explain why not all X-ray binary systems are observed to have cyclic flaring behaviour. We leave the calculation of accretion rates which satisfy this criterion to a future work.

7.7 Comparison to observations

The existence and behaviour of this disc instability is particularly relevant when considering the observed transition in spectral states of X-ray binaries. It has long been observed that X-ray binaries exhibit different spectral states which change cyclically over time. The states are broadly characterised by a high/soft state, a low/hard state, a very high/hard state and a quiescent state. The spectrum spends much of its time in the quiescent state periodically flaring over a period of weeks/months (Remillard and McClintock [2006]). The physical mechanism behind these transitions is currently not well understood and has been posited to be due to transitions between a radiatively efficient thin disc and a hot ADAF caused by variations

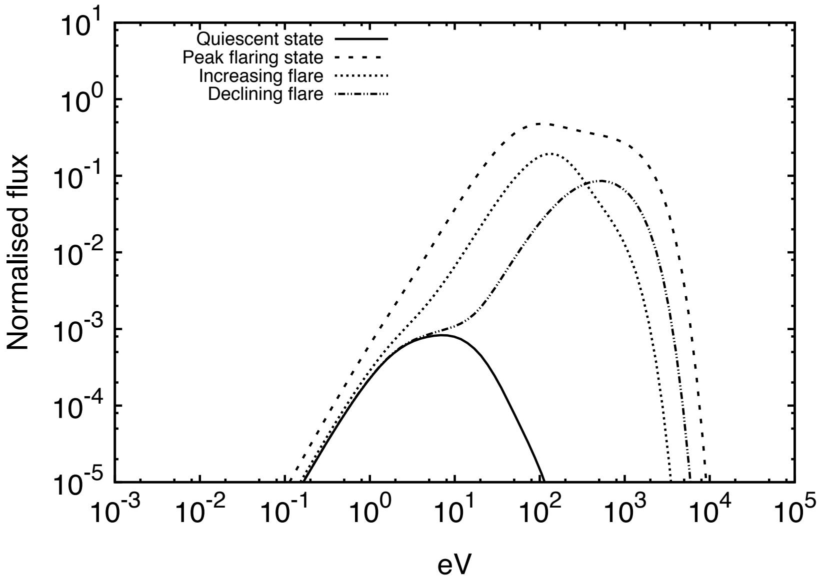

Figure 7.3: The emitted spectrum in the quiescent, flaring and intermediate disc states (as shown in Figure 7.2).

in the disc accretion rate. We feel that this mechanism seems somewhat forced and artificial since a physical process which causes a thin disc to transition to an ADAF has not yet been convincingly demonstrated.

In this Chapter we have shown that if α depends on the magnetic Prandtl number (as found in simulations), then an instability can exist in the accretion disc which naturally produces flaring and quiescent disc states if $\alpha \propto \mathrm{Pm}^n$ and $n > 2/3$. In Figure 7.3 we plot the spectrum of the disc in the different states corresponding to those shown in Figure 7.2. In the quiescent state the inner disc is depleted of mass and so the disc spectrum is cool since we only observe the outer parts of the disc. As the inner disc refills with mass we see an increasing contribution of the inner disc to the observed spectrum, which becomes brighter and hotter. Once the inner regions of the disc become unstable the spectrum increases dramatically in X-ray flux and flares because of the increased accretion rate of the inner part of the disc. The spectrum then transitions back to the initial quiescent state once the mass in the inner part of the disc has been accreted onto the black hole.

This scenario has enough flexibility to explain the variation in the observed spectral transitions in X-ray binaries. The timescales of the quiescent and flaring states are proportional to the relevant viscous timescales which depend on the values of α_{min} and α_{max}. The noisiness of the flaring activity depends on the value of u in our numerical simulations, with smaller unstable u producing noisier disc state transitions. This flexibility, depending on a few physical parameters is required to reproduce the different qualitative behaviour of the spectral transitions in different X-ray binaries and could help to constrain the value of physical parameters, such as α, in accretion discs.

Finally, we wish to comment on the relation between spectral states and jet production (see Fender et al. [2004]). In this simple model we have not treated the acceleration of non-thermal particles in the accretion disc corona or jet and so we are not able to reproduce the power-law component visible in the hard X-ray spectrum. In a thin disc in which the viscosity is primarily due to the MRI, the magnetic energy density can be estimated to be, $U_B \approx 3U_p\alpha/2$, where $U_p = \rho k_B T_c/(\mu m_p)$ is the thermal energy density in particles. In the flaring state when $\alpha \approx \alpha_{\rm max}$, the increased accretion rate and temperature are accompanied by a corresponding increase in the magnetic field strength in the disc, which is the basis for α depending on the magnetic Prandtl number in simulations. We expect the large field strength would lead to a more powerful disc corona and jet which would increase the amount of non-thermal particle acceleration.

In disc models with local dissipation of heat, the mass accretion rate onto the black hole is proportional to the surface temperature of the innermost part of the disc (since $\dot{M} \propto T^4_{surf}$). In the simplest case we expect the jet power to be proportional to the mass accretion rate onto the black hole, so the jet power would be proportional to the surface temperature of the innermost disc. Here we expect the flaring state of the disc to be associated with the onset of jet production and radio emission while the quiescent state is associated with a weak jet or no jet at all. These simple assumptions are not consistent with radio observations of a jet in the low/hard state and no jet in the high/soft state. This tells us that jet production is not simply proportional to the disc accretion rate but must also depend on additional disc properties such as the disc height, magnetic field structure and the structure and rate of the accretion flow close to the black hole. We leave the detailed comparison of observations to disc and jet spectra for a future investigation.

7.8 Conclusion

In this Chapter we have considered the effect of a variable α parameter which depends on the physical conditions of a plasma. We have shown that an α parameter which increases with the magnetic Prandtl number can cause an accretion instability analogous to the instability in dwarf novae discs. We have calculated the general condition for this instability to occur in a standard thin disc which is in radiative equilibrium. For both the electron scattering opacity and Kramers' opacity this instability criterion becomes $\partial \ln \alpha / \partial \ln \Sigma < -5/4$. We consider the case where α depends on the magnetic Prandtl number Pm^n, as suggested by numerical simulations, and find the inner region of the disc is unstable if $n > 2/3$, in agreement with the work by Takahashi and Masada [2011].

We use a 1D time-dependent simulation of a thin accretion disc in order to investigate the global behaviour of this instability in X-ray binary systems. We find that if α satisfies the instability criterion this results in a limit cycle. This induces an unstable cyclic flaring behaviour in the disc as the value of α cycles between small and large values causing an unsustainable increase in accretion rate of the inner region of the disc. This high accretion rate drains mass from the inner region of the disc ($R \lesssim 1000 r_s$) and this is followed by a quiescent period in which this mass is replenished.

We find these results particularly relevant to explaining observations of cyclic flaring behaviour in X-ray binary systems. We calculate the observed spectrum of the disc in the different disc states and show that the instability is able to reproduce the thermal properties of flares in X-ray binaries. In the quiescent state the inner part of the disc is cool, whilst in the flaring state the accretion rate and temperature in the inner part of the disc increases substantially producing X-ray emission. We find the flaring timescale depends on the viscous timescale of the disc.

The discovery of an instability which can plausibly explain observations of flaring in X-ray binary accretion discs is very exciting since this is a long standing problem. In the near future we wish to investigate whether this instability operates in a 3D MHD simulation of an X-ray binary disc.

Chapter 8

A gauge-invariant approach to interactions in the dark sector

In this Chapter I investigate the observational consequences of an interaction between a scalar field (quintessence) model of dark energy with dark matter. I use a gauge-invariant covariant formalism to calculate the matter power spectrum and integrated Sachs-Wolfe (ISW) effect for three interactions including the unstable decay of dark energy or dark matter and a scalar-tensor interaction. I rule out several interactions using simple physical arguments and find that the scalar-tensor interaction increases the clustering on very large scales. I constrain the interaction strength using the ISW effect.

8.1 Introduction

Observation of type Ia supernovae at high redshift, large-scale structure surveys and observations of the cosmic microwave background (CMB) all indicate that the Universe is currently undergoing accelerated expansion (Abazajian et al. [2009]; Komatsu et al. [2009]; Kowalski et al. [2008]; Riess et al. [1998]). The most convincing explanation for this phenomenon is that the Universe is filled in great abundance with a form of energy with negative pressure. This so-called 'dark energy' (DE) can lead to an accelerated cosmic expansion if its equation of state w satisfies $w < -1/3$, although observations currently constrain w to be close to -1. At present, the cosmological constant model in which w is exactly -1 appears to be the most robust model for dark energy (Efstathiou [2001]; Komatsu et al. [2009]).

However, there remain unsolved problems with the physical origin and the exact value of the cosmological constant. It is well-known that the value of the cosmological constant, interpreted as vacuum energy arising from particle-antiparticle annihilation, and that consistent with observation can differ by as much as 120 orders of magnitude (Djorgovski and Gurzadyan [2007]). Moreover, the value of the cosmological constant, however minuscule, must be set at its precise value at the initial inflationary epoch, with the slightest deviation from this value leading to disastrous consequences (Carroll et al. [1992]).

Over a decade since the discovery of cosmic acceleration, there are now an overwhelming number of dark energy alternatives to the cosmological constant (see e.g. Copeland et al. [2006] for a review). One of the earliest and the simplest of such models is that of a single light scalar-field model of dynamical dark energy dubbed 'quintessence' (Dave et al. [2002]; Ratra and Peebles [1988]; Wetterich [1988]). Unlike the cosmological constant, many quintessence models exhibit an attractor behaviour and thus do not require initial conditions that are extremely fine-tuned. The late-time acceleration can also be dynamically 'switched on' without requiring a cosmic coincidence (Skordis and Albrecht [2002]).

Since quintessence can be interpreted as a field with non-zero mass, it is possible that dark energy could cluster like dark matter, or even interact with dark matter. The possibility that there may be interactions in the dark sector has previously been explored by several authors (Amendola and Quercellini [2003]; Bean et al. [2008]; Chongchitnan [2009]; Corasaniti [2008]; He et al. [2009]; Jackson et al. [2009]; Koivisto [2005]; La Vacca and Colombo [2008]; Mainini and Bonometto [2007]; Olivares et al. [2006]; Pettorino and Baccigalupi [2008]; Tarrant et al. [2011]; Vacca et al. [2009]; Väliviita et al. [2008, 2010]; Wetterich [1995]). It is common in the previous works to neglect either dark energy perturbations or model dark energy using some phenomenological form of w (e.g. $w =$ constant). These simplistic approaches may not accurately reproduce the dynamics of quintessence models as suggested by Jennings et al. [2010]; Park et al. [2009].

The primary aim of this Chapter is to investigate the prospects of detecting the observational signatures of dark sector interactions. We shall consider three well-known models of quintessence and study the effects of dark sector interactions in both the background and in the linear perturbations. In particular, we shall examine the effects of non-zero interactions on the linear matter power spectrum and the integrated Sachs-Wolfe (ISW) using the gauge-invariant approaches of Kodama and Sasaki (Kodama and Sasaki [1984]). Unlike previous works on this subject, our approach takes into account dark energy perturbations, including the perturbative effects of energy and momentum transfer in the dark sector. Issues of instabilities previously discovered in Chongchitnan [2009]; Väliviita et al. [2008, 2010] will also be addressed.

8.2 Quintessence models

Quintessence refers to a scalar field, ϕ, evolving along a potential, $V(\phi)$, which becomes sufficiently flat at late times, leading to cosmic acceleration (see e.g. Copeland et al. [2006]). At early times, the dark energy contribution to the overall energy density is small (Ferreira and Joyce [1998]). Some classes of potentials exhibit tracking behaviour whereby the dark energy density tracks below that of matter and radiation and only comes to dominate the universe at late times (Copeland et al. [1998]). Another interesting feature of quintessence is the existence of attractor solutions (Ferreira and Joyce [1998]) which greatly reduce the need for the initial values of the dark energy parameters to be finely tuned.

We will focus our analysis on three models of quintessence, namely, the Ratra-Peebles, SUGRA and double exponential potentials summarised below. From this point on, all equations will be in natural units with $c = \hbar = 1$. We also write $\bar{\kappa}^2 = 8\pi G$.

8.2.1 Ratra-Peebles

Ratra and Peebles (RP, Ratra and Peebles [1988]) showed that the class of inverse power law potentials of the form

$$V(\phi) = \frac{M^{4+\alpha}}{\phi^\alpha}, \quad \alpha > 0, \tag{8.1}$$

tracks the equation of state during matter and radiation-dominated eras, and dark energy only becomes dominant at late times. This behaviour holds for a wide range of initial conditions. We will use $M = 4.1 \times 10^{-28} m_{\rm Pl}$ and $\alpha = 0.5$ as indicated by Alimi et al. [2010] who obtained these values from a likelihood analysis of the WMAP 5-year data (Komatsu et al. [2009]) and the 'union' supernovae data (Kowalski et al. [2008]).

8.2.2 SUGRA

The SUGRA model with potential

$$V(\phi) = \frac{M^{4+\alpha} \exp\left(\frac{1}{2}\bar{\kappa}^2\phi^2\right)}{\phi^\alpha}, \tag{8.2}$$

is motivated by supersymmetry and differs from the Ratra-Peebles (RP) potential by an exponential 'supergravity' correction factor (Brax and Martin [1999]). This factor can be shown to push the equation of state closer to -1 at late times. We will use the values $M = 1.7 \times 10^{-25} m_{\rm Pl}$ and $\alpha = 1$ as indicated by Alimi et al. [2010]. Again, the SUGRA potential has attractor solutions and is viable for a wide range of initial conditions.

8.2.3 Double exponential

The double exponential (DExp) potential

$$V(\phi) = M_1 e^{-\lambda_1 \phi} + M_2 e^{-\lambda_2 \phi}, \tag{8.3}$$

allows dark energy to track the equation of state of radiation and matter and leads to acceleration at late times (Barreiro et al. [2000]). We shall use $M_1 = 10^{-14} m_{\rm Pl}$, $M_2 = 10^{-13} m_{\rm Pl}$, $\lambda_1 = 9.43$ and $\lambda_2 = 1$ which, as shown in Bassett et al. [2008], should give rise to observables that are significantly different from the cosmological constant but are still broadly consistent with observational constraints.

8.3 Evolution of background energy densities

We assume an isotropic, homogeneous and spatially flat background as described by the Friedmann-Robertson-Walker (FRW) metric,

$$ds^2 = -dt^2 + a(t)^2 dx^i dx_i, \tag{8.4}$$

where $a(t)$ is the scale factor as a function of cosmic time t and summation is implied over $i = 1, 2, 3$. We assume that the background energy density comprises matter, radiation and dark energy (denoted by subcripts m, r and ϕ respectively). The total energy density, $\rho = \rho_m + \rho_r + \rho_\phi$, satisfies the Friedmann and acceleration equations

$$H^2 \equiv \left(\frac{\dot{a}}{a}\right)^2 = \frac{\bar{\kappa}^2}{3}(\rho_m + \rho_r + \rho_\phi), \tag{8.5}$$

$$\dot{H} = -\frac{\bar{\kappa}^2}{2}\left(\rho_m + \frac{4}{3}\rho_r + \rho_\phi + 3p_\phi\right), \tag{8.6}$$

as well as the energy conservation equation

$$\dot{\rho} + 3H(\rho + p) = 0. \tag{8.7}$$

Here overdots are derivatives with respect to t and p_x is the pressure of component x related to its energy density via the equation of state $w_x = p_x/\rho_x$. In the above, we have used $w_m = 0$, $w_r = 1/3$ and w_ϕ defined below.

The quintessence field evolves via the Klein-Gordon equation

$$\ddot{\phi} + 3H\dot{\phi} + V'(\phi) = 0. \tag{8.8}$$

Its energy density, pressure and equation of state are given by

$$\rho_\phi = \frac{\dot{\phi}^2}{2} + V(\phi), \quad p_\phi = \frac{\dot{\phi}^2}{2} - V(\phi), \tag{8.9}$$

$$w_\phi = \frac{p_\phi}{\rho_\phi} = \frac{\dot{\phi}^2/2 - V(\phi)}{\dot{\phi}^2/2 + V(\phi)}. \tag{8.10}$$

The case in which $\dot{\phi} = 0$ reduces to the cosmological constant with $w_\Lambda = -1$. Note that at present w_ϕ is observationally constrained at low redshift to a value close to $w_\phi = -1$ with $\sim 10\%$ accuracy (Komatsu et al. [2011]; Riess et al. [2011]).

We model interactions between dark matter and dark energy by including a source term, Q_x, in the evolution equations for the dark energy and dark matter background energy densities.

$$\dot{\rho_x} = -3H\rho_x(1+w_x) + Q_x. \tag{8.11}$$

Non-zero Q thus represents the energy flow from one component to another. To conserve the total energy, we require

$$\sum_x Q_x = 0. \tag{8.12}$$

If interactions are purely between the dark matter and dark energy (i.e. interactions only in the dark sector) then

$$Q_m = -Q_\phi. \tag{8.13}$$

8.3.1 Evolution equations

To evolve the background energy densities with time, we use the set of dimensionless 'energy' variables defined in Copeland et al. [1998],

$$x = \frac{\bar{\kappa}\dot{\phi}}{\sqrt{6}H}, \qquad y = \frac{\bar{\kappa}}{H}\sqrt{\frac{V}{3}},$$

$$r = \frac{\bar{\kappa}}{H}\sqrt{\frac{\rho_r}{3}}, \quad m = \frac{\bar{\kappa}}{H}\sqrt{\frac{\rho_m}{3}}, \quad \lambda = -\frac{1}{\bar{\kappa}V}\frac{dV}{d\phi}. \tag{8.14}$$

Intuitively, x, y, r and m can be thought of as (the square-root of) the ratio of energy density of each component to the total energy density ($\sim 3H^2$). Converting the time variable in Equations 8.6, 8.7 and 8.8 to the 'e-fold' number, $N = \ln a$, we obtain

$$\frac{d\ln H}{dN} = -\frac{3}{2}\left(1 + x^2 - y^2 + \frac{r^2}{3}\right), \tag{8.15}$$

$$\frac{dx}{dN} = \sqrt{\frac{3}{2}}\lambda y^2 - x\left(3 + \frac{d\ln H}{dN}\right) + \frac{\bar{\kappa}^2}{6H^3 x}Q_\phi, \tag{8.16}$$

$$\frac{dy}{dN} = -\sqrt{\frac{3}{2}}\lambda xy - y\frac{d\ln H}{dN}, \tag{8.17}$$

$$\frac{dr}{dN} = -r\left(2 + \frac{d\ln H}{dN}\right), \tag{8.18}$$

$$\frac{dm}{dN} = -m\left(\frac{3}{2} + \frac{d\ln H}{dN}\right) + \frac{\bar{\kappa}^2}{6H^3 m}Q_m. \tag{8.19}$$

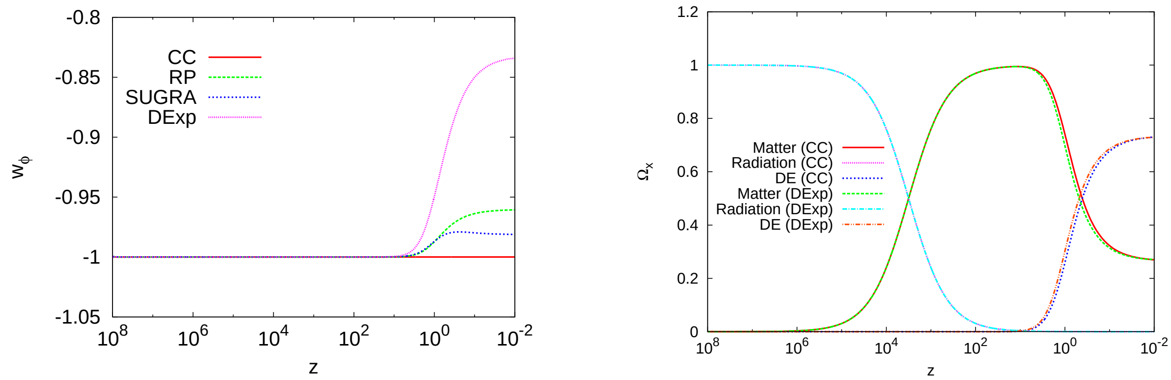

Figure 8.1: *Left:* The equation of state $w_\phi(z)$ of dark energy for the cosmological constant (CC), Ratra-Peebles (RP), SUGRA and double exponential (DExp) models (see section 8.2). *Right:* The evolution of the density parameter $\Omega_x = \rho_x/\rho$ for the CC and DExp models. Apparently large deviations from $w_\phi = -1$ lead to subtle differences in Ω at late times.

These variables obey the Friedmann constraint derived from dividing Equation 8.5 by H.

$$x^2 + y^2 + r^2 + m^2 = 1, \tag{8.20}$$

We solved these coupled differential equations by integrating them numerically from redshift $z = 10^8$ until $z = 0$ (today). Initial values were chosen by requiring that the final ($z = 0$) values of the component energy densities agreed broadly with those measured today: $\Omega_m = 0.27$, $\Omega_r = 8.6 \times 10^{-5}$, $\Omega_\phi = 1 - \Omega_m - \Omega_r$ and $H_0 = 70.8$ kms^{-1}Mpc^{-1}, where $\Omega_x \equiv \rho_x/\rho$.

The evolution of w_ϕ for the four models and the background energy densities for the CC and DExp models are shown in Figure 8.1, in which the eras of radiation, matter and dark energy domination are clearly seen in that order. The quintessence and CC models all satisfy $w_\phi \simeq -1$ until $z \sim 1$. Despite an apparently large deviation in w_ϕ from -1 at very low redshift, the differences in the background density between the DExp and CC models are surprisingly small. Thus, it may be more fruitful to try to distinguish between quintessence and the cosmological constant via perturbations.

8.4 Perturbations

We consider only scalar perturbations to the FRW metric. Working in the Newtonian gauge and ignoring anisotropic stresses, the perturbed metric takes the form

$$ds^2 = -(1+2\Phi)dt^2 + a(t)^2(1-2\Phi)dx^i dx_i, \tag{8.21}$$

where Φ is the Newtonian potential (for details see Ma and Bertschinger [1995]). The components of the energy-momentum tensor, $T_\mu{}^\nu$ are

$$T_0{}^0 = -\rho, \quad T_i{}^0 = -\frac{1}{k}(\rho+p)v_{,i}, \quad T_i{}^j = p\delta_i{}^j, \tag{8.22}$$

where k is the Fourier wavenumber, v_i is the peculiar velocity of the perturbation for species i and a comma denotes a partial derivative. Each energy density can be decomposed as $\rho = \overline{\rho} + \delta\rho$ where barred quantities are the background values. We then define the variables:

$$\delta_m \equiv \frac{\delta\rho_m}{\overline{\rho}_m}, \qquad \delta_r \equiv \frac{\delta\rho_r}{\overline{\rho}_r}, \qquad \delta\phi \equiv \phi - \overline{\phi}.$$

Physically, δ is a measure of density fluctuations (overdensities and underdensities). To avoid unphysical gauge artefacts, we shall consider the gauge-invariant overdensities Δ_x defined as (Kodama and Sasaki [1984])

$$\Delta_m \equiv \delta_m + 3\left(\frac{aH}{k}\right)(1-q_m)v_m, \tag{8.23}$$

$$\Delta_r \equiv \delta_r + 4\left(\frac{aH}{k}\right)(1-q_r)v_r, \tag{8.24}$$

$$\Delta_\phi \equiv \frac{\dot\phi\delta\dot\phi + (3H\dot\phi + V'(\phi))\delta\phi - \dot\phi^2\Phi}{\rho_\phi}, \tag{8.25}$$

$$= \delta_\phi + 3\frac{aH}{k}(1+w_\phi)v_\phi + \frac{3}{2}(1+w_\phi)\left(\frac{aH}{k}\right)^2\overline{\Delta}, \tag{8.26}$$

$$\text{where} \quad v_\phi = \frac{k\delta\phi}{a\dot\phi}, \tag{8.27}$$

$$q_x = \frac{Q_x}{3H\rho_x(1+w_x)}. \tag{8.28}$$

It will also be necessary to consider the perturbative effects arising from the dark sector interactions. We define ϵ to be the perturbation in the energy transfer $Q_x \to \widetilde{Q}_x$

$$\widetilde{Q}_x = Q_x(1+\epsilon_x), \tag{8.29}$$

and note that ϵ_x obeys the conservation equation

$$\sum_x Q_x \epsilon_x = 0. \tag{8.30}$$

Similarly, the gauge-invariant variable for energy transfer, E_x, can be constructed as (Kodama and Sasaki [1984])

$$E_x = \epsilon_x - \frac{a\dot{Q}_x}{kQ_x} v_x. \tag{8.31}$$

8.4.1 Covariant formulation of dark sector interactions

We now describe how dark sector interactions can be covariantly formulated and incorporated into the gauge-invariant system (see He et al. [2009]; Väliviita et al. [2008, 2010] for previous attempts in this direction for simple dark energy models).

Dark sector interactions can be covariantly described by the conservation equation

$$\nabla_\nu T^{\mu\nu}_x = Q^\mu_x. \tag{8.32}$$

The 4-vector Q^μ_x can be constructed using the function Q_x by

$$Q_{(x)\mu} = Q_{(x)} u_{(a)\mu}, \tag{8.33}$$

where $u_{(a)\mu}$ is the 4-velocity of component a (which may be different from x). By perturbing (8.33), we find

$$\widetilde{Q}_{(x)\mu} = \widetilde{Q}_{(x)} \widetilde{u}_\mu + \widetilde{f}_{(x)\mu}, \tag{8.34}$$

where u_μ is the average velocity. The perturbed average 4-velocity $u_\mu \to \widetilde{u}_\mu$ and perturbed

4-velocity of component a ($u_{(a)\mu} \to \widetilde{u}_{(a)\mu}$) can be expressed as

$$\widetilde{u}_0 = \widetilde{u}_{(a)0} = -a(1+\Phi), \qquad \widetilde{u}_j = a\bar{v}Y_j, \qquad \widetilde{u}_{(a)j} = av_aY_j. \tag{8.35}$$

where Y_j is a basis vector constructed from harmonic functions (see Appendix C of Kodama and Sasaki [1984] for details). In 8.34, the vector $\widetilde{f}_{(x)\mu}$ can be interpreted as the momentum exchange with components given by

$$\widetilde{f}_{(x)0} = 0, \qquad \widetilde{f}_{(x)j} = aH\rho_x(1+w_x)f_xY_j, \tag{8.36}$$

where f_x is an ordinary scalar representing the amplitude of the momentum exchange. In addition, f_x satisfies the conservation of momentum

$$\sum_x \rho_x(1+w_x)f_x = 0. \tag{8.37}$$

As with the energy exchange, we can similarly recast f_x in a gauge-invariant form F_x

$$F_x \equiv f_x - \frac{Q_x(v_x - \bar{v})}{H\rho_x(1+w_x)}. \tag{8.38}$$

All the ingredients introduced so far are now sufficient to allow us to study the evolution of the perturbation variables $\{\Delta_m, \Delta_r, \Delta_\phi, v_m, v_r, v_\phi\}$. In the regime where perturbations are small, we find the following set of coupled differential equations (Kodama and Sasaki [1984])

$$\frac{d\Delta_m}{dN} = \frac{9}{2}\frac{aH}{k}(1+w)(\bar{v}-v_m) - \frac{Q_m\Delta_m}{aH\rho_m} - \frac{k}{aH}v_m + \frac{Q_mE_m}{\rho_m H} + F_m, \tag{8.39}$$

$$\frac{d\Delta_r}{dN} = 6\frac{aH}{k}(1+w)(\bar{v}-v_r) + \Delta_r - \frac{4k}{3aH}v_m, \tag{8.40}$$

$$\begin{aligned}\frac{d\Delta_\phi}{dN} = &\left(3w_\phi - \frac{Q_\phi}{H\rho_\phi}\right)\Delta_\phi + \\ &\frac{2x^2}{\rho_\phi}\left[\frac{9}{2}\frac{aH}{k}(1+w)(\bar{v}-v_\phi) - \frac{k}{aH}v_\phi\right] + \frac{Q_\phi E_\phi}{\rho_\phi H} + (1+w_\phi)F_\phi,\end{aligned} \tag{8.41}$$

$$\frac{dv_m}{dN} = -v_m - \frac{3aH}{2k}\bar{\Delta} + F_m, \tag{8.42}$$

$$\frac{dv_r}{dN} = -v_r + \frac{k}{4aH}\Delta_r - \frac{3aH}{2k}\bar{\Delta}, \tag{8.43}$$

$$\frac{dv_\phi}{dN} = -v_\phi + \frac{k}{(1+w_\phi)aH}\Delta_\phi - \frac{3aH}{2k}\bar{\Delta} + F_\phi, \tag{8.44}$$

where

$$\bar{v} = \frac{1}{1+w}\left(2x^2v_\phi + \frac{4}{3}r^2v_r + m^2v_m\right), \tag{8.45}$$

$$\bar{\Delta} = \left(m^2\Delta_m + r^2\Delta_r + (x^2+y^2)\Delta_\phi\right) + \frac{a}{k}\sum_x Q_xv_x, \tag{8.46}$$

$$w = \frac{1}{\rho}(\rho_rw_r + \rho_\phi w_\phi) = \frac{r^2}{3} + (x^2+y^2)w_\phi. \tag{8.47}$$

Note that by setting Q_x, E_x and F_x to 0, we recover the non-interacting case. The initial values of the perturbations are fixed using adiabatic initial conditions (Chongchitnan and King [2010]; Doran et al. [2003]) which we calculate to be

$$\frac{\Delta_m}{1-q_m} = \frac{3}{4}\Delta_r, \quad \Delta_\phi = 3\frac{\dot{\phi}^2}{\rho_\phi}\left(\frac{aH}{k}\right)^2\bar{\Delta}, \quad q_x = \frac{Q_x}{3aH\rho_x}$$

$$v_m = \frac{k}{3aH}\frac{\Delta_m}{1-q_m}, \quad v_r = \frac{k\Delta_r}{3aH}, \quad v_\phi = 0. \tag{8.48}$$

The only free variable is the initial matter density perturbation which is determined by normalising the matter power spectrum at a pivot scale which we take to be $k = 0.001\text{Mpc}^{-1}$. The power spectrum of energy component x is calculated by comparing the amplitudes of the growing mode at early and late times

$$P_x(k) = k^{n_s} \left[\frac{\Delta_x(z=0)}{\Delta_x(z=10^8)} \right]^2 , \tag{8.49}$$

where n_s is the primordial scalar spectral index taken to be 0.96.

8.4.2 Power spectra without interactions

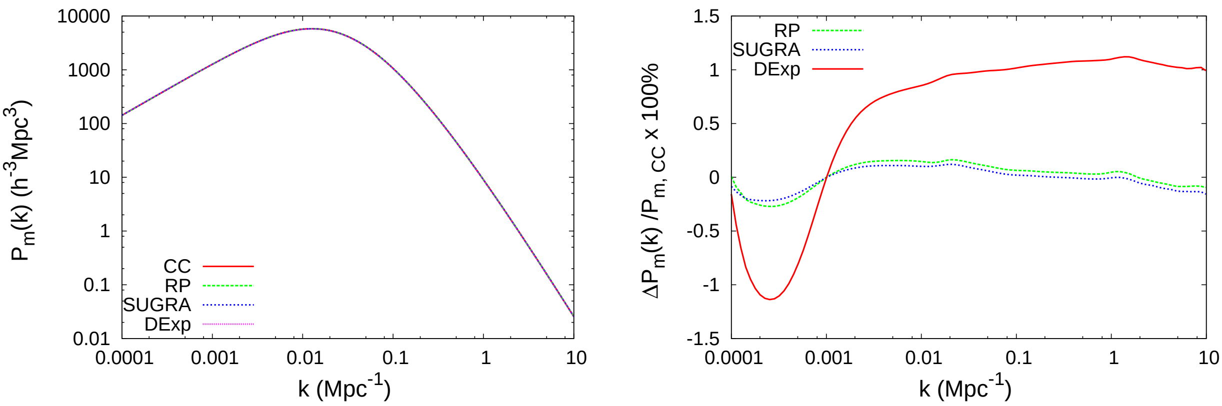

Figure 8.2: *Left:* If there is no interaction in the dark sector, the linear matter power spectra for all four 'best-fit' dark energy models are essentially indistinguishable. *Right:* the fractional percentage difference between the matter power spectra of the quintessence models and the cosmological constant. The best-fit models all exhibit sub-percent differences from the cosmological constant.

Figure 8.2 shows the matter power spectrum for all four dark energy models as well as the fractional difference in the matter power spectra for the quintessence models relative to the cosmological constant expressed as a percentage.

$$\frac{P_m(k)^{\text{model}} - P_m(k)^{CC}}{P_m(k)^{CC}} \times 100\%.$$

Note that our calculations are not valid for scales $k > 0.1$ where we expect a significant enhancement in the power spectra due to non-linearities. The equations governing the perturbations in the non-linear regime are beyond the scope of our work. To study the perturbations in this regime, one requires an $N-$body simulation as in Alimi et al. [2010]; Rasera et al. [2010] or a more sophisticated perturbation theory (Bernardeau et al. [2002]).

Differences between the models are small with the largest difference $\approx 1\%$ observed for the DExp potential. The quintessence models have an excess power for $k > 0.001\text{Mpc}^{-1}$ and a

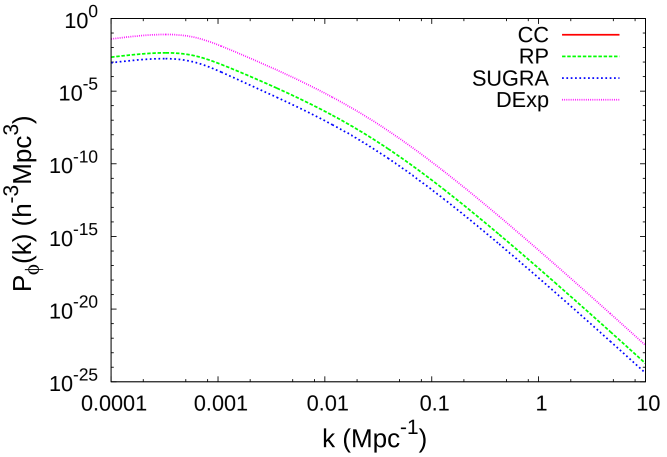

Figure 8.3: The linear power spectra for dark energy for the three quintessence models with no interactions. Note the 'turnover' on very large scales close to the Hubble radius ($\sim 2 \times 10^{-4}$Mpc^{-1}) indicating the typical size of dark energy perturbations.

power deficit for $k < 0.001$Mpc^{-1}. This correlates well with the 'turnover' to the dark energy spectra shown in Figure 8.3. Nevertheless, these small differences of order 1% in matter power spectra for the models are essentially unobservable.

The power spectrum for dark energy perturbations, shown in Figure 8.3, are roughly four orders of magnitude smaller than the matter power spectra. Thus, we do not expect to see large differences in the matter power spectra of the quintessence models due to dark energy clustering. We see that the large-scale clustering of dark energy enhances the clustering of dark matter on large scales. The dark energy power spectra are approximately constant on very large scales ($k < 0.001$Mpc^{-1}), and decay exponentially on small scales. In fact, dark energy clustering is significant mainly on large scales in all models in which the sound speed of dark energy equals the speed of light (de Putter et al. [2010]). The decay of the power spectrum is split into two regions with different exponents changing near the turnover scale in the matter power spectrum. The differences in the power spectra of the different quintessence models is due to the different values of w_ϕ at late times, since $\Delta_m \propto (1 + w)$ (see 8.39 and 8.47). We will shortly investigate the effects of dark sector interactions on these power spectra.

8.5 Integrated Sachs-Wolfe effect

The Integrated Sachs-Wolfe effect (ISW) is an effect observed in the CMB for small multipole number ℓ caused by the blueshifting of photons as the gravitational potential wells become shallower due to the late-time cosmic acceleration (Sachs and Wolfe [1967]). The gravitational potential Φ can be decomposed as:

$$\Phi = \Phi_m + \Phi_r + \Phi_\phi. \tag{8.50}$$

The potential Φ is related to the perturbation variables by the cosmological Poisson's equation

$$\Phi = -\frac{3}{2}\left(\frac{aH}{k}\right)^2 \overline{\Delta}. \tag{8.51}$$

Consider the CMB temperature anisotropy $\Delta T/T(\mathbf{n})$ along the line-of-sight unit vector $\mathbf{n}$. The CMB anisotropy power spectrum is given by

$$\left\langle \frac{\Delta T}{T}(\mathbf{n})\frac{\Delta T}{T}(\mathbf{m})\right\rangle_{\mathbf{n}\cdot\mathbf{m}=\mu} = \frac{1}{4\pi}\sum_\ell (2\ell+1)C_\ell P_\ell(\mu), \tag{8.52}$$

where C_ℓ is amplitude of the CMB angular power spectrum at the ℓ-th multipole and P_ℓ is the Legendre polynomial of order ℓ. By decomposing $\Delta T/T$ into the spherical harmonics and integrating over all directions we find (Durrer [2008])

$$C_\ell^{\mathrm{ISW}} \sim \int_0^\infty \int_{z_{\mathrm{dec}}}^0 k^2 \left| -\frac{H}{a}\frac{d\Phi}{dz} J_\ell^2\left(k\int_0^z \left[\frac{1}{H(z')(1+z')}\right] dz'\right)\right|^2 dz\, dk, \tag{8.53}$$

where z_{dec} is the redshift at which photon decoupling occurs (~ 1020) and $J_\ell(x)$ is the spherical Bessel function of order ℓ.

Figure 8.4 shows the squared percentage differences between C_ℓ^{ISW} for the three quintessence models and the cosmological constant model

$$\left(\frac{C_\ell^{\mathrm{quint}} - C_\ell^{\mathrm{CC}}}{C_\ell^{\mathrm{CC}}}\right)^2 \times 100\%,$$

in comparison with the cosmic variance

$$(C_\ell^{\mathrm{var}})^2 = \frac{2}{2\ell+1}. \tag{8.54}$$

The relative differences in the ISW effect for quintessence models and ΛCDM are completely overwhelmed by cosmic variance. They are also much smaller than indicated in other

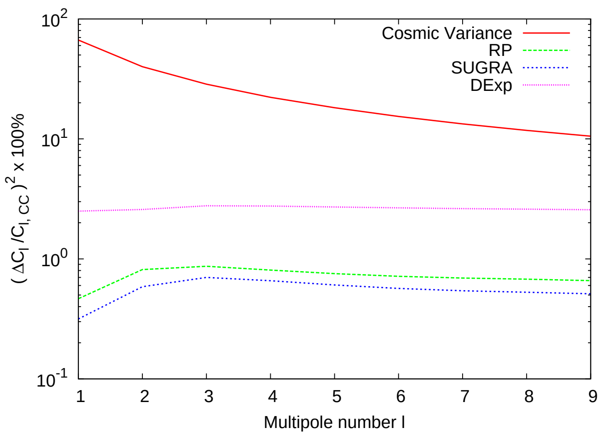

Figure 8.4: The percentage differences between $C_\ell^{\rm ISW}$ for the three quintessence models and the CC model. The contributions from quintessence are overwhelmed by cosmic variance, hence the models are observationally indistinguishable via the ISW effect.

investigations in which the equation of state for dark energy was parameterised by simple ansatz e.g. $w_\phi = w_0$ or $w_\phi = w_0 + w_1 z$ (where w_0 and w_1 are constants). This is perhaps not surprising since our 'best-fit' quintessence models can closely replicate ΛCDM dynamics whereas these parameterisations can diverge from ΛCDM dynamics substantially.

In summary, we find that the ISW is an ineffective discriminant between the cosmological constant and models of quintessence that deviate from $w = -1$ at very low redshifts. In the next section, we investigate whether this conclusion is changed if there are interactions between quintessence and dark matter.

8.6 Modelling dark sector interactions

In this section, we introduce three models of dark sector interactions and explain how they can be rewritten in covariant forms.

8.6.1 Dark matter decay

We first consider a dark sector interaction of the form

$$Q_m = -A\rho_m, \tag{8.55}$$

which represents the decay of dark matter into dark energy with a constant decay rate. The decay rate per unit energy density of dark matter is quantified by the positive constant A, which we refer to as the interaction strength. This form of interaction has been previously investigated in Väliviita et al. [2008].

In the covariant formulation, the interaction term is given by $A\rho_m u_m$, where $u_m = (-a, \mathbf{0})$, since this is the rate at which 4-momentum is transferred to dark energy. Hence,

$$Q_{(m)\mu} = -A\rho_m u_{(m)\mu}. \tag{8.56}$$

We perturb the above equation to find

$$\widetilde{Q}_{(m)\mu} = Q_m(1+\delta_m)\widetilde{u}_{(m)\mu}, \qquad \widetilde{Q}_\phi = Q_\phi(1+\delta_m)\widetilde{u}_{(m)\mu}. \tag{8.57}$$

Using Equations 8.23, 8.29, 8.31, 8.35 and the above, we find the gauge-invariant energy transfer

$$\epsilon_m = \delta_m, \qquad E_m = \Delta_m, \qquad E_\phi = \Delta_m + 3\frac{aH}{k}\left(1 - \frac{Q_m}{3H\rho_m}\right)(v_\phi - v_m). \tag{8.58}$$

Similarly, using Equations 8.34, 8.36, 8.37 and 8.38, we find the momentum transfer

$$f_m = \frac{Q_m(v_m - \bar{v})}{H\rho_m}, \qquad F_m = 0, \qquad F_\phi = \frac{Q_\phi(v_m - v_\phi).}{H\rho_\phi(1+w_\phi)}. \tag{8.59}$$

8.6.2 Dark energy decay

The second model represents the case in which dark energy decays into dark matter at a constant decay rate (Lima [1996]). This may be applicable, for instance, in the early dark energy scenario (Doran and Robbers [2006]). The interaction term has the form

$$Q_\phi = -A\rho_\phi, \qquad Q_m = A\rho_\phi, \qquad Q_{(\phi)\mu} = -A\rho_\phi u_{(\phi)\mu}. \tag{8.60}$$

Similarly, using Equations 8.29–8.38, we find the gauge-invariant energy and momentum transfers

$$E_\phi = \Delta_\phi - 3\frac{aH}{k}(1+w_\phi)\left[\frac{Q_\phi v_\phi}{3H\rho_\phi(1+w_\phi)} + \frac{aH}{2k}\overline{\Delta}\right], \tag{8.61}$$

$$E_m = \Delta_\phi + 3\frac{aH}{k}(1+w_\phi)\left[v_m - v_\phi - \frac{Q_\phi v_m}{3H\rho_\phi(1+w_\phi)} - \frac{aH}{2k}\overline{\Delta}\right]. \tag{8.62}$$

$$F_\phi = 0, \qquad F_m = \frac{Q_m(v_\phi - v_m)}{H\rho_\phi}. \tag{8.63}$$

Note that the momentum transfer F_m and F_ϕ are 'orthogonal' to those in the dark matter decay model.

8.6.3 Scalar-tensor model

Finally, let us consider an interaction term which appears in some scalar-tensor theories of gravity Amendola [2004]

$$Q_{(\phi)\mu} = A\rho_m\nabla_\mu\phi, \qquad Q_{(m)\mu} = -A\rho_m\nabla_\mu\phi. \tag{8.64}$$

Using Equation 8.34 we find

$$\widetilde{Q}_\phi = -\widetilde{u}^\mu A\rho_m(1+\delta_m)\partial_\mu\widetilde{\phi}, \qquad Q_\phi = A\rho_m\dot{\phi} \tag{8.65}$$

where u^μ is the average velocity. To calculate the gauge-invariant interaction, we use the following useful expressions for the perturbed scalar field

$$\frac{\partial\widetilde{\phi}}{\partial t} = \dot{\phi} - \Phi\dot{\phi} + \delta\dot{\phi}, \qquad \delta\phi = \frac{av_\phi\dot{\phi}}{k}, \tag{8.66}$$

$$\frac{\delta\dot{\phi}}{\dot{\phi}} = \frac{\Delta_\phi}{1+w_\phi} + \Phi - \frac{(3H\dot{\phi}+V')\delta\phi}{\dot{\phi}^2}. \tag{8.67}$$

Using Equations 8.12, 8.35 and 8.30, we find the gauge-invariant energy transfer variables

$$E_\phi = \Delta_m + \frac{\Delta_\phi}{1+w_\phi} + \frac{3aH}{k}\left(\frac{Q_m}{3H\rho_m} - 1\right)v_m + \frac{3}{2}\left(\frac{aH}{k}\right)^2\overline{\Delta}, \tag{8.68}$$

$$E_m = \Delta_m + \frac{\Delta_\phi}{1+w_\phi} + \frac{3aH}{k}\left(\frac{Q_m v_m}{3H\rho_m} - v_\phi\right) + \frac{3}{2}\left(\frac{aH}{k}\right)^2 \overline{\Delta} - \frac{3aH}{k}\frac{y^2\lambda}{\sqrt{6}x}(v_m - v_\phi). \quad (8.69)$$

Similarly, from 8.27, 8.36, 8.38 and 8.64, we find the gauge-invariant momentum transfer variables to be

$$f_\phi = \frac{A\rho_m\dot{\phi}(v_\phi - \bar{v})}{H\rho_\phi(1+w_\phi)}, \qquad F_\phi = 0, \qquad F_m = \frac{Q_\phi(v_m - v_\phi)}{H\rho_m}. \quad (8.70)$$

8.7 Results

We are now ready to calculate the observables for the different interaction models. In particular, we would like to establish whether dark sector interactions could give rise to observable imprints in the power spectrum or the ISW effect whilst satisfying the constraint that w is very close to -1. We use the SUGRA potential for the dark energy decay and scalar-tensor model because, at the background level, it behaves most similarly to the cosmological constant (see Figures 8.1 and 8.2). It is computationally more challenging to implement the SUGRA potential with the dark matter decay model due to the non-monotonic nature of the potential so the RP potential was used instead (where an analytic solution for ϕ can be calculated given the value of $V(\phi)$). In all cases, however, we did not find a sensitive dependence on the choice of potential.

8.7.1 Instability in the dark energy decay model

Our computation shows that the decaying dark energy model was found to suffer from an instability in the perturbations. From Equation 8.16, we see that significant values of interaction strength act to drive the value of x towards 0, causing $\mathrm{d}x/\mathrm{d}N$ and v_ϕ to become infinite. Below the critical value of interaction strength associated with this instability, there is no significant effect on the power spectra or ISW effect. An example of this instability is shown in Figure 8.5 in which the interaction strength A is chosen to be just above the critical value. Starting at $z = 10^8$, we see that x decreases to 0 at $\ln a = -12.3$ where the instability develops. By considering very early times, we can effectively set the limit on the interaction strength to 0 and

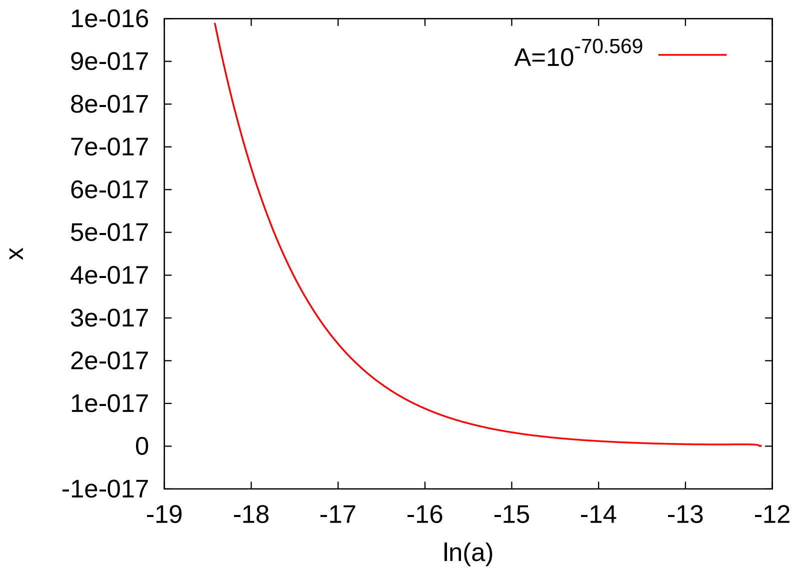

Figure 8.5: Evolution of the variable $x \propto \dot{\phi}$ in the decaying dark energy model using the SUGRA potential. x passes through zero and becomes negative at $\ln a = -12.336$ causing an instability in the power spectra. This behaviour occurs for interaction strengths larger than $\sim 10^{-70} m_{\rm Pl}$.

rule out this model of dark energy. This is because even small interaction strengths would, at early times, cause the small amount of scalar field kinetic energy to dissipate quickly, leading to this instability. In general, regardless of the choice of quintessence potential, we find that the susceptibility of the dark energy decay model to this instability makes it unviable as a model for interacting dark energy.

8.7.2 Dark matter decay

The primary effect of the dark matter decay model is to alter the time at which dark energy comes to dominate the Universe. This is because dark matter decay is most effective at early times when matter dominates over dark energy. This means that the background evolution of our 'best-fit' models is sensitive to the interaction strength. For instance, an interaction strength $A = 10^{-62} m_{\rm Pl}$ changes the dark energy density at $z = 0$ by roughly 1%, but leaves the matter power spectrum and ISW effect virtually unchanged.

Figure 8.6 shows the evolution of the x variable for interaction strengths in the range $10^{-63} - 10^{-60} m_{\rm Pl}$. We see that the dark energy density is sharply boosted at early times, as the energy is immediately transferred from dark matter to dark energy. In Figure 8.7, we show

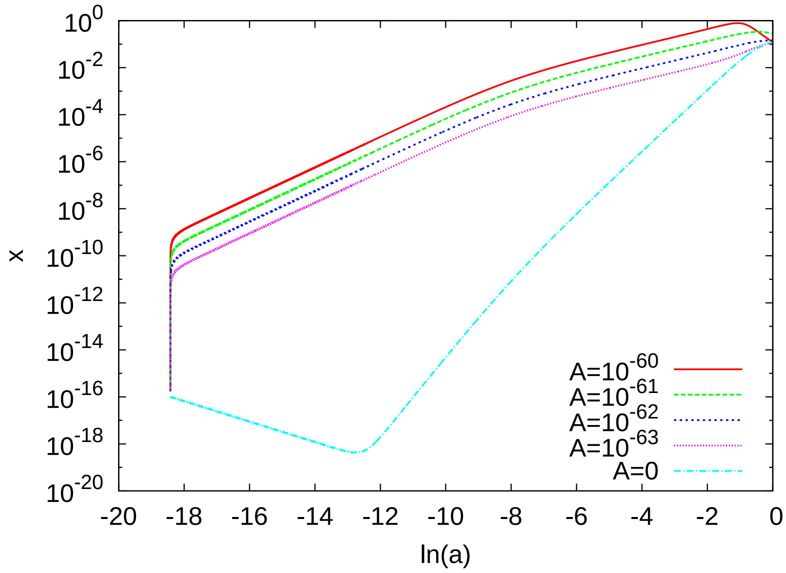

Figure 8.6: Evolution of the energy variable $x \propto \dot{\phi}$ in the decaying dark matter model using the RP potential. We see that increasing the interaction strength A boosts the value of x at early times which can lead to an increase in late time dark energy densities.

the evolution of w_ϕ over the same range of interaction strengths. We see the corresponding sharp rise in w_ϕ towards 1 at early times. This has the effect of redshifting away the excess dark energy at a rate $\rho_\phi \propto a^{-6}$. This rapid redshifting means that for a wide range of $V(\phi)$, dark energy does not come to dominate the universe too soon and so this model of interactions can indeed be reconciled with observations.

A number of previous investigations of this interaction have used simple parameterisations of w_ϕ. However, we see from Figure 8.6 that the complex redshifting behaviour of dark energy would be extremely difficult to reproduce with a simple analytic form of w_ϕ. In fact, an instability in this form of interaction was found in Väliviita et al. [2008] when considering dark energy parameterised by $w_\phi =$ constant. We can see that in a $w =$constant model where $w < 0$, the early boost in the dark energy density will not be redshifted away relative to the dark matter energy density and dark energy will come to dominate the Universe too soon for any appreciable interaction strength. It is interesting that due to the redshifting behaviour described above, our quintessence models do not encounter such an instability.

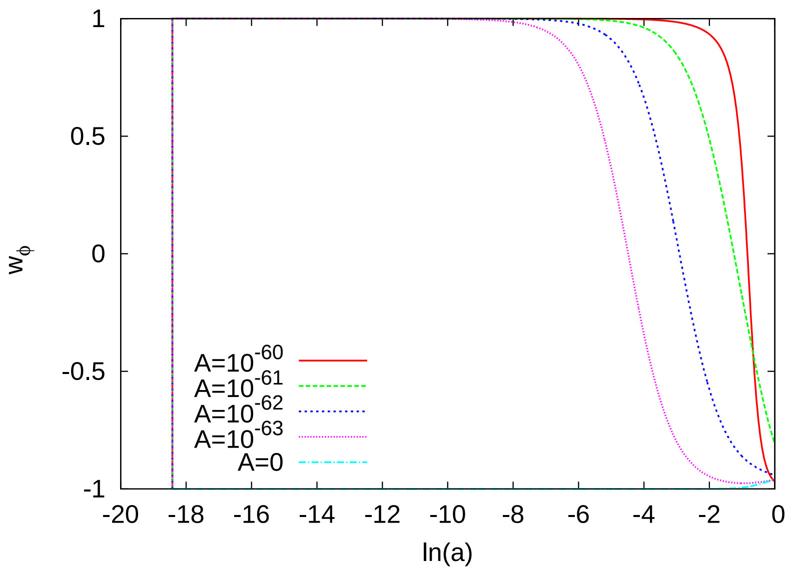

Figure 8.7: Evolution of w_ϕ for the dark matter decay models presented in Figure 8.6. At early times w_ϕ responds to the sharp increase in x by rising suddenly to a value of 1. See the text for further discussion.

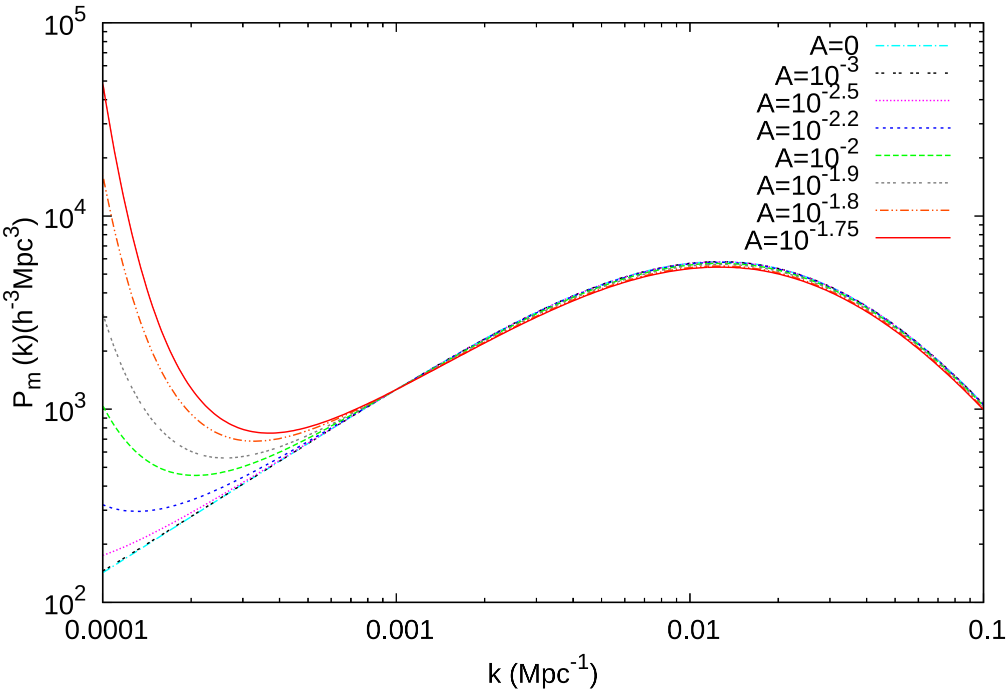

Figure 8.8: The linear matter power spectra in the SUGRA quintessence model with dark sector interaction of the 'scalar-tensor' form $Q_\phi = A\rho_m\dot{\phi}$. Large values of A cause a significant enhancement to the power spectrum on very large scales. The interaction also leads to a smaller $\sim 6\%$ difference between the power spectra of the largest interaction strength and no interaction on scales $k > 0.01\text{Mpc}^{-1}$.

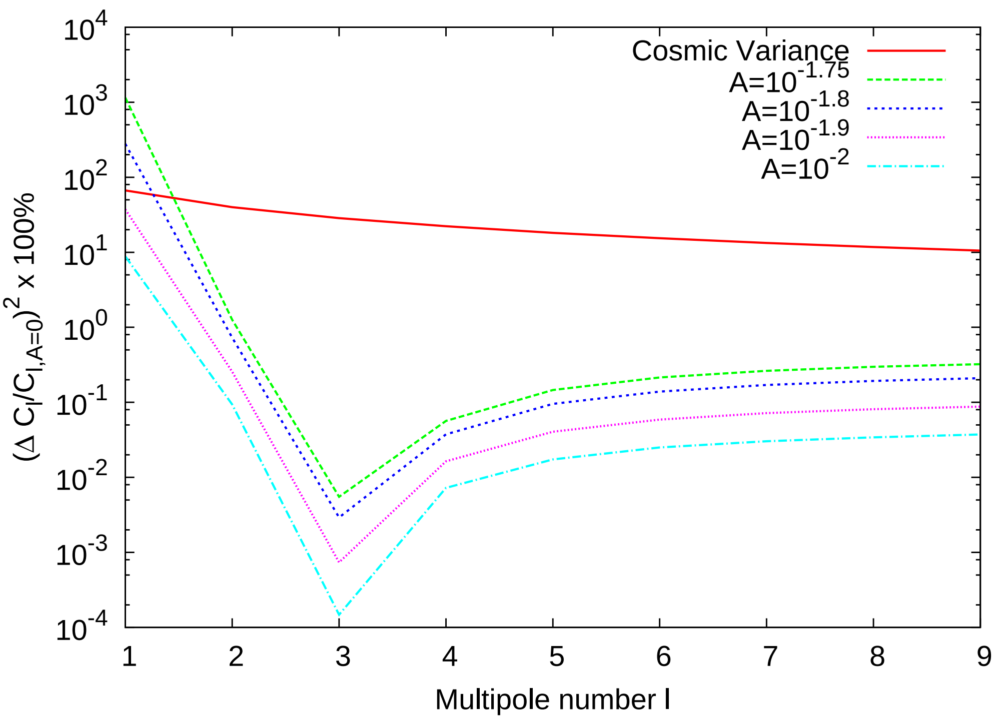

Figure 8.9: The fractional difference in the ISW effect in an interacting model relative to no interaction using the SUGRA potential. Only the $\ell = 1$ dipole moment of the largest two interaction strengths are observable above the cosmic variance. The largest interaction strength leads to an order of magnitude enhancement to the CMB dipole moment relative to ΛCDM.

8.7.3 Scalar-tensor model

The scalar-tensor model exhibits the most interesting behaviour of the three interaction models considered in this work. The sign of the interaction can be changed to represent the flow of energy from one dark component to the other since the interaction depends both on dark matter and dark energy. If we choose $Q_\phi = A\rho_m\dot{\phi}$ where A is negative, we encounter the same instability in the x variable which we found in the dark energy decay model. From Equation 8.16, we can easily deduce whether a model with $Q_\phi \propto x^n$ would develop an instability or not. When $n < 1$, the interaction term becomes increasingly negative as x decreases, hence leading to an instability. For models where $n > 1$, however, the negative constant tends to 0 as x tends to 0 and so an instability is avoided. In this model $n = 1$ and to avoid an instability we require that the sign of the interaction term should represent the flow of energy from dark matter to dark energy, i.e. $Q_\phi = A\rho_m\dot{\phi}$ with $A > 0$. This supports the conclusion in Chongchitnan [2009] which found no background instabilities in this model.

We find that this form of interaction does not change the energy density of dark energy significantly at early times since $Q_\phi \propto \dot{\phi}$ and $\dot{\phi}$ is small at early times. The energy transfer becomes significant only at late times when dark energy becomes dominant. As we increase the interaction strength we see an enhancement in the matter power spectrum on large scales, as shown in Figure 8.8. The power spectrum on smaller scales $k > 0.01\text{Mpc}^{-1}$ decreases by $\sim 6\%$ relative to ΛCDM for the largest interaction strength shown.

We have shown that a scalar-tensor interaction can lead to an enhancement in the matter power spectrum on large scales. In order to detect this intrinsic enhancement we must be able to distinguish it from other artificial and observational effects such as gauge artifacts, the scale dependence of the galaxy bias and redshift space distortions which can also cause enhancements to the matter power spectrum on large scales and mimic our result (see Yoo et al. [2009], Bruni et al. [2011], Challinor and Lewis [2011] and Bonvin and Durrer [2011]). We will now address these effects in more detail and explain how we can break the degeneracy between an intrinsic large-scale enhancement due to a scalar-tensor interaction and a similar enhancement caused by the effects above.

The work by Yoo et al. [2009] showed that calculating matter power spectra using gauge-dependent quantities can introduce gauge modes which can cause artificial large-scale enhancement in the power spectrum. We have used gauge-invariant quantities in our calculations and so the large-scale enhancement we have found is not due to such a gauge artifact. The linear bias is a linear relation between fractional overdensities of galaxies and matter ($\delta_g \propto \delta_m$) which is used to infer the total matter power spectrum from a galaxy survey. Work by Bruni et al. [2011] showed that the linear bias is scale-independent only in the comoving-synchronous gauge and using perturbations defined in a different gauge leads to the linear bias having a scale-dependence. They showed that if the linear bias is used as a scale-independent relation in a different gauge it can lead to an artificial large-scale enhancement in the matter power spectrum (Bruni et al. [2011]). So it is important to use the correct form of the linear bias relation for a gauge because otherwise it could artificially replicate the signal from a scalar-tensor interaction.

Redshift space distortions are caused by the peculiar velocities of the luminous matter we observe. These small peculiar velocities produce an additional Doppler shift in the observed photon frequency relative to the average redshift caused by the background expansion velocity of the region. For large-scale overdensities the surrounding infalling matter will have an additional component of their peculiar velocities directed towards the overdensity. This leads to the region appearing compacted in redshift space which causes an apparent enhancement to the overdensity (since redshift is used as a proxy for distance).

We can take account of the effects of redshift space distortions, magnification by gravitational lensing and distortions to the luminosity distances of sources using the results of the recent work by Yoo et al. [2009], Challinor and Lewis [2011] and Bonvin and Durrer [2011]. They calculate photon geodesics in a perturbed universe, this takes into account the deflection and redshifting of observed photons through interactions with overdensities. They then use the perturbed geodesics of the photons we observe to relate gauge-invariant observables from galaxy surveys (like the matter power spectrum) to the cosmological quantities calculated in theoretical models such as ours. Using the results of Yoo et al. [2009], Bruni et al. [2011], Challinor and Lewis [2011] and Bonvin and Durrer [2011] we can break the degeneracy between an intrinsic large-scale enhancement due to interactions in the dark sector and enhancements due to the observational effects discussed above.

A recent work by Tarrant et al. [2011] investigated the effect of an interaction of the form (8.64) on the background evolution, matter power spectrum and halo mass function using quintessence models. They found that significant negative values of the interaction strength A could lead to an enhancement in the matter power spectrum relative to ΛCDM, in agreement with our findings. The authors did not use fully gauge-invariant perturbation variables or include the effects of momentum transfer in their investigation, although they did include baryons and non-linear effects which we have neglected. They did not find the instability in the x variable when $A < 0$, corresponding to dark energy decaying to dark matter. We expect that this is due to the substantially different treatment of the perturbations and the quintessence potentials they used.

The production of large-scale enhancement of the matter power spectrum is interesting and would be a very significant result if this could be resolved in future observations. Recent work by Macaulay et al. [2011] used peculiar velocities to constrain the matter power spectrum and found that an enhancement to the matter power spectrum on large scales was favoured by the data. However, due to large errors primarily from cosmic variance, the findings were also consistent with ΛCDM. Nevertheless, peculiar velocities could potentially be used to constrain the large-scale matter power spectrum in the future when a greater number of accurate measurements are available.

Finally, Figure 8.9 shows how the ISW signal changes with increasing interaction strength. We observe that the interaction yields an enhancement in the ISW signal around only the lowest multipoles (since the dark energy spectrum peaks at small k corresponding to small ℓ). Only the $\ell = 1$ moment of the two strongest interaction strengths plotted ($A = 10^{-1.75} m_{\rm Pl}^{-1}$ and $A = 10^{-1.8} m_{\rm Pl}^{-1}$) are observable above cosmic variance. The largest interaction strength leads to an order of magnitude enhancement to the CMB dipole moment relative to ΛCDM.

The recent high redshift survey by Thomas et al. [2010] found evidence of an excess clustering on large scales ($k < 0.01h\text{Mpc}^{-1}$) at 4σ significance from ΛCDM. They used photometric redshifts from a sample of SDSS galaxies to measure the angular power spectrum and found an excess in the lowest multipoles of the angular power spectrum. This is a very promising result, since it can be interpreted as the effect of the dark sector interaction as shown in Figures 8.8 and 8.9. These authors also tested the analysis of their data and biases and concluded that the large-scale enhancement was a real effect which hinted at an exotic form of dark energy.

We find the recent evidence for enhanced power in $P(k)$ on large scales to be encouraging in light of our findings. However, we can see from Figures 8.8 and 8.9 that even if there were significant increments in the matter power spectrum at these near-horizon scales, they are only detectable in the dipole moment of the CMB, a measurement which is dominated by the Doppler shift caused by our own peculiar velocity. Unfortunately, the enhancements to the matter power spectrum on scales $k < 0.001\text{Mpc}^{-1}$ are well beyond the scales probed in current galaxy surveys ($k \sim 0.01\text{Mpc}^{-1}$), so we do not expect that a direct detection of this large-scale enhancement via galaxy counts will be possible in the near future.

Using the cross-correlation of the CMB and large-scale structure from galaxy surveys is likely to be one of the most promising observational probes of our results. This technique allows us to isolate the ISW effect from other contributions to the CMB at low multipole moments since perturbations at the surface of last scattering were small compared to the observed large-scale structure today. Large-scale structure is correlated with the ISW effect since the

ISW effect is caused by the evolution of gravitational potentials. Using the cross-correlation allows us to measure the ISW effect and compare this to the enhancement predicted in the scalar-tensor model for large interaction strengths (Figure 8.9). The work by Giannantonio et al. [2008] calculated the cross-correlation using WMAP 7 and several galaxy surveys and found an excess ISW cross-correlation of 1σ from ΛCDM. This excess is interesting as it could be explained by a scalar-tensor dark sector interaction.

8.8 Conclusion and discussion

In this Chapter, we have calculated the background evolution, matter and dark energy power spectra and ISW effect for three quintessence models with and without dark sector interactions. Our calculations are based on gauge-invariant perturbation theory originally developed to calculate inflationary perturbations. We feel that our calculations are more reliable than those obtained when dynamical dark energy is parameterised by phenomenological ansatz for w, since in our approach the clustering of dark energy can be directly linked to the underlying scalar-field perturbations.

We found that without interactions our quintessence models differ from ΛCDM by at most a few percent in observable quantities, meaning that any differences are essentially unobservable.

We have shown how a covariant treatment of dark sector interactions can give rise to momentum exchanges in the dark sector, which many authors have overlooked. Our approach complements and extends the work of Väliviita et al. [2008], who examined momentum exchanges in constant w models using the dark matter decay interaction. We demonstrate our techniques on three models of interactions, namely, the dark energy decay, dark matter decay and scalar-tensor type of interaction.

The dark energy decay model was found to have an instability in the perturbations, in agreement with previous works on this interaction, and thus can be ruled out. In the decaying dark matter model, we found that its primary effect was to change the evolution of the background energy densities, with no observable differences in the power spectra or ISW effect. We explained why w =constant models, when associated with this interaction, will lead to an instability, which is absent when field dynamics are taken into account.

The scalar-tensor model of interactions appears to be the most interesting and robust of all three. We showed that it is stable if energy flows from dark matter to dark energy. For this case, we found that the interaction enhances the clustering of dark energy and dark matter on very large scales ($k < 0.001\text{Mpc}^{-1}$) and produced an enhanced ISW effect which, unfortunately, exceeds cosmic variance only in the lowest multipoles. We also found that the interaction produces a significant enhancement in the matter power spectra on very large scales.

We find the recent indications of enhanced large-scale clustering via peculiar velocity measurements (Macaulay et al. [2011]) and enhancement to the lowest multipoles of the angular power spectrum (Thomas et al. [2010]) encouraging, although, measurements on these scales are very difficult to make and are often dominated by cosmic variance and our own peculiar velocity.

Overall, the prospects of constraining dark sector interactions via the matter power spectrum and ISW effect appear daunting. The enhancement to the matter power spectrum on scales $k < 0.001\text{Mpc}^{-1}$ is too large to be probed by current galaxy surveys $k \sim 0.01\text{Mpc}^{-1}$. There are certainly other observational probes, however, which may reveal the presence of interactions in the dark sector, including i) cross-correlation of the ISW with galaxy and quasar distributions (Giannantonio [2008]; Giannantonio et al. [2008]; Mainini and Mota [2010]), ii) the growth rates of large-scale structures at high redshift, (Kwan et al. [2011]; Orsi et al. [2010]; Simpson [2010]), iii) effects of large super-horizon perturbations on the CMB (Bielby et al. [2011]; Grishchuk and Zeldovich [1978]), iv) gravitational lensing of the CMB using EPIC (Martinelli et al. [2010]). We envisage that our calculation techniques can be adapted to explore these issues at least in the linear regime.

Finally, there will almost certainly be interesting non-linear effects on the matter power spectrum and CMB anisotropies arising from dark sector interactions. However, analytic progress in this regime is extremely challenging (though not impossible, Bernardeau et al. [2002]). N-body simulations such as those initiated by Rasera et al. [2010] may hold the key to understanding the non-linear effects of dark sector interactions.

Chapter 9

Conclusions

In this thesis I have developed a flexible, rigorous model for the emission from a relativistic jet including a detailed treatment of the relevant physical processes. The model has a magnetically dominated accelerating parabolic base transitioning to a slowly decelerating conical jet where the plasma approaches equipartition (referred to as the transition region). The jet geometry is set by radio observations of the jet in M87 and consistent with simulations and theory. I have shown that this model is able to fit very well to the spectra of all 38 blazars with known redshifts and simultaneous multiwavelength observations. This model offers a significant improvement on existing models for jet emission which typically represent the jet's structure as one or two spherical blobs and are unable to reproduce the observed radio emission.

Through fitting this sample of blazars including both BL Lacs and FSRQs I have found that the spectra of FSRQs are best fitted by powerful jets with high bulk Lorentz factors and large radius transition regions. The inverse-Compton emission of most BL Lacs is produced by SSC emission whilst the inverse-Compton emission of FSRQs is best fitted by scattering of CMB photons at large distances along the jet due to the large bulk Lorentz factors. I have shown that the synchrotron break in the radio, where the synchrotron emission of the jet transitions from optically thick to optically thin, can be used to constrain the radius of the transition region, where the jet first approaches equipartition. I calculated an analytic expression for this radius and confirmed the numerical results of my model. By fitting the synchrotron break at radio frequencies I show that FSRQ jets require large radius transition regions, incompatible with having the brightest synchrotron emitting region within the BLR or dusty torus as is usually assumed in the literature.

I postulated that the blazar sequence is due to a relation between the radius of the jet transition region and the jet power (as we might expect if jets scale linearly with black hole mass and blazars accrete at the same Eddington fraction). In this scenario BL Lacs with low jet powers, small radius transition regions and low bulk Lorentz factors have larger magnetic field strengths at the equipartition region of the jet than higher power FSRQs with larger radius transition regions. This results in high synchrotron peak frequencies and inverse-Compton emission which is due primarily to high frequency SSC emission in BL Lacs. The synchrotron emission of FSRQs has a correspondingly lower peak frequency and the inverse-Compton emission is due to scattering CMB photons at large distances along the jet due to the large bulk Lorentz factor of the jet. The Compton-dominance is due to the lower magnetic field strength producing less synchrotron emission and a larger bulk Lorentz factor leading to larger amounts of external-Compton emission. This provides an explanation for the observed blazar sequence.

I fitted all 38 blazars with multiwavelength observations and confirmed this hypothesis finding a linear correlation between the jet radius at equipartition and the jet power across 3 orders of magnitude in radius and jet power. I found the bulk Lorentz factor of FSRQs to be systematically larger than those of BL Lacs. I postulated two hypotheses to interpret these results depending on the distribution of black hole masses in blazars.

My first hypothesis assumes a universal jet geometry which scales linearly with the black hole mass of a blazar (as we might expect naively and as used in MHD jet simulations and theory). In this scenario I predicted a linear correlation between the transition region radius and the jet power if all blazars are accreting at the same Eddington fraction. Assuming all jets transition from parabolic to conical at $10^5 r_s$ as in M87, I found a plausible range of black hole masses $10^7 - 10^{10} M_\odot$ in agreement with galaxy surveys. In this scenario BL Lacs have smaller black hole masses than FSRQs resulting in smaller transition region radii. For the few FSRQs with visible accretion disc spectra, the black hole mass fitted independently to the disc spectrum agreed with that inferred for the jet only if the transition region occured at a distance of $10^5 r_s$ as in M87. However, indirect measurements of black hole masses of blazars suggest that, in fact, BL Lacs have slightly larger masses than FSRQs and so this scenario is disfavoured.

The observation of similar black hole masses for FSRQs and BL Lacs leads to a second hypothesis; an accretion mode dichotomy between BL Lacs and FSRQs. Assuming similar black hole masses in BL Lacs and FSRQs I found a bimodal Eddington accretion rate with BL Lacs having sub-Eddington accretion rates and FSRQs having accretion rates close to Eddington. This scenario is appealing due to its similarity to the relation between X-ray binary disc states and the onset of jet production. BL Lacs with radiatively inefficient, thick discs produce more mass loading in the jet due to entrainment of disc material and producing the lower maximum Lorentz factor compared to FSRQs, with thin discs and lighter mass loading. The smaller bulk Lorentz factors could be explained by the shorter accelerating region in low power BL Lacs compared to FSRQs. I found that the radio spectra of FSRQs were systematically steeper than BL Lacs requiring the jet to become particle dominated at large distances, while BL Lac jets were fitted by jets which remained close to equipartition. Together these properties could produce the morphological differences between FRI and FRII jets.

The new results from this model are very exciting and for the first time allow us to understand the physics behind the blazar sequence. In addition the model provides empirical evidence for the unification of BL Lac and FRI type jets, FSRQs and FRII type jets and their dependence on the accretion mode of the black hole.

In Chapter 7 I calculated the conditions for an accretion instability in a Shakura-Sunyaev α disc model. I showed that if α depends on the magnetic Prandtl number as suggested by simulations this can lead to an accretion instability for sensitive dependencies. I used a 1D fluid simulation to investigate the global behaviour of this instability in a realistic accretion disc. I found that the instability results in an unsustainable increase in the accretion rate in the innermost section of the disc and this increased accretion rate propagates out to radii of $\sim 1000r_s$ depleting the mass in the inner disc. This produces a cyclic flaring behaviour in the disc in which the disc temperature increases during the unstable flaring state before entering a quiescent period in which the disc inner temperature and accretion rate are low while the mass in the disc refills before becoming unstable again and flaring. This is a very significant result since it could offer the first plausible physical mechanism for the observed cyclic flaring behaviour in X-ray binary accretion discs. I showed that the behaviour of the flaring was consistent with observations of flaring disc spectra.

In Chapter 8 I investigated the observable effects of a scalar field model of dark energy interacting with dark matter in cosmology. I used a gauge-invariant covariant formalism to calculate expressions for several possible interactions between dark energy and dark matter including the unstable decay of dark matter into dark energy and vice-versa, and transfer of energy and momentum from dark matter to dark energy through a scattering type interaction. I calculated the effects of these interactions on the observed matter power spectrum and ISW effect and found that the unstable decay of dark energy to dark matter suffered from an instability. I found that the scalar-tensor type interaction produced a measurable enhancement to the ISW effect and matter power spectrum on horizon scales and used this to constrain the strength of this interaction.

9.1 Future work and limitations

There are several logical extentions to my work on blazars which would allow us to better understand the blazar population and to test whether my results and interpretation hold. The first is to use the luminosity function of AGN along with my jet model to simulate the observed population of FSRQ and BL Lac type blazars as a function of redshift. This would provide a convincing test of my hypothesis along with that of AGN unification based on observation angle.

I have used my jet model to fit to the quiescent observations of blazar spectra, however, blazars are well known for their short timescale variability and large magnitude flares. Reproducing the spectra of flaring blazars with their associated timescales would provide a challenging test for my model. This would allow us to try to constrain the location of the emission and particle acceleration responsible for the observed short duration gamma-ray flares, which is currently one of the most popular questions in the literature.

The main limitation of my jet model is the inability to simultaneously solve both the MHD and radiation processes in the jet, due to contraints set by computation time. I have based the geometry and kinematic properties of my model on observations of M87 and simulations. We do not yet know how the geometry of jets depends on the jet power, bulk Lorentz factor, accretion disc and environment due to the limited number of jets which we are able to observe and resolve in detail. I have made my jet model flexible so that it can easily incorporate developments in our understanding of the physical properties of jets in the future.

In Chapter 7 I showed that an accretion instability exists if the thin disc α parameter is not constant but depends on the properties of the plasma as found in MHD simulations. I investigated the time-dependent global behaviour of this instability using a simple 1D simulation and found that the instability produced flaring behaviour consistent with the observations of X-ray binaries. I intend to use a more detailed 3D MHD simulation to investigate whether in a more realistic simulation the instability can still produce the cyclic flaring behaviour indicated by observations.

Scalar field models of dark energy are interesting alternatives to a cosmological constant, however, in modern cosmology there are a miriad of models for dark energy which can closely mimic a cosmological constant. At what stage is it necessary to use Occam's razor to discard complicated alternatives to a cosmological constant which are finely tuned to be observationally indistinguishable? This is a fundamental problem with alternative theories of gravity, however, what they seem to lack in definite observational predictions they often make up for with a better physical motivation than a cosmological constant. In Chapter 8, I investigated the possibility of interactions between scalar field dark energy models and dark matter which have no equivalent in ΛCDM and so predicts new physics. In order to improve on my numerical predictions, an N-body simulation could be used to calculate the matter power spectrum and ISW effect to investigate the effect of non-linear behaviour at small scales.

The work in this thesis represents a substantial contribution to our understanding of jets and accretion discs and an interesting insight into the nature of dark energy and dark matter.

References

K. N. Abazajian, J. K. Adelman-McCarthy, M. A. Agüeros, S. S. Allam, C. Allende Prieto, D. An, K. S. J. Anderson, S. F. Anderson, J. Annis, N. A. Bahcall, and et al. The Seventh Data Release of the Sloan Digital Sky Survey. *ApJS*, 182:543–558, June 2009. doi: 10.1088/0067-0049/182/2/543. 179

A. A. Abdo, M. Ackermann, I. Agudo, M. Ajello, H. D. Aller, M. F. Aller, E. Angelakis, A. A. Arkharov, M. Axelsson, U. Bach, and et al. The Spectral Energy Distribution of Fermi Bright Blazars. *ApJ*, 716:30–70, June 2010a. doi: 10.1088/0004-637X/716/1/30. 9, 25, 44, 45, 50, 75, 94, 96, 117, 125, 142, 143, 152

A. A. Abdo, M. Ackermann, M. Ajello, M. Axelsson, L. Baldini, J. Ballet, G. Barbiellini, D. Bastieri, B. M. Baughman, K. Bechtol, and et al. A change in the optical polarization associated with a γ-ray flare in the blazar 3C279. *Nature*, 463:919–923, February 2010b. doi: 10.1038/nature08841. 134

A. A. Abdo, M. Ackermann, M. Ajello, E. Antolini, L. Baldini, J. Ballet, G. Barbiellini, D. Bastieri, K. Bechtol, R. Bellazzini, B. Berenji, R. D. Blandford, E. Bonamente, and Borgland. The First Fermi Multifrequency Campaign on BL Lacertae: Characterizing the Low-activity State of the Eponymous Blazar. *ApJ*, 730:101, April 2011a. doi: 10.1088/0004-637X/730/2/101. 41, 43, 47

A. A. Abdo, M. Ackermann, M. Ajello, L. Baldini, J. Ballet, G. Barbiellini, D. Bastieri, K. Bechtol, R. Bellazzini, B. Berenji, and et al. Fermi Large Area Telescope Observations of Markarian 421: The Missing Piece of its Spectral Energy Distribution. *ApJ*, 736:131, August 2011b. doi: 10.1088/0004-637X/736/2/131. 125

J. Abraham, P. Abreu, M. Aglietta, E. J. Ahn, D. Allard, J. Allen, J. Alvarez-Muñiz, M. Ambrosio, L. Anchordoqui, S. Andringa, and et al. Measurement of the energy spectrum of cosmic rays above 10^{18} eV using the Pierre Auger Observatory. *Physics Letters B*, 685: 239–246, March 2010. doi: 10.1016/j.physletb.2010.02.013. 17

I. Agudo, S. G. Jorstad, A. P. Marscher, V. M. Larionov, J. L. Gómez, A. Lähteenmäki, M. Gurwell, P. S. Smith, H. Wiesemeyer, C. Thum, J. Heidt, D. A. Blinov, and F. D. D'Arcangelo. Location of γ-ray Flare Emission in the Jet of the BL Lacertae Object OJ287 More than 14 pc from the Central Engine. *ApJL*, 726:L13, January 2011. doi: 10.1088/2041-8205/726/1/L13. 134

F. Aharonian, A. G. Akhperjanian, A. R. Bazer-Bachi, B. Behera, M. Beilicke, W. Benbow, D. Berge, K. Bernlöhr, C. Boisson, O. Bolz, and et al. An Exceptional Very High Energy Gamma-Ray Flare of PKS 2155-304. *ApJL*, 664:L71–L74, August 2007. doi: 10.1086/520635. 88, 117

J.-M. Alimi, A. Füzfa, V. Boucher, Y. Rasera, J. Courtin, and P.-S. Corasaniti. Imprints of dark energy on cosmic structure formation - I. Realistic quintessence models and the non-linear matter power spectrum. *MNRAS*, 401:775–790, January 2010. doi: 10.1111/j.1365-2966.2009.15712.x. 181, 182, 190

L. Amendola. Linear and nonlinear perturbations in dark energy models. *Phys. Rev. D*, 69 (10):103524–+, May 2004. doi: 10.1103/PhysRevD.69.103524. 195

Luca Amendola and Claudia Quercellini. Tracking and coupled dark energy as seen by the wilkinson microwave anisotropy probe. *Phys. Rev. D*, 68(2):023514, Jul 2003. doi: 10.1103/PhysRevD.68.023514. 180

R. Antonucci. Unified models for active galactic nuclei and quasars. *ARA&A*, 31:473–521, 1993. doi: 10.1146/annurev.aa.31.090193.002353. 3, 10

C. Arbeiter, M. Pohl, and R. Schlickeiser. The influence of dust on the inverse Compton emission from jets in Active Galactic Nuclei. *A&A*, 386:415–426, May 2002. doi: 10.1051/0004-6361:20020221. 80

K. Asada and M. Nakamura. The Structure of the M87 Jet: A Transition from Parabolic to Conical Streamlines. *ArXiv e-prints*, October 2011. 9, 12, 25, 49, 52, 95, 121, 140, 142

W. I. Axford, E. Leer, and G. Skadron. The acceleration of cosmic rays by shock waves. In *International Cosmic Ray Conference*, volume 11 of *International Cosmic Ray Conference*, pages 132–137, 1977. 15

S. A. Balbus and J. F. Hawley. A powerful local shear instability in weakly magnetized disks. I - Linear analysis. II - Nonlinear evolution. *ApJ*, 376:214–233, July 1991. doi: 10.1086/170270. 18

S. A. Balbus and J. F. Hawley. Instability, turbulence, and enhanced transport in accretion disks. *Reviews of Modern Physics*, 70:1–53, January 1998. doi: 10.1103/RevModPhys.70.1. 7, 162, 164, 165

S. A. Balbus and P. Henri. On the Magnetic Prandtl Number Behavior of Accretion Disks. *ApJ*, 674:408–414, February 2008. doi: 10.1086/524838. 162, 164, 168

S. A. Balbus and J. C. B. Papaloizou. On the Dynamical Foundations of alpha Disks. *ApJ*, 521:650–658, August 1999. doi: 10.1086/307594. 161, 164

J. M. Bardeen, W. H. Press, and S. A. Teukolsky. Rotating Black Holes: Locally Nonrotating Frames, Energy Extraction, and Scalar Synchrotron Radiation. *ApJ*, 178:347–370, December 1972. doi: 10.1086/151796. 6

T. Barreiro, E. J. Copeland, and N. J. Nunes. Quintessence arising from exponential potentials. *Phys. Rev. D*, 61(12):127301–+, June 2000. doi: 10.1103/PhysRevD.61.127301. 182

B. A. Bassett, M. Brownstone, A. Cardoso, M. Cortês, Y. Fantaye, R. Hlozek, J. Kotze, and P. Okouma. Is the dynamics of scaling dark energy detectable? *JCAP*, 7:7–+, July 2008. doi: 10.1088/1475-7516/2008/07/007. 182

S. A. Baum, E. L. Zirbel, and C. P. O'Dea. Toward Understanding the Fanaroff-Riley Dichotomy in Radio Source Morphology and Power. *ApJ*, 451:88, September 1995. doi: 10.1086/176202. 3

Rachel Bean, Éanna É. Flanagan, Istvan Laszlo, and Mark Trodden. Constraining interactions in cosmology's dark sector. *Phys. Rev. D*, 78(12):123514, Dec 2008. doi: 10.1103/PhysRevD.78.123514. 180

M. C. Begelman, R. D. Blandford, and M. J. Rees. Theory of extragalactic radio sources. *Reviews of Modern Physics*, 56:255–351, April 1984. doi: 10.1103/RevModPhys.56.255. 31

M. C. Begelman, A. C. Fabian, and M. J. Rees. Implications of very rapid TeV variability in blazars. *MNRAS*, 384:L19–L23, February 2008. doi: 10.1111/j.1745-3933.2007.00413.x. 124, 136

A. R. Bell. The acceleration of cosmic rays in shock fronts. I. *MNRAS*, 182:147–156, January 1978. 15, 16, 29, 59, 72, 130

A. R. Bell, K. M. Schure, and B. Reville. Cosmic ray acceleration at oblique shocks. *MNRAS*, 418:1208–1216, December 2011. doi: 10.1111/j.1365-2966.2011.19571.x. 15, 17, 29, 72, 112, 130

N. Bennert, B. Jungwiert, S. Komossa, M. Haas, and R. Chini. Size and properties of the narrow-line region in Seyfert-1 galaxies from spatially-resolved optical spectroscopy. *A&A*, 459:55–69, November 2006. doi: 10.1051/0004-6361:20065477. 68

F. Bernardeau, S. Colombi, E. Gaztanaga, and R. Scoccimarro. Large-scale structure of the universe and cosmological perturbation theory. *Phys. Rept.*, 367:1–248, 2002. doi: 10.1016/S0370-1573(02)00135-7. 190, 205

V. S. Beskin and E. E. Nokhrina. The effective acceleration of plasma outflow in the paraboloidal magnetic field. *MNRAS*, 367:375–386, March 2006. doi: 10.1111/j.1365-2966.2006.09957.x. 11, 49, 53, 146

G. V. Bicknell. Relativistic Jets and the Fanaroff-Riley Classification of Radio Galaxies. *ApJS*, 101:29, November 1995. doi: 10.1086/192232. 147

R. M. Bielby, T. Shanks, P. M. Weilbacher, L. Infante, N. H. M. Crighton, C. Bornancini, N. Bouché, P. Héraudeau, D. G. Lambas, J. Lowenthal, D. Minniti, N. Padilla, P. Petitjean, and T. Theuns. The VLT LBG Redshift Survey - I. Clustering and dynamics of ≈1000 galaxies at z≈ 3. *MNRAS*, pages 649–+, May 2011. doi: 10.1111/j.1365-2966.2011.18338.x. 205

R. D. Blandford and A. Königl. Relativistic jets as compact radio sources. *ApJ*, 232:34–48, August 1979. doi: 10.1086/157262. 25, 47, 50

R. D. Blandford and J. P. Ostriker. Particle acceleration by astrophysical shocks. *ApJL*, 221: L29–L32, April 1978. doi: 10.1086/182658. 15

R. D. Blandford and D. G. Payne. Hydromagnetic flows from accretion discs and the production of radio jets. *MNRAS*, 199:883–903, June 1982. 7, 11

R. D. Blandford and M. J. Rees. A 'twin-exhaust' model for double radio sources. *MNRAS*, 169:395–415, December 1974. 3, 146

R. D. Blandford and R. L. Znajek. Electromagnetic extraction of energy from Kerr black holes. *MNRAS*, 179:433–456, May 1977. 7, 49, 72

M. Błażejowski, M. Sikora, R. Moderski, and G. M. Madejski. Comptonization of Infrared Radiation from Hot Dust by Relativistic Jets in Quasars. *ApJ*, 545:107–116, December 2000. doi: 10.1086/317791. 80

G. R. Blumenthal and R. J. Gould. Bremsstrahlung, Synchrotron Radiation, and Compton Scattering of High-Energy Electrons Traversing Dilute Gases. *Reviews of Modern Physics*, 42:237–271, 1970. doi: 10.1103/RevModPhys.42.237. 37

M. Boettcher. Models for the Spectral Energy Distributions and Variability of Blazars. *ArXiv e-prints*, June 2010. 128

Camille Bonvin and Ruth Durrer. What galaxy surveys really measure. 2011. 201, 202

M. Böttcher and S. D. Bloom. Analyzing the Multiwavelength Spectrum of BL Lacertae during the 1997 July Outburst. *AJ*, 119:469–477, February 2000. doi: 10.1086/301201. 61, 81

M. Böttcher and J. Chiang. X-Ray Spectral Variability Signatures of Flares in BL Lacertae Objects. *ApJ*, 581:127–142, December 2002. doi: 10.1086/344155. 12, 25, 43, 50

M. Böttcher and D. Principe. Optical Variability of the Quasar 3C 279: The Signature of a Decelerating Jet? *ApJ*, 692:1374–1381, February 2009. doi: 10.1088/0004-637X/692/2/1374. 50

M. Böttcher, A. Reimer, and A. P. Marscher. Implications of the very High Energy Gamma-Ray Detection of the Quasar 3C279. *ApJ*, 703:1168–1175, September 2009. doi: 10.1088/0004-637X/703/1/1168. 124

T. Boutelier, G. Henri, and P.-O. Petrucci. An inhomogeneous jet model for the rapid variability of TeV blazars. *MNRAS*, 390:L73–L77, October 2008. doi: 10.1111/j.1745-3933.2008.00539.x. 51

P. H. Brax and J. Martin. Quintessence and supergravity. *Physics Letters B*, 468:40–45, November 1999. doi: 10.1016/S0370-2693(99)01209-5. 182

J. N. Bregman. Diffusive shock acceleration and quasar photospheres. *ApJ*, 288:32–42, January 1985. doi: 10.1086/162760. 59

Marco Bruni et al. Disentangling non-Gaussianity, bias and GR effects in the galaxy distribution. 2011. 201, 202

G. R. Burbidge. Estimates of the Total Energy in Particles and Magnetic Field in the Non-Thermal Radio Sources. *ApJ*, 129:849, May 1959. doi: 10.1086/146680. 73, 110

S. M. Carroll, W. H. Press, and E. L. Turner. The cosmological constant. *ARA&A*, 30:499–542, 1992. doi: 10.1146/annurev.aa.30.090192.002435. 180

B. Carter. *PhRvL*, 26:331, 1970. 4

Joan Centrella, John G. Baker, Bernard J. Kelly, and James R. van Meter. The final merger of black-hole binaries. *Annual Review of Nuclear and Particle Science*, 60(1):75–100, 2010. doi: 10.1146/annurev.nucl.010909.083246. URL http://www.annualreviews.org/doi/abs/10.1146/annurev.nucl.010909.083246. 4

B. Cerutti, G. R. Werner, D. A. Uzdensky, and M. C. Begelman. Beaming and Rapid Variability of High-energy Radiation from Relativistic Pair Plasma Reconnection. *ApJL*, 754:L33, August 2012. doi: 10.1088/2041-8205/754/2/L33. 15, 72

Anthony Challinor and Antony Lewis. The linear power spectrum of observed source number counts. 2011. 201, 202

S. Chandrasekhar. The Maximum Mass of Ideal White Dwarfs. *ApJ*, 74:81, July 1931. doi: 10.1086/143324. 2

P. Charlot, D. C. Gabuzda, H. Sol, B. Degrange, and F. Piron. Simultaneous radio-interferometric and high-energy TeV observations of the γ-ray blazar Mkn 421. *A&A*, 457:455–465, October 2006. doi: 10.1051/0004-6361:20054078. 134, 137

S. Chongchitnan. Cosmological perturbations in models of coupled dark energy. *Phys. Rev. D*, 79(4):043522–+, February 2009. doi: 10.1103/PhysRevD.79.043522. 180, 181, 200

S. Chongchitnan and L. King. Imprints of dynamical dark energy on weak-lensing measurements. *MNRAS*, 407:1989–1997, September 2010. doi: 10.1111/j.1365-2966.2010.17054.x. 189

S. Ciprini. Analytical and numerical time-dependent modelling of SSC blazars variability. In *Blazar Variability across the Electromagnetic Spectrum*, 2008. 43

J. G. Cohen and A. Ryzhov. The Dynamics of the M87 Globular Cluster System. *ApJ*, 486:230, September 1997. doi: 10.1086/304518. 66

E. J. Copeland, A. R. Liddle, and D. Wands. Exponential potentials and cosmological scaling solutions. *Phys. Rev. D*, 57:4686–4690, April 1998. doi: 10.1103/PhysRevD.57.4686. 181, 184

E. J. Copeland, M. Sami, and S. Tsujikawa. Dynamics of Dark Energy. *International Journal of Modern Physics D*, 15:1753–1935, 2006. doi: 10.1142/S021827180600942X. 180, 181

Pier Stefano Corasaniti. Slow-roll suppression of adiabatic instabilities in coupled scalar field-dark matter models. *Phys. Rev. D*, 78(8):083538, Oct 2008. doi: 10.1103/PhysRevD.78.083538. 180

J. H. Croston, M. J. Hardcastle, D. E. Harris, E. Belsole, M. Birkinshaw, and D. M. Worrall. An X-Ray Study of Magnetic Field Strengths and Particle Content in the Lobes of FR II Radio Sources. *ApJ*, 626:733–747, June 2005. doi: 10.1086/430170. 32, 43, 72

R. Dave, R. R. Caldwell, and P. J. Steinhardt. Sensitivity of the cosmic microwave background anisotropy to initial conditions in quintessence cosmology. *Phys. Rev. D*, 66(2):023516–+, July 2002. doi: 10.1103/PhysRevD.66.023516. 180

R. de Putter, D. Huterer, and E. V. Linder. Measuring the speed of dark: Detecting dark energy perturbations. *Phys. Rev. D*, 81(10):103513–+, May 2010. doi: 10.1103/PhysRevD.81.103513. 191

D. S. De Young. How Does Radio AGN Feedback Feed Back? *ApJ*, 710:743–754, February 2010. doi: 10.1088/0004-637X/710/1/743. 49, 53, 71

C. D. Dermer and J. Chiang. Electron acceleration and synchrotron radiation in decelerating plasmoids. *New Astron.*, 3:157–173, April 1998. doi: 10.1016/S1384-1076(98)00004-9. 50

C. D. Dermer and R. Schlickeiser. Model for the High-Energy Emission from Blazars. *ApJ*, 416:458, October 1993. doi: 10.1086/173251. 61

C. D. Dermer, R. Schlickeiser, and A. Mastichiadis. High-energy gamma radiation from extragalactic radio sources. *A&A*, 256:L27–L30, March 1992. 61

C. D. Dermer, J. D. Finke, H. Krug, and M. Böttcher. Gamma-Ray Studies of Blazars: Synchro-Compton Analysis of Flat Spectrum Radio Quasars. *ApJ*, 692:32–46, February 2009. doi: 10.1088/0004-637X/692/1/32. 62, 63, 67, 81

C. D. Dermer, K. Murase, and H. Takami. Variable Gamma-ray Emission Induced by Ultra-High Energy Neutral Beams: Application to 4C +21.35. *ArXiv e-prints*, March 2012. 124

S. G. Djorgovski and V. G. Gurzadyan. Dark Energy From Vacuum Fluctuations. *Nuclear Physics B Proceedings Supplements*, 173:6–10, November 2007. doi: 10.1016/j.nuclphysbps.2007.08.056. 180

M. Doran and G. Robbers. Early dark energy cosmologies. *JCAP*, 6:26–+, June 2006. doi: 10.1088/1475-7516/2006/06/026. 194

M. Doran, C. M. Müller, G. Schäfer, and C. Wetterich. Gauge-invariant initial conditions and early time perturbations in quintessence universes. *Phys. Rev. D*, 68(6):063505–+, September 2003. doi: 10.1103/PhysRevD.68.063505. 189

R. Durrer. *The Cosmic Microwave Background*. Cambridge University Press, 2008. 192

G. Efstathiou. CMB Anisotropies and the Determination of Cosmological Parameters. In R. G. Crittenden & N. G. Turok, editor, *NATO ASIC Proc. 565: Structure Formation in the Universe*, pages 179–+, 2001. 179

A. Einstein. Die Feldgleichungen der Gravitation. *Sitzungsberichte der Königlich Preußischen Akademie der Wissenschaften (Berlin), Seite 844-847.*, pages 844–847, 1915. 2

M. Elitzur. The obscuring torus in AGN. *NewA Rev.*, 50:728–731, November 2006. doi: 10.1016/j.newar.2006.06.027. 68

S. M. Faber, S. Tremaine, E. A. Ajhar, Y.-I. Byun, A. Dressler, K. Gebhardt, C. Grillmair, J. Kormendy, T. R. Lauer, and D. Richstone. The Centers of Early-Type Galaxies with HST. IV. Central Parameter Relations. *AJ*, 114:1771, November 1997. doi: 10.1086/118606. 65

B. L. Fanaroff and J. M. Riley. The morphology of extragalactic radio sources of high and low luminosity. *MNRAS*, 167:31P–36P, May 1974. 3, 10, 147

J. Faulkner, D. N. C. Lin, and J. Papaloizou. On the evolution of accretion disc flow in cataclysmic variables. I - The prospect of a limit cycle in dwarf nova systems. *MNRAS*, 205: 359–375, October 1983. 167

R. P. Fender, T. M. Belloni, and E. Gallo. Towards a unified model for black hole X-ray binary jets. *MNRAS*, 355:1105–1118, December 2004. doi: 10.1111/j.1365-2966.2004.08384.x. 149, 177

E. Fermi. On the Origin of the Cosmic Radiation. *Physical Review*, 75:1169–1174, April 1949. doi: 10.1103/PhysRev.75.1169. 15

A. Ferrari. Modeling Extragalactic Jets. *ARA&A*, 36:539–598, 1998. doi: 10.1146/annurev.astro.36.1.539. 3

P. G. Ferreira and M. Joyce. Cosmology with a primordial scaling field. *Phys. Rev. D*, 58(2): 023503–+, July 1998. doi: 10.1103/PhysRevD.58.023503. 181

S. Fine, S. M. Croom, J. Bland-Hawthorn, K. A. Pimbblet, N. P. Ross, D. P. Schneider, and T. Shanks. The CIV linewidth distribution for quasars and its implications for broad-line region dynamics and virial mass estimation. *MNRAS*, 409:591–610, December 2010. doi: 10.1111/j.1365-2966.2010.17107.x. 131

J. D. Finke, C. D. Dermer, and M. Böttcher. Synchrotron Self-Compton Analysis of TeV X-Ray-Selected BL Lacertae Objects. *ApJ*, 686:181–194, October 2008. doi: 10.1086/590900. 43, 134

G. Fossati, L. Maraschi, A. Celotti, A. Comastri, and G. Ghisellini. A unifying view of the spectral energy distributions of blazars. *MNRAS*, 299:433–448, September 1998. doi: 10.1046/j.1365-8711.1998.01828.x. 10, 75, 94, 128, 148

J. Frank, A. King, and D. Raine. *Accretion power in astrophysics.* 1992. 20, 165

J. Frank, A. King, and D. J. Raine. *Accretion Power in Astrophysics: Third Edition*. January 2002. 18, 21, 161, 163, 165, 166, 167

S. Fromang, J. Papaloizou, G. Lesur, and T. Heinemann. MHD simulations of the magnetorotational instability in a shearing box with zero net flux. II. The effect of transport coefficients. *A&A*, 476:1123–1132, December 2007. doi: 10.1051/0004-6361:20077943. 162

M. Georganopoulos and D. Kazanas. Relativistic and Slowing Down: The Flow in the Hot Spots of Powerful Radio Galaxies and Quasars. *ApJL*, 589:L5–L8, May 2003. doi: 10.1086/375796. 51

M. Georganopoulos and A. P. Marscher. A Viewing Angle-Kinetic Luminosity Unification Scheme for BL Lacertae Objects. *ApJ*, 506:621–636, October 1998. doi: 10.1086/306273. 51

G. Ghisellini and A. Celotti. The dividing line between FR I and FR II radio-galaxies. *A&A*, 379:L1–L4, November 2001. doi: 10.1051/0004-6361:20011338. 10

G. Ghisellini and L. Maraschi. Bulk acceleration in relativistic jets and the spectral properties of blazars. *ApJ*, 340:181–189, May 1989. doi: 10.1086/167383. 51

G. Ghisellini and F. Tavecchio. The blazar sequence: a new perspective. *MNRAS*, 387: 1669–1680, July 2008. doi: 10.1111/j.1365-2966.2008.13360.x. 67, 81, 132, 143

G. Ghisellini and F. Tavecchio. Compton rockets and the minimum power of relativistic jets. *MNRAS*, 409:L79–L83, November 2010. doi: 10.1111/j.1745-3933.2010.00952.x. 7

G. Ghisellini, L. Maraschi, and A. Treves. Inhomogeneous synchrotron-self-Compton models and the problem of relativistic beaming of BL Lac objects. *A&A*, 146:204–212, May 1985. 25, 50

G. Ghisellini, L. Maraschi, and F. Tavecchio. The Fermi blazars' divide. *MNRAS*, 396:L105–L109, June 2009a. doi: 10.1111/j.1745-3933.2009.00673.x. 11, 132, 143

G. Ghisellini, F. Tavecchio, and G. Ghirlanda. Jet and accretion power in the most powerful Fermi blazars. *MNRAS*, 399:2041–2054, November 2009b. doi: 10.1111/j.1365-2966.2009.15397.x. 10, 21, 84, 85, 92, 130

G. Ghisellini, F. Tavecchio, L. Foschini, and G. Ghirlanda. The transition between BL Lac objects and flat spectrum radio quasars. *MNRAS*, 414:2674–2689, July 2011. doi: 10.1111/j.1365-2966.2011.18578.x. 125

Tommaso Giannantonio. Measuring dark energy with the integrated Sachs-Wolfe effect. 2008. 205

Tommaso Giannantonio et al. Combined analysis of the integrated Sachs-Wolfe effect and cosmological implications. *Phys. Rev.*, D77:123520, 2008. doi: 10.1103/PhysRevD.77.123520. 204, 205

R. J. Gould and G. P. Schréder. Pair Production in Photon-Photon Collisions. *Physical Review*, 155:1404–1407, March 1967. doi: 10.1103/PhysRev.155.1404. 122

P. B. Graff, M. Georganopoulos, E. S. Perlman, and D. Kazanas. A Multizone Model for Simulating the High-Energy Variability of TeV Blazars. *ApJ*, 689:68–78, December 2008. doi: 10.1086/592427. 50

L. P. Grishchuk and I. B. Zeldovich. Long-wavelength perturbations of a Friedmann universe, and anisotropy of the microwave background radiation. *SvA*, 22:125–129, April 1978. 205

K. Hada, A. Doi, M. Kino, H. Nagai, Y. Hagiwara, and N. Kawaguchi. An origin of the radio jet in M87 at the location of the central black hole. *Nature*, 477:185–187, September 2011. doi: 10.1038/nature10387. 9, 12, 25, 49, 102

M. J. Hardcastle. Hotspots, Jets and Environments. In T. A. Rector and D. S. De Young, editors, *Extragalactic Jets: Theory and Observation from Radio to Gamma Ray*, volume 386 of *Astronomical Society of the Pacific Conference Series*, page 46, June 2008. 3

M. J. Hardcastle and J. H. Croston. Modelling TeV γ-ray emission from the kiloparsec-scale jets of Centaurus A and M87. *MNRAS*, 415:133–142, July 2011. doi: 10.1111/j.1365-2966.2011.18678.x. 61, 65, 66, 112

M. J. Hardcastle, D. M. Worrall, M. Birkinshaw, R. A. Laing, and A. H. Bridle. A Chandra observation of the X-ray environment and jet of 3C 296. *MNRAS*, 358:843–850, April 2005. doi: 10.1111/j.1365-2966.2005.08765.x. 53, 71

M. J. Hardcastle, D. A. Evans, and J. H. Croston. Hot and cold gas accretion and feedback in radio-loud active galaxies. *MNRAS*, 376:1849–1856, April 2007. doi: 10.1111/j.1365-2966.2007.11572.x. 147

M. J. Hardcastle, D. A. Evans, and J. H. Croston. The active nuclei of z 1.0 3CRR radio sources. *MNRAS*, 396:1929–1952, July 2009. doi: 10.1111/j.1365-2966.2009.14887.x. 147

S. W. Hawking. Gravitational Radiation from Colliding Black Holes. *Physical Review Letters*, 26:1344–1346, May 1971. doi: 10.1103/PhysRevLett.26.1344. 4

S. W. Hawking. Black holes in general relativity. *Communications in Mathematical Physics*, 25:152–166, June 1972. doi: 10.1007/BF01877517. 4

J. F. Hawley and S. A. Balbus. A Powerful Local Shear Instability in Weakly Magnetized Disks. II. Nonlinear Evolution. *ApJ*, 376:223, July 1991. doi: 10.1086/170271. 18

Jian-Hua He, Bin Wang, and Pengjie Zhang. Imprint of the interaction between dark sectors in large scale cosmic microwave background anisotropies. *Phys. Rev. D*, 80(6):063530, Sep 2009. doi: 10.1103/PhysRevD.80.063530. 180, 187

S. Hirose, O. Blaes, and J. H. Krolik. Turbulent Stresses in Local Simulations of Radiation-dominated Accretion Disks, and the Possibility of the Lightman-Eardley Instability. *ApJ*, 704:781–788, October 2009a. doi: 10.1088/0004-637X/704/1/781. 170

S. Hirose, J. H. Krolik, and O. Blaes. Radiation-Dominated Disks are Thermally Stable. *ApJ*, 691:16–31, January 2009b. doi: 10.1088/0004-637X/691/1/16. 170

L. C. Ho. On the Relationship between Radio Emission and Black Hole Mass in Galactic Nuclei. *ApJ*, 564:120–132, January 2002. doi: 10.1086/324399. 116

M. P. Hobson, G. P. Efstathiou, and A. N. Lasenby. *General Relativity*. February 2006. 5

D. W. Hogg. Distance measures in cosmology. *ArXiv Astrophysics e-prints*, May 1999. 21

D. C. Homan, Y. Y. Kovalev, M. L. Lister, E. Ros, K. I. Kellermann, M. H. Cohen, R. C. Vermeulen, J. A. Zensus, and M. Kadler. Intrinsic Brightness Temperatures of AGN Jets. *ApJL*, 642:L115–L118, May 2006. doi: 10.1086/504715. 32, 72

P. A. Hughes. *Beams and jets in astrophysics*. 1991. 33

W. Israel. Event Horizons in Static Vacuum Space-Times. *Physical Review*, 164:1776–1779, December 1967. doi: 10.1103/PhysRev.164.1776. 4

Werner Israel. Event horizons in static electrovac space-times. *Communications in Mathematical Physics*, 8(3):245–260, 1968. ISSN 0010-3616. doi: 10.1007/BF01645859. URL `http://dx.doi.org/10.1007/BF01645859`. 4

B. M. Jackson, A. Taylor, and A. Berera. On the large-scale instability in interacting dark energy and dark matter fluids. *Phys. Rev. D*, 79(4):043526–+, February 2009. doi: 10.1103/PhysRevD.79.043526. 180

O. Jamil, R. P. Fender, and C. R. Kaiser. iShocks: X-ray binary jets with an internal shocks model. *MNRAS*, 401:394–404, January 2010. doi: 10.1111/j.1365-2966.2009.15652.x. 25, 43, 50, 72

A. Janiuk and B. Czerny. On different types of instabilities in black hole accretion discs: implications for X-ray binaries and active galactic nuclei. *MNRAS*, 414:2186–2194, July 2011. doi: 10.1111/j.1365-2966.2011.18544.x. 170

E. Jennings, C. M. Baugh, R. E. Angulo, and S. Pascoli. Simulations of quintessential cold dark matter: beyond the cosmological constant. *MNRAS*, 401:2181–2201, February 2010. doi: 10.1111/j.1365-2966.2009.15819.x. 180

S. Jester, H.-J. Röser, K. Meisenheimer, R. Perley, and R. Conway. HST optical spectral index map of the jet of 3C 273. *A&A*, 373:447–458, July 2001. doi: 10.1051/0004-6361:20010593. 71, 90

C. Jin, M. Ward, C. Done, and J. M. Gelbord. A Combined Optical and X-ray Study of Unobscured Type 1 AGN. I. Optical Spectra and SED Modeling. *ArXiv e-prints*, September 2011. 41

S. G. Jorstad, A. P. Marscher, J. R. Mattox, A. E. Wehrle, S. D. Bloom, and A. V. Yurchenko. Multiepoch Very Long Baseline Array Observations of EGRET-detected Quasars and BL Lacertae Objects: Superluminal Motion of Gamma-Ray Bright Blazars. *ApJS*, 134:181–240, June 2001. doi: 10.1086/320858. 9, 109

C. R. Kaiser. The flat synchrotron spectra of partially self-absorbed jets revisited. *MNRAS*, 367:1083–1094, April 2006. doi: 10.1111/j.1365-2966.2006.10030.x. 26, 46, 47, 70

C. R. Kaiser, R. Sunyaev, and H. C. Spruit. Internal shock model for microquasars. *A&A*, 356:975–988, April 2000. 25, 43, 50, 72

S. Kaspi, D. Maoz, H. Netzer, B. M. Peterson, M. Vestergaard, and B. T. Jannuzi. The Relationship between Luminosity and Broad-Line Region Size in Active Galactic Nuclei. *ApJ*, 629:61–71, August 2005. doi: 10.1086/431275. 67, 110

R. P. Kerr. Gravitational Field of a Spinning Mass as an Example of Algebraically Special Metrics. *Physical Review Letters*, 11:237–238, September 1963. doi: 10.1103/PhysRevLett.11.237. 4

J. G. Kirk and P. Schneider. On the acceleration of charged particles at relativistic shock fronts. *ApJ*, 315:425–433, April 1987. doi: 10.1086/165147. 17

J. G. Kirk, F. M. Rieger, and A. Mastichiadis. Particle acceleration and synchrotron emission in blazar jets. *A&A*, 333:452–458, May 1998. 25, 43, 50

H. Kodama and M. Sasaki. Cosmological Perturbation Theory. *Progress of Theoretical Physics Supplement*, 78:1–+, 1984. doi: 10.1143/PTPS.78.1. 181, 186, 187, 188, 189

S. Kohler and M. C. Begelman. Magnetic Domination of Recollimation Boundary Layers in Relativistic Jets. *ArXiv e-prints*, August 2012. 87

Tomi Koivisto. Growth of perturbations in dark matter coupled with quintessence. *Phys. Rev. D*, 72(4):043516, Aug 2005. doi: 10.1103/PhysRevD.72.043516. 180

E. Komatsu, J. Dunkley, M. R. Nolta, C. L. Bennett, B. Gold, G. Hinshaw, N. Jarosik, D. Larson, M. Limon, L. Page, D. N. Spergel, M. Halpern, R. S. Hill, A. Kogut, S. S. Meyer, G. S. Tucker, J. L. Weiland, E. Wollack, and E. L. Wright. Five-Year Wilkinson Microwave Anisotropy Probe Observations: Cosmological Interpretation. *ApJS*, 180:330–376, February 2009. doi: 10.1088/0067-0049/180/2/330. 179, 181

E. Komatsu, K. M. Smith, J. Dunkley, C. L. Bennett, B. Gold, G. Hinshaw, N. Jarosik, D. Larson, M. R. Nolta, L. Page, D. N. Spergel, M. Halpern, R. S. Hill, A. Kogut, M. Limon, S. S. Meyer, N. Odegard, G. S. Tucker, J. L. Weiland, E. Wollack, and E. L. Wright. Seven-year Wilkinson Microwave Anisotropy Probe (WMAP) Observations: Cosmological Interpretation. *ApJS*, 192:18–+, February 2011. doi: 10.1088/0067-0049/192/2/18. 75, 183

S. S. Komissarov and S. A. E. G. Falle. The large-scale structure of FR-II radio sources. *MNRAS*, 297:1087–1108, July 1998. doi: 10.1046/j.1365-8711.1998.01547.x. 72

S. S. Komissarov, M. V. Barkov, N. Vlahakis, and A. Königl. Magnetic acceleration of relativistic active galactic nucleus jets. *MNRAS*, 380:51–70, September 2007. doi: 10.1111/j.1365-2966.2007.12050.x. 9, 11

S. S. Komissarov, N. Vlahakis, A. Königl, and M. V. Barkov. Magnetic acceleration of ultrarelativistic jets in gamma-ray burst sources. *MNRAS*, 394:1182–1212, April 2009. doi: 10.1111/j.1365-2966.2009.14410.x. 11, 12, 54, 72, 110, 143, 146, 150

A. Königl. Relativistic jets as X-ray and gamma-ray sources. *ApJ*, 243:700–709, February 1981. doi: 10.1086/158638. 25, 50, 101, 103

Y. Y. Kovalev, M. L. Lister, D. C. Homan, and K. I. Kellermann. The Inner Jet of the Radio Galaxy M87. *ApJL*, 668:L27–L30, October 2007. doi: 10.1086/522603. 9, 25

M. Kowalski, D. Rubin, G. Aldering, R. J. Agostinho, A. Amadon, R. Amanullah, C. Balland, K. Barbary, G. Blanc, P. J. Challis, A. Conley, N. V. Connolly, and et al. Improved Cosmological Constraints from New, Old, and Combined Supernova Data Sets. *ApJ*, 686: 749–778, October 2008. doi: 10.1086/589937. 179, 182

Thomas P. Krichbaum, I. Agudo, U. Bach, A. Witzel, and J. A. Zensus. VLBI at the highest frequencies - AGN studied with micro- arcsecond resolution. 2006. 9, 25, 49

G. F. Krymskii. A regular mechanism for the acceleration of charged particles on the front of a shock wave. *Akademiia Nauk SSSR Doklady*, 234:1306–1308, June 1977. 15

J. Kwan, G. F. Lewis, and E. V. Linder. Mapping Growth and Gravity with Robust Redshift Space Distortions. *ArXiv e-prints*, May 2011. 205

G. La Vacca and L. P. L. Colombo. Gravitational lensing constraints on dynamical and coupled dark energy. *JCAP*, 4:7–+, April 2008. doi: 10.1088/1475-7516/2008/04/007. 180

M. Lacy, S. A. Laurent-Muehleisen, S. E. Ridgway, R. H. Becker, and R. L. White. The Radio Luminosity-Black Hole Mass Correlation for Quasars from the FIRST Bright Quasar Survey and a "Unification Scheme" for Radio-loud and Radio-quiet Quasars. *ApJL*, 551: L17–L21, April 2001. doi: 10.1086/319836. 116

R. A. Laing and A. H. Bridle. Relativistic models and the jet velocity field in the radio galaxy 3C 31. *MNRAS*, 336:328–352, October 2002. doi: 10.1046/j.1365-8711.2002.05756.x. 3, 53, 71

R. A. Laing and A. H. Bridle. Adiabatic relativistic models for the jets in the radio galaxy 3C 31. *MNRAS*, 348:1459–1472, March 2004. doi: 10.1111/j.1365-2966.2004.07471.x. 87

H. N. Latter and J. C. B. Papaloizou. Hysteresis and thermal limit cycles in MRI simulations of accretion discs. *MNRAS*, 426:1107–1120, October 2012. doi: 10.1111/j.1365-2966.2012.21748.x. 167

T. R. Lauer, E. A. Ajhar, Y.-I. Byun, A. Dressler, S. M. Faber, C. Grillmair, J. Kormendy, D. Richstone, and S. Tremaine. The Centers of Early-Type Galaxies with HST.I.An Observational Survey. *AJ*, 110:2622, December 1995. doi: 10.1086/117719. 65, 66

G. Lesur and P.-Y. Longaretti. Impact of dimensionless numbers on the efficiency of magnetorotational instability induced turbulent transport. *MNRAS*, 378:1471–1480, July 2007. doi: 10.1111/j.1365-2966.2007.11888.x. 162

H. Li and M. Kusunose. Temporal and Spectral Variabilities of High-Energy Emission from Blazars Using Synchrotron Self-Compton Models. *ApJ*, 536:729–741, June 2000. doi: 10.1086/308960. 12, 25, 50

A. P. Lightman and D. M. Eardley. Black Holes in Binary Systems: Instability of Disk Accretion. *ApJL*, 187:L1, January 1974. doi: 10.1086/181377. 170

J. A. S. Lima. Thermodynamics of decaying vacuum cosmologies. *Phys. Rev. D*, 54:2571–2577, August 1996. doi: 10.1103/PhysRevD.54.2571. 194

Y. Liu, D. R. Jiang, and M. F. Gu. The Jet Power, Radio Loudness, and Black Hole Mass in Radio-loud Active Galactic Nuclei. *ApJ*, 637:669–681, February 2006. doi: 10.1086/498639. 116

A. Lobanov. Physical properties of blazar jets from VLBI observations. *ArXiv e-prints*, October 2010. 29

A. P. Lobanov. Ultracompact jets in active galactic nuclei. *A&A*, 330:79–89, February 1998. 101

M. S. Longair. *High energy astrophysics. Vol.2: Stars, the galaxy and the interstellar medium.* 1994. 33, 44

M. S. Longair. *High Energy Astrophysics.* February 2011. 13, 14, 17, 34

P.-Y. Longaretti and G. Lesur. MRI-driven turbulent transport: the role of dissipation, channel modes and their parasites. *A&A*, 516:A51, June 2010. doi: 10.1051/0004-6361/201014093. 162, 168

C.-P. Ma and E. Bertschinger. Cosmological Perturbation Theory in the Synchronous and Conformal Newtonian Gauges. *ApJ*, 455:7–+, December 1995. doi: 10.1086/176550. 186

E. Macaulay, H. Feldman, P. G. Ferreira, M. J. Hudson, and R. Watkins. A slight excess of large-scale power from moments of the peculiar velocity field. *MNRAS*, pages 391–+, March 2011. doi: 10.1111/j.1365-2966.2011.18426.x. 202, 205

R. Mainini and S. Bonometto. Limits on coupling between dark components. *JCAP*, 6:20–+, June 2007. doi: 10.1088/1475-7516/2007/06/020. 180

Roberto Mainini and David F. Mota. ISW-LSS cross-correlation in coupled Dark Energy models with massive neutrinos. 2010. 205

L. Maraschi and F. Tavecchio. The Jet-Disk Connection and Blazar Unification. *ApJ*, 593: 667–675, August 2003. doi: 10.1086/342118. 29, 44

L. Maraschi, L. Foschini, G. Ghisellini, F. Tavecchio, and R. M. Sambruna. Testing the blazar spectral sequence: X-ray-selected blazars. *MNRAS*, 391:1981–1993, December 2008. doi: 10.1111/j.1365-2966.2008.14030.x. 94, 104

S. Markoff, H. Falcke, and R. Fender. A Jet Model for the Broadband Spectrum of XTE J1118+480: Implications for the Nature of the XRB Low/Hard X-ray State. In *American Astronomical Society Meeting Abstracts*, volume 32 of *Bulletin of the American Astronomical Society*, pages 1546–+, December 2000. 25, 50

A. P. Marscher. Relativistic jets and the continuum emission in QSOs. *ApJ*, 235:386–391, January 1980. doi: 10.1086/157642. 25, 50

A. P. Marscher. The compact jets of TeV blazars. *Astroparticle Physics*, 11:19–25, June 1999. doi: 10.1016/S0927-6505(99)00019-5. 136

A. P. Marscher and W. K. Gear. Models for high-frequency radio outbursts in extragalactic sources, with application to the early 1983 millimeter-to-infrared flare of 3C 273. *ApJ*, 298: 114–127, November 1985. doi: 10.1086/163592. 25, 43, 50

Matteo Martinelli, Laura Lopez Honorez, Alessandro Melchiorri, and Olga Mena. Future CMB cosmological constraints in a dark coupled universe. *Phys. Rev.*, D81:103534, 2010. doi: 10.1103/PhysRevD.81.103534. 205

J. C. McKinney. General relativistic magnetohydrodynamic simulations of the jet formation and large-scale propagation from black hole accretion systems. *MNRAS*, 368:1561–1582, June 2006. doi: 10.1111/j.1365-2966.2006.10256.x. 8, 9, 11, 49, 53, 54, 72, 103, 110, 143

J. C. McKinney and R. D. Blandford. Stability of relativistic jets from rotating, accreting black holes via fully three-dimensional magnetohydrodynamic simulations. *MNRAS*, 394: L126–L130, March 2009. doi: 10.1111/j.1745-3933.2009.00625.x. 9, 11

J. C. McKinney, A. Tchekhovskoy, and R. D. Blandford. General relativistic magnetohydrodynamic simulations of magnetically choked accretion flows around black holes. *MNRAS*, 423:3083–3117, July 2012. doi: 10.1111/j.1365-2966.2012.21074.x. 11, 143, 150

R. J. McLure and M. J. Jarvis. The relationship between radio luminosity and black hole mass in optically selected quasars. *MNRAS*, 353:L45–L49, October 2004. doi: 10.1111/j.1365-2966.2004.08305.x. 116

K. Meisenheimer, M. G. Yates, and H.-J. Roeser. The synchrotron spectra of radio hot spots. II. Infrared imaging. *A&A*, 325:57–73, September 1997. 71, 90

E. T. Meyer, G. Fossati, M. Georganopoulos, and M. L. Lister. From the Blazar Sequence to the Blazar Envelope: Revisiting the Relativistic Jet Dichotomy in Radio-loud Active Galactic Nuclei. *ApJ*, 740:98, October 2011. doi: 10.1088/0004-637X/740/2/98. 132

E. T. Meyer, G. Fossati, M. Georganopoulos, and M. L. Lister. Collective Evidence for Inverse Compton Emission from External Photons in High-Power Blazars. *ArXiv e-prints*, March 2012. 94, 125

F. Meyer, B. F. Liu, and E. Meyer-Hofmeister. Evaporation: The change from accretion via a thin disk to a coronal flow. *A&A*, 361:175–188, September 2000. 161

G. Migliori, P. Grandi, G. G. C. Palumbo, G. Brunetti, and C. Stanghellini. Radio Lobes of Pictor A: An X-Ray Spatially Resolved Study. *ApJ*, 668:203–208, October 2007. doi: 10.1086/520870. 43

Y. Mizuno, Y. Lyubarsky, K.-I. Nishikawa, and P. E. Hardee. Three-dimensional Relativistic Magnetohydrodynamic Simulations of Current-driven Instability. III. Rotating Relativistic Jets. *ApJ*, 757:16, September 2012. doi: 10.1088/0004-637X/757/1/16. 147

R. Mor, H. Netzer, and M. Elitzur. Dusty Structure Around Type-I Active Galactic Nuclei: Clumpy Torus Narrow-line Region and Near-nucleus Hot Dust. *ApJ*, 705:298–313, November 2009. doi: 10.1088/0004-637X/705/1/298. 68, 69

S. L. Mufson, D. J. Hutter, K. R. Hackney, R. L. Hackney, C. M. Urry, R. F. Mushotzky, Y. Kondo, W. Z. Wisniewski, H. D. Aller, and M. F. Aller. Coordinated multifrequency observations of the BL Lacertae objects MRK 180 and MRK 501. *ApJ*, 285:571–579, October 1984. doi: 10.1086/162531. 25, 50

L. M. Mullin and M. J. Hardcastle. Bayesian inference of jet bulk-flow speeds in Fanaroff-Riley type II radio sources. *MNRAS*, 398:1989–2004, October 2009. doi: 10.1111/j.1365-2966.2009.15232.x. 49, 53

R. Narayan and I. Yi. Advection-dominated Accretion: Underfed Black Holes and Neutron Stars. *ApJ*, 452:710, October 1995. doi: 10.1086/176343. 133, 162

M. Nenkova, M. M. Sirocky, Ž. Ivezić, and M. Elitzur. AGN Dusty Tori. I. Handling of Clumpy Media. *ApJ*, 685:147–159, September 2008a. doi: 10.1086/590482. 68

M. Nenkova, M. M. Sirocky, R. Nikutta, Ž. Ivezić, and M. Elitzur. AGN Dusty Tori. II. Observational Implications of Clumpiness. *ApJ*, 685:160–180, September 2008b. doi: 10.1086/590483. 68

K.-I. Nishikawa, P. Hardee, B. Zhang, I. Dutan, M. Medvedev, E. J. Choi, K. W. Min, J. Niemiec, Y. Mizuno, A. Nordlund, J. T. Frederiksen, H. Sol, M. Pohl, and D. H. Hartmann. Radiation from accelerated particles in relativistic jets with shocks, shear-flow, and reconnection. *ArXiv e-prints*, March 2013. 15, 17

Germa ń Olivares, Fernando Atrio-Barandela, and Diego Pavón. Matter density perturbations in interacting quintessence models. *Phys. Rev. D*, 74(4):043521, Aug 2006. doi: 10.1103/PhysRevD.74.043521. 180

J. R. Oppenheimer and G. M. Volkoff. On Massive Neutron Cores. *Physical Review*, 55: 374–381, February 1939. doi: 10.1103/PhysRev.55.374. 2

A. Orsi, C. M. Baugh, C. G. Lacey, A. Cimatti, Y. Wang, and G. Zamorani. Probing dark energy with future redshift surveys: a comparison of emission line and broad-band selection in the near-infrared. *MNRAS*, 405:1006–1024, June 2010. doi: 10.1111/j.1365-2966.2010.16585.x. 205

A. Y. K. N. Oshlack, R. L. Webster, and M. T. Whiting. Black Hole Mass Estimates of Radio-selected Quasars. *ApJ*, 576:81–88, September 2002. doi: 10.1086/341729. 116

F. N. Owen, S. R. Spangler, and W. D. Cotton. Simultaneous radio spectra of sources with strong millimeter components. *AJ*, 85:351–362, April 1980. doi: 10.1086/112683. 9, 24

A. G. Pacholczyk. *Radio astrophysics. Nonthermal processes in galactic and extragalactic sources*. 1970. 32, 33

P. Padovani, P. Giommi, and A. Rau. The discovery of high-power high synchrotron peak blazars. *MNRAS*, 422:L48, May 2012. doi: 10.1111/j.1745-3933.2012.01234.x. 120, 137, 140, 143

C.-G. Park, J.-C. Hwang, J.-H. Lee, and H. Noh. Roles of Dark Energy Perturbations in Dynamical Dark Energy Models: Can We Ignore Them? *Physical Review Letters*, 103(15): 151303–+, October 2009. doi: 10.1103/PhysRevLett.103.151303. 180

A. Pe'er and P. Casella. A Model for Emission from Jets in X-Ray Binaries: Consequences of a Single Acceleration Episode. *ApJ*, 699:1919–1937, July 2009. doi: 10.1088/0004-637X/699/2/1919. 50

R. Penrose. *Rev. Nuovo Cimento 1*, Special No. 252, 1969. 5

Valeria Pettorino and Carlo Baccigalupi. Coupled and extended quintessence: Theoretical differences and structure formation. *Phys. Rev. D*, 77(10):103003, May 2008. doi: 10.1103/PhysRevD.77.103003. 180

W. J. Potter and G. Cotter. Synchrotron and inverse-Compton emission from blazar jets - I. A uniform conical jet model. *MNRAS*, 423:756–765, June 2012. doi: 10.1111/j.1365-2966.2012.20918.x. 49, 95, 121, 143

W. J. Potter and G. Cotter. Synchrotron and inverse-Compton emission from blazar jets - II. An accelerating jet model with a geometry set by observations of M87. *MNRAS*, 429: 1189–1205, February 2013a. doi: 10.1093/mnras/sts407. 95, 121, 143

W. J. Potter and G. Cotter. Synchrotron and inverse-Compton emission from blazar jets - III. Compton-dominant blazars. *MNRAS*, 431:1840–1852, May 2013b. doi: 10.1093/mnras/stt300. 121, 143

W. J. Potter and G. Cotter. Synchrotron and inverse-Compton emission from blazar jets - IV. BL Lac type blazars and the physical basis for the blazar sequence. *ArXiv e-prints*, October 2013c. 143

J. E. Pringle. Accretion discs in astrophysics. *ARA&A*, 19:137–162, 1981. doi: 10.1146/annurev.aa.19.090181.001033. 164

Y. Rasera et al. Introducing the Dark Energy Universe Simulation Series (DEUSS). *AIP Conf. Proc.*, 1241:1134–1139, 2010. doi: 10.1063/1.3462610. 190, 205

B. Ratra and P. J. E. Peebles. Cosmological consequences of a rolling homogeneous scalar field. *Phys. Rev. D*, 37:3406–3427, June 1988. doi: 10.1103/PhysRevD.37.3406. 180, 181

A. Rau, P. Schady, J. Greiner, M. Salvato, M. Ajello, E. Bottacini, N. Gehrels, P. M. J. Afonso, J. Elliott, R. Filgas, D. A. Kann, S. Klose, T. Krühler, M. Nardini, A. Nicuesa Guelbenzu, F. Olivares E., A. Rossi, V. Sudilovsky, A. C. Updike, and D. H. Hartmann. BL Lacertae objects beyond redshift 1.3 - UV-to-NIR photometry and photometric redshift for Fermi/LAT blazars. *A&A*, 538:A26, February 2012. doi: 10.1051/0004-6361/201118159. 138

M. J. Rees. Appearance of Relativistically Expanding Radio Sources. *Nature*, 211:468–470, July 1966. doi: 10.1038/211468a0. 9

R. A. Remillard and J. E. McClintock. X-Ray Properties of Black-Hole Binaries. *ARA&A*, 44:49–92, September 2006. doi: 10.1146/annurev.astro.44.051905.092532. 21, 161, 175

S. P. Reynolds. Theoretical studies of compact radio sources. I - Synchrotron radiation from relativistic flows. *ApJ*, 256:13–37, May 1982. doi: 10.1086/159881. 25, 50

F. M. Rieger and K. Mannheim. Particle acceleration in rotating and shearing jets from AGN. *A&A*, 396:833–846, December 2002. doi: 10.1051/0004-6361:20021457. 72

A. G. Riess, A. V. Filippenko, P. Challis, A. Clocchiatti, A. Diercks, P. M. Garnavich, R. L. Gilliland, C. J. Hogan, S. Jha, R. P. Kirshner, B. Leibundgut, M. M. Phillips, D. Reiss, B. P. Schmidt, R. A. Schommer, R. C. Smith, J. Spyromilio, C. Stubbs, N. B. Suntzeff, and J. Tonry. Observational Evidence from Supernovae for an Accelerating Universe and a Cosmological Constant. *AJ*, 116:1009–1038, September 1998. doi: 10.1086/300499. 179

A. G. Riess, L. Macri, S. Casertano, H. Lampeitl, H. C. Ferguson, A. V. Filippenko, S. W. Jha, W. Li, and R. Chornock. A 3% Solution: Determination of the Hubble Constant with the Hubble Space Telescope and Wide Field Camera 3. *ApJ*, 730:119–+, April 2011. doi: 10.1088/0004-637X/730/2/119. 183

R. K. Sachs and A. M. Wolfe. Perturbations of a Cosmological Model and Angular Variations of the Microwave Background. *ApJ*, 147:73–+, January 1967. doi: 10.1086/148982. 192

A. A. Schekochihin, S. C. Cowley, S. F. Taylor, J. L. Maron, and J. C. McWilliams. Simulations of the Small-Scale Turbulent Dynamo. *ApJ*, 612:276–307, September 2004. doi: 10.1086/422547. 162

N. I. Shakura and R. A. Sunyaev. Black holes in binary systems. Observational appearance. *A&A*, 24:337–355, 1973. 18, 65, 161

N. I. Shakura and R. A. Sunyaev. A theory of the instability of disk accretion on to black holes and the variability of binary X-ray sources, galactic nuclei and quasars. *MNRAS*, 175:613–632, June 1976. 170

M. S. Shaw, R. W. Romani, G. Cotter, S. E. Healey, P. F. Michelson, A. C. S. Readhead, J. L. Richards, W. Max-Moerbeck, O. G. King, and W. J. Potter. Spectroscopy of Broad-line Blazars from 1LAC. *ApJ*, 748:49, March 2012. doi: 10.1088/0004-637X/748/1/49. 131, 148

M. S. Shaw, R. W. Romani, G. Cotter, S. E. Healey, P. F. Michelson, A. C. S. Readhead, J. L. Richards, W. Max-Moerbeck, O. G. King, and W. J. Potter. Spectroscopy of the Largest Ever γ-Ray-selected BL Lac Sample. *ApJ*, 764:135, February 2013. doi: 10.1088/0004-637X/764/2/135. 132, 148

Y. Shen, G. T. Richards, M. A. Strauss, P. B. Hall, D. P. Schneider, S. Snedden, D. Bizyaev, H. Brewington, V. Malanushenko, E. Malanushenko, D. Oravetz, K. Pan, and A. Simmons. A Catalog of Quasar Properties from Sloan Digital Sky Survey Data Release 7. *ApJS*, 194:45, June 2011. doi: 10.1088/0067-0049/194/2/45. 131

F. Shu, J. Najita, E. Ostriker, F. Wilkin, S. Ruden, and S. Lizano. Magnetocentrifugally driven flows from young stars and disks. 1: A generalized model. *ApJ*, 429:781–796, July 1994. doi: 10.1086/174363. 7

M. Sikora, M. C. Begelman, and M. J. Rees. Comptonization of diffuse ambient radiation by a relativistic jet: The source of gamma rays from blazars? *ApJ*, 421:153–162, January 1994. doi: 10.1086/173633. 61, 81

M. Sikora, H. Sol, M. C. Begelman, and G. M. Madejski. Radiation drag in relativistic active galactic nucleus jets. *MNRAS*, 280:781–796, June 1996. 7

M. Sikora, Ł. Stawarz, R. Moderski, K. Nalewajko, and G. M. Madejski. Constraining Emission Models of Luminous Blazar Sources. *ApJ*, 704:38–50, October 2009. doi: 10.1088/0004-637X/704/1/38. 67, 80

J. B. Simon and J. F. Hawley. Viscous and Resistive Effects on the Magnetorotational Instability with a Net Toroidal Field. *ApJ*, 707:833–843, December 2009. doi: 10.1088/0004-637X/707/1/833. 162

J. B. Simon, J. F. Hawley, and K. Beckwith. Resistivity-driven State Changes in Vertically Stratified Accretion Disks. *ApJ*, 730:94, April 2011. doi: 10.1088/0004-637X/730/2/94. 162, 168

Fergus Simpson. Scattering of Dark Matter and Dark Energy. *Phys. Rev.*, D82:083505, 2010. doi: 10.1103/PhysRevD.82.083505. 205

C. Skordis and A. Albrecht. Planck-scale quintessence and the physics of structure formation. *Phys. Rev. D*, 66(4):043523–+, August 2002. doi: 10.1103/PhysRevD.66.043523. 180

A. Sokolov, A. P. Marscher, and I. M. McHardy. Synchrotron Self-Compton Model for Rapid Nonthermal Flares in Blazars with Frequency-dependent Time Lags. *ApJ*, 613:725–746, October 2004. doi: 10.1086/423165. 43, 50

K. V. Sokolovsky, Y. Y. Kovalev, A. B. Pushkarev, and A. P. Lobanov. A VLBA survey of the core shift effect in AGN jets. I. Evidence of dominating synchrotron opacity. *A&A*, 532: A38, August 2011. doi: 10.1051/0004-6361/201016072. 9, 25, 27, 49, 101, 103, 104

M. Spada, G. Ghisellini, D. Lazzati, and A. Celotti. Internal shocks in the jets of radio-loud quasars. *MNRAS*, 325:1559–1570, August 2001. doi: 10.1046/j.1365-8711.2001.04557.x. 25, 43, 51, 72

E. J. Summerlin and M. G. Baring. Diffusive Acceleration of Particles at Oblique, Relativistic, Magnetohydrodynamic Shocks. *ApJ*, 745:63, January 2012. doi: 10.1088/0004-637X/745/1/63. 15, 17, 29, 72, 112, 130

H. R. Takahashi and Y. Masada. Stability of MRI-turbulent Accretion Disks. *ApJ*, 727:106, February 2011. doi: 10.1088/0004-637X/727/2/106. 162, 165, 168, 178

E. R. M. Tarrant, C. van de Bruck, E. J. Copeland, and A. M. Green. Coupled Quintessence and the Halo Mass Function. *ArXiv e-prints*, March 2011. 180, 202

F. Tavecchio, L. Maraschi, and G. Ghisellini. Constraints on the Physical Parameters of TeV Blazars. *ApJ*, 509:608–619, December 1998. doi: 10.1086/306526. 29

F. Tavecchio, J. Becerra-Gonzalez, G. Ghisellini, A. Stamerra, G. Bonnoli, L. Foschini, and L. Maraschi. On the origin of the γ-ray emission from the flaring blazar PKS 1222+216. *A&A*, 534:A86, October 2011. doi: 10.1051/0004-6361/201117204. 80

A. Tchekhovskoy, R. Narayan, and J. C. McKinney. Black Hole Spin and The Radio Loud/Quiet Dichotomy of Active Galactic Nuclei. *ApJ*, 711:50–63, March 2010. doi: 10.1088/0004-637X/711/1/50. 8, 9, 11, 143, 150

S. A. Thomas, F. B. Abdalla, and O. Lahav. Excess Clustering on Large Scales in the MegaZ DR7 Photometric Redshift Survey. *ArXiv e-prints*, December 2010. 203, 205

R. C. Tolman. Static Solutions of Einstein's Field Equations for Spheres of Fluid. *Physical Review*, 55:364–373, February 1939. doi: 10.1103/PhysRev.55.364. 2

S. Tremaine, D. O. Richstone, Y.-I. Byun, A. Dressler, S. M. Faber, C. Grillmair, J. Kormendy, and T. R. Lauer. A family of models for spherical stellar systems. *AJ*, 107:634–644, February 1994. doi: 10.1086/116883. 66

O. Tsang and J. G. Kirk. A synchrotron self-Compton model with low-energy electron cut-off for the blazar S5 0716+714. *A&A*, 476:1151–1160, December 2007. doi: 10.1051/0004-6361:20077962. 12, 25, 50

M.-H. Ulrich, L. Maraschi, and C. M. Urry. Variability of Active Galactic Nuclei. *ARA&A*, 35:445–502, 1997. doi: 10.1146/annurev.astro.35.1.445. 4, 44

C. M. Urry and P. Padovani. Unified Schemes for Radio-Loud Active Galactic Nuclei. *PASP*, 107:803–+, September 1995. doi: 10.1086/133630. 3, 8, 10, 24, 77, 132, 146

G. L. Vacca, L. P. L. Colombo, L. Vergani, and S. A. Bonometto. Dark Matter-Dark Energy Coupling Biasing Parameter Estimates from Cosmic Microwave Background Data. *ApJ*, 697:1946–1955, June 2009. doi: 10.1088/0004-637X/697/2/1946. 180

J. Väliviita, E. Majerotto, and R. Maartens. Large-scale instability in interacting dark energy and dark matter fluids. *JCAP*, 7:20–+, July 2008. doi: 10.1088/1475-7516/2008/07/020. 180, 181, 187, 194, 198, 204

J. Väliviita, R. Maartens, and E. Majerotto. Observational constraints on an interacting dark energy model. *MNRAS*, 402:2355–2368, March 2010. doi: 10.1111/j.1365-2966.2009.16115.x. 180, 181, 187

R. C. Vermeulen, P. M. Ogle, H. D. Tran, I. W. A. Browne, M. H. Cohen, A. C. S. Readhead, G. B. Taylor, and R. W. Goodrich. When Is BL Lac Not a BL Lac? *ApJL*, 452:L5, October 1995. doi: 10.1086/309716. 10, 41, 124

M. Vestergaard, X. Fan, C. A. Tremonti, P. S. Osmer, and G. T. Richards. Mass Functions of the Active Black Holes in Distant Quasars from the Sloan Digital Sky Survey Data Release 3. *ApJL*, 674:L1–L4, February 2008. doi: 10.1086/528981. 131

G. S. Vila, G. E. Romero, and N. A. Casco. An inhomogeneous lepto-hadronic model for the radiation of relativistic jets. Application to XTE J1118+480. *ArXiv e-prints*, December 2011. 50

J. Vink. Supernova remnants: the X-ray perspective. *A&ARv*, 20:49, December 2012. doi: 10.1007/s00159-011-0049-1. 15

N. Vlahakis and A. Königl. Relativistic Magnetohydrodynamics with Application to Gamma-Ray Burst Outflows. I. Theory and Semianalytic Trans-Alfvénic Solutions. *ApJ*, 596:1080–1103, October 2003. doi: 10.1086/378226. 11, 146

S. J. Wagner and A. Witzel. Intraday Variability In Quasars and BL Lac Objects. *ARA&A*, 33:163–198, 1995. doi: 10.1146/annurev.aa.33.090195.001115. 3

S. Weinberg. *The Quantum Theory of Fields*. June 1995. 37

C. Wetterich. Cosmology and the fate of dilatation symmetry. *Nuclear Physics B*, 302:668–696, June 1988. doi: 10.1016/0550-3213(88)90193-9. 180

C. Wetterich. An asymptotically vanishing time-dependent cosmological "constant". *A&A*, 301:321–+, September 1995. 180

J.-H. Woo and C. M. Urry. Active Galactic Nucleus Black Hole Masses and Bolometric Luminosities. *ApJ*, 579:530–544, November 2002. doi: 10.1086/342878. 116, 131

N. M. J. Woodhouse. *Special Relativity*. 1992. 6

J. Yoo, A. L. Fitzpatrick, and M. Zaldarriaga. New perspective on galaxy clustering as a cosmological probe: General relativistic effects. *Phys. Rev. D*, 80(8):083514–+, October 2009. doi: 10.1103/PhysRevD.80.083514. 201, 202

N. L. Zakamska, M. C. Begelman, and R. D. Blandford. Hot Self-similar Relativistic Magnetohydrodynamic Flows. *ApJ*, 679:990–999, June 2008. doi: 10.1086/587870. 12, 87

S. Zenitani and M. Hoshino. The Generation of Nonthermal Particles in the Relativistic Magnetic Reconnection of Pair Plasmas. *ApJL*, 562:L63–L66, November 2001. doi: 10.1086/337972. 15, 59, 112

S. Zenitani and M. Hoshino. Particle Acceleration and Magnetic Dissipation in Relativistic Current Sheet of Pair Plasmas. *ApJ*, 670:702–726, November 2007. doi: 10.1086/522226. 15, 59, 72, 112, 130